

(19) World Intellectual Property Organization  
International Bureau



A30517

(43) International Publication Date  
20 February 2003 (20.02.2003)

PCT

(10) International Publication Number  
WO 03/014674 A2

(51) International Patent Classification<sup>7</sup>: G01D

(21) International Application Number: PCT/US02/25246

(22) International Filing Date: 7 August 2002 (07.08.2002)

(25) Filing Language: English

(26) Publication Language: English

(30) Priority Data:

60/311,757	10 August 2001 (10.08.2001)	US
60/311,874	13 August 2001 (13.08.2001)	US
60/355,657	7 February 2002 (07.02.2002)	US

(71) Applicant: THE BOARD OF TRUSTEES OF THE LE-  
LAND STANFORD JUNIOR UNIVERSITY [US/US];  
Stanford University, Stanford, CA 94305 (US).

(72) Inventor: VAKOC, Benjamin, J.; 383 College Avenue,  
Palo Alto, CA 94306 (US).

(74) Agent: ALTMAN, Daniel, E.; KNOBBE, MARTENS,  
OLSON AND BEAR, LLP, 620 Newport Center Drive,  
16th Floor, Newport Beach, CA 92660 (US).

(81) Designated States (*national*): AE, AG, AL, AM, AT (util-  
ity model), AT, AU, AZ, BA, BB, BG, BR, BY, BZ, CA,  
CH, CN, CO, CR, CU, CZ (utility model), CZ, DE (util-  
ity model), DE, DK (utility model), DK, DM, DZ, EC, EE  
(utility model), EE, ES, FI (utility model), FI, GB, GD, GE,  
GH, GM, HR, HU, ID, IL, IN, IS, JP, KE, KG, KP, KR, KZ,  
LC, LK, LR, LS, LT, LU, LV, MA, MD, MG, MK, MN,  
MW, MX, MZ, NO, NZ, OM, PH, PL, PT, RO, RU, SD,  
SE, SG, SI, SK (utility model), SK, SL, TJ, TM, TN, TR,  
TT, TZ, UA, UG, UZ, VC, VN, YU, ZA, ZM, ZW.

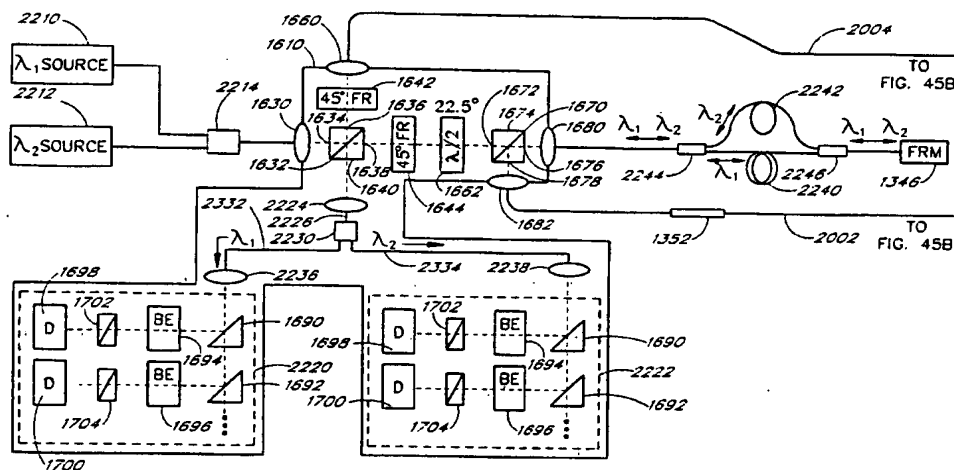
(84) Designated States (*regional*): ARIPO patent (GH, GM,  
KE, LS, MW, MZ, SD, SL, SZ, TZ, UG, ZM, ZW),  
Eurasian patent (AM, AZ, BY, KG, KZ, MD, RU, TJ, TM),  
European patent (AT, BE, BG, CH, CY, CZ, DE, DK, EE,  
ES, FI, FR, GB, GR, IE, IT, LU, MC, NL, PT, SE, SK,  
TR), OAPI patent (BF, BJ, CF, CG, CI, CM, GA, GN, GQ,  
GW, ML, MR, NE, SN, TD, TG).

Published:

— without international search report and to be republished  
upon receipt of that report

For two-letter codes and other abbreviations, refer to the "Guid-  
ance Notes on Codes and Abbreviations" appearing at the begin-  
ning of each regular issue of the PCT Gazette.

(54) Title: APPARATUS AND METHOD FOR PROCESSING OPTICAL SIGNALS FROM TWO DELAY COILS TO  
INCREASE THE DYNAMIC RANGE OF A SAGNAC-BASED FIBER OPTIC SENSOR ARRAY



**APPARATUS AND METHOD FOR PROCESSING OPTICAL SIGNALS  
FROM TWO DELAY COILS TO INCREASE THE DYNAMIC RANGE  
OF A SAGNAC-BASED FIBER OPTIC SENSOR ARRAY**

**Background of the Invention**

**Field of the Invention**

[0001] The present invention is in the field of fiber optic acoustic sensor arrays wherein light is propagated in the arrays and the effects of acoustic signals on the light returning from the arrays are analyzed to determine the characteristics of the acoustic signals.

**Description of the Related Art**

[0002] Fiber optic based acoustic sensors are promising alternatives to conventional electronic sensors. Included among their advantages are a high sensitivity, large dynamic range, light weight, and compact size. The ability to easily multiplex a large number of fiber optic sensors onto common busses also makes fiber optic sensors attractive for large-scale arrays. The recent successful incorporation of multiple small-gain erbium doped fiber amplifiers (EDFAs) into a fiber optic sensor array to increase the number of sensors that can be supported by a single fiber pair has made large-scale fiber optic sensor arrays even more competitive.

[0003] For acoustic detection, the fiber optic sensor of choice has been the Mach-Zehnder interferometric sensor. In any interferometric sensor, phase modulation is mapped into an intensity modulation through a raised cosine function. Because of this nonlinear transfer function, a sinusoidal phase modulation will generate higher order harmonics. An interferometer biased at quadrature (interfering beams  $\pi/2$  out of phase) has a maximized response at the first order harmonic and a minimized response at the second order harmonic. For this reason, quadrature is the preferred bias point. As the bias point drifts away from quadrature (for example, due to external temperature changes), the response at the first order harmonic decreases and the response at the second order harmonic increases. When the interferometer is biased at 0 or  $\pi$  out of phase, the first order harmonic disappears completely. This decreased

response at the first order harmonic (resulting from the bias points away from quadrature) is referred to as signal fading.

[0004] Because Mach-Zehnder interferometric sensors have an unstable bias point, they are especially susceptible to the signal fading problem just mentioned. In order to overcome signal fading, a demodulation of the returned signal is required. The typical demodulation technique is the Phase-Generated Carrier (PGC) scheme, which requires a path-mismatched Mach-Zehnder interferometric sensor. (See, for example, Anthony Dandridge, et al., *Multiplexing of Interferometric Sensors Using Phase Carrier Techniques*, Journal of Lightwave Technology, Vol. LT-5, No. 7, July 1987, pp. 947-952.) This path imbalance also causes the conversion of laser phase noise to intensity noise, which limits the performance of the Mach-Zehnder interferometric sensor arrays at low frequencies and places stringent requirements on the linewidth of the source. This narrow linewidth requirement has slowed the development of amplified Mach-Zehnder interferometric sensor arrays at 1.55  $\mu\text{m}$ .

[0005] The Sagnac interferometer has found widespread use in the fiber optic gyroscopes. (See, for example, B. Culshaw, et al., *Fibre optic gyroscopes*, Journal of Physics E (Scientific Instruments), Vol. 16, No. 1, 1983, pp. 5-15.) It has been proposed that the Sagnac interferometer could be used to detect acoustic waves. (See, for example, E. Udd, *Fiber-optic acoustic sensor based on the Sagnac interferometer*, Proceedings of the SPIE-The International Society for Optical Engineering, Vol. 425, 1983, pp. 90-91; Kjell Kråkenes, et al., *Sagnac interferometer for underwater sound detection: noise properties*, OPTICS LETTERS, Vol. 14, No. 20, October 15, 1989, pp. 1152-1145; and Sverre Knudsen, et al., *An Ultrasonic Fiber-Optic Hydrophone Incorporating a Push-Pull Transducer in a Sagnac Interferometer*, JOURNAL OF LIGHTWAVE TECHNOLOGY, Vol. 12, No. 9, September 1994, pp. 1696-1700.) Because of its common-path design, the Sagnac interferometer is reciprocal and therefore has a stable bias point, which eliminates signal fading and prevents the conversion of source phase noise into intensity noise. Therefore, the Sagnac interferometer is immune to the phase noise which limits the Mach-Zehnder interferometric sensors at low frequencies.

### Summary of the Invention

[0006] One aspect of the present invention is a sensor array that comprises a source of light and a first coupler that receives the light from the source. The first coupler couples a first portion of the light to a first coupler port and couples a second portion of the light to a second coupler port. An interferometric loop has a first end coupled to the first coupler port to receive the first portion of the light and has a second end coupled to the second coupler port to receive the second portion of the light. The interferometric loop propagates the first portion of the light in a first direction to the second coupler port and propagates the second portion of the light in a second direction opposite the first direction to the first coupler port. The interferometric loop comprises a plurality of sensors coupled in parallel between the first end of the interferometric loop and the second end of the interferometric loop. The sensors perturb light passing through the sensors in response to a sensed parameter (e.g., acoustic signals). A first plurality of couplers distribute the first portion of the light approximately equally to each of the sensors, collect the second portion of the light from each of the sensors, and propagate the collected light to the first end of the interferometric loop. A second plurality of couplers distribute the second portion of the light approximately equally to each of the sensors, collect the first portion of the light from each of the sensors, and propagate the collected light to the second end of the interferometric loop. At least one first amplifier is coupled between the first end of the interferometric loop and the first plurality of couplers. At least one second amplifier is coupled between the second end of the interferometric loop and the second plurality of couplers. A plurality of delay portions are connected between the first and second ends of the interferometric loops and the sensors. The delay portions have delays selected so that the light passing through each sensor is delayed by a different amount than the light passing through the other sensors. Preferably, the first plurality of couplers further comprise a first distribution coupler that receives the first portion of the light from the first amplifier and distributes the first portion of the light to a first plurality of internal amplifiers that are coupled between the first distribution coupler and a first plurality of internal couplers. The

first distribution coupler collects the second portion of the light from the first plurality of internal amplifiers and propagates the second portion of the light to the first amplifier. Also preferably, the second plurality of couplers further comprise a second distribution coupler that receives the second portion of the light from the second amplifier and distributes the second portion of the light to a second plurality of internal amplifiers that are coupled between the second distribution coupler and a second plurality of internal couplers. The second distribution coupler collects the first portion of the light from the second plurality of internal amplifiers and propagates the first portion of the light to the second amplifier. The first plurality of internal couplers distribute the first portion of the light to the plurality of sensors and collect the second portion of the light from the plurality of sensors. The second plurality of internal couplers distribute the second portion of the light to the plurality of sensors and collect the first portion of the light from the plurality of sensors. Advantageously, the source of light is a broadband source, such as, for example, a superfluorescent fiber source. Also advantageously, the first and second amplifiers and the first and second plurality of internal amplifiers are erbium-doped fiber amplifiers, and the first and second distribution couplers and the first and second pluralities of internal couplers comprise  $4 \times 4$  couplers.

[0007] Another aspect of the present invention is a method of sensing a parameter that comprises propagating light from a source of light through an interferometric loop such that approximately equal portions of the light counterpropagate in first and second directions in the loop. The light propagating in the first direction of the interferometric loop is amplified and coupled into a plurality of sensors such that approximately equal portions of the light propagating in the first direction are passed through each of the sensors. The light propagating in the second direction of the interferometric loop is amplified and coupled into the plurality of sensors such that approximately equal portions of the light propagating in the second direction are passed through each of the sensors. The light propagating in the first direction is caused to interfere with the light propagating in the second direction to generate a plurality of output signals responsive to light passing through each sensor in the first

and second directions. Each of the sensors perturbs light passing therethrough in response to a sensed parameter (e.g., an acoustic signal), and each of the sensors has a unique optical path length such that the light propagating in the first direction interferes with the light propagating in the second direction at a unique time.

[0008] Another aspect of the present invention is a sensor system that senses perturbations over first and second dynamic ranges. The sensor system comprises a source of input light pulses at a first wavelength and a source of input light pulses at a second wavelength. The system includes an array of sensors, a first optical delay path at the first wavelength, and a second optical delay path at the second wavelength. A first detection system is responsive to light at the first wavelength, and a second detection system is responsive to light at the second wavelength. An input/output system receives the input light pulses at the first wavelength and the second wavelength. The input/output system directs a first portion of each light pulse at the first wavelength having a first polarization through the array of sensors in a first direction, then through the first optical delay path, and then to the first detection system. The input/output system directs a second portion of each light pulse at the first wavelength in a second polarization orthogonal to the first polarization through the first optical delay path, then through the array of sensors in a second direction, and then to the first detection system. The first detection system detects variations in received light caused by perturbations varying over the first dynamic range. The input/output system directs a first portion of each light pulse at the second wavelength having a first polarization through the array of sensors in a first direction, then through the second optical delay path, and then to the second detection system. The input/output system directs a second portion of each light pulse at the second wavelength in a second polarization orthogonal to the first polarization through the second optical delay path, then through the array of sensors in a second direction, and then to the second detection system. The second detection system detects variations in received light caused by perturbations varying over the second dynamic range.

[0009] Another aspect of the present invention is an acoustic sensor system that senses acoustic signals over first and second dynamic ranges. The acoustic sensor

system comprises a source of input light pulses at a first wavelength and a source of input light pulses at a second wavelength. The acoustic sensor system further includes an array of acoustic sensors, a first optical delay path at the first wavelength, and a second optical delay path at the second wavelength. A first detection system is responsive to light at the first wavelength. A second detection system is responsive to light at the second wavelength. An input/output system receives the input light pulses at the first wavelength and the second wavelength. The input/output system directs a first portion of each light pulse at the first wavelength having a first polarization through the array of acoustic sensors in a first direction, then through the first optical delay path, and then to the first detection system. The input/output system directs a second portion of each light pulse at the first wavelength in a second polarization orthogonal to the first polarization through the first optical delay path, then through the array of acoustic sensors in a second direction, and then to the first detection system. The first detection system detects variations in received light caused by acoustic signals varying over the first dynamic range. The input/output system directs a first portion of each light pulse at the second wavelength having a first polarization through the array of acoustic sensors in a first direction, then through the second optical delay path, and then to the second detection system. The input/output system directs a second portion of each light pulse at the second wavelength in a second polarization orthogonal to the first polarization through the second optical delay path, then through the array of acoustic sensors in a second direction, and then to the second detection system. The second detection system detects variations in received light caused by acoustic signals varying over the second dynamic range.

[0010] Another aspect of the present invention is a method of sensing perturbations. The method comprises inputting light pulses of a first wavelength into an array of sensors that includes a first optical delay path at the first wavelength. Light pulses of a second wavelength are also input into the array of sensors. The array of sensors includes a second optical delay path at the second wavelength. The second optical delay path has a different optical length than the first optical delay path. A first portion of each light pulse at the first wavelength having a first polarization is

directed through the array of sensors in a first direction, then through the first optical delay path. A second portion of each light pulse at the first wavelength in a second polarization orthogonal to the first polarization is directed through the first optical delay path, then through the array of sensors in a second direction. Variations in the first and second portions of each light pulse at the first wavelength caused by perturbations varying over a first dynamic range are detected. A first portion of each light pulse at the second wavelength having a first polarization is directed through the array of sensors in a first direction, then through the second optical delay path. A second portion of each light pulse at the second wavelength in a second polarization orthogonal to the first polarization is directed through the second optical delay path, then through the array of sensors in a second direction. Variations in the first and second portions of each light pulse at the second wavelength caused by perturbations varying over a second dynamic range are detected. In particular embodiments of the method, the perturbations are acoustic signals.

#### **Brief Description of the Drawings**

[0011] The present invention will be described below in connection with the accompanying drawing figures in which:

[0012] Figure 1 illustrates an exemplary Sagnac interferometer having a single sensing loop;

[0013] Figure 2 illustrates a Sagnac sensor array in accordance with the present invention wherein each rung of a sensor array forms an additional Sagnac interferometer;

[0014] Figure 3 illustrates a Sagnac sensor array which includes erbium-doped fiber amplifiers to regenerate signal power lost to coupling and dissipative losses;

[0015] Figure 4 illustrates a graph of the frequency response of a Sagnac interferometer in accordance with present invention compared with the three dominant ocean floor noises;

[0016] Figure 5 illustrates graphs of the maximum and minimum acoustic signal detectable by a Mach-Zehnder interferometer and detectable by a Sagnac interferometer



in accordance with the present invention, showing the relatively constant dynamic range of a Sagnac interferometer over a wide range of frequencies;

[0017] Figure 6 illustrates graphs of the minimum detectable acoustic signal versus frequency for three Sagnac interferometer configurations having different lengths of fiber in the hydrophone and the delay loop;

[0018] Figure 7 illustrates a Sagnac interferometer in accordance with the present invention which includes an additional delay loop to increase the dynamic range of the interferometer;

[0019] Figure 8 illustrates a graph of the dynamic range provided by the interferometer of Figure 7;

[0020] Figure 9A illustrates the positioning of the delay loop of the interferometer in the dry end of a sensor array system;

[0021] Figure 9B illustrates the positioning of the delay loop of the interferometer in the wet end of a sensor array system;

[0022] Figure 10 illustrates the Sagnac interferometer of Figure 9B with annotations showing the lengths used in calculations of the effects of phase modulation;

[0023] Figure 11 illustrates a technique for winding the delay loop so as to reduce the effects of the acoustic wave upon the delay loop;

[0024] Figure 12 illustrates a Sagnac interferometer in accordance with the present invention which includes empty rungs which detect distributed pick-up noise which can be subtracted from the signals generated by the sensors;

[0025] Figure 13 illustrates a Sagnac interferometer in accordance with the present invention which includes a depolarizer to reduce the effects of polarization induced fading;

[0026] Figure 14 illustrates a Sagnac interferometer which utilizes frequency divisional multiplexing;

- [0027] Figure 15 illustrates a graph which shows the generation of the beat signals between the delayed modulation signal and the returning sensor signals in the interferometer of Figure 14;
- [0028] Figure 16 illustrates a Sagnac interferometer which utilizes code division multiplexing;
- [0029] Figure 17 illustrates the architecture of a folded Sagnac acoustic fiber sensor array;
- [0030] Figure 18 illustrates a graph of the number of returned pulses per time interval, showing the separation in time of signal pulses and noise pulses;
- [0031] Figure 19 illustrates a folded Sagnac acoustic fiber sensor array having a second delay loop to provide extended dynamic range;
- [0032] Figure 20 illustrates a folded Sagnac acoustic fiber sensor array having a phase modulator and nulling circuitry in place of the reflector in Figure 17;
- [0033] Figure 21 illustrates a further alternative embodiment of Figure 19 in which the two delay loops are connected to different ports of the coupler;
- [0034] Figure 22 illustrates an alternative embodiment of a fiber optic acoustic sensor array system using a Faraday rotating mirror;
- [0035] Figures 23A, 23B and 23C illustrate further alternative embodiments of a fiber optic acoustic sensor array which utilize an unpolarized light source in combination with a depolarizer, a polarization beam splitter and a Faraday rotating mirror;
- [0036] Figure 24 illustrates an alternative embodiment of a folded fiber optic acoustic sensor array which utilizes an unpolarized light source in combination with an optical circulator, a 2×2 coupler, and a non-reciprocal phase shifter;
- [0037] Figure 25 illustrates an alternative embodiment of a folded fiber optic acoustic sensor array similar to Figure 24 in which the depolarizer is located in the second array input/output fiber;

- [0038] Figure 26 illustrates a first preferred embodiment of the non-reciprocal  $\pi/2$  phase shifter in Figures 24 and 25, which illustrates the effect on the polarization of the light propagating in a first direction through the phase shifter;
- [0039] Figure 27 illustrates the effect on the polarization of the light propagating in a second (opposite) direction through the phase shifter of Figure 26;
- [0040] Figure 28 illustrates an alternative preferred embodiment of the non-reciprocal  $\pi/2$  phase shifter in Figures 24 and 25, which illustrates the effect on the polarization of the light propagating in a first direction through the phase shifter;
- [0041] Figure 29 illustrates the effect on the polarization of the light propagating in a second (opposite) direction through the phase shifter of Figure 28;
- [0042] Figure 30 illustrates a further alternative embodiment of a folded fiber optic acoustic sensor array, which utilizes polarization-based biasing for multiple detectors, wherein each detector has a bias point which can be set independently of the bias points of the other detectors;
- [0043] Figure 31 illustrates an alternative embodiment of a folded fiber optic acoustic sensor array similar to Figure 30 in which the depolarizer is located in the second array input/output fiber;
- [0044] Figure 32 illustrates an alternative embodiment of a folded fiber optic acoustic sensor array similar to Figure 30 in which an optical circulator replaces the 2×2 coupler;
- [0045] Figure 33 illustrates an alternative embodiment of a folded fiber optic acoustic sensor array similar to Figure 32 in which the depolarizer is located in the second array input/output fiber;
- [0046] Figure 34 illustrates a further alternative embodiment of a folded Sagnac sensor array, which includes a combined input/output subsystem;
- [0047] Figure 35 illustrates an alternative embodiment of a folded fiber optic acoustic sensor array similar to Figure 34 in which the depolarizer is located in the second array input/output fiber;

- [0048] Figure 36 illustrates a further alternative embodiment of a folded fiber optic acoustic sensor array similar to Figures 34 and 35 in which the detectors are coupled to the input/output subsystem by optical fibers to permit the detectors to be located remotely;
- [0049] Figure 37 illustrates an alternative embodiment of a 16-sensor array for use in combination with the front end systems described in Figures 30-36;
- [0050] Figure 38, comprising Figure 38A and 38B, illustrates an alternative sensor array that includes 16 sensors in an amplified tree-structure telemetry using a polarization-based front end similar to the system described above in connection with Figures 30-36;
- [0051] Figure 39A illustrates the returned pulse train measured at one of the detectors in Figure 38A for a pulse width of 50 nanoseconds and a repetition frequency of 0.942 MHz (1.06-microsecond spacing);
- [0052] Figure 39B illustrate the returned pulse train measured at one of the detectors in Figure 38A for a pulse width of 50 nanoseconds and a repetition frequency of 1.042 MHz (0.96-microsecond spacing);
- [0053] Figure 40A illustrates an oscilloscope trace representing the measured power detected from one of the sensors in Figure 38B when a peak-to-peak phase modulation of greater than  $\pi$  is induced in a PZT transducer in series with the sensor;
- [0054] Figure 40B illustrates the results of measuring the visibility of the sensor in accordance with Figure 40A for eight random settings of a common polarization controller positioned in one of the input/output fibers of the array in Figure 38B;
- [0055] Figure 41 illustrates the results of measurement of the detected response from a single detector configuration when a fiber wrapped PZT is used to simulate an acoustic signal and an amplitude modulation at 3.6 kHz was placed on the optical signal from the source using a lithium niobate modulator in the signal path from the source to the collimator in Figure 38A;

[0056] Figures 42A, 42B and 42 C illustrate the effects of source power on the measured noise at the detector (receiver) as a function of sensor count for DC source currents of 1.4  $\mu\text{A}$ , 4.05  $\mu\text{A}$  and 9.89  $\mu\text{A}$ , respectively;

[0057] Figure 43A illustrates a plot of the minimum detectable acoustic signal in a 1-second integration time and also illustrates a plot of the maximum detectable signal defined as that which produces a  $1 \text{ rad}/\sqrt{\text{Hz}}$  phase signal for a delay time through the delay loop of 50 microseconds;

[0058] Figure 43B illustrates a plot of the minimum detectable acoustic signal in a 1-second integration time and also illustrates a plot of the maximum detectable signal defined as that which produces a  $1 \text{ rad}/\sqrt{\text{Hz}}$  phase signal for the same parameters as in Figure 43A but for a delay time through the delay loop of 500 nanoseconds;

[0059] Figure 44A illustrates the phase variation in a sensor caused an acoustic signal applied to one of the sensors of Figure 38B;

[0060] Figures 44B and 44C are plots of the induced phase difference due to the phase signal of Figure 44A for the signal which travels through the longer delay loop (Figure 44B) and the shorter delay loop (Figure 44C);

[0061] Figures 45A illustrates a front end for an acoustic sensor array, which is similar to the front end of Figure 38A except that the front end of Figure 45A includes a first signal source that outputs a first sequence of optical signal pulses at a first wavelength  $\lambda_1$  and includes a second signal source that outputs a second sequence of optical signal pulses at a second wavelength  $\lambda_2$ , and includes a first delay loop for the optical signal pulses at the first wavelength and a second delay loop for the optical signal pulses at the second wavelength;

[0062] Figure 45B illustrates an acoustic sensor array connected to the front end of Figure 45A;

[0063] Figure 46A is a plot of the signal from a given sensor that passes through the longer delay loop of Figure 45A;

[0064] Figure 46B illustrates the use of linear extrapolation to predict a fringe count of  $\beta(2\tau)$  from the plot of Figure 46A; and

[0065] Figure 47 is a plot of the maximum value of A before fringe count errors occur as a function of frequency for  $T_d^{\lambda} = 100$  microseconds,  $\tau = 50$  microseconds, and for  $T_d^{\lambda} = 100$  nanoseconds.

### Detailed Description of the Preferred Embodiments

[0066] The present invention is described below in connection with an array of acoustic sensors (e.g., hydrophones) in a Sagnac loop. Before describing the preferred embodiments, a brief review of the operation of a single loop Sagnac acoustic sensor is provided.

#### Single Loop Sagnac Acoustic Sensor

[0067] A simple Sagnac-based acoustic sensor 100 is shown in Figure 1. The Sagnac loop is divided into two portions, a delay loop 102 and a hydrophone 104. The delay loop 102 is simply a large length of fiber, typically greater than 1 km. The hydrophone 104 is a portion of fiber in which an acoustic wave is transformed into a phase modulation of an optical signal propagating through the fiber. A high responsivity to acoustic waves is typically accomplished by selecting optimized coatings for the section of fiber in the hydrophone 104, and wrapping the fiber around a mandrel of suitable composition. (See, for example, J.A. Bucaro, et al., *Optical fibre sensor coatings*, Optical Fiber Sensors, Proceedings of the NATO Advanced Study Institute, 1986, pp. 321-338.) The length of fiber wrapped around the hydrophone 104 is typically 10 meters to 100 meters. Light from a source 110, such as, for example, a superfluorescent fiber source (SFS), is split into clockwise (CW) and counter-clockwise (CCW) beams by a 3×3 coupler 112. The operation of the 3×3 coupler 112 is well-known and is described, for example, in Sang K. Sheem, *Fiber-optic gyroscope with [3×3] directional coupler*, Applied Physics Letters, Vol. 37, No. 10, 15 November 1980, pp. 869-871.

[0068] Although described herein as using a 3×3 coupler 112, other couplers (e.g., a 2×2 coupler, a 4×4 coupler, etc.) can be used with alternative embodiments of the

present invention. For example, to use a 2×2 coupler, both ports of one side are used to create the Sagnac interferometer. One port of the other side is a detection port. The remaining port is used to launch light into the array and can also be used as a detection port if a coupler or circulator is employed (in a similar manner as is done with fiber optic gyroscopes). In general, any n×m coupler can be employed by using two ports of one side of the coupler to create the Sagnac interferometer and using the ports on the other side of the coupler as detection ports, launching ports, or both.

[0069] After splitting, the CW beam travels through the delay loop 102 first and then through the hydrophone 104, while the CCW beam travels through the hydrophone 104 first and then through the delay loop 102. During a time delay  $T_{delay}$  between a time when the CW beam travels through the hydrophone 104 and a time when the CCW beam travels through the hydrophone 104, the acoustic signal and likewise the acoustically induced phase modulation in the hydrophone 104 changes. This change in phase modulation is mapped into a phase difference between the counter-propagating beams, which is converted into an intensity modulation when the beams recombine at the 3×3 coupler 112. This intensity modulation is then detected by a first detector 120 and a second detector 122 or by only one of the two detectors.

[0070] More explicitly, if an acoustic signal induces a phase modulation  $\phi_h \cos(\Omega t)$  in the fiber of the hydrophone 104, the resulting phase modulation between the interfering beams at the hydrophone 104,  $\phi_{int}(t)$ , is given by:

$$\begin{aligned}\phi_{int}(t) &= \phi_h \cos(\Omega t) - \phi_h \cos(\Omega(t + T_{delay})) \\ &= 2\phi_h \sin\left(\frac{\Omega \cdot T_{delay}}{2}\right) \sin\left(\Omega t + \frac{\Omega \cdot T_{delay}}{2}\right)\end{aligned}\quad (1)$$

where  $T_{delay}$  is the travel time through the delay loop. Thus,  $\phi_{int}(t)$  is a function of the hydrophone modulation  $\phi_h$  and the product of the acoustic modulation frequency,  $\Omega$ , with the loop delay,  $T_{delay}$ . This differs from a Mach-Zehnder interferometric sensor in which  $\phi_{int}(t)$  is a function of only the hydrophone modulation  $\phi_h$ . Maximum sensitivity is achieved in the Sagnac loop acoustic sensor when the product of the

acoustic frequency,  $\Omega$ , and the time delay,  $T_{\text{delay}}$ , is an odd multiple of  $\pi$  (maximum value of the first sine term in Equation 1). The acoustic frequency which makes this product  $\pi$  is called the proper frequency of the loop, which is the lowest frequency at which maximum sensitivity is achieved. Most underwater sensing applications are concerned with the detection of acoustic frequencies below 10 kHz. For the proper loop frequency to be less than 10 kHz, a delay time of at least 50 microseconds and therefore a delay loop length of at least 10 km is required. Thus, the Sagnac acoustic sensor 100 requires a large amount of fiber for the detection of low acoustic frequencies ( $<10$  kHz).

[0071] The common-path design inherent to the Sagnac interferometer has many advantages over a Mach-Zehnder interferometer in addition to the stable bias point and elimination of phase noise already mentioned. A Sagnac interferometer allows the use of a short-coherence length, broadband source, such as a superfluorescent fiber source (SFS), an example of an amplified spontaneous emission (ASE) source. Such sources are inexpensive and can readily provide high powers. It has been shown that the use of the  $3 \times 3$  coupler passively biases the Sagnac acoustic sensor near quadrature. (See, Sang K. Sheem, *Fiber-optic gyroscope with  $[3 \times 3]$  directional coupler*, Applied Physics Letters, Vol. 37, No. 10, 15 November 1980, pp. 868-871; and H. Poisel, et al., *Low-cost fibre-optic gyroscope*, Electronics Letters, Vol. 26, No. 1, 4<sup>th</sup> January 1990, pp. 69-70.) By subtracting the signals from the two detection ports of the  $3 \times 3$  coupler, the source excess noise, which is the limiting noise source of SFS sources, can be subtracted while phase-modulation induced intensity variations due to the hydrophone are added. This allows a Sagnac interferometer to approach near shot-noise limited performance. (See, Kjell Kråkenes, et al., *Sagnac interferometer for underwater sound detection: noise properties*, OPTICS LETTERS, Vol. 14, No. 20, October 15, 1989, pp. 1152-1145.)

[0072] Previous work on Sagnac-based acoustic sensors has been limited to a single sensor configuration. Because of the inherent advantages of the Sagnac interferometer, Applicants have determined that it is desirable to replace the Mach-Zehnder interferometric sensors in a large-scale array with Sagnac based sensors.



Each Sagnac sensor 100 discussed above requires many kilometers of fiber, making the insertion of numerous such sensors into a large-scale array impractical. Research into using recirculating delay loops to reduce the fiber length requirement has produced sensors which use significantly less fiber but suffer from high noise due to the incorporation of EDFAs within the recirculating loop. (See, for example, J.T. Kringlebotn, et al., *Sagnac Interferometer Including A Recirculating Ring With An Erbium-doped Fibre Amplifier*, OFS '92 Conference Proceedings, pp. 6-9.) A novel approach for decreasing the fiber required is described below.

#### **Novel Sensor Array Based on the Sagnac Interferometer**

[0073] As set forth below, Applicants have discovered a novel system which reduces the amount of fiber needed for a Sagnac-based large scale array by multiplexing multiple sensors onto the same delay loop, producing a practical Sagnac sensor array (SSA). As illustrated in Figure 2, a Sagnac sensor array 200 in accordance with the present invention includes an array 210 of hydrophones 212(i) in a ladder configuration which are attached to a single delay loop 214. For example, Figure 2 shows a Sagnac sensor array 210 having N hydrophones 212(1), 212(2) ... 212(N) in respective rungs 216(1), 216(2) ... 216(N). Each rung 216(i) in the Sagnac sensor array 210 comprises a single fiber wrapped around a respective hydrophone 212(i). Every path from a 3×3 coupler 220 through the delay loop 214 and array 210 and back to the coupler 220 comprises a separate Sagnac interferometer. Therefore, for an array of N sensors 212, there are N separate Sagnac interferometers, each of which behaves like the single loop Sagnac sensor 100 shown in Figure 1. Each Sagnac interferometer measures the acoustic signal at a separate point in space, i.e., the location of the hydrophone 212(i). For example, the Sagnac interferometer comprising the delay loop 214 and the rung 216(1) measures the acoustic signal at hydrophone 212(1). In addition, each Sagnac interferometer also picks up acoustic signals (e.g., noise) elsewhere in the loop, which noise is advantageously reduced, as will be discussed below.

[0074] The Sagnac sensor array 200 is easiest understood in a time-division multiplexed (TDM) configuration (non-TDM schemes are discussed later). A source

222 (which may advantageously comprise a conventional pulsed source or may comprise a cw source with an external modulator) generates a light pulse which enters the Sagnac loop via a third port of the coupler 220 and propagates in both the CW and CCW directions as indicated in Figure 2. Upon reaching the array 210, the CCW pulse is split into a train of N separate pulses. At this point, the CW input pulse has not yet reached the array 210 and is still a single pulse. When the CW pulse reaches the array 210, it also is split into a train of N pulses. Each pulse in the CW train returns to the 3×3 coupler 220 after traveling through a respective rung 216(i) and interferes with the pulse in the CCW train which has traveled the same rung 216(i) in the opposite direction. Thus, N pulses are detected by a first detector 230 and a second detector 232, and each pulse comprises the CW and CCW pulses of one of the N Sagnac loops (i.e., the two pulses which have traveled in opposite directions through the same respective rung 216(i)). Because the pulses which travel through different combinations of rungs do not travel identical optical paths, such pulses are not coincident in time at the coupler 220, and thus do not interfere with each other at the coupler 220. The pulse widths should be smaller than the differential delay between adjacent sensors so that the pulses from adjacent sensors do not overlap.

[0075] As illustrated in Figure 3, small-gain erbium doped fiber amplifiers (EDFAs) 240 are advantageously added to the array portion 210 just as EDFAs have been added to Mach-Zehnder interferometric sensor arrays. (See, for example, Craig W. Hodgson, et al., *Optimization of Large-Scale Fiber Sensor Arrays Incorporating Multiple Optical Amplifiers-Part I: Signal-to-Noise Ratio*, JOURNAL OF LIGHTWAVE TECHNOLOGY, Vol. 16, No. 2, February 1998, pp. 218-223; Craig W. Hodgson, et al., *Optimization of Large-Scale Fiber Sensor Arrays Incorporating Multiple Optical Amplifiers-Part II: Pump Power*, JOURNAL OF LIGHTWAVE TECHNOLOGY, Vol. 16, No. 2, February 1998, pp. 224-231; Jefferson L. Wagener; et al., *Novel Fiber Sensor Arrays Using Erbium-Doped Fiber Amplifiers*, JOURNAL OF LIGHTWAVE TECHNOLOGY, Vol. 15, No. 9, September 1997, pp. 1681-1688; and C.W. Hodgson, et al., *Large-scale interferometric fiber sensor arrays with multiple optical amplifiers*, OPTICS

LETTERS, Vol. 22, No. 21, November 21, 1997, pp. 1651-1653.) The EDFAs 240 increase the number of sensors which can be supported by a single array 210 by regenerating the signal power which is lost to coupling and dissipative losses. The EDFAs are advantageously pumped by one or more pump laser sources 242 via a splitting coupler 244 and via a first wavelength division multiplexing (WDM) coupler 246 and a second WDM coupler 248.

[0076] Because it uses the Sagnac architecture, the Sagnac sensor array 200 has all of the advantages of the single loop Sagnac based sensor 100 discussed above. The common-path design eliminates the conversion of source phase noise into intensity noise at the interfering coupler 220. The source 222 can be a fiber ASE (amplified spontaneous emission) source (i.e., the SFS discussed above), which provides high powers inexpensively at 1.55  $\mu\text{m}$ . Passive biasing near quadrature is achievable for all sensors by using the 3 $\times$ 3 coupler 220. Also, the 3 $\times$ 3 coupler 220 provides a convenient means to detect two interferometric outputs at the detectors 230, 232, and to use the outputs of the two detectors to subtract source excess noise. (See, for example, K. Krakenes, et. al., *Sagnac interferometer for underwater sound detection: noise properties*, OPTICS LETTERS, Vol. 14, 1989, pp. 1152-1154, which shows the use of two detectors in combination with a single Sagnac interferometer.)

[0077] The properties of this novel Sagnac sensor array 200 will be discussed more specifically below followed by a more detailed discussion of the frequency response and dynamic range which result from the use of a Sagnac interferometer. Thereafter, a calculation of the magnitude of the distributed pick-up from the non-hydrophone fiber loop segments will be described, along with a technique for reducing this pick-up magnitude. Polarization will also be addressed below. New sources of noise which are introduced by the Sagnac design are then discussed. Finally, multiplexing schemes other than TDM for the Sagnac sensor array are presented.

[0078] Although the present invention is described above with respect to a single sensor in each rung 216(i) of the array 210, it should be understood that each rung 216(i) may advantageously comprise a subarray having multiple sensors, such as are

described, for example, in allowed U.S. Patent Application No. 08/814,548, filed on March 11, 1997, which is incorporated by reference herein. (See, also, C.W. Hodgson, et al., *Large-scale interferometric fiber sensor arrays with multiple optical amplifiers*, Optics Letters, Vol. 22, 1997, pp. 1651-1653; J.L. Wagener, et al., *Novel fiber sensor arrays using erbium-doped fiber amplifiers*, Journal of Lightwave Technology, Vol. 15, 1997, pp. 1681-1688; C.W. Hodgson, et al., *Optimization of large-scale fiber sensor arrays incorporating multiple optical amplifiers, Part I: signal-to-noise ratio*, Journal of Lightwave Technology, Vol. 16, 1998, pp. 218-223; and C.W. Hodgson, et al., *Optimization of large-scale fiber sensor arrays incorporating multiple optical amplifiers, Part II: pump power*, Journal of Lightwave Technology, Vol. 16, 1998, pp. 224-231.)

### Frequency Response

[0079] As set forth above, the Sagnac sensor has a frequency dependent response given by Equation 1. At frequencies well below the proper frequency of the loop, defined as  $1/(2 \cdot T_{\text{delay}})$ , the minimum detectable acoustic signal scales with the inverse of acoustic frequency. This decreased acoustic sensitivity at low frequencies has been a major concern for the Sagnac acoustic sensor. However, it has been pointed out that this decreased sensitivity at low frequencies is fortunately matched by an increasing ocean noise floor (See, for example, Sverre Knudsen, *Ambient and Optical Noise in Fiber-Optic Interferometric Acoustic Sensors*, Fiber-Optic Sensors Based on the Michelson and Sagnac Interferometers: Responsivity and Noise Properties, Thesis, Chapter 3, Norwegian University of Science and Technology, 1996, pp. 37-40.) Ideally, it would be desirable if the minimum detectable acoustic signal of an array at a given frequency were to be a constant amount below the ocean noise floor at that frequency. Thus, the minimum detectable acoustic signal would also increase at lower frequencies to match the increasing ocean noise floor. The frequency response of the Sagnac sensor array 200 of the present invention in fact does provide a good match between the ocean noise floor and acoustic sensitivity. This is illustrated in Figure 4, where the minimum detectable acoustic signal for a Sagnac sensor array is plotted as a curve 250 assuming an optical noise floor of  $10 \mu\text{rad}/\sqrt{\text{Hz}}$ , a hydrophone

phase responsivity of  $3.2 \times 10^{-7}$  rad/ $\mu$ Pa and a delay loop length of 20 km. (The vertical axis is in dB relative to a baseline of 1  $\mu$ rad/ $\sqrt{\text{Hz}}$ .) Also plotted in Figure 4 are the ocean noise floors for the three dominant ocean noise sources at these frequencies and a resulting sum of the noise from the three sources. A curve 252 represents the noise from ocean turbulence, earthquakes, volcanic eruptions, and the like. A curve 253 represents light shipping noise. A curve 254 represents DSS0 (distant shipping and storms) noise. A curve 256 represents the sum of the noise floors from the three dominant sources (i.e., the sum of the curves 252, 253 and 254). (See, for example, Robert J. Urick, *The noise background of the sea: ambient noise level*, Principles of Underwater Sound, 3rd Ed., Chapter 7, McGraw-Hill, 1983, pp. 202-236.) The minimum detectable acoustic signal of the Sagnac sensor array 200 increases in such a way as to provide a nearly constant amount of detectable signal below the ocean noise floor at all frequencies below 10 kHz. Thus, the frequency-dependent response of the Sagnac sensor array 200 does not prohibit low-frequency acoustic detection. The Mach-Zehnder array shows the same trend as the Sagnac sensor array, namely a decreasing sensitivity towards lower frequencies, but in the Mach-Zehnder array, the decreasing sensitivity is smaller than in the Sagnac-based sensor.

[0080] Although both the Mach-Zehnder interferometer and Sagnac sensor array 200 have similar frequency-dependent responses, the source of their frequency responses is fundamentally different. The increasing minimum detectable signal in the Mach-Zehnder interferometer sensor array is due to an increasing optical noise floor. The cause of this increasing optical noise floor is the phase noise introduced by the path-imbalanced Mach-Zehnder interferometer. Thus, although the noise floor is 10  $\mu$ rad/ $\sqrt{\text{Hz}}$  at 10 kHz, it increases towards lower frequencies. In the Sagnac sensor array 200, the increasing minimum detectable acoustic signal is due to the  $\sin(\Omega T_{\text{delay}}/2)$  term in Equation 1, and not to an increasing optical noise floor. The optical noise floor remains a constant 10  $\mu$ rad/ $\sqrt{\text{Hz}}$  over the entire frequency range.

[0081] The significance of this difference can be seen by examining the dynamic range of the Mach-Zehnder interferometric sensor array and Sagnac sensor array 200,

illustrated in Figure 5. The dynamic range of a sensor is limited by the minimum and maximum detectable phase shifts. For interferometric sensors, the maximum detectable phase shift is limited by the nonlinear response of the interferometer and the minimum detectable phase shift by the optical noise floor. Both the Mach-Zehnder interferometric sensor array and the Sagnac sensor array have maximum detectable phase shifts which are constant over the acoustic frequency range. However, the Sagnac sensor array 200 also has a flat minimum detectable phase shift because it has a flat optical noise floor, while the Mach-Zehnder interferometric sensor array suffers an increasing minimum detectable phase shift due to an increasing optical noise floor caused by the phase noise introduced by the path imbalanced interferometer. The Sagnac sensor array 200 thus has a constant dynamic range at all acoustic frequencies, while the Mach-Zehnder interferometric sensor array has a decreased dynamic range at low acoustic frequencies. This is illustrated in Figure 5, wherein the minimum and maximum detectable acoustic signals (in dB arbitrary units) are plotted for the Sagnac sensor array 200 and a Mach-Zehnder interferometric sensor array. As shown in Figure 5, both arrays have an approximately 100 dB dynamic range above 1 kHz, where phase noise does not limit the Mach-Zehnder interferometric sensor array. At 10 Hz, phase noise dominates the Mach-Zehnder interferometric sensor array, and its dynamic range is reduced to approximately 74 dB. Meanwhile, the dynamic range of the Sagnac sensor array 200 remains at approximately 100 dB.

[0082] It is interesting to examine the frequency response of the Sagnac sensor array 200 at frequencies well below the loop proper frequency as a function of the delay loop length and hydrophone responsivity. At these frequencies, the  $\sin(\Omega T_{\text{delay}}/2)$  factor in Equation 1 can be approximated as  $\Omega T_{\text{delay}}/2$ , showing that the responsivity of the Sagnac sensor array 200 is proportional to the product of  $\phi_h$  and  $T_{\text{delay}}$ .  $\phi_h$  itself is proportional to the amount of fiber in each hydrophone 212(i), and  $T_{\text{delay}}$  is proportional to the amount of fiber in the delay loop 214. Thus, the responsivity at frequencies well below the loop proper frequency is proportional to the product of the hydrophone fiber length and delay fiber length. Figure 6 plots the

minimum detectable acoustic signal for several Sagnac sensor array configurations in which the product of the length of the fiber in each hydrophone 212(i) and the length of the fiber in the delay loop 214 is constant, but the relative distribution of fiber between the delay loop 214 and each hydrophone 212(i) changes. For example, a curve 260 represents the frequency response of a Sagnac sensor array 200 having 45 km of fiber in its delay loop 214 and 100 meters of fiber in each hydrophone 212(i); a curve 262 represents the frequency response of a Sagnac sensor array 200 having 30 km of fiber in its delay loop 214 and 150 meters of fiber in each hydrophone 212(i); and a curve 264 represents the frequency response of a Sagnac sensor array 200 having 15 km of fiber in its delay loop 214 and 300 meters of fiber in each hydrophone 212(i). As illustrated, each Sagnac sensor array 200 has the same sensitivity at low frequencies, but approaches a maximum sensitivity at different frequencies given by their respective loop proper frequencies. Thus, for a given minimum detectable acoustic signal at low frequencies, there is still some freedom in choosing the fiber lengths of the delay loop 214 and the hydrophones 212(i). This freedom may be used to help the Sagnac sensor array 200 satisfy other criteria, such as minimizing the total amount of fiber required or minimizing the delay loop length.

#### **Increasing the Dynamic Range of the Sagnac sensor array**

[0083] As discussed above, the Sagnac sensor array 200 has a larger dynamic range at low acoustic frequencies than the Mach-Zehnder interferometric sensor array because it is immune to phase noise. Ideally, an array 200 provides enough dynamic range to detect the strongest and weakest acoustic signal which are likely to be encountered. This requirement often translates into a required dynamic range of approximately 150 dB. In order to achieve such a large dynamic range in a Mach-Zehnder interferometric sensor array, two separate sensors with different phase responsivities are required, with each detecting a fraction of the total 150 dB dynamic range. The obvious disadvantage to this scheme is that it requires two sensor arrays (i.e., twice as many hydrophones, rungs, sources and detectors). Effectively, an array which can support N hydrophones can detect the acoustic signal at only N/2 points.

[0084] In the Sagnac sensor array 200, it is possible to achieve a large dynamic range without using additional hydrophones 212. Because the phase responsivity in the Sagnac sensor array is a function of the hydrophone responsivity and delay loop length, as shown in Equation 1, the phase responsivity of the entire array of hydrophones can be changed by modifying the delay loop length. By simultaneously using two separate delay loops 214(1) and 214(2) of length  $L_1$  and  $L_2$ , respectively, as shown in a modified sensor array 266 in Figure 7, the detection range of the array 266 can be dramatically increased. The array 266 now has  $2N$  separate Sagnac loops. Each hydrophone 212(i) returns a separate signal for each of the two delay loop paths, and the length of each delay loop 214(1), 214(2) determines the acoustic detection range of that signal. The total acoustic detection range of each hydrophone 212(i) is the union of the detection ranges of each of the two Sagnac loop sensors which enclose the hydrophone 212(i). The lengths of  $L_1$  and  $L_2$  set the acoustic detection range. The length  $L_1+L_2$  is chosen to allow the array 266 to detect the smallest acoustic signal of interest. The length  $L_1$  of the delay loop 214(1) is then chosen to place the detection range of the signals which travel only this shorter delay loop on top of the detection range of the signals which travel both delay loops 214(1), 214(2). In a TDM system, as a result of the insertion of a second loop, the repetition frequency of the source pulses are halved in order to allow time for  $2N$  pulses to return, and the lengths of the delay loops 214(1), 214(2) are chosen such that there is no pulse overlap. Because the repetition frequency is halved, the dynamic range of each individual signal decreases by 3 dB. This decrease is more than offset by the increase in the total dynamic range achieved by piggybacking the dynamic range of two separate signals. In Figure 7, the second delay loop 214(2) is positioned such that all light passing through the second delay loop 214(2) passes through the first delay loop 212(1). It should be understood that, alternatively, the two delay loops 214(1), 214(2) can be optically in parallel such that the light which passes through the second delay loop 214(2) does not pass through the first delay loop 214(1). In such case, the fiber length of the second delay loop 214(2) would have to be the sum of the first length and the second length (i.e.,  $L_1+L_2$ ). But, since  $L_1$  is considerably shorter than



$L_2$ , this adjustment is not essential. The embodiment of Figure 7 reduces the total fiber requirements by adding the length of the first delay loop to the second delay loop.

[0085] Figure 8 illustrates the extended dynamic range made possible by using the two delay loops 214(1), 214(2) in the array 266 in which the dynamic range of each signal is 100 dB and the ratio  $L_1/L_2$  was set to be 5000. As shown, the array 266 is now able to detect over the entire dynamic range of interest (approximately a 160-dB range) without increasing the hydrophone count.

### **Distributed Sensing**

[0086] In the Sagnac sensor array 266, any phase modulation in the interferometer can be transferred into an intensity modulation at the interfering  $3 \times 3$  coupler 220. This distributed sensing over the entire Sagnac loop is disadvantageous for an acoustic sensor array. In order to be practical, the acoustic sensor array should sample the acoustic signal at a number of discrete points in space (i.e., at the hydrophones) and return these signals independently. Mach-Zehnder interferometric sensor arrays achieve this because the interferometer is confined within a small space and thus only senses at that point. In order for the Sagnac sensor array 266 to be practical, the distributed sensing of the Sagnac loop must be decreased.

[0087] The bulk of the fiber in the interferometer constitutes the delay loop 214, which can be located in two positions. The first is with the source 222 and the detection electronics (i.e., the detector 230 and the detector 232) in the dry end (i.e., out of the water), as shown in Figure 9A. Here the delay loop 214 can be environmentally shielded to minimize any external modulation. However, download fibers 270, 272 which connect the wet end to the array portion 210 are part of the interferometer. The second possibility is to locate the delay loop 214 in the wet end (i.e., in the water) with the array 210, as shown in Figure 9B. As such, the delay loop 214 cannot be isolated to the same extent as it could if it were located in the dry end, but the download fibers 270, 272, 274 are outside of the interferometer and thus are non-sensing. The relative magnitude of the download and delay loop distributed pick-up dictates which configuration is best suited for a particular application. It should be

noted that if the delay loop 214 is located in the dry end (Figure 9A), the download fibers 270, 272 must remain stationary to prevent physical movements, such as bending and vibrations, of these fibers, which can induce extremely large phase modulations. These are fiber motion induced phase modulations as opposed to acoustically-induced phase modulations. (Such physical movements are problems in towed arrays, but may not be significant problems in stationary arrays.) Thus, if the delay loop 214 is located in the dry end (Figure 9A), the entire wet end of the Sagnac sensor array 210 must be stationary. However, with the delay loop 214 located in the wet end (Figure 9B), only the portion to the right of the 3×3 coupler 220 in Figure 9B must remain stationary since the download fibers 270, 272, 274 are not then part of the interferometer. When the delay loop 214 is located in the wet end (Figure 9B), the delay loop fiber must be desensitized. The delay loop 214 can be made stationary by wrapping the delay loop fibers around a desensitized cylinder (not shown), thereby eliminating fiber motion and making acoustic pick-up the dominant source of distributed pick-up signal. Because it is easier to desensitize fiber to acoustically-induced phase modulation than it is to desensitize fiber to movement-induced phase modulation, the configuration which locates the delay loop 214 in the wet end (Figure 9B) is preferable for towed array applications and will be described in more detail below.

#### **Calculation of the Acoustic Pick-up Noise Induced in the Delay Loop**

[0088] In this section, estimates are derived for the magnitude of the acoustically induced distributed pick-up noise as compared to the acoustically induced hydrophone phase modulation in the Sagnac sensor array 210 of Figure 9(b). The intensity modulation due to the distributed phase modulations resulting from the pick-up of acoustic signals in the delay loop and bus fiber (the fiber connecting each hydrophone to the delay loop and the 3×3 coupler) can be considered a source of noise. For the following discussion, consider one loop of the Sagnac sensor array as comprising only delay fiber of length  $L_d$ , a bus fiber of length  $L_b$ , a hydrophone fiber of length  $L_h$ , and a total length  $L$ , as shown in Figure 10. Also assume that  $L_d$  is much larger than  $L_b$  and  $L_h$ . The phase responsivity of fiber to acoustic signals results from a pressure

dependent propagation constant,  $\beta$ . In general, the pressure dependent component of the propagation constant at a position  $l$  and time  $t$  can be written as:

$$\beta(l, t) = \beta_0 R(l) P(l, t) \quad (2)$$

where  $\beta_0$  is the zero-pressure propagation constant,  $R(l)$  is the normalized phase responsivity of the fiber, and  $P(l, t)$  is the pressure as a function of space and time. If a sinusoidal acoustic signal of frequency  $\Omega$  is assumed, Equation 2 can be rewritten as:

$$\beta(l, t) = \beta_0 R(l) [P_0 + P_m \sin(\Omega t + \theta(l))] \quad (3)$$

where  $P_0$  is the steady-state pressure,  $P_m$  is the amplitude of the pressure modulation (assumed to be independent of  $l$ ), and  $\theta(l)$  contains the spatial phase variation of the acoustic wave. In general, the induced phase difference between interfering beams in a Sagnac loop due to acoustically induced phase modulation from  $l=l_1$  to  $l=l_2$  is given by the integral:

$$\phi_{\text{int}}(t) = \int_{l_1}^{l_2} \left[ \beta\left(l, t + \frac{(l-L)}{\nu}\right) - \beta\left(l, t - \frac{l}{\nu}\right) \right] dl \quad (4)$$

where  $\nu$  is the speed of light in the fiber, and  $L$  is the loop length. Substituting Equation 3 into Equation 4 yields:

$$\phi_{\text{int}}(t) = \beta_0 P_m \int_{l_1}^{l_2} R(l) \left[ \sin\left(\Omega\left(t + \frac{l-L}{\nu}\right) + \theta(l)\right) - \sin\left(\Omega\left(t - \frac{l}{\nu}\right) + \theta(l)\right) \right] dl \quad (5)$$

Equation 5 can be used to determine the phase difference between interfering beams due to acoustic modulation of the hydrophone, bus, and delay fibers.

[0089] For the hydrophone fiber, Equation 5 is integrated from  $l_1=l_d+l_b/2$  to  $l_2=l_d+l_b/2+l_h$ . It is assumed that  $\theta(l)$  is constant over this range (i.e., that the acoustic wavelength is much larger than the dimension of the hydrophone). It is also assumed that the normalized phase responsivity of the fiber,  $R(l)$ , is constant and is equal to  $R_h$  in this range. Equation 5 then gives a phase difference amplitude between interfering beams due to hydrophone fiber modulation:

$$\phi_{\text{int}}^h = 2\beta_0 R_h P_m L_h \sin\left(\frac{\Omega \cdot T_{\text{delay}}}{2}\right) \quad (6)$$

where it is assumed that  $\Omega L_h/2v \ll 1$ . Note that Equation 2 agrees with the expression given in Equation 1.

[0090] For the bus fiber, Equation 5 is integrated first from  $l_1=l_d$  to  $l_2=l_d+l_b/2$ , and then from  $l_1=L-l_b/2$  to  $l_2=L$  to include both the upper and lower bus lines. Again, it is assumed that  $R(l)$  is constant and equal to  $R_b$  for all bus fiber, such that  $\theta(l)$  is constant in the integral of Equation 5. The phase difference amplitude between interfering beams due to fiber modulation becomes:

$$\phi_{\text{int}}^b = 2\beta_0 R_b P_m L_b \sin\left(\frac{\Omega \cdot T_{\text{delay}}}{2}\right), \quad (7)$$

where it is assumed that  $\Omega L_h/2v \ll 1$ . It should be emphasized that the assumptions on the constancy of  $\theta(l)$  and the amplitude of  $\Omega L_h/2v$  act to increase  $\phi_{\text{int}}^b$ , thus giving a worst case scenario for the bus fiber.

[0091] For the delay fiber, Equation 5 is integrated from  $l_1=0$  to  $l_2=l_d$ , and, as before, it is assumed that  $\theta(l)$  is constant over this range (i.e., the delay loop coil is much smaller than the acoustic wavelength), and that  $R(l)$  is constant and equal to  $R_d$  over the integral. Equation 5 then yields a phase difference amplitude between interfering beams due to delay fiber modulation given by:

$$\phi_{\text{int}}^d = 2\beta_0 R_d P_m (L - L_d) \sin\left(\frac{\Omega T_{\text{delay}}}{2}\right) = 2\beta_0 R_d (L_b + L_h) \sin\left(\frac{\Omega T_{\text{delay}}}{2}\right), \quad (8)$$

where it is assumed that  $\Omega(L_b+L_h)/2v \ll 1$ .

[0092] With Equations 6-8, the relative magnitude of these phase modulations amplitudes can be computed. First, it is noted that a standard plastic coated fiber has a normalized phase responsivity,  $R$ , of  $-328$  dB re  $1/\mu\text{Pa}$ , as described, for example, in J.A. Bucaro, et al., *Optical fibre sensor coatings*, Optical Fiber Sensors, Proceedings of the NATO Advanced Study Institute, 1986, pp. 321-338. On the other hand, as described, for example, in C.C. Wang, et al., *Very high responsivity fiber optic hydrophones for commercial applications*, Proceedings of the SPIE-The International Society for Optical Engineering, Vol. 2360, 1994, pp. 360-363, a fiber wrapped around current hydrophones made from air-backed mandrels has a normalized phase sensitivity of  $-298$  dB re  $1/\mu\text{Pa}$ , an increase of 30 dB over standard fiber. If we

assume that the delay loop and the bus fiber have the normalized phase responsivity of standard plastic coated fiber, and that the hydrophone fiber is wrapped around an air-backed mandrel, then the ratio of  $R_h$  to  $R_b$  or  $R_d$  is approximately 30 dB. Therefore, under the simplifying assumption made to reach Equations 6-8, it can be found that:

$$\frac{\phi_{\text{int}}^h}{\phi_{\text{int}}^d} \approx \left( \frac{31}{1 + (L_b/L_h)} \right) \quad (9)$$

and

$$\frac{\phi_{\text{int}}^h}{\phi_{\text{int}}^b} \approx \left( \frac{31}{L_b/L_h} \right). \quad (10)$$

[0093] The ratio  $L_b/L_h$  is a function of the hydrophone position. For the first hydrophone,  $L_b/L_h \approx 0$  making  $\phi_{\text{int}}^h/\phi_{\text{int}}^d = 31$  and  $\phi_{\text{int}}^h/\phi_{\text{int}}^b$  extremely large. For the last hydrophone, typical values of 100 meters and 1 km for  $L_h$  and  $L_b$ , respectively, are used to arrive at  $\phi_{\text{int}}^h/\phi_{\text{int}}^d \approx \phi_{\text{int}}^h/\phi_{\text{int}}^b \approx 3$ . Thus, despite the fact that the hydrophone fiber constitutes a relatively small amount of the overall Sagnac loop, the magnitude of the acoustically induced phase modulations in the hydrophone fiber are greater than the acoustically induced phase modulations in the delay loop fiber and in the bus fiber for even the furthest hydrophone. The following section describes a means for dealing with this level of distributed pick-up noise using empty rungs.

[0094] In order to evaluate the integral in Equation 5 for the delay loop fiber, it is assumed that  $R(l) = R_d$  for all  $l$  less than  $L_d$ . It was this constancy of  $R(l)$  which eliminated any contribution to the integral of Equation 5 from  $l = (L - L_d)$  to  $L_d$  (because the integrand became an odd function about  $L/2$ ). However, coiling a long length of fiber will result in some dependence in  $R(l)$  on  $l$  (possibly because the inner layer of fiber has a different  $R$  than the outer layer). These variations in  $R(l)$  increase the delay loop pick-up from  $l = L - L_d$  to  $L_d$ . In order to reduce this pick-up, it is first noted that  $R(l)$  need only be an even function around  $L/2$  to make the integrand of Equation 5 an odd function about  $L/2$ .  $R(l)$  can be forced to be more symmetric about  $L/2$  by wrapping the delay loop in such a way as to position symmetric points of the fiber loop next to each other as shown in Figure 11. Such a wrapping ensures that symmetric points of the delay loop are positioned in proximity to each other so that

any variations in  $R(l)$  due to the position of the fiber on the coil are as symmetric about  $L/2$  as possible, thereby making the delay loop pick-up as close to the expression of Equation 8 as possible. Note that, because each Sagnac loop in the Sagnac sensor array has a different  $L/2$  point, only one loop can be wrapped exactly as shown in Figure 11, thereby introducing a small degree of oddness in  $R(l)$  to all but one of the Sagnac loops.

[0095] It should also be mentioned that in addition to enhancing the acoustic sensitivity of fiber with a hydrophone, it is possible to desensitize fibers by applying a metallic coating of a particular diameter. (See, for example, J.A. Bucaro, *Optical fibre sensor coatings*, cited above.) Measured normalized phase responsivities as low as -366 dB re  $1/\mu\text{Pa}$  have been reported. If such fibers are used in the delay or bus lines, the ratio of  $R_h$  to  $R_b$  or the ratio of  $R_h$  to  $R_d$  approaches 68 dB (instead of 30 dB with plastic coated delay and bus fibers), increasing the hydrophone induced signal over the delay and bus induced signal by 38 dB.

#### **Reducing the Distributed Pick-up Noise by Using Empty Rungs**

[0096] In order to further eliminate distributed pick-up signal, the hydrophone-induced acoustic modulation can be isolated from the distributed pick-up modulation by placing empty rungs 300 that do not contain a hydrophone in the array 210, as shown in Figure 12. Each rung 216(i) which contains a hydrophone 212(i), called a sensing rung, is preceded by one of the empty rungs 300(i). The fact that the non-sensing fiber of each loop which encloses an empty rung 300(i) is nearly identical to the non-sensing fiber of the loop which encloses the corresponding sensing rung 212(i) means the empty rung 300(i) and the corresponding sensing rung 212(i) will have nearly the same distributed pick-up signal. By treating this empty rung 300(i) as another sensor in the array 210 and properly timing the pulses (in the TDM scheme) from the empty rungs 300(i) and the sensing rungs 212(i) so that they do not overlap, the distributed pick-up signal present on each sensing rung 212(i) can be measured. After detection, this signal can be subtracted from the sensing rung signal, leaving only intensity variations produced by phase modulations in the hydrophone fiber.

Implementing such a scheme requires  $2N$  rungs for an  $N$  sensor array 210, thereby reducing the duty cycle of individual signals by one half.

[0097] If desensitizing the bus portion of the array 210 is not required, a single empty rung 300 can be placed in the array 210 to measure the distributed pick-up signal associated with the delay loop 214, thereby requiring only  $N+1$  rungs ( $N$  sensing rungs 212(i) and one empty rung 300) for  $N$  sensors. If one empty rung 300 does not adequately measure the distributed pick-up signal for each sensing rung 212(i), more empty rungs 300 can be added at periodic intervals along the array, until the distributed pick-up signal present on each sensing rung 212(i) can be adequately measured by the nearest of these empty rungs 300. Using fewer empty rungs results in a higher duty cycle for individual signals. Figure 12 depicts the extreme in which an empty rung was added for every sensing rung.

### **Polarization**

[0098] For maximum contrast in any interferometric sensor, the state of polarization (SOP) of the interfering beams must be identical when they recombine. If they are orthogonal, there is no interference and thus no amplitude-modulated signal. This is referred to as polarization-induced signal fading. Because each sensor in the Sagnac sensor array is a Sagnac loop, the research carried out so far on polarization-induced signal fading in the Sagnac fiber gyroscope applies to the Sagnac sensor array as well. One promising solution is to place a depolarizer within the Sagnac loop. (See, for example, K. Böhm, et al., *LOW-DRIFT FIBRE GYRO USING A SUPERLUMINESCENT DIODE*, ELECTRONICS LETTERS, Vol. 17, No. 10, 14th May 1981, pp. 352-353.) The depolarizer ensures that at least half of the optical power is returning to the  $3 \times 3$  coupler in the correct SOP at all times. This general approach produces a constant visibility regardless of the loop birefringence. (See, for example, William K. Burns, et al., *Fiber-Optic Gyroscopes with Depolarized Light*, JOURNAL OF LIGHTWAVE TECHNOLOGY, Vol. 10, No. 7, July 1992, pp. 992-999). The simplest configuration uses an unpolarized source such as a fiber superfluorescence source and a depolarizer in the loop. As illustrated in Figure 13, in the Sagnac sensor array 200, one depolarizer 310 is placed at a point which is

common to all the Sagnac loops. The depolarizer 310 ensures that each sensor 212(i) has this constant visibility independent of birefringence as long as the loop birefringence remains constant. This represents a great simplification in the handling of polarization-induced signal fading over those methods used in Mach-Zehnder interferometric sensor arrays.

[0099] Although slow changes in the birefringence will be sufficiently canceled by the reciprocal nature of the Sagnac interferometer, birefringence modulations at frequencies in the acoustic range of interest will produce polarization noise. Most birefringence modulation at these frequencies occurs as a result of physical fiber movement. Thus, the Sagnac loop should remain stationary in order to reduce the polarization noise (as well as the distributed pick-up signal).

#### **Noise Sources Introduced by the use of the Sagnac Interferometer**

##### **Thermal Phase Noise**

[0100] Because the index of refraction of the fiber changes with temperature, thermal fluctuations in a fiber will produce phase fluctuations in the light traveling through it. These index variations are uncorrelated over the length of fiber, and thus the resulting phase fluctuations scale as the square root of length. Because Mach-Zehnder interferometers typically use less than 100 meters of fiber in each arm, the magnitude of this thermal phase noise is negligible. The Sagnac interferometer has a great deal more fiber in the interferometer and as a result, thermal phase noise can become a limiting noise source. The magnitude of this thermal phase noise in a Sagnac interferometer has been described theoretically and confirmed by experiment. (See, for example, Sverre Knudsen, et al., *Measurements of Fundamental Thermal Induced Phase Fluctuations in the Fiber of a Sagnac Interferometer*, IEEE Photonics Technology Letters, Vol. 7, No. 1, 1995, pp. 90-93; and Kjell Kråkenes, et al., *Comparison of Fiber-Optic Sagnac and Mach-Zehnder Interferometers with Respect to Thermal Processes in Fiber*, JOURNAL OF LIGHTWAVE TECHNOLOGY, Vol. 13, No. 4, April 1995, pp. 682-686.). For loops greater than 2 km, the thermal



phase noise can exceed  $1 \mu\text{rad}/\sqrt{\text{Hz}}$  in the frequency range of interest, which is on the order of the required array sensitivity.

[0101] The thermal phase noise can be considered as a source of distributed pick-up noise, akin to an external modulation to the delay loop, and as such can be reduced by using empty rungs, as described above. Thermal phase noise can also be reduced by shortening the loop length. As discussed above, the loop length can be shortened without changing the low frequency sensitivity by increasing the hydrophone fiber length by the same factor as that by which the delay loop was decreased. For example a 40-km delay loop with 50 meters of hydrophone fiber has the same low-frequency response as a 20-km delay loop with 100 meters of fiber. The latter combination however will suffer less thermal phase noise because the total delay loop length is shorter by almost a factor of two.

#### **Kerr Effect Induced Phase Noise**

[0102] Kerr-induced phase shifts which can be generated in a Sagnac interferometer have received a great deal of attention for the fiber optic gyroscope. (See, for example, R.A. Bergh, et al., *Source statistics and the Kerr effect in fiber-optic gyroscopes*, OPTICS LETTERS, Vol. 7, No. 11, November 1982, pp. 563-565; R.A. Bergh, et al., *Compensation of the optical Kerr effect in fiber-optic gyroscopes*, OPTICS LETTERS, Vol. 7, No. 6, June 1982, pp. 282-284; and N.J. Frigo, et al., *Optical Kerr effect in fiber gyroscopes: effects of nonmonochromatic sources*, OPTICS LETTERS, Vol. 8, No. 2, February 1983, pp. 119-121.) The demands of the gyroscope and the acoustic sensor, however, are different because the gyroscope measures DC levels. Small DC offsets created by Kerr-induced phase shifts which would limit a fiber gyroscope are non-issues with an acoustic sensor. The Kerr-induced DC phase shift is not a problem as long as it does not move the bias point too far away from quadrature. The intensity noise on the light source can produce a Kerr induced phase noise on the output. However, the magnitude of this Kerr-induced AC phase noise is small as long as the Kerr-induced DC phase shift remains small. The origin of Kerr-induced phase shifts in the Sagnac sensor array is different than in the fiber gyroscope. The asymmetry of the Sagnac sensor array invites such a Kerr phase

shift much more readily than the nominally symmetric gyroscope does. That asymmetry results from the array portion as well as any placement of EDFAs which are asymmetric, in that one beam sees gain before propagating through the delay loop, then sees loss, while the counter-propagating beam sees loss, then sees gain. It is possible to balance these asymmetries and null the Kerr-induced phase shift by choosing the proper location for EDFAs in the delay loop. The specifics depend on the exact array configuration and which multiplexing scheme is used.

#### Non-linear phase modulation resulting from the EDFAs

[0103] The population inversions created in the EDFAs induce a phase shift on the signal light that passes through it. (See, for example, M.J.F. Digonnet, et al., *Resonantly Enhanced Nonlinearity in Doped Fibers for Low-Power All-Optical Switching: A Review*, OPTICAL FIBER TECHNOLOGY, Vol. 3, No. 1, January 1997, pp. 44-64.) This phenomenon has been used to produce all-optical interferometric switches. In a Sagnac sensor array, the EDFAs within the interferometer create a nonlinear phase shift via the same mechanism. Variations in the population inversion due to pump or signal power fluctuations will produce phase modulations which will be converted to an intensity noise.

[0104] In order to estimate the magnitude of this noise source, a determination must be first made as to how the inverted population responds to pump and signal power fluctuations. This is relatively straightforward to do by invoking the rate equations for an erbium system:

$$N_1 + N_2 = N_0, \quad (11)$$

$$\frac{d}{dt}N_2 = \frac{I_p \sigma_p^a}{h\nu_p A_{eff}} N_1 + \frac{I_s \sigma_s^a}{h\nu_s A_{eff}} N_1 - \frac{I_p \sigma_p^e}{h\nu_p A_{eff}} N_2 - \frac{I_s \sigma_s^e}{h\nu_s A_{eff}} N_2 - \frac{N_2}{\tau_2}, \quad (12)$$

where  $N_1$  and  $N_2$  are the population densities of the lower and excited states respectively,  $N_0$  is the total population density,  $I$  is the intensity,  $\sigma$  is the cross section,  $A_{eff}$  is the effective mode area in the fiber, and  $\tau_2$  is the lifetime of level two. The subscripts  $p$  and  $s$  denote pump and signal, respectively, and the superscripts  $a$  and  $e$  denote absorption and emission, respectively.

[0105] By splitting  $N_1$ ,  $N_2$ ,  $I_p$ , and  $I_s$  into their steady-state and time-varying components, then substituting this into Equation 12 and combining Equation 12 with Equation 11, the result is:

$$\begin{aligned} \frac{d}{dt} N_2(t) = & \left[ \frac{N_o \sigma_p^a + N_2^{ss} (\sigma_p^e + \sigma_p^a)}{h \nu_p} \right] I_p(t) + \left[ \frac{N_o \sigma_s^a + N_2^{ss} (\sigma_s^e + \sigma_s^a)}{h \nu_s} \right] I_s(t) + \\ & \left[ \frac{I_p^{ss} (\sigma_p^e + \sigma_p^a)}{h \nu_p} + \frac{I_s^{ss} (\sigma_s^e + \sigma_s^a)}{h \nu_s} + \frac{1}{\tau_2} \right] N_2(t) - \left[ \frac{(\sigma_p^e + \sigma_p^a)}{h \nu_p} \right] I_p(t) N_2(t) - \\ & \left[ \frac{(\sigma_s^e + \sigma_s^a)}{h \nu_s} \right] I_s(t) N_2(t), \end{aligned} \quad (13)$$

where the superscript  $ss$  denotes steady-state values, and the time-varying components are now written as explicit functions of time ( $N_2 = N_2^{ss} + N_2(t)$ ). If it is assumed that  $N_2(t)$  is much smaller than  $N_2^{ss}$ , then the last two terms in Equation 13 can be neglected. By writing  $I_p(t) = I_p^m \sin(f_p t)$  and  $I_s(t) = I_s^m \sin(f_s t)$  (where  $I_p^m$  and  $I_s^m$  denote the modulation amplitudes of  $I_p(t)$  and  $I_s(t)$ , respectively, and  $f_p$  and  $f_s$  respectively denote the pump and signal modulation frequencies) and solving the resulting differential equations, it can be found that:

$$\frac{|N_2(f_p)|}{N_2^{ss}} \approx \left( \frac{\sigma_s^a (\sigma_p^e + \sigma_p^a) - \sigma_p^a (\sigma_s^e + \sigma_s^a)}{(\sigma_p^e + \sigma_p^a)^2} \cdot \frac{\nu_p}{\nu_s} \right) \left( \frac{1}{\sqrt{1 + f_p^2 / f_o^2}} \right) \cdot \frac{I_s^{ss} I_p^m}{I_p^{ss^2}} \quad (14)$$

$$\frac{|N_2(f_s)|}{N_2^{ss}} \approx \left( \frac{\sigma_s^a}{\sigma_p^a} - \frac{\sigma_s^e + \sigma_s^a}{\sigma_p^e + \sigma_p^a} \right) \cdot \frac{\nu_p}{\nu_s} \cdot \left( \frac{1}{\sqrt{1 + f_p^2 / f_o^2}} \right) \cdot \frac{I_s^m}{I_p^{ss}} \quad (15)$$

where:

$$f_o = \frac{\sigma_p^e + \sigma_p^a}{h \nu_p} I_p^{ss} + \frac{\sigma_s^e + \sigma_s^a}{h \nu_s} I_s^{ss} + \frac{1}{\tau_2} \approx \frac{\sigma_p^e + \sigma_p^a}{h \nu_p} I_p^{ss} \quad \text{when } I_p^{ss} \gg I_s^{ss}. \quad (16)$$

[0106] If it is assumed that  $\lambda_p=1480$  nm,  $\lambda_s=1550$  nm, and  $I_p^{ss}=1$  W, and if typical erbium-silica cross sections are assumed, then Equations 14 and 15 simplify to:

$$\frac{|N_2(f_p)|}{N_2^{ss}} \approx \left( \frac{0.9}{\sqrt{1 + f_p^2/4.3 \text{ kHz}}} \right) \cdot \frac{I_s^{ss} I_p^m}{I_p^{ss^2}} \quad (17)$$

$$\frac{|N_2(f_s)|}{N_2^{ss}} \approx \left( \frac{1.2}{\sqrt{1 + f_s^2/4.3 \text{ kHz}}} \right) \cdot \frac{I_s^m}{I_p^{ss}} \quad (18)$$

[0107] The pump-induced population inversion fluctuations (Equation 17) will be analyzed first. If  $I_s^{ss}=1$  mW,  $I_p^{ss}=1$  W, and it is assumed that  $I_p^m/I_p^{ss}=10^{-6}/\sqrt{\text{Hz}}$  (120 dB/ $\sqrt{\text{Hz}}$  electronic SNR), then  $|N_2(f_p)|/N_2^{ss} = 9 \times 10^{-10} \sqrt{\text{Hz}}^{-1}$  at frequencies well below 4.3 kHz. In order to convert this figure to a phase modulation, the fact that 10 mW of pump power absorbed in an erbium-doped fiber induces approximately 7 radians of phase shift at 1550 nm can be used. (See, for example, M.J.F. Digonnet, et al., *Resonantly Enhanced Nonlinearity in Doped Fibers for Low-Power All-Optical Switching: A Review*, OPTICAL FIBER TECHNOLOGY, Vol. 3, No. 1, January 1997, pp. 44-64.) Using simulations, 10 mW of absorbed pump power in a typical erbium-doped fiber provides approximately 6 dB of small signal gain at 1550 nm, which is close to the gain required by each amplifier in an array with distributed EDFAs. (See, for example, Craig W. Hodgson, et al., *Optimization of Large-Scale Fiber Sensor Arrays Incorporating Multiple Optical Amplifiers-Part I: Signal-to-Noise Ratio*; Craig W. Hodgson, et al., *Optimization of Large-Scale Fiber Sensor Arrays Incorporating Multiple Optical Amplifiers-Part II: Pump Power*; Jefferson L. Wagener, et al., *Novel Fiber Sensor Arrays Using Erbium-Doped Fiber Amplifiers*; and C.W. Hodgson, et al., *Large-scale interferometric fiber sensor arrays with multiple optical amplifiers*, cited above.) Therefore, each amplifier provides approximately 7 radians of DC phase shift. Since the nonlinear phase shift is proportional to the upper state population,  $N_2$ , it can be written that  $\Delta N_2/N_2^{ss}=\Delta\phi/\phi^{ss}$ .

Using this relation and Equation 17 again for  $I_s^{ss}=1$  mW,  $I_p^{ss}=1$  W,  $I_p^m/I_p^{ss}=10^{-6}/\sqrt{\text{Hz}}$  and  $f_s \ll 4.3$  kHz, the low-frequency phase noise induced by each EDFA is  $(7 \text{ radians}) \times (9 \times 10^{-10}) \sqrt{\text{Hz}}^{-1} = 6.3 \times 10^{-9} \text{ rad}/\sqrt{\text{Hz}}$ . If it is assumed that there are a total of 500 such amplifiers and that the phase modulations from all 500 amplifiers add coherently, the total pump noise induced phase shift can be estimated to be  $3.2 \mu\text{rad}/\sqrt{\text{Hz}}$ . The target phase noise floor is typically set to  $1 \mu\text{rad}/\sqrt{\text{Hz}}$ , indicating that the nonlinear phase-noise induced by the EDFAs due to pump power fluctuations is close to but not significantly larger than the required phase noise floor. In practice, the amplifiers' phase modulations will not add coherently, which will reduce the  $3.2 \mu\text{rad}/\sqrt{\text{Hz}}$  figure.

[0108] Calculations of the induced phase shift due to signal power fluctuations are more complicated because the signal power not only has intensity noise but is also modulated by the multiplexing scheme. Again considering the TDM case, in general, while a given pulse is traveling through a particular EDFA, there may or may not be a counter-propagating pulse traveling through that EDFA at the same time. Taking the worst case in which there is always a counter-propagating pulse,  $I_s^m$  is twice the intensity noise of each individual pulse. For the amplifiers,  $I_s^m$  is typically 1.5 to 2 times the intensity noise of each individual pulse. Assuming the signal light has an electronic SNR of  $120 \text{ dB}/\sqrt{\text{Hz}}$  at acoustic frequencies (i.e.,  $I_s^m/I_s^{ss}=10^{-6}/\sqrt{\text{Hz}}$ ), and inserting this figure into Equation 18 along with  $I_p^{ss}=1$  W and  $I_s^m=2$  mW, it can be calculated that  $|N_2(f_s)|/N_2^{ss}$  is approximately  $2.4 \times 10^{-9} \sqrt{\text{Hz}}^{-1}$  at frequencies much lower than 4.3 kHz and that the phase noise induced by signal intensity noise in each EDFA is thus  $1.68 \times 10^{-8} \text{ rad}/\sqrt{\text{Hz}}$ . Again assuming 500 amplifiers and coherent addition of all EDFA-induced phase modulation, the total EDFA induced phase noise on each pulse is  $8.4 \mu\text{rad}/\sqrt{\text{Hz}}$ , a level which could again limit the performance of the Sagnac sensor array. However, a more detailed study taking into account the multiplexing scheme and exact timing of the array is needed for a more accurate calculation.

## **Multiplexing Schemes in a Sagnac array**

### **Time-Division Multiplexing**

[0109] It has been assumed thus far that the Sagnac sensor array is operated in a TDM configuration. It should be noted that, in the Sagnac sensor array, the source requirements for such a TDM system are not as demanding as those of a Mach-Zehnder interferometric sensor array in a TDM configuration. The reason for this is the use of the broadband source in the Sagnac sensor array. In the Mach-Zehnder interferometric sensor array, the light from adjacent rungs is coherent due to the narrow linewidth source, and thus extremely high extinction ratios on the input pulse are required to prevent multi-path coherent interference. These high extinction ratio requirements are achieved by placing multiple modulators in series, which results in a complicated, high loss, and expensive source. In the Sagnac sensor array, the required extinction ratio need not be as high because the broadband source eliminates any possibility of multi-path coherent interference. In addition, the narrow linewidths required by the Mach-Zehnder interferometric sensor array prevent the use of a pulsed laser source in place of a continuous wave (cw) laser source which is externally modulated with Lithium Niobate intensity modulators. In the Sagnac sensor array, either a continuous-wave ASE source which is externally modulated, a pulsed ASE source, or some combination thereof could be used to construct the source. Again, the reason for this is that the Sagnac sensor array does not require a narrow linewidth source. Although the present invention does not require a narrow linewidth source, it should be understood that the Sagnac sensor array of the present invention can be used with a narrow linewidth source, such as, for example, a laser.

### **Frequency Division Multiplexing**

[0110] The use of the broadband source also allows the Sagnac sensor array to operate in non-TDM configurations without changing the design or requiring additional sources. Frequency division multiplexing (FDM) is commonly used with Mach-Zehnder interferometric sensor arrays using the Phase-Generated Carrier (PGC) scheme but is also compatible with the Sagnac sensor array. Figure 14 shows a basic

Sagnac sensor array 400 using a FDM scheme. A fiber superfluorescent source (SFS) 402 (or other broadband source, such as, for example, an LED) generates input light. A chirped intensity modulation is applied to the input light via an intensity modulator 404 which is controlled by a chirped frequency generator 406. The modulated light enters a sensor array 410 via a 3×3 coupler 412. The light passes through a delay loop 414 and plural sensing rungs 416(i) having respective sensors 418(i). Empty rungs (not shown) can also be included if desired. After passing through the delay loop 414 and the rungs 416(i), the light exits from the sensor array 410 through the coupler 412 and is detected by a detector 420 which generates an electrical output signal responsive to the detected light. The electrical output signal from the detector 420 is mixed in a mixer 422 with the same chirped frequency which has been time delayed by a delay 424 which delays the chirped frequency by a time  $\Delta t$ . In the setup illustrated in Figure 14, the output of the mixer 422 is applied to a spectrum analyzer 426. In an operational embodiment, the output of the mixer 422 is applied to a signal processing subsystem (not shown) which analyzes the output of the mixer 422 to reproduce the acoustic signals impinging on the array 410.

[0111] The signals returning from the sensors 418(i) in the various rungs 416(i) are further delayed with respect to the delayed chirp frequency. This is illustrated by the graphs in Figure 15 by the original chirped frequency 450, the delayed chirped frequency 452 from the delay 424, the chirped return signal 460 from the first rung, the chirped return signal 462 from the second rung and the chirped return signal 464 from the third rung. In the mixer 422, separate beat frequencies  $f_{b1}$  470,  $f_{b2}$  472,  $f_{b3}$  474, respectively (shown in Figure 14), are formed between the mixing chirped frequency 452 and each of the signals returning from the various rungs in the Sagnac sensor array 410. (See, for example, S.F. Collins, et al., *A Multiplexing Scheme For Optical Fibre Interferometric Sensors Using An FMCW Generated Carrier*, OFS '92 Conference Proceedings, pp. 209-211.) Although only three chirped return signals 460, 462, 464 are illustrated in Figure 15, it is contemplated that up to N return signals can be provided, where N is the number of rungs in the array 410. The chirped return signals from the Nth rung causes a beat frequency  $f_{bN}$  in the mixer 422.

[0112] As illustrated by a pictorial representation of a spectral output in Figure 14, acoustic modulation of the signals will appear as upper sidebands 480, 481, 482 and lower sidebands 484, 485, 486 to the beat frequencies. An advantage of this FDM scheme is that the demands on the array timing are greatly relaxed over those required in a TDM system. A TDM system requires a specific delay between adjacent rungs in order to prevent pulses from overlapping, and this can present a demanding engineering problem. In FDM, variations in fiber lengths shift beat frequencies but do not induce overlap between signals as long as these beat frequencies are separated by twice the acoustic detection range. The latter is accomplished by selecting the proper chirp rate. Unlike in a TDM system, all paths return light at all times, which can result in phase noise between the different incoherent signals. The broadband ASE light source minimizes the magnitude of this phase noise. (See, for example, Moslehi, *Analysis of Optical Phase Noise in Fiber-Optic Systems Employing a Laser Source with Arbitrary Coherence Time*, Journal of Lightwave Technology, Vol. LT-4, No. 9, September 1986, pp. 1334-1351.)

#### Code Division Multiplexing

[0113] Code division multiplexing (CDM) has received increased attention lately for its use in sensor arrays. (See, for example, A.D. Kersey, et al., *Code-division Multiplexed Interferometric Array With Phase Noise Reduction And Low Crosstalk*, OFS '92 Conference Proceedings, pp. 266-269; and H.S. Al-Raweshidy, et al., *Spread spectrum technique for passive multiplexing of interferometric optical fibre sensors*, SPIE, Vol. 1314 Fibre Optics '90, pp. 342-347.) As illustrated for a Sagnac sensor array 600 in Figure 16, in CDM, the input light from a fiber superfluorescent source 602 (or other broadband source, such as, for example, an LED) is modulated in an intensity modulator 604 according to a pseudo-random code generated by a code generator 606. The modulated light is applied to an interferometric loop 608 via a 3×3 coupler 610 and propagates through a delay loop 614 and a plurality of rungs 616(i) in an array 612. In the illustrated embodiment, each rung 616(i) includes a respective sensor 618(i). Empty rungs (not shown) can also be included if desired. The light returns from the loop via the 3×3 coupler 610 and is detected by a detector



620. The electrical output of the detector 620 is applied to a correlator 622 along with the output of the code generator 606, which output is delayed for a duration  $\tau_{cor}$  by a delay 624. The bit duration of the pseudo-random code is shorter than the propagation delay between adjacent rungs in the array 612. When  $\tau_{cor}$  is equal to one of the loop travel times  $\tau_i$ , through a respective rung 616(i), then the signal returning from this sensor in the rung 616(i) is correlated to the delayed pseudo-random code. The other signals, which have delays  $\tau_j$  where  $|\tau_j - \tau_i| > \tau_{bit}$  correlate to zero. The correlation process involves, for example, multiplying the detected signal by 1 or -1 (or gating the signal in an electronic gate 630 to the non-inverting and inverting inputs of a differential amplifier 632) depending on whether the correlating code is on or off. The output of the differential amplifier on a line 634 is the correlated output. The signal is then time averaged over a period  $t_{avg}$  equal to the duration of the code. The uncorrelated signals time average to zero, thereby isolating the signal from sensor 618(i).  $\tau_{cor}$  is scanned to retrieve sequentially the signals from all sensors.

[0114] An advantage of CDM over TDM is that the delay between sensors does not have to be controlled accurately. Any loop delays  $\tau_j$  in which  $|\tau_j - \tau_{j \pm 1}| > \tau_{bit}$  is acceptable (where  $\tau_{bit}$  is the duration of a pulse in the code). Correlating requires a knowledge of the  $\tau_j$ 's, which are easily measured. As with FDM, the use of a broadband source benefits reducing the phase noise which results from the addition of all the signals together.

[0115] The foregoing described a novel design for an acoustic sensor array based on the Sagnac interferometer. The major advantages of this design are the use of common-path interferometers. This eliminates the conversion of source phase noise into intensity noise, which is prevalent in Mach-Zehnder interferometric sensors, and allows the use of a cheap, high-power ASE source or other broadband source. The response of the Sagnac sensor array as a function of acoustic frequency is shown to match the ocean noise floor. The design also allows the dynamic range to be dramatically increased without adding hydrophones by using one additional, very short delay loop. A technique for eliminating polarization-induced signal fading was discussed above. The Sagnac sensor array also allows the use of several multiplexing

schemes in a simpler form than is achievable with a standard Mach-Zehnder array. Because of these features, the Sagnac sensor array design provides a very promising alternative to Mach-Zehnder-interferometer-based sensor arrays.

### **Folded Sagnac Sensor Array**

[0116] Figures 17-20 illustrate alternative embodiments of a distributed acoustic sensor array based upon the Sagnac effect which has an architecture modified to reduce the distributed pick-up from the downlead fibers. In particular, Figure 17 illustrates a basic folded Sagnac acoustic fiber sensor array 700 which comprises a source 702, a first detector 704 and a second detector 706. Preferably, the source 702, the first detector 704 and the second detector 706 are located in the dry end of the sensor array 700 (e.g., on shore or on board a ship).

[0117] The source 702 generates light pulses which are coupled to a 3×3 coupler 710 via a downlead fiber 708. As illustrated, the 3×3 coupler is located in the wet end (e.g., proximate to the ocean floor). The 3×3 coupler 710 has a first output port coupled to one end of a common fiber rung (rung 0) 712, has a second output port coupled to a first array input/output fiber 714 of an array 716, and has a third output port which is non-reflectively terminated. Approximately 33 percent of the light from the source 702 is coupled to each of the first and second ports of the 3×3 coupler and thus approximately 33 percent of the light propagates to the common fiber rung 712 and approximately 33 percent of the light propagates to the array 716. As discussed above, although described herein as a 3×3 coupler 710, other n×m couplers (e.g., a 2×2 coupler, a 4×4 coupler, etc.) can be used with the embodiment of Figure 17 and the alternative embodiments of the present invention described below.

[0118] The array 716 comprises a plurality of rungs 718(i) (i.e., 718(1), 718(2) ... 718(N)) coupled between the first array input/output fiber 714 and a second array input/output fiber 720. Each rung 718(i) includes a respective acoustic sensor (i.e., hydrophone) 722(i). The array 716 advantageously includes distributed erbium doped fiber amplifiers (EDFAs) 724, such as described above in connection with Figure 3. (The pump source for the EDFAs 724 is not shown in Figure 17.) Although described

herein with respect to the array 716, other array configurations can also advantageously be used in the present invention.

[0119] The second array input/output fiber 720 couples the array 716 to a first port of a  $2 \times 2$  coupler 730. A second end of the common rung (rung 0) 712 is coupled to a second port of the  $2 \times 2$  coupler 730. Although described herein as an array 716 comprising plural sensors 722(i), it should be understood that the present invention has applications for a sensor system having only a single sensor 722.

[0120] A third port of the  $2 \times 2$  coupler 730 is nonreflectively terminated at a terminal 732. A fourth port of the  $2 \times 2$  coupler 730 is coupled to a delay loop download fiber 740. The delay loop download fiber 740 couples the fourth port of the  $2 \times 2$  coupler to a first end of a delay loop 750. The delay loop 750 may be located either in the dry end as shown or in the wet end. A second end of the delay loop 750 is coupled to a reflector 752 such that light exiting the second end of the delay loop 750 is reflected back into the delay loop 750, propagates through the delay loop 750 and propagates through the delay loop download fiber 740 back to the fourth port of the  $2 \times 2$  coupler 730. The light returned from the loop download fiber 740 is divided by the  $2 \times 2$  coupler 730 with substantially equal portions propagating in the common rung 712 and in the array 716 with both portions propagating toward the  $3 \times 3$  coupler 710. The two portions are combined in the  $3 \times 3$  coupler 710 where light pulses which have traveled the same distance through the array 716 and through the common rung 712 interfere and light pulses which have traveled different distances do not interfere. The signals resulting from the interference are output from the  $3 \times 3$  coupler 710 as first and second output signals which respectively propagate to the first detector 704 via a first detector download fiber 770 and propagate to the second detector 706 via a second detector download fiber 772. The detectors 704, 706 generate electrical output signals which are analyzed by electronics (not shown) in a conventional manner to reproduce the acoustic signals impinging on the sensors 722(i). As discussed below, the signals which interfere within the  $3 \times 3$  coupler 710 return from each sensor 722(i) at different times, and can therefore be separated by time division multiplexing,

frequency multiplexing, code division multiplexing, or the like, as discussed above. The non-interfering signals do not generate detectable output signals and are ignored.

[0121] The embodiment of Figure 17 can be further modified by inserting a depolarizer (not shown) in one of the fiber segments 712, 714 or 720 in conjunction with an unpolarized source, as described above in connection with the Sagnac interferometer. Such embodiments will be described below in connection with Figures 23A, 23B and 23C.

[0122] The light in a single pulse from the source 702 will now be traced through the sensor array 700. A source pulse from the source 702 is launched and travels down the source download 708 and through the  $3 \times 3$  coupler 710 to the common rung 712 and to the array 716. Together, the common rung 712 and the  $N$  rungs 718(i) in the array 716 provide  $N+1$  separate paths for the source pulses to travel to the  $2 \times 2$  coupler 730. Because there are  $N+1$  separate paths for the source pulse to travel, the source pulse is split into  $N+1$  separate pulses which pass through the  $2 \times 2$  coupler 730 and travel down the delay loop download 740 to the delay loop 750. After passing through the delay loop 750, the  $N+1$  pulses are reflected by the reflector 752 and then propagate back through the delay loop 750, down the delay loop download 740 to the  $2 \times 2$  coupler 730 in the wet end, still as  $N+1$  separate pulses. Each of the  $N+1$  pulses is again split into  $N+1$  pulses in the common rung 712 and the  $N$  rungs 718(i). After passing back through the common rung 712 and the rungs 718(i), the  $(N+1)^2$  pulses are combined in the  $3 \times 3$  coupler 710 and then return down the detector downloads 770, 772 back to the dry end where the pulses are detected by the first and second detectors 704, 706 and analyzed.

[0123] Because there are  $(N+1)^2$  possible separate combinations of paths from the source 702 to the reflector 752 and back to the detectors 704, 706, there are  $(N+1)^2$  returned pulses. The only pulses that will interfere in a useable manner are pairs of pulses which travel the same exact path length but in opposite order. For the purposes of the following discussion, a pulse will be identified by two numbers where the first number identifies the path taken by the pulse from the source 702 to the reflector 752, and the second number identifies the path taken by the pulse from the reflector 752

back to the detectors 704, 706. For example, the pulse 0,1 travels through the common rung (rung 0) 712, then through the delay loop 750, to the reflector 752, back through the delay loop 750, and then through rung 718(1). The pulse 1,0 travels first through the rung 718(1), then through the delay loop 750, to the reflector 752, back through the delay loop 750, and then through the common rung (rung 0) 712. Because the distance traveled by the pulse 0,1 is identical with the distance traveled by the pulse 1,0, the pulse 0,1 and the pulse 1,0 interfere when combined at the 3×3 coupler 710 and therefore define a common-path interferometer (i.e., a folded Sagnac interferometer) in the same manner as the Sagnac interferometers described above. Acoustic sensing results from the hydrophone 722(1) which is placed in rung 1 which responds to acoustic modulation. The interfering pulses 0,1 and 1,0 see the hydrophone 722(1) at different times and thus pick-up a phase difference due to the time varying acoustic modulation of the hydrophone 722(1). At the 3×3 coupler 710, this phase difference is converted into an intensity modulation which is transmitted down the detector downleads 770, 772 to the detectors 704, 706. The same effect occurs for the pulses 0,2 and 2,0, for the pulses 0,3 and 3,0, etc.

[0124] Because the folded Sagnac interferometer is common-path, the source 702 can have a short coherence length, which means that interference will only occur between pulses which have traveled nearly identical paths. Therefore, pulse  $i,j$  will interfere with pulse  $j,i$  only. As stated above, there are  $N$  interferometers of interest (pulse 0, $i$  interfering with pulse  $i,0$  for  $i=1$  to  $N$ ). There are also the many other interferometers which do not include the common rung (rung 0) 712 (e.g., pulse 1,2 interfering with pulse 2,1, pulse 1,3 interfering with pulse 3,1, etc.). Such interfering pulses contribute noise to the useful pulses, and shall be referred to herein as noise pulses. These noise pulses carry two types of noise. As with all pulses, they carry additional shot noise, ASE-signal beat noise (in an amplified array), phase noise, etc., which increase the detected noise. The noise pulses which form an unwanted interferometer (pulse 1,2 interfering with pulse 2,1, etc.) also carry intensity modulation due to interferometric sensing of acoustic waves. This intensity modulation is an unwanted signal and can be viewed as a source of noise. It is

important to note that these unwanted interferometers have as their interfering point couplers 780(1) through 780(N) where the rungs 718(1) through 718(N) couple to the first input/output fiber 714 of the array 716, whereas the signal pulses interfere at the 3×3 coupler 710. Because the noise pulses interfere before they reach the 3×3 coupler 710, the intensity modulation of the noise pulses is provided symmetrically to both detectors 704 and 706. The signal pulses which interfere at the 3×3 coupler 710 however produce an asymmetric intensity modulation. Therefore, by differentially amplifying the currents from the detectors 704, 706, the intensity modulation of the signal pulses adds and the intensity modulation of the noise pulses subtracts, thus reducing the noise contribution of the unwanted interferometers.

[0125] To completely eliminate all the noise added by these noise pulses, the pulses of interest can be separated from the noise pulses by using a time division multiplexing scheme and properly choosing delay lengths. In particular, the optical path length from the 3×3 coupler 710 through the common rung 712 to the 2×2 coupler 730 is selected to correspond to a propagation time  $\tau$ . The optical path length of a fiber portion from the 3×3 coupler to the coupler 780(1), through the first rung 718(1), to a corresponding coupler 790(1) and to the 2×2 coupler 730 is selected to be  $(N+1)\tau$ . A portion of the optical path length is a common path from the 3×3 coupler 710 to the coupler 780(1) and from the coupler 790(1) to the 2×2 coupler 730, and a portion of the optical path length is through the rung 718(1). The optical path lengths through each of the rungs 718(i) are preferably selected to be approximately equal. The total length of the optical path from the coupler 780(1) to the coupler 780(2) and the optical path from a coupler 790(2) to the coupler 790(1) is selected to be  $\tau$  such the total optical path length from the 3×3 coupler 710 to the 2×2 coupler 730 through the second rung 718(2) is  $\tau$  longer than the total optical path length from the 3×3 coupler 710 to the 2×2 coupler 730 through the first rung 718(1) (i.e., the total optical path length between the two couplers 710, 730 through the second rung 718(2) is  $(N+2)\tau$ ). The total additional optical path length for each successive rung is selected to be  $\tau$ . Thus, the travel time of light from the 3×3 coupler 710 through a rung 718(i) to the 2×2 coupler 730 is defined as the delay time  $T_i$  of the rung 718(i).

[0126] In accordance with the foregoing description,  $T_i$  is determined by the optical path lengths through the rungs as follows:

$$T_i = \tau \quad i = 0 \quad (\text{for the common rung 712})$$

$$T_i = (N+i)\tau \quad 1 \leq i \leq N \quad (\text{for each of the sensing rungs 718(1), 718(2), etc.})$$

From the foregoing, it can be seen that the optical path length through the farthest rung  $N$  is  $(N+N)\tau$  or  $2N\tau$ .

[0127] The duration of each pulse is selected to be no more than  $\tau$ . Thus, as illustrated in Figure 18, the first pulse 800 returned to the  $3 \times 3$  coupler 710 will be the pulse which traveled through the common rung 712 (i.e., rung 0) from the source 702 to the reflector 752 and back to the detectors 704, 706. This pulse has a total propagation time of  $2\tau$ . (In comparing propagation times, the propagation time of each pulse to the reflector 752 through the delay loop 750 and back is ignored because the propagation time is common to all pulses and simply operates as an offset (not shown) to the timing diagram in Figure 18.) The next set 810 of pulses returned to the detectors 702, 706 are the pulses which travel through the common rung 712 in one direction and travel through a sensing rung 718(i) in the opposite direction (i.e., the pulses 0,1 and 1,0; 0,2 and 2,0; 0,3 and 3,0, through 0,N and N,0). These pulses have respective propagation times of  $2\tau+N\tau$ ,  $3\tau+N\tau$ ,  $4\tau+N\tau$ , through  $(N+1)\tau+N\tau$ . Thus, all the useful pulses are received between a time  $(N+2)\tau$  and a time  $(2N+2)\tau$  (including the duration  $\tau$  of the last pulse received). In contrast, the interfering pulses which travel through a sensing rung 718(i) in both directions (i.e., the pulses, 1,1, 1,2 and 2,1, 1,3 and 3,1 ... 2,2, 2,3 and 3,2, ... etc.) are received as a set of pulses 820 between a time  $2(N+2)\tau$  and a time  $(4N+1)\tau$ . Thus, the signal pulses are separated from the noise pulses.

[0128] For example, in Figure 18, the number of returned pulses as a function of time is plotted for  $N=50$ . As illustrated, a single pulse is received at a time  $2\tau$ . Thereafter, no pulses are received during the interval  $3\tau$  through  $52\tau$ . Then, from  $52\tau$  through  $102\tau$ , two pulses are received during each time interval. The noise pulses then return from a time  $102\tau$  to a time  $201\tau$ . In this way, the signal pulses are separated in time from the noise pulses, thus preventing the noise pulses from adding

noise to the signal pulses. The electronics (not shown) are readily synchronized to only look at the pulses received between the time  $52\tau$  and the time  $102\tau$ .

[0129] It should be noted that the source 702 can be activated to send out the next pulse at the at a time interval of  $150\tau$  relative to the previous pulse because the  $0\tau$  to  $50\tau$  interval in response to the next pulse can overlap the  $150\tau$  to  $200\tau$  interval of noise pulses returning in response to the previous source pulse. Thus, a next set 830 of useful pulses can begin arriving at a time 201. Therefore, the embodiment of Figures 17 and 18 has an overall duty cycle of roughly 1/3 for useable signal information.

[0130] The advantage of the folded Sagnac acoustic fiber sensor 700 over the Sagnac loop illustrated in the previous figures is that the delay fiber 750 is insensitive to modulation. Because the downleads are often quite long and are subjected to large movements and vibrations, distributed downlead pickup is a potentially serious limitation to a Sagnac acoustic fiber sensor. In the folded Sagnac acoustic fiber sensor 700, the source 708 and detector downleads 770, 772 are insensitive because they occur outside the interferometer. The delay loop downlead 740 is insensitive because all the interfering pulses travel this same fiber separated by small time delays (approximately 1 microsecond) and thus see the same perturbations. Any low frequency (much less than approximately 1 MHz) modulation to the delay loop downlead and delay loop itself is seen substantially equally by both interfering pulses and thus does not contribute to a phase difference. The array portion 716 and the common rung 712 comprise the only sensitive fibers in the interferometer 700.

[0131] As shown in Figure 17, the remotely pumped distributed erbium doped fiber amplifiers (EDFAs) 724 can be located throughout the array 716 to regenerate power, as discussed above.

[0132] The  $3\times 3$  coupler 710 is used to passively bias each sensor 722(i) near quadrature and to allow source noise subtraction. Noise subtraction results from the fact that each detector 704, 706 is biased on an opposite slope (because of the way the signals coming out of the  $3\times 3$  coupler 710 are phased with respect to each other), causing phase modulation to asymmetrically affect the intensity at each detector,



while source excess noise symmetrically affects the intensity at each detector. Therefore, by differentially amplifying the detector outputs, the phase modulation induced intensity variations are added and the source's intensity noise is subtracted in the same manner that the signals from the unwanted interferometers would be subtracted.

[0133] It should be understood with respect to Figures 17 and 18 that a similar time divisional multiplexing effect can be accomplished by providing a longer optical path length through the common rung 712 and shorter optical path lengths through the sensing rungs 718(i). For example, the common rung 712 can advantageously be selected to have an optical path length of  $2N\tau$  (i.e.,  $T_0 = 2N$ ), and the optical paths through the rungs can advantageously be selected to be  $\tau, 2\tau, 3\tau, \dots N\tau$ . The foregoing can be summarized as:

$$T_i = 2N\tau \quad i = 0 \quad (\text{for the common rung 712})$$

$$T_i = i\tau \quad 1 \leq i \leq N \quad (\text{for each of the sensing rungs 718(1), 718(2), etc.})$$

[0134] Thus, the first signal to return will have an optical propagation time (again subtracting out the propagation time through the delay loop 750 which is common to all signals) of  $2\tau$  which is the time required to pass through the first rung 718(1) in both directions. The longest delay of any signal which passes through one of the sensing rungs 718(i) in both directions is  $2N$  for a signal pulse which travels both directions through the farthest sensing rung 718(N). The first useable signal to return is a signal which results from the interference of a signal which travels in to the reflector 752 through the common rung 712 and returns through the first sensing rung 718(1) with a signal which travels to the reflector 752 through the first sensing rung 718(1) and returns through the common rung 712. The interference signal will arrive at a time  $(2N+1)\tau$  which is later than the last unwanted signal. The last useable signal will arrive at a time  $(2N+N)\tau$  (i.e.,  $3N\tau$ ). Finally, a signal produced by a pulse which traveled to and from the reflector 752 in the common rung 712 arrives at a time  $4N\tau$ , which is well separated from the useable interference signals.

[0135] It is desirable for acoustic sensors to have as large a dynamic range (range of detectable acoustic modulation amplitudes) as possible. Without using

demodulation techniques such as the phase-generated carrier scheme, the minimum detectable phase modulation is set by the noise performance of the array, and the maximum detectable phase modulation (approximately 1 rad) is set by the nonlinear response function of an interferometer. In a Mach-Zehnder sensor, the mapping of acoustic modulation to phase modulation is a function of only the hydrophone's responsivity. Thus, these limits on the detectable phase modulation along with this mapping of acoustic modulation into phase modulation give the range of acoustic modulation the sensor can detect.

[0136] In a folded Sagnac acoustic fiber sensor array, the mapping of acoustic modulation into phase modulation is a function of both the responsivity of each of the hydrophones (sensors) 722(i) and the length of the delay loop 750. Thus by changing the length of the delay loop 750, the dynamic range of the sensors 722(i) can be adjusted without modifying the hydrophones 722(i) themselves. In addition, if two reflectors 752(1) and 752(2) are used, each sensor 718(i) can have two different delay loops 750(1) and 750(2), as shown in a sensor 850 in Figure 19. This allows each sensor 722(i) to return two signals which have different dynamics ranges, as discussed above with respect to Figures 7 and 8, thereby greatly increasing the total dynamic range of each sensor 722(i). The penalty is a reduction in duty cycle for each individual signal by a factor of  $1/(\text{number of delay loops})$ .

[0137] Figure 20 illustrates a sensor 900 which implements a phase-nulling technique similar to techniques which have been used in fiber gyroscopes. The delay loop reflector 752 of Figure 17 is not used in the sensor 900 of Figure 20. Rather, the pulses are instead returned via a return download 910 into the previously unused port of the  $2 \times 2$  coupler 730. An optical isolator 912 is inserted in the return download 910 to prevent light from traveling the delay loop 750 in both directions. The sensor 900 of Figure 20 behaves identically to the sensor 700 of Figure 17 with the reflector 752. However, the sensor 900 allows the addition of a phase modulator 920 to be inserted into the return download 910. The phase modulator 920 is activated to add a phase shift to each pulse individually. By feeding the detected phase shift into the phase modulator 920 via a differential amplifier 922, phase changes are nulled out, and the

required applied phase shift in the phase modulator 920 becomes the signal. In this phase nulling method, the dynamic range of the array 900 is limited only by the maximum phase shift that the phase modulator 920 can provide.

[0138] Figure 21 illustrates a further alternative embodiment of Figure 19 in which the two delay loops 750(1) and 750(2) are not connected to the same delay loop download. Rather, the first end of the first delay loop 750(1) is connected to a first delay loop download 740(1) which is connected to the fourth port of the 2×2 coupler 730 as in Figure 19. The second end of the first delay loop 750(1) is coupled to the first reflector 752(1) as before. The first end of the second delay loop 750(2) is coupled to the third port of the 2×2 coupler 730 via a second delay loop download 740(2), and the second end of the second delay loop 750(2) is coupled to the second reflector 752(2). Approximately half the light from the 2×2 coupler 730 is coupled to each of the downloads 740(1), 740(2). The light in each download 740(1), 740(2) is delayed in the respective delay loop 750(1), 750(2) and is reflected back to the 2×2 coupler 730 as before. The reflected light is coupled to the common rung 712 and to the array 716. The delays of the delay loops 750(1), 750(2) are selected so none of the N+1 pulses which propagate from the fourth port of the 2×2 coupler 730 through the first delay loop 750(1) overlap in time with any of the N+1 pulses which propagate from the third port of the 2×2 coupler 730 through the second delay loop 750(2). Thus, the embodiment of Figure 21 provides similar functionality to the embodiment of Figure 19; however, the embodiment of Figure 21 utilizes the light which was coupled out of the third port of the 2×2 coupler 730 in Figure 19 and discarded.

[0139] Figure 22 illustrates an alternative embodiment of a fiber optic acoustic sensor system 1000 using a folded Sagnac sensor array. In the system 1000, a source 1004 is coupled to a first port of a 2×2 polarization maintaining coupler 1006 by an X-polarizer 1008. A detector 1002 is connected to a second port of the 2×2 coupler 1006 via a X-polarizer 1010. A second detector (not shown) may advantageously be included in the embodiment of Figure 22 by coupling light from the fiber leading to the source 1004. The X-polarizer 1008 only passes light from the source 1004 having a first polarization (e.g., an X-polarization). Thus, the polarization maintaining

coupler 1006 receives light having an X-polarization from the source 1004 and couples the light to a common rung 1020 via a third port and to a sensor array 1022 via a fourth port. The sensor array 1022 has a similar structure to the sensor array 716 of Figure 17, and like elements have been numbered accordingly.

[0140] Note that the two X-polarizers 1008, 1010 can be replaced by one or more X-polarizers in alternative locations in the system 1000.

[0141] The common rung 1020 is coupled via an X-polarizer 1030 to a first port of a second polarization maintaining 2×2 coupler 1032. The light propagating to the array 1022 first passes through a depolarizer 1034 and then to the first input/output fiber 714. The depolarizer 1034 couples substantially equal amounts of the X polarized light to X polarized light and to Y polarized light. Thus, approximately 50 percent of the light propagates in the array 1022 as X-polarized light, and approximately 50 percent propagates in the array 1022 as Y-polarized light.

[0142] After passing through the rungs of the array 1022, the light propagates via the second input/output fiber 720 and a Y-polarizer 1040 to a second port of the second coupler 1032. The Y-polarizer 1040 allows only Y-polarized light to enter the second coupler 1032. The coupler 1032 combines the light from the array 1022 and from the common rung 1020. Approximately half the light entering the coupler 1032 is coupled via a third port of the coupler 1032 to a light absorbing termination 1042, and approximately half of the light is coupled to a downlead fiber 1050 which propagates the light to a first end of a delay loop 1052.

[0143] Light passes through the delay loop 1052 to a Faraday rotating mirror (FRM) 1054. The operation of the Faraday rotating mirror 1054 is well known and will not be described in detail. Basically, when light is incident onto the Faraday rotating mirror 1054 in one polarization, it is reflected in the orthogonal polarization. Thus, the X-polarized light which passed through the common rung 1020 is reflected as Y-polarized light, and the Y-polarized light which passed through the array is reflected as X-polarized light.

[0144] The reflected light passes back through the delay 1052 and enters the fourth port of the coupler 1032. The light is coupled to the common rung 1020 and to

the array 1022. The X-polarizer 1030 in the common rung passes only the light in the X-polarization which originally propagated through the array 1022. Similarly, the Y-polarizer 1040 in the array 1022 passes only Y-polarized light which originally propagated through the common rung 1020.

[0145] After propagating through the array 1022, the returning Y-polarized light is depolarized in the depolarizer 1034 to produce both X-polarized light and Y-polarized light. The light from the common rung 1020 enters the third port of the coupler 1006, and light from the depolarizer 1034 enters the fourth port of the coupler 1006. The light combines in the coupler, and the X-polarized light from the two ports which has traveled the same optical distance interferes and is coupled to the first and second ports. The portion coupled to the second port propagates through the X-polarizer 1010 to the detector 1002 where the interfering signals are detected.

[0146] It should be understood that only the light which originally traveled different paths to and from the Faraday rotating mirror 1054 interferes at the coupler 1006. The only light allowed to propagate through the common rung 1020 in the reflected direction is X-polarized light which originally propagated in the array 1022 as Y-polarized light. Similarly, the only light allowed to propagate through any of the rungs of the array 1022 in the reflected direction is Y-polarized light which originally propagated in the common rung 1020 as X-polarized light. Potentially interfering light cannot travel through the rungs in both directions to produce the noise signals described above in connection with the above-described embodiments. Thus, each of the pulses generated in the array 1022 from the reflected pulse that originally traveled in the common rung 1020 can interfere with only a single one of the pulses which was originally generated in the array 1022 and which propagated in the common rung 1020 after it was reflected. Thus, it is not necessary in the embodiment of Figure 22 to include additional delays to separate the useable signal pulses from noise pulses.

[0147] Figures 23A, 23B and 23C illustrate further alternative embodiments of the present invention. A sensor array 1100 in the embodiments of Figures 23A, 23B and 23C is similar to the sensor array 700 in the embodiment of Figure 17, and like elements have been numbered accordingly. The embodiments of Figures 23A, 23B

and 23C include an unpolarized source 1102. The  $2 \times 2$  coupler 730 of Figure 17 is replaced with a polarization beam splitter (PBS) 1104 in Figures 23A, 23B and 23C. The use of the polarization beam splitter 1104 saves approximately 6 dB of power compared to the coupler 730 in Figure 17 and the coupler 1130 in Figure 22. The reflector 752 in Figure 17 is replaced with a Faraday rotating mirror (FRM) 1106, which is similar to the Faraday rotating mirror 1054 of Figure 22. The  $3 \times 3$  coupler 710 in Figures 23A, 23B and 23C does not have to be a polarization maintaining coupler.

[0148] Each of Figures 23A, 23B and 23C includes a depolarizer 1110. In Figure 23A, the depolarizer 1110 is located on the first array input/output fiber 714. In Figure 23B, the depolarizer 1110 is located on the common rung 712. In Figure 23C, the depolarizer 1110 is located on the second array input/output fiber 720.

[0149] In the embodiment of Figure 23A, light from the unpolarized source 1102 enters the  $3 \times 3$  coupler 710 and is coupled in approximately equal portions to the common rung 712 and to the first array input/output fiber 714. As discussed above in connection with Figures 3 and 17, the use of the  $3 \times 3$  coupler provides passive biasing near quadrature. The light propagating in the first array input/output fiber 714 passes through the depolarizer 1110, which has the effect of causing substantially half of the light entering the array in one polarization (e.g., the X-polarization) to be coupled into the orthogonal polarization (e.g., the Y-polarization), and likewise half of the light entering the array in the Y-polarization to be coupled to the X-polarization. Thus, after the depolarizer 1110, half of the light in the X-polarization originated in the X-polarization and the other half of the light in the X-polarization originated in the Y-polarization. Likewise, after the depolarizer 1110, half of the light in the Y-polarization originated in the Y-polarization and the other half of the light in the Y-polarization originated in the X-polarization. Effectively, the depolarizer 1110 scrambles the unpolarized light.

[0150] The light passes through the array 716 in the manner described above in connection with the other embodiments. The light exiting the array 716 propagates through the second array input/output fiber 720 to a first port 1121 of the polarization

beam splitter 1104. The polarization beam splitter 1104 splits the incident light into the two orthogonal polarizations (i.e., the X-polarization and the Y-polarization). For the purpose of this discussion, it is assumed that the polarization beam splitter 1104 operates like a polarization-dependent mirror oriented at 45°, wherein light entering the first port 1121 in one polarization (e.g., the X-polarization) is reflected to a second port 1122 and light entering the first port 1121 in the other polarization (e.g., the Y-polarization) is transmitted to a third port 1123. In the embodiment shown, the light exiting the second port 1122 is nonreflectively absorbed by the terminator 732. The Y-polarized light exiting the third terminal 1123 propagates through the delay loop downlead fiber 740, through the delay loop 750 to the Faraday rotating mirror 1106. Note that this Y-polarized light from the array portion 716 traveled through the depolarizer 1110 and half of it was originally X-polarized light and half of it was originally Y-polarized light. As discussed above, the Faraday rotating mirror 1106 causes the incident light to be coupled to the orthogonal polarization. Thus, the Y-polarized light is coupled to the X-polarization.

[0151] The X-polarized light reflected by the Faraday rotating mirror 1106 passes through the delay loop 750 and the delay loop downlead fiber 740 back to the third port 1123 of the polarization beam splitter. Because the light is now in the X-polarization, the light is reflected to a fourth port 1124 rather than being transmitted to the first port 1121. Thus, the Y-polarized light which was originally incident on the polarization beam splitter from the array 716 is coupled to the common rung 712 to propagate back to the 3×3 coupler 710 in the X-polarization.

[0152] Unpolarized light which propagates from the 3×3 coupler 710 to the polarization beam splitter 1104 via the common rung 712 enters the polarization beam splitter 1104 via the fourth port 1124. The components of the light in the Y-polarization are transmitted to the second port 1122 and are nonreflectively terminated by the terminator 732. The components of the light in the X-polarization are reflected to the third port 1123 and propagate to the Faraday rotating mirror 1106 via the delay loop downlead fiber 740 and the delay loop 750. (The reason for including the depolarizer 1110 can now be understood. Because only the X-polarized

light from the common rung 712 is coupled to the delay loop download fiber 740, the depolarizer 1110 ensures that the light coupled from the array 716 to the delay loop download fiber 740 also includes some light which was originally X-polarized.) The Faraday rotating mirror 1106 reflects the light as Y-polarized light, and the Y-polarized light propagates through the delay loop and the download fiber to the third port 1123 of the polarization beam splitter 1104.

[0153] The Y-polarized light incident on the third port 1123 of the polarization beam splitter 1104 is transmitted to the first port 1121 and thus to the second array input/output fiber 720. The Y-polarized light propagates through the array 716 to the first array input/output fiber 714 and then passes through the depolarizer 1110 to the 3×3 coupler 710. The depolarizer 1110 operates to convert approximately 50 percent of the Y-polarized light to X-polarized light. The X-polarized light from the depolarizer 1110 interferes with the X-polarized light from the common rung 712. The resulting combined light is detected by the detector 704 or the detector 706 in accordance with the phase relationship between the interfering light signals in the 3×3 coupler 710.

[0154] Note that the X-polarized light incident on the 3×3 coupler 710 from the depolarizer 1110 and the X-polarized light from the common rung 712 travel identical path lengths. For example, light which propagates through the common rung 712 first, propagates in the X-polarization through the common rung 712 and then propagates through the array 716 in the Y-polarization. On the other hand, the light which propagates through the array 716 first propagates in the Y-polarization through the array 716 and then propagates in the X-polarization through the common rung. Because the two "counterpropagating" light signals are in the same polarizations when propagating through the corresponding portions of the interferometric path, the propagation lengths are identical except for the effect of incident noise sensed by the array 716.

[0155] It should be understood that the terminator 732 coupled to the second port 1122 of the polarization beam splitter 1104 can be replaced with a second delay loop (not shown) and a second Faraday rotating mirror (not shown) to provide a second



interferometric path for light which interferes in the Y polarization. By adjusting the delay provided by the second delay loop, the return signals from the second interferometric path can be precluded from overlapping with the return signals from the first interferometric path.

[0156] The embodiment of Figure 23B is similar to the embodiment of Figure 23A except that the depolarizer 1110 is positioned in the common rung 712. The effect of the depolarizer 1110 in Figure 23B is (1) to cause a portion of the light in the common rung 712 returning from the polarization beam splitter 1104 in a single polarization (e.g., the X-polarization) to be coupled to the orthogonal polarization and (2) to scramble the unpolarized light which travels from the 3×3 coupler 710 through the common rung 712 towards the polarization beam splitter 1104. This ensures that the light interferes when it recombines at the 3×3 coupler 710 (the same reason the depolarizer 1110 was added to the fiber 714 of Figure 23A).

[0157] The embodiment of Figure 23C is also similar to the embodiment of Figure 23A except that the depolarizer 1110 is positioned in the second array input/output fiber 720. The embodiment of Figure 23C is functionally equivalent to the embodiment of Figure 23A because it does not matter whether the light passes through the array portion 716 and then passes through the depolarizer 1110 or passes through the depolarizer 1110 and then passes through the array portion 716. Thus, the function of the embodiment of Figure 23C is substantially the same as the function of the embodiment of Figure 23A, as described above.

[0158] Figure 24 illustrates a further alternative embodiment of the present invention in which a folded Sagnac sensor array 1200 includes the polarization beam splitter (PBS) 1104, the Faraday rotating mirror (FRM) 1106, and the depolarizer 1110 connected as shown in the array 1100 in Figure 23A. Other components from Figure 23A are also numbered as before. Unlike the array 1100 in Figure 23A which has the 3×3 coupler 710, the folded Sagnac sensor array 1200 has a polarization maintaining (PM) 2×2 coupler 1220 connected in like manner as the 2×2 coupler 1006 in Figure 22. One port of the 2×2 coupler 1220 is connected to a first port of an optical circulator 1222 via a first polarizer 1224. A second port of the optical

circulator 1222 is connected to a first detector 1226. A third port of the optical circulator 1222 is connected to an unpolarized source 1228 (e.g., an intensity modulated fiber superfluorescent source). A second port of the 2×2 coupler 1220 is connected to a second detector 1230 via a second polarizer 1232. The detectors 1226 and 1230 and the unpolarized source 1228 are connected to the circulator 1222 by standard (not polarization maintaining) fibers. The polarizers 1224 and 1232 are coupled to the polarization maintaining coupler 1220 via the polarization maintaining fiber such that the polarizers 1224, 1232 are aligned with a same axis of the polarization maintaining 2×2 coupler 1220. Alternatively, if a polarized source is used in place of the unpolarized source 1228, the polarized source (not shown) is connected to a polarization maintaining circulator (not shown) by polarization maintaining fiber, and the polarization maintaining circulator is connected to the polarizer 1224 by polarization maintaining fiber. The polarization maintaining components are connected such that the polarized light from the source passes through the polarizer 1224. The connections from the polarization maintaining circulator to the detectors 1226 and 1230 are provided by standard (not polarization maintaining) fibers.

[0159] The folded Sagnac sensor array 1200 further includes a non-reciprocal phase shifter 1250. The phase shifter 1250 is coupled to the common rung 712 via a first optical fiber 1252 having a first end 1254 and a second end 1256 and via a second optical fiber 1258 having a first end 1260 and a second end 1262. The first end 1254 of the first optical fiber 1252 is coupled to the common rung 712 proximate to the 2×2 coupler 1220 via a first coupler 1264. The first end 1260 of the second optical fiber 1258 is coupled to the common rung 712 proximate to the polarization beam splitter 1104 via a second coupler 1266. The respective second ends 1256, 1262 of the first and second optical fibers 1252, 1258 are coupled to the phase shifter 1250, as discussed below in connection with Figures 25 and 26.

[0160] Preferably, the common rung 712, the first fiber 1252 and the second fiber 1258 are polarization maintaining (PM) fibers, and the first coupler 1264, the second coupler 1266 and the 2×2 coupler 1220 are polarization maintaining (PM) couplers.

Also, preferably, the first coupler 1264 and the second coupler 1266 are 50/50 couplers which couple approximately 50 percent of the light entering the common rung 712 in either direction to the phase shifter 1250 while approximately 50 percent of the light remains in the common rung. Thus, the non-reciprocal phase shifter 1250 and the associated fibers form a second rung 1268 in parallel with the common rung 712.

[0161] Preferably, one of the rungs 712, 1268 (e.g., the common rung 712) includes a delay element (e.g., a delay loop 1269) that introduces a time delay in one rung sufficient to prevent the pulses propagating through the rungs from overlapping. Thus, the light returning to 2×2 coupler 1220 from the sensor array 716 comprises two pulses for each sensor that are spaced apart in time from each other. One pulse comprises the combined light that passes through the common rung 712 in each direction. The other pulse comprises the combined light that passes through the non-reciprocal phase shifter 1250 in each direction. It should be understood that the light pulse that passes through the phase shifter 1250 in one direction and the light pulse that passes through the common rung 712 in the other direction have substantially different propagation times and will not overlap in the coupler 1220. Thus, they will not interfere.

[0162] The light that passes through the common rung 712 in one direction does not undergo any phase shift within the common rung 712 relative to the light that passes through the common rung in the other direction. Thus, the combined light that passes through the common rung 712 in both directions has a relative phase bias of zero. However, as discussed below, the non-reciprocal phase shifter 1250 does introduce a shift of the light in one direction with respect to the light in the other direction. In particular, in a preferred embodiment, the phase shifter 1250 introduces a relative  $\pi/2$  phase shift between the light in the two directions. Thus, the light entering the coupler 1220 that has propagated through the phase shifter 1250 in both directions will combine in the coupler 1220 with a  $\pi/2$  phase bias.

[0163] One skilled in the art will appreciate that the 50 percent coupler 1220 in the interferometric configuration shown in Figure 24 couples returning light to the

output port corresponding to the original input port when the returning light at the two input ports interferes in the coupler and has a relative phase difference of  $0$ ,  $2\pi$ ,  $4\pi$ , etc., and couples returning light to the other output port when the light has a relative phase difference of  $\pi$ ,  $3\pi$ ,  $5\pi$ , etc. When the returning light has a relative phase difference that is not a multiple of  $\pi$ , a portion of the returning light is output from both ports. For example, when the relative phase difference is an odd multiple of  $\pi/2$  (e.g.,  $\pi/2$ ,  $3\pi/2$ , etc.), approximately 50 percent of the returning light is coupled to each output port. By providing two independent propagation paths, each detector 1226, 1230 receives two signals that are spaced apart in time and can therefore be separately detected. One signal has a  $0$  phase bias, and one signal has a  $\pi/2$  phase bias so that when one signal is least sensitive to perturbation, the other signal is most sensitive to perturbation, and vice versa. It should be understood that additional rungs in parallel with the common rung 712 and with differing amounts of relative phase shift can be included to provide pulses with different phase biasing.

[0164] Figure 25 illustrates an alternative configuration of a folded Sagnac sensor array 1200', which is substantially similar to the folded Sagnac sensor array 1200 of Figure 24. In the folded Sagnac sensor array 1200' of Figure 25, the depolarizer 1110 is located in the second array input/output fiber 720 rather than in the first array input/output fiber 714. Because of the reciprocal structure of the sensor array 716, the relocation of the depolarizer 1110 to the fiber 720 does not change the overall operation of the folded Sagnac sensor array 1200' with respect to the operation of the folded Sagnac sensor array 1200. Thus, the operation of the folded Sagnac sensor array 1200' will not be described in detail herein.

[0165] The embodiments of Figures 24 and 25 include the sensor array 716, which was described in detail above. It should be understood that other configurations of amplified sensor arrays can also be used in place of the sensor array 716 in the embodiments of Figures 24 and 25.

[0166] Figure 26 illustrates a first preferred embodiment of the non-reciprocal  $\pi/2$  phase shifter 1250 of Figures 24 and 25. As illustrated in Figure 26, the phase shifter 1250 comprises a first collimating lens 1270, a first  $45^\circ$  Faraday rotator 1272, a

quarter-wave plate 1274, a second 45° Faraday rotator 1276, and a second collimating lens 1278. In the illustrated embodiment, the first Faraday rotator 1272, the second Faraday rotator 1276 and the quarter-wave plate 1274 comprise bulk optic devices that are commercially available, but may advantageously comprise fiber optic or other waveguide devices. The collimating lenses 1270, 1278 are positioned proximate to second ends 1256, 1262 of the PM fibers 1252, 1258 to focus light from the fiber ends 1256, 1262 onto the Faraday rotators 1272, 1276, respectively, and to focus light from the Faraday rotators 1272, 1276 into the fiber ends 1256, 1262. Each of the Faraday rotators 1272, 1276 operates in a well-known manner to cause light input to the Faraday rotator with its polarization at a particular angle to have the polarization rotated so that the polarization is at a new angle rotated by a predetermined amount with respect to the original angle. For example, in the preferred embodiment, each Faraday rotator 1272, 1276 rotates the polarization of the incident light by 45° in the counterclockwise (ccw) direction. Thus, as illustrated in Figure 26, light emitted from the end 1256 of the PM fiber 1252 having its polarization oriented horizontally, will be rotated by 45° counterclockwise in the first Faraday rotator 1272 such that the polarization is oriented at an angle of 45° in the clockwise direction with respect to the original orientation when it emerges from the first Faraday rotator 1272.

[0167] The quarter-wave plate 1274 is positioned between the two Faraday rotators 1272, 1276. The quarter-wave plate 1274 has a first birefringent axis 1280 and an orthogonal second birefringent axis 1282. Light propagating in a polarization oriented along one birefringent axis (e.g., the first birefringent axis 1280) has a slower propagation velocity than the light propagating in a polarization oriented along the other birefringent axis (e.g., the second birefringent axis 1282). The quarter-wave plate 1274 is oriented so that the first birefringent axis 1280, for example, is oriented at 45° in the clockwise direction to the vertical, and is therefore oriented so that the light emerging from the first Faraday rotator 1272 is oriented along the first birefringent axis 1280 and is orthogonal to the second birefringent axis 1282. Because of the difference in propagation velocities along the two axes, the quarter-wave plate 1274 introduces a  $\pi/2$  or 90° phase shift in the light polarized along the

first birefringent axis 1280 with respect to the light polarized along the second birefringent axis 1282. Thus, in accordance with this example, the light that originally propagated in the horizontal polarization that was rotated to be in alignment with the first birefringent axis 1280 incurs a relative phase shift of  $90^\circ$  with respect to any light that propagates along the second birefringent axis 1282.

[0168] After passing through the quarter-wave plate 1274, the light passes through the second Faraday rotator 1276 and is again rotated by  $45^\circ$  in the counterclockwise direction. The light emerging from the second Faraday rotator 1276 passes through the second collimating lens 1278 and is focused into the second end 1262 of the second PM optical fiber 1258. It should be understood from the foregoing description that any light output from the first PM optical fiber 1252 in the horizontal polarization enters the second PM optical fiber 1258 in the vertical polarization. As discussed above, the light entering the second PM optical fiber 1258 in the vertical polarization will have propagated along the slow birefringent axis 1280 of the quarter-wave plate 1274 and will incur a relative  $\pi/2$  phase difference with respect to light that propagates along the fast birefringent axis 1282.

[0169] As indicated by its description, the non-reciprocal phase shifter 1250 operates in a non-reciprocal manner because of the operation of the Faraday rotators 1272, 1276. As described above, the light passing through the Faraday rotators 1272, 1276 from the first PM fiber 1252 to the second PM fiber 1258 is rotated  $45^\circ$  counterclockwise by each rotator with respect to the direction of propagation of the light shown in Figure 25. If the Faraday rotators were reciprocal, light propagating through the Faraday rotators 1272, 1276 in the opposite direction would also be rotated in the counterclockwise direction with respect to the direction of propagation of the light; however, because the Faraday rotators are non-reciprocal, the light is rotated in the opposite direction (i.e., clockwise with respect to the propagation direction of the light). The non-reciprocal effect is illustrated in Figure 27 for light passing from the second end 1262 of the second PM fiber 1258, through the non-reciprocal phase shifter 1250, to the second end 1256 of the first PM fiber 1252. Note that when viewed as in Figure 27, the rotation appears to again be in the

counterclockwise direction; however, the light is now propagating toward the viewer. Thus, light emitted from the second end 1262 of the second PM optical fiber 1258 in the vertical polarization passes through the second collimating lens 1278 and through the second Faraday rotator 1276 and is rotated to an orientation in alignment with the second (fast) birefringent axis 1282 of the quarter-wave plate 1274. Thus, the light originally in the vertical polarization does not experience a relative delay as it propagates through the quarter-wave plate 1274. After passing through the quarter-wave plate, 1274, the light passes through the first Faraday rotator 1272 such that the light is rotated an additional  $45^\circ$  to the horizontal polarization. The light is then focused through the first collimating lens 1270 onto the second end 1256 of the first PM optical fiber 1252.

[0170] From the foregoing, it can be seen that the horizontally polarized light passing in the first direction from the first PM fiber 1252 to the second PM fiber 1258 via the non-reciprocal phase shifter 1250 propagates through the slow birefringent axis 1280 of the quarter-wave plate 1274 and experiences a relative phase delay of  $90^\circ$  or  $\pi/2$ . The horizontally polarized light propagating in the first direction is rotated such that the light is oriented in the vertical polarization when it enters the second PM fiber 1258. Conversely, vertically polarized light passing from the second PM fiber 1258 to the first PM fiber 1252 via the non-reciprocal phase shifter 1250 in the second direction propagates through the fast birefringent axis 1282 of the quarter-wave plate 1274 and does not experience a relative phase delay. The vertically polarized light propagating in the second direction is rotated such that the light is oriented in the horizontal polarization when it enters the first PM fiber 1252. As will be discussed more fully below, the relative phase shift between the horizontally polarized light propagating in the first direction with respect to the vertically polarized light propagating in the second direction provides a  $\pi/2$  phase bias.

[0171] Figures 28 and 29 illustrate an alternative embodiment of the non-reciprocal phase shifter 1250, in which the first Faraday rotator 1272 is positioned between the quarter-wave plate 1274 (now referred to as the first quarter-wave plate) and a second quarter-wave plate 1294. In Figure 28, light from the second end 1256

of the first PM fiber 1252 is collimated by the first collimating lens 1270, as before. The light is originally in the horizontal polarization. When the light passes through the first quarter-wave plate 1274, it is converted to light having a circular polarization. The circular polarized light passes through the first Faraday rotator 1272, which causes the circularly polarized light to incur a phase shift of  $\phi$ . In the preferred embodiment, the first Faraday rotator 1272 is selected to cause a phase shift of  $\pi/4$ . The light from the Faraday rotator 1272 remains circularly polarized and passes through the second quarter-wave plate 1294, which converts the circularly polarized light to linearly polarized light in the vertical polarization orientation. In addition to being in the vertical polarization, the light has experienced a phase shift of  $\phi$  (e.g.,  $\pi/4$ ).

[0172] Figure 29 illustrates the operation of the alternative embodiment of the non-reciprocal phase shifter 1250 for light propagating in the opposite direction. In Figure 29, vertically polarized light from the second end 1262 of the second PM fiber 1260 is collimated by the second collimating lens 1278 and passes through the second quarter-wave plate 1294. The second quarter-wave plate 1294 converts the vertically polarized light to light having a circular polarization. The circularly polarized light passes through the first Faraday rotator 1272 and experiences a phase shift as before. Because the light is propagating through the first Faraday rotator 1272 in the opposite direction, the light experiences an opposite phase shift of  $-\phi$  (e.g.,  $-\pi/4$ ). The light from the first Faraday rotator 1272 then passes through the first quarter-wave plate 1274, where the circularly polarized light is converted to linearly polarized light with a horizontal polarization. Thus, the light propagating in the two directions experiences a total relative phase shift of  $2\phi$  (e.g.,  $\pi/2$ ), which has the same effect as the first embodiment of the non-reciprocal phase shifter 1250 illustrated in Figures 26 and 27.

[0173] The effect of the non-reciprocal phase shifter 1250 on the orientation of the polarization and the phase delay provides the biasing effect described above and explained again in connection with Figure 24. As shown in Figure 24, the light entering the second PM fiber 1258 in the vertical polarization is combined at the



second PM coupler 1266 with the light that propagated through the common rung 712 from the first PM coupler 1264 to the second PM coupler 1266. For reasons that will become apparent in the following discussion, it is desirable that the light entering the second PM coupler 1266 from the common rung 712 have the same polarization as the light entering the second PM coupler from the second PM fiber 1258. Thus, in the preferred embodiment, either the second PM fiber 1258 or the common rung 712 is rotated by  $90^\circ$  so that the light in the vertical polarization in the second PM fiber 1258 is oriented in the same direction as the light in the horizontal polarization of the common rung 712. This is readily accomplished by rotating the second end 1262 of the second PM fiber 1258 proximate to the second collimating lens 1278 so that the vertically polarized light enters the second end 1262 with its state of polarization oriented along the horizontal polarization axis of the second PM fiber 1258. Thus, the light that exits the non-reciprocal phase shifter 1250 in the vertical state of polarization is applied to the coupler 1266 as light in the horizontal state of polarization with respect to the polarization axes of the coupler 1266. Accordingly, the light from the non-reciprocal phase shifter 1250 has the same state of polarization as the light from the common rung 712.

[0174] The light that passes through the common rung 712 and the light that passes through the non-reciprocal phase shifter 1250 next enter the port 1124 of the polarization beam splitter (PBS) 1104. The light in the horizontal polarization is output from the port 1123 of the PBS 1104 to the fiber 740. The fiber 740 includes the delay loop 750 and is terminated at the Faraday rotating mirror (FRM) 1106. The delay loop 750 and the FRM 1106 operate as discussed above, and the reflected and delayed pulses are returned to the port 1123 of the PBS 1104 in the vertical polarization. The pulses are output from the port 1121 of the PBS 1104 to the array 716 via the fiber 720 and propagate in the clockwise direction through the sensors 722(i) of the array 716.

[0175] The pulses are output from the array 716 via the fiber 714 and the depolarizer 1110 to the  $2 \times 2$  coupler 1220 where the clockwise propagating light is combined with the counterclockwise propagating light. The counterpropagating light

also starts out as horizontally polarized light. The light is depolarized and passes through the sensor array 716. Light emerging from the sensor array 716 in the vertical polarization is reflected by the PBS 1123 and is discarded via the port 1122 and the terminator 732. Light emerging from the sensor array 716 in the horizontal polarization passes through the PBS 1123, is delayed by the loop 750, and is rotated to the vertical polarization by the FRM 1106. The return light, which is in the vertical polarization, is reflected by the PBS 1123 to the port 1124 and is thus directed to the second PM coupler 1266. A portion of the light passes through the delay loop 1269 of the common rung 712 and a portion of the light passes through the non-reciprocal phase shifter 1250. As discussed above, light entering the non-reciprocal phase shifter 1250 in the vertical polarization propagates through the fast birefringent axis 1282 of the quarter-wave plate 1274 (Figure 27) and does not experience a relative phase delay. Thus, the two pulses of counterclockwise light propagate to the coupler 1220 where they are combined with the clockwise propagating light pulses. The light signals that passed through the common rung 712 and the delay loop 1269 in both directions experience no relative phase shift and combine as discussed above. The light signals that passed through the non-reciprocal phase shifter 1250 in both directions experience a relative phase shift of  $\pi/2$  between the clockwise propagating signal and the counterclockwise propagating signal and thus have a  $\pi/2$  phase bias, as discussed above. At both outputs of the coupler 1220, a portion of the two pulses of light returning from the sensor array 1200 is directed to the polarizer 1224, and the remaining portion is directed to the polarizer 1232. The role of the two polarizers 1224 and 1232 is to ensure that the light entering the loop has the same polarization as the light leaving the loop, which guarantees reciprocity. As described earlier, the two pulses reaching the detector 1230 are in phase quadrature, which allows the use of a number of signal processing techniques well-known in the art to avoid signal fading. Similar comments apply to the detector 1226. In the embodiment of Figure 24, the generation of two pulses in phase quadrature is the main reason for incorporating the rung containing the non-reciprocal phase shifter 1250.

[0176] Figures 30-36 illustrate further alternative embodiments of the present invention in which a folded Sagnac sensor array utilizes polarization-based biasing for multiple detectors, wherein each detector has a bias point which can be set independently of the bias points of the other detectors. The embodiments of Figures 30-36 include the sensor array 716, which was described in detail above. It should be understood that other configurations of amplified sensor arrays can also be used in place of the sensor array 716 in the embodiments of Figures 30-36.

[0177] In a folded Sagnac sensor array 1300 illustrated in Figure 30, a polarized fiber superfluorescent source (SFS) 1310 is coupled to a polarization controller 1312 via a fiber 1314. The fiber 1314 further couples the polarization controller 1312 to a first port of a 2×2 coupler 1316. A second port of the coupler 1316 is an output port, which will be discussed below. A third port of the coupler 1316 is coupled via a fiber 1318 to a non-reflective terminator 1320. A fourth port of the coupler 1316 is coupled to a first port 1330 of a polarization beam splitter (PBS) 1332 via a common array input/output fiber 1334. A second port 1336 of the polarization beam splitter 1332 is coupled to a first horizontal polarizer 1338. The first horizontal polarizer 1338 is coupled to the second array input/output fiber 720 of the array 716. A third port 1340 of the polarization beam splitter 1332 is connected to a common delay fiber 1342, which is formed into a delay loop 1344 and which is terminated at a Faraday rotating mirror (FRM) 1346. A fourth port 1348 of the polarization beam splitter 1332 is coupled to a second horizontal polarizer 1350 and then to a depolarizer 1352. The depolarizer 1352 is coupled to the first array input/output fiber 714.

[0178] The second port of the coupler 1316 is coupled to a detector subsystem 1360 via a fiber 1362. In the embodiment of Figure 30, the detector subsystem 1360 comprises a 1×n coupler 1364 which has a single input port that receives the light from the second port of the coupler 1316. A first output port of the 1×n coupler 1364 is coupled to a polarization controller 1366. The polarization controller 1366 is coupled to a polarizer 1368, which is in turn coupled to a first detector 1370. A second output port of the 1×n coupler 1364 is coupled to a polarization controller 1372. The polarization controller 1372 is coupled to a polarizer 1374, which is

coupled to a second detector 1376. Additional polarization controllers, polarizers and detectors (not shown) can be connected to additional ports (not shown) of the  $1 \times n$  coupler 1364.

[0179] The folded Sagnac sensor array 1300 of Figure 30 operates in the following manner. The polarized SFS 1310 provides a polarized output signal which passes through the polarization controller 1312 via the fiber 1314. The polarization controller 1312 is adjustable to vary the polarization to a desired state of polarization. For example, in Figure 30, the state of polarization is adjusted to provide linearly polarized light oriented at  $45^\circ$  with respect to the vertical and horizontal axes at the input to the polarization beam splitter 1332. The light remains in the fiber 1314 and is provided as the input to the coupler 1316. The coupler 1316 couples approximately 50 percent of the incoming light to the first output fiber 1318 and is thus discarded at the non-reflective terminator 1320. The coupler 1316 couples approximately 50 percent of the incoming light to the common array input/output fiber 1334.

[0180] The common array input/output fiber 1334 guides the light to the polarization beam splitter 1330, which reflects horizontally polarized light to the second port 1336 and which passes vertically polarized light to the third port 1340. The reflected horizontally polarized light from the second port 1336 passes through the first horizontal polarizer 1338 to the second array input/output fiber 720 and propagates in a clockwise direction through the array 716. The clockwise propagating light exits the array 716 via the depolarizer 1352 and the array input/output fiber 714. As discussed above, the depolarizer 1352 assures that the exiting light is substantially equally distributed in the horizontal polarization mode and the vertical polarization mode after passing through the sensors in the array 716. The clockwise propagating light then passes through the second horizontal polarizer 1350, which eliminates the portion of the light in the vertical polarization. The clockwise propagating light in the horizontal polarization then enters the fourth port 1348 of the polarization beam splitter 1330 and is reflected to the third port 1340 to propagate in the common delay fiber 1342. The returning clockwise light passes through the delay loop 1344 to the Faraday rotating mirror 1346 where it is reflected as vertically polarized light. The

vertically polarized light returns to the third port 1340 of the polarization beam splitter 1332 and is passed through to the first port 1330.

[0181] As discussed above, the light which was originally incident at the first port 1330 of the polarization beam splitter 1332 was oriented at approximately  $45^\circ$  to the horizontal and vertical polarizations. Thus, approximately 50 percent of the light corresponding to the vertically polarized component of the light passed through the polarization beam splitter 1332 to the third port 1340 and thus to the common delay fiber 1342. The vertically polarized light propagates through the delay loop 1344 and is reflected by the Faraday rotating mirror 1346 as horizontally polarized light. The reflected horizontally polarized light passes through the delay loop 1344 and back to the third port 1340 of the polarization beam splitter 1332. Because the light is horizontally polarized, the light is reflected to the fourth port 1348 of the polarization beam splitter 1332 and is thus caused to propagate via the first array input/output fiber 714, through the second horizontal polarizer 1350, through the depolarizer 1352 and into the array 716 to propagate therein in a counterclockwise direction. The depolarizer 1352 assures that the counterclockwise propagating light has components in all polarizations so that when the counterclockwise propagating light emerges from the array 716, there will be at least a portion of the light in the horizontal polarization.

[0182] The counterclockwise propagating light emerges from the array 716 via the second array input/output fiber 720, and the horizontally polarized component of the light passes through the first horizontal polarizer 1338, which eliminates the light at other polarization orientations. The horizontally polarized light resulting from the counterclockwise propagating portion of the light enters the second port 1336 of the polarization beam splitter 1332 and is reflected to the first port 1330 of the polarization beam splitter 1332 where it is combined with the vertically polarized light which resulted from the clockwise propagating portion of the light.

[0183] The combined light propagates to the fourth port of the coupler 1316 where approximately 50 percent of the combined light is coupled to the second port of the coupler 1316 and thus to the detector subsystem 1360 via the fiber 1362. The  $1 \times n$  coupler 1364 divides the light into N portions. For example, in Figure 30, N is equal

to 2, and a first portion of the light is coupled to the polarization controller 1366 to propagate through the polarizer 1368 to the first detector 1370, and a second portion of the light is coupled to the polarization controller 1372 to propagate through the polarizer 1374 to the second detector 1376. The orientations of the polarization controllers 1366, 1372 and the polarizers 1368, 1374 can be adjusted to bias the optical signals incident on the first detector 1370 and the second detector 1376 at different phases. For example, the signal applied to the second detector 1376 can be biased to be in quadrature with the signal applied to the first detector 1370 so that when one signal has minimum sensitivity, the other signal has maximum sensitivity, and vice versa.

[0184] As discussed above, each of the two signal portions travels the same distance through the array 716, through the common delay fiber 1342, and through the delay loop 1344. Thus, in the absence of perturbations caused by acoustic signals or other noise impinging on the sensors in the array 716, the two portions will be in phase and will constructively interfere to generate a combined optical signal having a linear polarization of  $45^\circ$ ; however, the light has a state of polarization orthogonal to the original state of polarization. Thus, if the original state of polarization was  $+45^\circ$ , then the state of polarization of the output light (again in the absence of a phase perturbation) is  $-45^\circ$ .

[0185] In the presence of an acoustic signal, the clockwise propagating light and the counterclockwise propagating light experience a relative phase shift. With increasing relative phase shift, the state of polarization of the two interfering beams changes from  $-45^\circ$  linear polarization to left-hand circular polarization to  $+45^\circ$  polarization to right-hand circular polarization and back to  $-45^\circ$  polarization. The progression through these four states of polarization define a circle on the Poincaré sphere. The state of polarization at the output of the polarization beam splitter 1332 corresponds to a point along this circle on the Poincaré sphere whose location on the circle is a function of the acoustically-induced non-reciprocal phase shift.

[0186] After traveling from the output of the polarization beam splitter 1332, through the common array input/output fiber 1334, through the coupler 1316 and to

the detector subsystem 1360, the state of polarization of the combined signal is altered arbitrarily by the unknown birefringence of the fiber 1334. The polarization controller 1366 proximate to polarizer 1368 in front of the first detector 1370 and the polarization controller 1372 proximate to the polarizer 1374 in front of the second detector 1376 are used to re-orient the states of polarization to a respective selected state of polarization for each detector 1370, 1376. The polarization controllers 1366, 1372 are set, for example, when no acoustic signals are applied to the array 716, and thus no relative phase shift is introduced to the counterpropagating optical signals.

[0187] For example, to provide a bias point of  $\pm 90^\circ$  for the first detector 1370, the polarization controller 1376 is set so that when the combined light at the output of the polarization beam splitter 1332 has a left-hand circular state of polarization, the first detector 1370 detects either a maximum intensity or a minimum intensity of the light. For other states of polarization of the output light, the first detector 1370 detects light having an intensity between the maximum intensity and the minimum intensity.

[0188] As a further example, the second detector 1376 can advantageously be set to a different bias point, such as, for example,  $0^\circ$  and  $180^\circ$ . For this bias point, the polarization controller 1372 is set so that when the light at the output of the polarization beam splitter 1332 has a  $-45^\circ$  state of polarization, the second detector 1376 detects either a maximum intensity or a minimum intensity of the light. For other states of polarization of the output light, the second detector 1376 detects light having an intensity between the maximum intensity and the minimum intensity.

[0189] It should be understood that the light applied to the input of the polarization beam splitter 1332 can have a state of polarization other than  $\pm 45^\circ$ . For example, if the input light has an original left-hand circular state of polarization, the polarization controllers 1366, 1372 are set accordingly to provide the appropriate bias points to the first detector 1370 and the second detector 1376.

[0190] Figure 31 illustrates an alternative configuration of a folded Sagnac sensor array 1300', which is substantially similar to the folded Sagnac sensor array 1300 of Figure 30. In the folded Sagnac sensor array 1300' of Figure 31, the depolarizer 1352 is located in the second array input/output fiber 720 rather than in the first array

input/output fiber 714. Because of the reciprocal structure of the sensor array 716, the relocation of the depolarizer 1352 to the fiber 720 does not change the overall operation of the folded Sagnac sensor array 1300' with respect to the operation of the folded Sagnac sensor array 1300. The operation of the folded Sagnac sensor array 1300' is similar to the operation of the folded Sagnac sensor array 1300 and will not be described in detail herein.

[0191] Figure 32 illustrates a further alternative embodiment of a folded Sagnac acoustic sensor array 1400, which is similar to the folded Sagnac sensor array 1300 of Figure 30, and like elements have been numbered accordingly. Unlike the folded Sagnac sensor array 1300, the folded Sagnac sensor array 1400 replaces the 2×2 coupler 1316 with a polarization independent optical circulator 1410. The optical circulator performs a similar function as the 2×2 coupler 1316; however, in the folded Sagnac sensor array 1300 approximately 50 percent of the input light is lost when the input light is split at the coupler 1316 and approximately 50 percent of the output light is lost when it is split at the coupler 1316. In the embodiment 1400, substantially all the input light is passed from the polarized SFS 1310 through the circulator 1410 to the polarization beam splitter 1332 and substantially all the output light is passed from the polarization beam splitter 1332 through the circulator 1410 to the detector subsystem 1360.

[0192] Figure 33 illustrates an alternative configuration of a folded Sagnac sensor array 1400', which is substantially similar to the folded Sagnac sensor array 1400 of Figure 32. In the folded Sagnac sensor array 1400' of Figure 33, the depolarizer 1352 is located in the second array input/output fiber 720 rather than in the first array input/output fiber 714. Because of the reciprocal structure of the sensor array 716, the relocation of the depolarizer 1352 to the fiber 720 does not change the overall operation of the embodiment 1400' with respect to the operation of the folded Sagnac sensor array 1400. Thus, the operation of the folded Sagnac sensor array 1400' will not be described in detail herein.

[0193] Figure 34 illustrates a further alternative embodiment of a folded Sagnac sensor array 1600 in accordance with the present invention, which includes a



combined input/output subsystem 1610 which is coupled to the array 716 in a manner similar to the manner described above in connection with Figures 30-33.

[0194] In Figure 34, a polarized source 1620 provides linearly polarized input light along an axis of a polarization maintaining fiber 1622. The polarization maintaining fiber 1622 is rotated such that the polarization axis is oriented at  $\pm 45^\circ$  with respect to the vertical polarization axis of the input output system 1610. The light from the fiber 1622 is coupled to the input/output subsystem 1610 via a first collimating lens 1630. The first collimating lens 1630 directs the light toward a first port 1634 of a first polarization beam splitter (PBS) 1632, which also has a second port 1636, a third port 1638 and a fourth port 1640. The second port 1636 directs a portion of the input light toward a first  $45^\circ$  Faraday rotator ( $45^\circ$  FR) 1642. The third port 1638 directs a portion of the input light toward a second  $45^\circ$  Faraday rotator 1644. As will be described below, the fourth port 1640 directs a selected portion of output light to a detection subsystem 1650.

[0195] The light passing through the first Faraday rotator 1642 is collimated by a second collimating lens 1660 and is coupled into the array input/output fiber 720 and thus propagates to the sensor portion of the array 716 to propagate in a clockwise direction therein.

[0196] The light passing through the second Faraday rotator 1644 passes through a half-wave ( $\lambda/2$ ) plate 1662. The half-wave plate 1662 has first and second birefringent axes (not shown). One of the birefringent axes is oriented at an angle of  $22.5^\circ$  with respect to the vertical polarization axis of the incoming light and at  $-22.5^\circ$  with respect to the  $45^\circ$  polarization of the light traveling toward it from the source (i.e., the axis lies between vertical and the polarization of the light). The purpose of this orientation will be described below. The light passing through the half-wave plate 1662 enters a first port 1672 of a second polarization beam splitter 1670, which also has a second port 1674, a third port 1676 and a fourth port 1678. As discussed below, the second port 1674 is not coupled to additional elements. Light output from the third port 1676 is directed toward a third collimating lens 1680. Light output from the from the fourth port 1678 is directed toward a fourth collimating lens 1682.

[0197] The light passing through the fourth collimating lens 1682 is coupled into the first array input/output fiber 714 and passes through the depolarizer 1352 into the sensor portion of the array 716 to propagate in a counterclockwise direction therein.

[0198] The light passing through the third collimating lens 1680 is focused onto the end of the common delay fiber 1342, propagates through the delay loop 1344 to the Faraday rotating mirror 1346, back through the delay loop 1344 and back to the collimating lens 1680. The reflected light is thus directed back into the third port 1676 of the second polarization beam splitter 1670.

[0199] As discussed above, the light from the fourth port 1640 of the first polarization beam splitter 1632 enters the detection subsystem 1650. The detection subsystem 1650 comprises a first beam splitter 1690, a second beam splitter 1692, a first birefringent element 1694, a second birefringent element 1696, a first detector 1698, a second detector 1700, a first polarizer 1702, and a second polarizer 1704. A first percentage of the light from the fourth port 1640 is reflected by the first beam splitter 1690 and passes through the first birefringent element 1694 and the first polarizer 1702 to the first detector 1698. The remaining portion of the light from the fourth port 1640 passes through the first beam splitter 1690 and is incident on the second beam splitter 1692 where a second percentage of the light is reflected by the second beam splitter 1692 to pass through the second birefringent element 1696 and the second polarizer 1704 to the second detector 1700. The remaining portion of the light passes through the second beam splitter 1692 to additional elements (not shown). If only two detectors are provided, the first percentage of coupling is advantageously 50 percent and the second percentage is advantageously 100 percent so that both detectors 1698, 1700 receive approximately the same amount of light. If a third detector (not shown) is included, then the first percentage is advantageously about  $33\frac{1}{3}$  percent, and the second percentage is advantageously about 50 percent so that the second detector 1700 detector also receives approximately  $33\frac{1}{3}$  percent of the original light. The third detector would then receive the remaining  $33\frac{1}{3}$  percent.

[0200] The folded Sagnac sensor array 1600 of Figure 34 operates in the following manner. As discussed above, the light incident on the first lens 1630 is

oriented at  $45^\circ$  to the vertical and horizontal polarization axes. Thus, the light passing through the lens 1630 and entering the first port 1634 of the first polarization beam splitter 1632 has a component in the horizontal state of polarization and a component in the vertical state of polarization. The horizontal component is reflected by the polarization beam splitter 1632 to the second port 1636, and the vertical component is passed through the polarization beam splitter 1632 to the third port 1638.

[0201] The horizontal component from the second port 1636 passes through the first Faraday rotator 1642, and the state of polarization is rotated by  $45^\circ$  in a first direction (e.g., clockwise) so that the light emerging from the first Faraday rotator 1642 and incident on the second lens 1660 has a linear state of polarization at  $45^\circ$ . The light passes through the second lens 1660 and enters the second array input/output fiber 720 to propagate in the clockwise direction through the array 716. The light may encounter changes in polarization within the array 716. Thus, as described above, the light exiting the array 716 via the first array input/output fiber 714 passes through the depolarizer 1352, which assures that at least a portion of the light is in the horizontal and vertical states of polarization.

[0202] The clockwise propagating light from the first array input/output fiber 714 enters the input/output subsystem 1610 via the fourth lens 1682 and is incident on the second polarization beam splitter 1670. The vertical component of the light passes through the second polarization beam splitter 1670 is output from the second port 1674 and is discarded. The horizontally polarized component of the light is reflected to the third port 1676 of the second polarization beam splitter 1670 and passes through the third lens 1680 to the common delay fiber 1342 to cause the light to propagate through the delay loop 1344, be reflected by the Faraday rotating mirror 1346 in the vertical state of polarization, pass back through the delay loop 1344 and the common delay fiber 1342 to the third lens 1680. The reflected light in the vertical state of polarization passes from the third port 1676 to the first port 1672 of the second polarization beam splitter 1670, passes through the half-wave plate 1662 to the second Faraday rotator 1644 to the third port 1638 of the first polarization beam splitter 1632. Because the half-wave plate 1662 is oriented with one of its

birefringent axes at  $22.5^\circ$  with respect to the vertical polarization axis, the vertical light incident on the half-wave plate 1662 is caused to be mirrored about the birefringent axis so that the state of polarization of the light emerging from the half-wave plate 1662 is oriented at  $45^\circ$  with respect to vertical and horizontal axes. The second Faraday rotator 1644 rotates the state of polarization by a further  $45^\circ$  to cause the light emerging from the second Faraday rotator 1644 and incident on the third port 1638 of the first polarization beam splitter 1632 to have a horizontal state of polarization. Thus, the light entering the third port 1638 is reflected to the fourth port 1640 and enters the detection subsystem 1650 in the horizontal state of polarization.

[0203] As set forth above, the vertical component of the input light incident on the first port 1634 of the first polarization beam splitter 1632 passes through to the third port 1638. The state of polarization of the light is rotated by  $45^\circ$  by the second Faraday rotator 1644 to a  $45^\circ$  state of polarization with respect to the vertical and horizontal polarization axes. The state of polarization of the light is then mirrored about the birefringent axis of the half-wave plate 1662 so that the state of polarization of the light emerging from the half-wave plate is again oriented in the vertical direction. It will be understood by one skilled in the art that the non-reciprocal action of the second Faraday rotator 1644 causes the vertically polarized light that passes from left to right through the second Faraday rotator 1644 and then through the half-wave plate 1646 to first be rotated to a  $45^\circ$  state of polarization and then to be mirrored back to a vertical state of polarization. In contrast, the vertically polarized light that passes from right to left is first mirrored by the half-wave plate 1646 to a  $45^\circ$  state of polarization and is then rotated by the second Faraday rotator 1644 to a horizontal state of polarization.

[0204] The vertically polarized light from the half-wave plate 1662 enters the first port 1672 of the second polarization beam splitter 1670 and passes through to the third port 1676 to the third lens 1680. The vertically polarized light passes through the common delay fiber 1342, through the delay loop 1344, to the Faraday rotating mirror 1346, and is reflected back through the delay loop 1344 and the common delay fiber 1342 as horizontally polarized light. The horizontally polarized light passes

through the third lens 1680 to the third port 1676 of the polarization beam splitter 1670. The horizontally polarized light is reflected to the fourth port 1678 and passes through the fourth lens to 1682 to the first array input/output fiber 714 and through the depolarizer 1352 to propagate in a counterclockwise direction through the array 716.

[0205] The counterclockwise propagating light emerges from the array 716 via the second array input/output fiber 720 and passes through the second lens 1660 to the first Faraday rotator 1642. The first Faraday rotator 1642 rotates state of polarization of the light by  $45^\circ$ . Since the light was effectively depolarized by the depolarizer 1352, the light that passes through the first Faraday rotator 1642 to the second port 1634 of the first polarization beam splitter 1632 includes light that has horizontally and vertically polarized components. The horizontally polarized components of the light are reflected to the first port 1634 and are output through the first lens 1630 to the input fiber 1622. An isolator (not shown) is advantageously included to absorb the light.

[0206] The vertically polarized components of the counterclockwise propagating light entering the second port 1636 of the first polarization beam splitter 1632 pass to the fourth port 1640 and are combined with the horizontally polarized components of the clockwise propagating light. As discussed above in connection with Figure 30, if the counterpropagating light experiences no relative phase shift, the light is combined as linearly polarized light at a  $45^\circ$  state of polarization. A relative phase shift causes the state of polarization to vary, as further discussed above.

[0207] The birefringent elements 1694, 1696 are included to selectively bias the light incident on the detectors 1698, 1900 by introducing a relative phase shift for the light in the two different polarizations (e.g., the horizontal and vertical polarizations, the  $+45^\circ$  and  $-45^\circ$  polarizations, or the left-hand circular and right-hand circular polarizations). The birefringent elements may advantageously comprise linear or circular waveplates (e.g., quarter-wave plates, half-wave plates, Faraday rotators, or the like).

[0208] Figure 35 illustrates an embodiment of a folded Sagnac acoustic sensor array 1750 similar to the folded Sagnac acoustic sensor array 1600 of Figure 34, and

like elements are identified with the same numbers as in Figure 34. Unlike the embodiment of Figure 34, the folded Sagnac acoustic sensor array 1750 includes an unpolarized light source 1720 instead of the polarized light source 1620. In order to utilize the unpolarized light source 1720, the folded Sagnac acoustic sensor array 1750 includes a 45° polarizer 1730 between the first collimating lens 1630 and the first polarization beam splitter 1632. The 45° polarizer 1730 causes the light incident on the first port 1634 of the first polarization beam splitter 1632 to be oriented at 45° and to thus have substantially equal components in the horizontal and vertical polarizations. Thus, the folded Sagnac acoustic sensor array 1750 of Figure 35 operates in substantially the same manner as the folded Sagnac acoustic sensor array 1600 of Figure 34, and the operation of the folded Sagnac acoustic sensor array 1750 will not be described in further detail.

[0209] Figure 36 illustrates a further embodiment of a folded Sagnac acoustic sensor array 1800 similar to the folded Sagnac acoustic sensor arrays 1600 and 1750 of Figures 34 and 35, respectively, and like elements are identified with the same numbers as in Figures 34 and 35. Unlike the embodiments of Figures 34 and 35, the folded Sagnac acoustic sensor array 1800, the light signals passing through the polarizers 1702 and 1704 are not directed to the detectors 1698 and 1700. Rather, the folded Sagnac acoustic sensor array 1800 includes a collimating lens 1810 positioned proximate to the polarizer 1702 and a collimating lens 1812 positioned proximate to the polarizer 1704. The collimating lens 1810 directs the light from the polarizer 1702 into a first end 1822 of a fiber 1820. The fiber 1820 has a second end 1824 proximate to the first detector 1698 such that the light entering the fiber 1820 from the collimating lens 1810 is incident on the first detector 1698. Similarly, the collimating lens 1812 directs the light from the polarizer 1704 into a first end 1832 of a fiber 1830. The fiber 1830 has a second end 1834 proximate to the second detector 1700 such that the light entering the fiber 1830 from the collimating lens 1812 is incident on the second detector 1700. By including the collimating lenses 1810 and 1812 and the fibers 1820 and 1830, the fibers are able to transport the light for a distance to the

detectors 1698 and 1700 so that the detectors may be located in remote locations proximate to the detection electronics (not shown).

[0210] Note that in Figures 34, 35 and 36, the depolarizer 1352 can be relocated from the first array input/output fiber 714 to the second array input/output fiber 720 without significantly affecting the operating characteristics of the folded Sagnac acoustic sensor array 1600, the folded Sagnac acoustic sensor array 1750 or the folded Sagnac sensor array 1800.

[0211] In the foregoing embodiments of Figures 17-36, an amplified sensor array 716 receives two counterpropagating signals from and returns two perturbed counterpropagating signals to a respective front end system which generates the signals and detects the perturbations. In the foregoing embodiments, the sensor array 716 is depicted as a ladder structure with the sensors 722(i) in respective rungs 718(i). A plurality of erbium doped fiber amplifiers (EDFAs) 724 distributed within the ladder structure to amplify the signals distributed to and received from the sensors 722(i).

[0212] Figure 37 illustrates an alternative embodiment of a 16-sensor array 2000 for use in combination with the front end systems described in Figures 30-36 in place of the sensor array 716. In particular, the sensor array 2000 is interposed between a first input/output fiber 2002 and a second input/output fiber 2004. The first input/output fiber 2002 corresponds to the first input/output fiber 714 in Figures 30-36 for example, and the second input/output fiber 2004 corresponds to the second input/output fiber 720 in Figures 30-36. Thus, light entering the sensor array 2000 via the first input/output fiber 2002 propagates from right to left through the sensor array 2000 in Figure 37 and exits via the second input/output fiber 2004, and the light entering the sensor array 2000 via the second input/output fiber 2004 propagates from left to right through the sensor array 2000 and exits via the first input/output fiber 2002. Thus, the right-to-left propagating light in Figure 37 corresponds to the counterclockwise propagating light in Figures 30-36, and the left-to-right propagating light in Figure 37 corresponds to the clockwise propagating light in Figures 30-36.

[0213] The sensor array 2000 is implemented as a tree structure that comprises an outer layer 2010 of amplifiers 2012(1), 2012(2), each having an gain of  $g_1$ . Each outer layer amplifier 2012(i) is followed by a respective splitter 2014(1), 2012(2).

[0214] The sensor array 2000 further comprises an inner layer 2020 of amplifiers 2022(1), 2022(2), 2022(3), 2022(4), 2022(5), 2022(6), 2022(7), 2022(8), each having a respective gain  $g_2$ . Each inner layer amplifier 2022(i) is followed by a respective splitter 2024(1), 2024(2), 2024(3), 2024(4), 2024(5), 2024(6), 2024(7), 2024(8).

[0215] In the illustrated preferred embodiments, each of the splitters 2014(i), 2024(i) is advantageously a 4×4 splitter having two sets of four input/output ports, with one set of ports at each end of the splitter. Light entering the splitter via one of the input/output ports at one end exits the four input/output ports at the other end in substantially equal portions. In Figure 37, each splitter 2024(i) in the inner layer 2020 is illustrated with four ports at a first end and one port at a second end. It should be understood that the three unused ports (not shown) at the second end are non-reflectively terminated. Thus, light entering the single used port at the second end is split between the four ports at the first end, and approximately one-fourth of the light entering each of the four ports at the first end is coupled to the single used port at the second end. The remaining three-fourths of the light from each of the ports at the first end is lost via the three unused ports. Thus, each of the 4×4 splitters 2024(i) operates as a 1-to-4 splitter for light propagating in one direction and as a 4-to-1 combiner for light propagating in the opposite direction.

[0216] Because of the layout illustrated in Figure 37, each layer, 2010, 2020 comprises a respective left portion 2010L, 2020L and a respective right portion 2010R, 2020R.

[0217] The right portion 2010R of the outer layer 2010 comprises the amplifier 2012(1) followed by the splitter 2014(1). The left portion 2010L of the outer layer 2010 comprises the amplifier 2012(2) followed by the splitter 2014(2).

[0218] The right portion 2020R of the inner layer 2020 comprises the amplifiers 2022(1), 2022(2), 2022(3), 2022(4) and the splitters 2024(1), 2024(2), 2024(3), 2024(4). The left portion 2020L of the inner layer 2020 comprises the amplifiers



2022(5), 2022(6), 2022(7), 2022(8) and the splitters 2024(5), 2024(6), 2024(7), 2024(8).

[0219] The outer layer 2010 and the inner layer 2020 are symmetrical about a sensor layer 2030 that comprises a plurality of sensors 2032(1) ... 2032(16). The sensors 2032(1) ... 2032(16) are organized as a four groups 2040(1) ... 2040(4) of sensors.

[0220] Each of the four sensors 2032(1) ... 2032(4) in the first group 2040(1) are connected between a respective one of the four input/output ports at the first end of the splitter 2024(1) and a respective one of the four input/output ports at the first end of the splitter 2024(5).

[0221] Each of the four sensors 2032(5) ... 2032(8) in the second group 2040(2) is connected between a respective one of the four input/output ports at the first end of the splitter 2024(2) and a respective one of the four input/output ports at the first end of the splitter 2024(6).

[0222] Each of the four sensors 2032(9) ... 2032(12) in the third group 2040(3) is connected between a respective one of the four input/output ports at the first end of the splitter 2024(3) and a respective one of the four input/output ports at the first end of the splitter 2024(7).

[0223] Each of the four sensors 2032(13) ... 2032(16) in the fourth group 2040(4) is connected between a respective one of the four input/output ports at the first end of the splitter 2024(4) and a respective one of the four input/output ports at the first end of the splitter 2024(8).

[0224] Within each group 2040(i) of sensors 2032(i), three of the sensors include delay fibers 2042(i) interposed in the path between the input/output ports of the two splitters 2024(i) coupled to the group. The delay fibers 2042(i) have suitable lengths selected to provide proper timing of the time-division multiplexed (TDM) pulses passing through the sensors 2032(i).

[0225] The first sensor in each group (i.e., the sensors 2032(1), 2032(5), 2032(9), 2032(13)) has no additional delay other than the inherent propagation delay of the path between the respective two splitters.

[0226] The second sensor in each group (i.e., the sensors 2032(2), 2032(6), 2032(10), 2032(14)) has an additional delay of  $\tau$  provided by first and second delay fibers 2042(1), each having delay of  $\tau/2$ .

[0227] The third sensor in each group (i.e., the sensors 2032(3), 2032(7), 2032(11), 2032(15)) has an additional delay of  $2\tau$  provided by third and fourth delay fibers 2042(2), each having delay of  $\tau$ .

[0228] The fourth sensor in each group (i.e., the sensors 2032(4), 2032(8), 2032(12), 2032(16)) has an additional delay of  $3\tau$  provided by a fifth and sixth delay fibers 2042(3), each having delay of  $3\tau/2$ .

[0229] The single used input/output port at the second end of each of the splitters 2024(1) ... 2024(8) is coupled to a first input/output terminal of a respective one of the amplifiers 2022(1) ... 2022(8). In the illustrated embodiment, the splitter 2024(1) is coupled to the amplifier 2022(1), the splitter 2024(2) is coupled to the amplifier 2022(2), and so on.

[0230] A second input/output port of each of the amplifiers 2022(1) ... 2022(4) is coupled to a respective one of the four input/output ports of the splitter 2014(1). A second input/output port of each of the amplifiers 2022(5) ... 2022(8) is coupled to a respective one of the four input/output ports of the splitter 2014(2).

[0231] The amplifiers 2022(1), 2022(5) are coupled to the splitters 2014(1), 2014(2) without any additional delay interposed in the path other than inherent propagation delay.

[0232] The amplifiers 2022(2), 2022(6) are coupled to the splitters 2014(1), 2014(2) via respective delay fibers 2044(1), which each provide an additional delay of  $2\tau$ . Thus, the total additional delay to all the sensors in the second group 2040(2) is  $4\tau$ .

[0233] The amplifiers 2022(3), 2022(7) are coupled to the splitters 2014(1), 2014(2) via respective delay fibers 2044(2), which each provide an additional delay of  $4\tau$ . Thus, the total additional delay to all the sensors in the third group 2040(3) is  $8\tau$ .

[0234] The amplifiers 2022(4), 2022(8) are coupled to the splitters 2014(1), 2014(2) via respective delay fibers 2044(3), which each provide an additional delay of

$6\tau$ . Thus, the total additional delay to all the sensors in the fourth group 2040(4) is  $12\tau$ .

[0235] It can be readily determined that the total additional delay between the splitters 2014(1) and 2014(2) through the first sensor 2032(1) is  $0\tau$ . The total additional delays between the splitters 2014(1) and 2014(2) through the remaining sensors 2032(2) ... 2032(16) are as follows:

2023(2)	$\tau$
2032(3)	$2\tau$
2023(4)	$3\tau$
2032(5)	$4\tau$
2023(6)	$5\tau$
2032(7)	$6\tau$
2023(8)	$7\tau$
2032(9)	$8\tau$
2023(10)	$9\tau$
2032(11)	$10\tau$
2023(12)	$11\tau$
2032(13)	$12\tau$
2023(14)	$13\tau$
2032(15)	$14\tau$
2023(16)	$15\tau$

[0236] As discussed above, the value of  $\tau$  is selected to be sufficient to adequately separate the pulses in time after propagating through each sensor 2032(i). For example, in one embodiment, the value of  $\tau$  is advantageously 60 nanoseconds so that 50-nanosecond pulses are separated by 10-nanosecond guardbands.

[0237] As shown in Figure 37, the outer layer  $4 \times 4$  splitters 2014(1) and 2014(2) are configured with the four input/output ports on the first end directed toward the sensors 2032(i) and connected as described above. Two of the input/output ports on the second end are non-reflectively terminated and are not shown in Figure 37. A first input/output port of the amplifier 2012(1) is coupled to one of the remaining input/output ports on the second end of the splitter 2014(1). A first input/output port of the amplifier 2012(2) is coupled to one of the remaining input/output ports on the second end of the splitter 2014(2). A second remaining input/output port on the second end of the splitter 2014(1) is coupled to a first pump source 2050(1). A

second remaining input/output port on the second end of the splitter 2014(2) is coupled to a second pump source 2050(2).

[0238] A second input/output port of the amplifier 2012(1) is coupled to the first input/output fiber 2002 via a first input/output port at a first end of a first wavelength division multiplexing (WDM) coupler 2060(1). A second input/output port at a second end of the first WDM coupler 2060(1) is coupled to the first input/output fiber 2002. A third input/output port, also at the second end of the first WDM coupler 2060(1), is coupled to receive pump light from a third pump source 2062(1).

[0239] The first WDM coupler 2060(1) is configured so that all the light entering the first input/output port at a signal wavelength  $\lambda_s$  (e.g., 1,560 nanometers) passes through the coupler to the second input/output port. Similarly, light at the signal wavelength  $\lambda_s$  entering the second input/output port passes through the coupler to the first input/output port.

[0240] Since substantially no coupling occurs at the signal wavelength  $\lambda_s$ , substantially all the light entering the array 2000 via the first input/output fiber 2002 passes through the first WDM coupler 2060(1) from right to left in Figure 37 and enters the amplifier 2012(1). Similarly, substantially all the light exiting the array 2000 from left to right via the amplifier 2012(1) passes through the first WDM coupler 2060(1) to the first input/output fiber 2002.

[0241] In contrast to the light at the signal wavelength, substantially all the pump light at a pump wavelength  $\lambda_p$  (e.g., 1,480 nanometers) from the pump source 2062(1) enters the third input/output port of the first WDM coupler 2060(1) and is coupled to the second input/output port of the coupler to thereby propagate to the amplifier 2012(1).

[0242] Similarly, a second input/output port of the amplifier 2012(2) is coupled to the second input/output fiber 2004 via a first input/output port at a first end of a second wavelength division multiplexing (WDM) coupler 2060(2). A second input/output port at a second end of the second WDM coupler 2060(2) is coupled to the second input/output fiber 2004. A third input/output port, also at the second end

of the second WDM coupler 2060(2), is coupled to receive pump light from a fourth pump source 2062(2).

[0243] As described above for the first WDM coupler 2060(1), substantially all the light at the signal wavelengths  $\lambda_s$  passes through the second WDM coupler 2060(2) without coupling, and substantially all the light from the pump source 2062(2) is coupled to the second input/output port of the second WDM coupler 2060(2) and propagates to the amplifier 2012(2).

[0244] Unlike the two WDM couplers 2060(1) and 2060(2), the 4×4 splitters 2014(1), 2014(2) and the splitters 2024(1) ... 2024(8) are broadband couplers. That is, the splitters have substantially the same coupling coefficients over the range of wavelengths from 1,480 nanometers to 1,560 nanometers. Thus, the light at the signal wavelengths  $\lambda_s$  and the light at the pump wavelengths  $\lambda_p$  are coupled substantially the same. In addition, the splitters are preferably characterized so that coupling coefficients are substantially similar so that the light at the signal wavelength  $\lambda_s$  and the light at the pump wavelength  $\lambda_p$  entering the array 2000 are divided substantially equally among the four outputs of each splitter and so that the light at the signal wavelength from each sensor are combined substantially equally.

[0245] In operation, the pump source 2062(1) provides pump light to the first WDM coupler 2060(1). The pump light propagates to the amplifier 2012(1) and is absorbed therein so that the amplifier provides gain to light entering the amplifier at the signal wavelength. Any residual pump light not absorbed by the amplifier 2012(1) passes through the splitter 2014(1) and is divided substantially equally among the four amplifiers 2022(1) ... 2022(4). In addition, light from the pump source 2050(1) enters the splitter 2014(1) and is divided substantially equally to propagate to the four amplifiers 2022(1) ... 2022(4). The pump light is absorbed in the four amplifiers to provide amplification for the signal light.

[0246] In like manner, light from the pump source 2062(2) is coupled to the amplifier 2012(2) via the second WDM coupler 2060(2), and any residual pump light is split among the four amplifiers 2024(5) ... 2024(8) via the splitter 2014(2). In

addition, pump light from the pump source 2050(2) is split by the splitter 2014(2) and provided to the four amplifiers 2024(1) ... 2024(4).

[0247] A signal light pulse having a duration of approximately 50 nanoseconds enters the array 2000 via the first input/output fiber 2002 and is first amplified by the amplifier 2012(1). The amplified light pulse is then split into four substantially equal portions by the splitter 2014(1). The first portion is amplified by the amplifier 2022(1) and then enters the first sensor group 2040(1) via the splitter 2024(1) which divides the first portion into four subportions. A first subportion passes through the sensor 2032(1). A second subportion passes through the sensor 2032(2). A third subportion passes through the sensor 2032(3). A fourth subportion passes through the sensor 2032(4).

[0248] The first subportion encounters no additional delay. The second subportion is delayed by the two  $\tau/2$  delay fibers 2042(1) for a total delay of  $\tau$ . The third subportion is delayed by the two  $\tau$  delay fibers 2042(2) for a total delay of  $2\tau$ . The fourth subportion is delayed by the two  $3\tau/2$  delay fibers 2042(3) for a total delay of  $3\tau$ .

[0249] The four subportions in the first sensor group 2040(1) are recombined by the splitter 2024(5). However, because of the respective propagation times through the sensors and the delays, the first subportion arrives at the splitter approximately 60 nanoseconds before the second subportion. The second subportion arrives approximately 60 nanoseconds before the third subportion. The third subportion arrives approximately 60 nanoseconds before the fourth subportion. Thus, the output of the splitter 2024(5) comprises four 50-nanosecond pulses at 60-nanosecond intervals.

[0250] The pulses output from the splitter 2024(5) are amplified by the amplifier 2022(5) and then propagate to the splitter 2014(2), where the pulses are combined with pulses that passed through the second sensor group 2040(2), the third sensor group 2040(3) and the fourth sensor group 2040(4).

[0251] Within the second, third and fourth sensor groups, the signal pulse is split into four subportions, the four subportions are selectively delayed and are then

recombined as discussed above with respect to the first sensor group. In addition, the portion of light entering the second sensor group 2040(2) is first delayed by the first  $2\tau$  delay 2044(1) before being amplified by the amplifier 2022(2) and split by the splitter 2024(2). The signal pulses output by the second sensor group 2040(2) are recombined by the splitter 2046(6) and amplified by the amplifier 2022(6) and are then delayed by a second  $2\tau$  delay 2044(1) before arriving at the splitter 2014(2). Because of the extra  $4\tau$ -delay provided by the two  $2\tau$  delays 2044(1), the first signal pulse arriving at the splitter 2014(2) from the second sensor group arrives 60 nanoseconds after the fourth signal pulse from the first sensor group.

[0252] In like manner, the signal pulses outputted from the third sensor group are delayed by an additional  $8\tau$  by the two delays 2044(2) so that the first signal pulse from the third sensor group arrives 60 nanoseconds after the fourth signal pulse from the second sensor group.

[0253] Similarly, the signal pulses outputted from the fourth sensor group are delayed by an additional  $12\tau$  by the two delays 2044(3) so that the first signal pulse from the fourth sensor group arrives 60 nanoseconds after the fourth signal pulse from the third sensor group.

[0254] The signal pulses from the four sensor groups are combined in the splitter 2014(2). The signal pulses are then amplified by the amplifier 2012(2) and are output from the array via the second input/output fiber 2004.

[0255] In like manner, a 50-nanosecond light pulse entering the sensor array 2000 via the second input output fiber 2004 and traveling from left to right through the array is first amplified by the amplifier 2012(2) and split by the splitter 2014(2) into four pulses. The four pulses are selectively delayed and further split, as discussed above for the right to left propagating signal, so that sixteen 50-nanosecond pulses at 60-nanosecond intervals arrive at the splitter 2014(1). The sixteen pulses are combined by the splitter 2014(1) and are amplified by the amplifier 2012(1) before exiting the array via the first input/output fiber 2002.

[0256] It should be understood that the pulse widths and the delay times can be varied. Furthermore, additional splitters, amplifiers and delays can be provided to increase the number of sensors in the array 2000.

[0257] The amplifiers 2012(i), 2022(i) that precede each splitter 2014(i), 2024(i) compensate for the splitting loss in the respective coupler. The tree-structure telemetry of Figure 37 has the advantage of directing unused pump power from earlier amplifiers into later amplifiers. In an exemplary system wherein the pump light has a pump wavelength  $\lambda_p$  of, for example, 1,480 nanometers, and wherein the signal has a signal wavelength  $\lambda_s$  of, for example, 1,550 nanometers, the splitting couplers must be either dual band or broadband to have similar coupling ratios across the pump and signal wavelengths. Such couplers are commercially available from, for example, Gould Fiber Optics, 1121 Benfield Boulevard, Millersville, Maryland. The embodiment of Figure 37 has a further advantage that, if additional pump power is required to power the later stage amplifiers, the additional pump power can be added at one of the unused ports of one of the 4×4 splitters 2012. Thus, only the first-stage amplifiers (i.e., the amplifiers 2012 in the outer layer 2010) require additional WDM couplers.

[0258] As discussed above, the sensor telemetry must be constructed to provide increasing differential delays between the sensor paths to prevent pulses from overlapping. This time division multiplexing (TDM) scheme is accomplished by placing delay fibers 2042(i), 2044(i) as shown in Figure 37, where each delay is a fraction of or a multiple of a time interval  $\tau$ . The time interval  $\tau$  is the sensor interrogation window. The duration of each pulse (i.e., the pulse width) is selected to be less than  $\tau$  to avoid overlap. The prescribed delays include the effect of the delay coil and the fiber connecting the nearest components. For example, the longest delay of  $8\tau$  is from the first splitting coupler 2014(1) to the splitting coupler 2024(4). It can be easily seen that the total travel time through each sensor increments by  $\tau$  with these delays, in accordance with TDM requirements.

[0259] Unlike previously described telemetries (i.e., array structures), the tree structure EDFA telemetry described above is advantageous because of its ability to be



pumped by a large number of smaller-power pump lasers (instead of a few larger-power pump lasers). In particular, the pump light can be introduced at various levels in the tree structure rather than at one or two locations.

[0260] Figure 38, comprising Figure 38A and 38B, illustrates an alternative sensor array 2100 that includes 16 sensors 2110(i) in an amplified tree-structure telemetry using a polarization-based front end 2120 similar to the system described above in connection with Figures 30-36, for example.

[0261] Figure 38A illustrates a front end 2120 similar to the front end shown in Figure 34, and like elements are numbered accordingly. Unlike the front end shown in Figure 34, the front end 2120 in Figure 38A includes a bandpass interference filter 2130 of approximately 10-nanometer width centered at 1,550 nanometers positioned between the output of the polarized superfluorescent source 1620 and the collimator 1630. The filter 2130 narrows the light from the source 1620 in order to reduce any deleterious impact of the wavelength-dependence of the Faraday rotators 1642, 1644. An additional pair of bandpass interference filters 2132, 2134 are positioned in the output path between the fourth port 1640 of the first polarization beam splitter 1632 beamsplitter 1634 and the first beamsplitter 1690.

[0262] The amplified array 2100 in Figure 38B is similar to the amplified tree-structure design shown in Figure 37. Again, the timing is based on 60-nanosecond windows which accommodated 50-nanosecond pulses with 10-nanosecond guardbands between pulses. The array timing is measured during the construction of the array 2100 to ensure that, not only is the overall timing of the sensors correct, but also that each sensor 2110(i) is placed symmetrically in the sensor telemetry, thereby ensuring the same phase sensitivity at each sensor.

[0263] The first input/output fiber 2002, the second input/output fiber 2004, the third pump source 2062(1), the fourth pump source 2062(2), the first WDM coupler 2060(1), the second WDM coupler 2060(2), the first amplifier 2012(1) with the gain  $g_1$ , and the second amplifier 2012(2) with the gain  $g_1$  operate as described above in connection with Figure 37, and are labeled accordingly.

[0264] Unlike the array 2000 of Figure 37, the array 2100 of Figure 38B utilizes four levels of  $2 \times 2$  broadband couplers 2140(i) instead of the two levels of  $4 \times 4$  broadband splitters 2014(i), 2024(i). The array 2100 again uses two levels of amplification.

[0265] The counterclockwise propagating signal light incident to the array 2100 via the first input/output fiber 2002 and any residual pump light from the amplifier 2012(i) passes through a first  $2 \times 2$  coupler 2140(1), which splits the light into two substantially equal portions, a first portion (upper in Figure 38B) and second portion (lower in Figure 38B).

[0266] The first portion then enters a first input/output port of second  $2 \times 2$  coupler 2140(2), which splits the first portion of the light into two substantially equal portions, a third (upper) portion at a third input/output port and a fourth (lower) portion at a fourth input/output port. Similarly, the second portion then enters a first input/output port of a third  $2 \times 2$  coupler 2140(3), which splits the second portion of the light into two substantially equal portions, a fifth (upper) portion at a third input/output port and a sixth (lower) portion at a fourth input/output port.

[0267] The third, fourth, fifth and sixth portions enter respective amplifiers 2150(1), 2150(2), 2150(3), 2150(4), which are pumped by pump light from the first pump source 2050(1) via a  $2 \times 2$  coupler 2160(1), which divides the pump light into two substantially equal portions. A first portion of the pump light is provided to a second input/output port of the second coupler 2140(2), and a second portion of the pump light is provided to a second input/output port of the third coupler 2140(3). Thus, the pump light is further divided by the couplers 2140(2), 2140(3) so that approximately one-fourth of the original pump light is provided to each of the amplifiers 2150(1), 2150(2), 2150(3), 2150(4).

[0268] The amplified signal light from the amplifier 2150(1) is provided as an input to a fourth  $2 \times 2$  coupler 2140(4). The amplified signal light from the amplifier 2150(2) is provided as an input to a fifth  $2 \times 2$  coupler 2140(5). The amplified signal light from the amplifier 2150(3) is provided as an input to a sixth  $2 \times 2$  coupler

A30517

2140(6). The amplified signal light from the amplifier 2150(4) is provided as an input to a seventh 2×2 coupler 2140(7).

[0269] The light incident on each coupler 2140(4), 2140(5), 2140(6), 2140(7) is divided substantially equally into two portions.

[0270] A first portion of the light from the fourth coupler 2140(4) is provided as an input to the first sensor 2110(1) and the second sensor 2110(2) via an eighth 2×2 coupler 2140(8), which divides the first portion of the light into two substantially equal portions. A second portion of the light from the fourth coupler 2140(4) is provided as an input to the third sensor 2110(3) and the fourth sensor 2110(4) via a ninth 2×2 coupler 2140(9), which divides the second portion of the light into two substantially equal portions. Thus, each of the sensors 2110(1), 2110(2), 2110(3), 2110(4) receives approximately one-sixteenth of the original signal light incident on the first coupler 2140(1).

[0271] Similarly, the fifth sensor 2110(5) and the sixth sensor 2110(6) each receive approximately one-sixteenth of the original signal light from the fifth coupler 2140(5) via a tenth 2×2 coupler 2140(10). The seventh sensor 2110(7) and the eighth sensor 2110(8) each receive approximately one-sixteenth of the original signal light from the fifth coupler 2140(5) via an eleventh 2×2 coupler 2140(11).

[0272] The ninth sensor 2110(9) and the tenth sensor 2110(10) each receive approximately one-sixteenth of the original signal light from the sixth coupler 2140(6) via a twelfth 2×2 coupler 2140(12). The eleventh sensor 2110(11) and the twelfth sensor 2110(12) each receive approximately one-sixteenth of the original signal light from the sixth coupler 2140(6) via a thirteenth 2×2 coupler 2140(13).

[0273] The thirteenth sensor 2110(13) and the fourteenth sensor 2110(14) each receive approximately one-sixteenth of the original signal light from the seventh coupler 2140(7) via a fourteenth 2×2 coupler 2140(14). The fifteenth sensor 2110(15) and the sixteenth sensor 2110(16) each receive approximately one-sixteenth of the original signal light from the seventh coupler 2140(7) via a fifteenth 2×2 coupler 2140(15).

[0274] Note that at each level of division and amplification, couplers and amplifiers are numbered from the middle of the figure towards the bottom of the figure so that the lower-numbered couplers and amplifiers propagate the counterclockwise-propagating signal light to the lower-numbered sensors.

[0275] The light incident to the array 2100 via the second input/output fiber 2004 is similarly divided by a plurality of couplers 2140(16) ... 2140(30) into sixteen substantially equal portions that are provided to the sensors 2110(1) ... 2110(16) in the opposite (i.e., clockwise direction). Pump light from the second pump source 2050(2) is divided substantially equally by a coupler 2160(2), and is further divided by the couplers 2140(16) and 2140(17) so that four approximately equal portions of the pump light are provided as inputs to four amplifiers 2150(5), 2150(6), 2150(7), 2150(8), which operate to amplify the signal light propagating in the clockwise direction. Note that the couplers and the amplifiers are numbered from the middle toward the upper portion of Figure 38B so that the lower-numbered couplers and amplifiers provide the signal light to the lower-numbered sensors for the clockwise-propagating signal light.

[0276] In order to provide the time division multiplexing characteristics described above in connection with Figure 37, the embodiment of Figure 38B includes a plurality of delay fibers in the array 2100. For example, a first delay fiber 2180(1) is positioned between the coupler 2140(8) and the second sensor 2110(2), and a second delay fiber 2180(1) is positioned between the coupler 2140(23) and the second sensor 2110(2). Similar delay fibers 2180(1) are positioned between the sensors 2110(2), 2110(4), 2110(6), 2110(8), 2110(10), 2110(12), 2110(14), 2110(16) and the respective couplers. Each delay fiber 2180(1) has a length of approximately 6 meters to provide 30 nanoseconds of delay so that the light propagating through the second sensor in each pair of sensors is separated by approximately 60 nanoseconds from the light propagating through the first sensor in the pair of sensors.

[0277] The pairs of signals passing through the first sensor 2110(1) and the second sensor 2110(2) are separated from the pairs of signals passing through the third sensor 2110(3) and the fourth sensor 2110(4) by an additional 120 nanoseconds

of delay provided by a first delay fiber 2180(2) in the path from the coupler 2140(4) to the coupler 2140(9) and a second delay fiber 2180(2) in the path from the coupler 2140(19) to the coupler 2140(24). Each of the delay fibers 2180(2) has a delay of approximately 60 nanoseconds provided by a fiber having a length of approximately 12 meters.

[0278] In like manner, a first 120-nanosecond delay fiber 2180(3) is interposed in the path between the coupler 2140(5) and the coupler 2140(10), and a second 120-nanosecond delay fiber 2180(3) is interposed in the path between the coupler 2140(20) the coupler 2140(25). A first 180-nanosecond delay fiber 2180(4) is interposed in the path between the coupler 2140(5) and the coupler 2140(11), and a second 180-nanosecond delay fiber 2180(4) is interposed in the path between the coupler 2140(20) the coupler 2140(26).

[0279] For the remaining eight sensors, a first 225-nanosecond delay fiber 2180(5) is interposed between the coupler 2140(1) and the coupler 2140(3), and a second 225-nanosecond delay fiber 2180(5) is interposed between the coupler 2150(16) and the coupler 2140(18).

[0280] A first 15-nanosecond delay fiber 2140(6) is interposed between the coupler 2140(6) and the coupler 2140(12), and a second 15-nanosecond delay fiber 2140(6) is interposed between the coupler 2140(21) and the coupler 2140(27) so that the total additional delay to the sensors 2110(9) and 2110(10) is 480 nanoseconds. It should be understood that the equivalent delay could be provided by increasing the delay of the delay fibers 2180(5) to 240 nanoseconds and not including the 15-nanosecond delay fibers 2140(6).

[0281] A first 75-nanosecond delay fiber 2180(7) is interposed in the path between the coupler 2140(6) and the coupler 2140(13), and a second 75-nanosecond delay fiber 2180(7) is interposed in the path between the coupler 2140(21) the coupler 2140(28). A first 135-nanosecond delay fiber 2180(8) is interposed in the path between the coupler 2140(7) and the coupler 2140(14), and a second 135-nanosecond delay fiber 2180(7) is interposed in the path between the coupler 2140(22) the coupler 2140(29). A first 195-nanosecond delay fiber 2180(9) is interposed in the path

between the coupler 2140(7) and the coupler 2140(15), and a second 195-nanosecond delay fiber 2180(9) is interposed in the path between the coupler 2140(22) the coupler 2140(30).

[0282] Each of the 2×2 couplers is advantageously characterized before construction so that the couplers can be arranged in the array such that the transmission of each sensor path was as equal as possible. The ten amplifiers 2012(1), 2012(2), 2150(1) ... 2150(8) in Figure 38B are preferably erbium-doped fiber amplifiers (EDFAs). In Figure 38B, the gain  $g_1$  of the amplifiers 2012(1), 2012(2) and the gain  $g_2$  of the amplifiers 2150(1) ... 2150(8) are substantially the same. In the preferred embodiments, the length of the fiber in each amplifier is approximately 1.45 meter to provide approximately 8.2 dB of gain.

[0283] The total gain seen by a given sensor path from the first input/output fiber 2002 to the second input/output fiber 2004 in each direction is 32.8 dB (8.2 dB × 4 amplifiers). This roughly compensates for the total splitting loss (3.1 dB per coupler × 8 couplers) plus the insertion loss of the WDM coupler and the excess loss due to splices and fiber bending. The transmission through an exemplary sensor array constructed in accordance with Figure 38B was measured to be a few dB greater than unity. The amplifiers 2012(1), 2012(2), 2150(1) ... 2150(8) are pumped by the pump sources 2050(1), 2050(2), 2062(1), 2062(2), which advantageously comprise four low-power (e.g., 60 mW) 1,480-nm lasers. As discussed above, the pump light from the pump sources 2062(1), 2062(2) are coupled into the array 2100 through the WDM couplers 2060(1), 2060(2) to pump the first-stage amplifiers 2012(1), 2012(2). The second-stage amplifiers 2150(1) ... 2150(8) are pumped by the unused power from the first-stage amplifiers along with the power added by the pump sources 2050(1), 2050(2). The pump power is sufficiently large (and the signal power is sufficiently low) to pump saturate all of the amplifiers 2012(1), 2012(2), 2150(1) ... 2150(8). Preferably, the pump sources 2050(1), 2050(2), 2062(1), 2062(2) are coupled to the array 2100 via one-way isolators 2190 so that any light returning from the array 2100 does not propagate to the pump sources and perturb the source.

[0284] In order to test the sensors 2110(i), an additional PZT transducer wrapped with fiber is placed in series with each sensor 2110(i) so that the effect of an acoustic signal can be simulated for each sensor by selectively activating one or more of the PZT transducers. (The PZT transducers are for testing purposes only and are not part of the preferred embodiment. Therefore, the PZT transducers are not shown in the drawings.) Figures 39A and 39B illustrate the returned pulse train measured at one of the detectors 1698, 1700 (Figure 38A) for a pulse width of 50 nanoseconds and repetition frequencies of 0.942 MHz (1.06-microsecond spacing) and 1.042 MHz (0.96-microsecond spacing), respectively. Each signal pulse applied to the array results in a train of sixteen output pulses which return at 60-nanosecond intervals. Thus, at the lower repetition frequency (Figure 39A), there are gaps between the trains of 16 pulses that return from the sensor array. The power from all of the sensors return with a variation of less than 1.7 dB. These power variations result from the insertion-loss differences of the various couplers and splices.

[0285] Figure 39B illustrates the optimal operating condition in which the pulse trains repeat continuously (i.e., the sixteenth pulse of one pulse train occurs approximately 60 nanoseconds before the first pulse of the next pulse train). The pulse timing was verified to be correct to within 1 nanosecond (20 centimeters) for all the sensor paths.

[0286] In practice, demultiplexing is achieved post detection by digital processing. In an experimental embodiment, a lithium niobate amplitude modulator 2192 is connected to one of the input/output fibers (e.g., the second input/output fiber 2004 in Figure 38A) and is used to pass a single pulse corresponding to the signal to be demultiplexed. The lithium niobate modulator 2192 provides clean switching, eliminating the large noise associated with electronic switches used after the photodiodes.

[0287] To measure the polarization sensitivity of the array, a large phase modulation was induced in the fifth sensor 2110(5) by activating the respective series connected PZT transducer for the fifth sensor. The signal from the fifth sensor was demultiplexed and its detected power was monitored on a digital scope. When a

peak-to-peak phase modulation of greater than  $\pi$  is induced in the signal, the visibility of the sensor can be measured by recording the maximum and minimum voltage obtained on the digital scope. Such a trace is illustrated in Figure 40A, yielding a measured visibility of 0.9. As described above, a significant advantage of the polarization-based front-end design is that polarization-induced signal fading is passively eliminated, and the visibility should ideally be unity on each sensor, independently of the loop birefringence.

[0288] To test this prediction, the visibility of the fifth sensor was measured for eight random settings of a common polarization controller 2194 positioned in one of the input/output fibers (e.g., the first input/output fiber 2002 in Figure 38A). The results of the measurements are shown in Figure 40B, which demonstrate the expected polarization independence. The visibility is short of unity due mainly to the presence of distributed amplifier ASE power at the detector.

[0289] To illustrate the impact and importance of noise subtraction in a Sagnac-based array using a broadband ASE source, a phase modulation at 4 kHz was placed on one of the sensors using the respective fiber wrapped PZT to simulate an acoustic signal, and an amplitude modulation at 3.6 kHz was placed on the optical signal from the source 1620 using a lithium niobate ( $\text{LiNbO}_3$ ) modulator 2196 in the signal path from the source 1620 to the collimator 1630 in Figure 38A. The detected response was measured in a single-detection configuration using only one detector and a balanced-detection configuration in which the outputs of the two detectors 1698, 1700 are connected in such a way that the DC currents from the detectors are subtracted to remove the source amplitude noise. Figure 41 illustrates the results of the measurements. For the single-detection configuration, the amplitude modulation at 3.6 kHz is clearly seen while the phase modulation at 4 kHz is not visible under the broadband source amplitude noise (ASE-ASE beat noise). In the balanced-detection configuration, the amplitude modulation is subtracted by over 50 dB. The phase modulation tone becomes easily visible due to the reduced broadband noise (ASE-ASE beat noise subtraction) and the increased phase modulation signal. As



illustrated, the balanced-detection configuration achieves a large degree of noise subtraction.

[0290] The optical noise floor of a Sagnac-based array with distributed optical amplifiers is a function of the optical power at the receiver. The noise  $N_s^{bd}$  for a balanced-detection receiver is given as:

$$N_s^{bd} = 4B(s + a) + \frac{8B}{\Delta\nu_{sa}}(sa) + \frac{16B}{\Delta\nu_a}(a_{cw}a_{ccw}) \quad (19)$$

where  $B$  is the detection bandwidth; where  $s$ ,  $a_{cw}$ ,  $a_{ccw}$  are the source, clockwise distributed amplifier, and counterclockwise distributed amplifier ASE photon fluxes (#/s); and where  $a = a_{cw} + a_{ccw}$ . In Equation 19,  $\Delta\nu_a$  is the bandwidth of the distributed amplifier photons arriving at the detectors caused by spontaneous emission in the distributed amplifiers, as defined by:

$$\Delta\nu_a = \frac{\left(\int P(\nu_a) d\nu_a\right)^2}{\int (P(\nu_a))^2 d\nu_a} \quad (20)$$

where  $P(\nu_a)d\nu_a$  is the optical power in the frequency band  $\nu_a$  to  $\nu_a + d\nu_a$ .

[0291] Further in Equation 19,  $\Delta\nu_{sa}$  is defined by:

$$\frac{1}{\Delta\nu_{sa}} = \frac{1}{\Delta\nu_{s+a}} \left[ 1 + \frac{s}{2a} \left( 1 - \frac{\Delta\nu_{s+a}}{\Delta\nu_s} \right) + \frac{a}{2s} \left( 1 - \frac{\Delta\nu_{s+a}}{\Delta\nu_a} \right) \right] \quad (21)$$

where  $\Delta\nu_s$  is the bandwidth of source photons arriving at the detector and  $\Delta\nu_{s+a}$  is the combined source and distributed amplifier photons arriving at the receiver defined in accordance with Equation 20 by substituting  $\nu_a$  and  $\nu_{s+a}$  for  $\nu_a$ .

[0292] The noise expression of Equation 19 is given as a photon count fluctuation per unit bandwidth. Equation 19 can be rewritten as follows for a detector current noise,  $\langle \Delta I^2 \rangle$ :

$$\langle \Delta I^2 \rangle = 4Be(I_s + I_a) + \frac{8B}{\Delta\nu_{sa}}(I_s I_a) + \frac{16B}{\Delta\nu_a}(I_{acw} I_{accw}). \quad (22)$$

where  $B$  is the detection bandwidth.

[0293] Equation 22 is confirmed experimentally by measuring the optical noise of the 16-sensor array 2100. An excess noise factor  $F$  is first defined as the ratio of the detected noise to the shot-noise limit and is given by:

$$F \equiv \frac{\langle \Delta I^2 \rangle}{4eB(I_s + I_a)}$$

$$= 1 + \frac{2}{e\Delta\nu_{sa}} \left( \frac{I_s I_a}{I_s + I_a} \right) + \frac{4}{e\Delta\nu_a} \left( \frac{I_{acw} J_{accw}}{I_s + I_a} \right). \quad (23)$$

[0294] By measuring the detector currents  $I_s$ ,  $I_{acw}$ , and  $I_{accw}$  along with their optical spectra (to get  $\Delta\nu_{sa}$  and  $\Delta\nu_a$ ), the expected excess noise factor can be calculated and compared with the measured noise. To measure distributed amplifier currents and spectra ( $I_{acw}$ ,  $I_{accw}$ , and  $\Delta\nu_a$ ), the source is turned off and the output is simply measured. Since the distributed amplifier power cannot be switched off, the source current/spectrum is found by measuring the total output current/spectrum and subtracting the distributed amplifier current/spectrum. This can be done because the distributed amplifiers are pump saturated and their ASE output is not affected by the presence of the small source power in the array (experimentally verified).

[0295] With these output currents and spectra measured, the predicted excess noise factor can be calculated through Equation 23. To measure the noise factor, the output noise is measured directly along with the DC receiver currents. The shot noise level is then calculated from the DC currents, and the excess noise factor is found by taking the ratio of the measured noise and the shot noise. The predicted and measured excess noise factors can then be compared.

[0296] In an experimental setup, the measurements are done for a series of DC source currents at the receiver. These currents are controlled by adjusting the source power with the DC bias of the LiNbO<sub>3</sub> modulator 2196. For each DC source current, the measurements are taken for sensor counts of 4, 8, 12, and 16. The sensor counts were controlled by darkening one, two, or three 4-sensor subarrays by inducing large bend losses in the fibers addressing these subarrays. As the sensor count is changed, the pulse repetition frequency is adjusted to keep a continuous train of pulses at the output. Because of this, the average source power at the detector is the same for each

sensor count within a given set of measurements, and the only change is the amount of distributed amplifier ASE. Therefore, by taking measurements as a function of the sensor count, the noise trend as a function of the ASE power can be found and compared with the predictions of Equation 23.

[0297] The results of the foregoing measurements are shown in Figures 42A, 42B, 42C for three DC source receiver currents. As shown in Figure 42A for the lowest DC source current (1.4  $\mu\text{A}$ ), the agreement between the predicted and measured noise is excellent. For larger source powers and therefore larger DC source receiver currents (4.05  $\mu\text{A}$  in Figure 42B and 9.89  $\mu\text{A}$  in Figure 42C), the measured noise rises above the predicted noise as the source current is increased. This is due, at least in part, to the pick-up of acoustic room noise in the array, a persistent problem in the testing of the Sagnac acoustic sensor designs. As the source power is increased, the sensitivity of the array increases, and room noise picked up in the fiber making up the sensor array and timing coils becomes non-negligible. Although this noise makes measurements of the optical noise floor difficult in the laboratory, it is not a troublesome source of noise in practice since this acoustic pick-up is, in real applications, the signal which is intended to be measured.

[0298] In the Mach-Zehnder based arrays, the sensor response is determined by the length of fiber wrapped around the hydrophone and by the normalized hydrophone responsivity, both of which cannot be changed once the sensor is constructed. In the Sagnac sensor arrays described above, the response is determined in part by these same parameters and is also determined in part by the length of the delay loop, which is shared amongst all the sensors. Because this delay loop can be remotely located away from the sensors, where it is accessible, it is feasible to change the length of the delay loop. It was realized early in the development of Sagnac-based arrays that this ability to affect the response of all of the sensors by changing a single parameter, namely the delay loop length, could be of great benefit to the dynamic range performance of the array. For example, Figures 7, 19 and 21 illustrate embodiments having two delay loops of different lengths to extend the dynamic range of the sensor array.

[0299] To illustrate how the response can be tuned by changing the delay loop length, consider a Sagnac array with an effective delay coil time of 50 microseconds (e.g., approximately a delay loop length of approximately 10 kilometers in an unfolded configuration or a delay loop length of approximately 5 kilometers in a folded configuration), a hydrophone responsivity,  $R$ , of -135 dB rad/ $\mu$ Pa, and a flat optical noise floor of 1  $\mu$ rad/ $\sqrt{\text{Hz}}$ . The minimum detectable acoustic signal,  $a_{\min}(f)$ , can be expressed as:

$$a_{\min}(f) = \frac{\phi\sqrt{T}}{2R\sin(\pi f T_d)} \quad (24)$$

where  $\phi$  is the phase noise per unit bandwidth,  $T$  is the integration time,  $R$  is the hydrophone responsivity (rad/ $\mu$ Pa),  $f$  is the frequency, and  $T_d$  is the delay coil time. Using the foregoing numbers, the minimum detectable acoustic signal in a 1-second integration time is plotted in Figure 43A. Also plotted in Figure 43A is the maximum detectable signal defined as that which produces a 1 rad/ $\sqrt{\text{Hz}}$  phase signal. (This is only an approximation of the upper limit, but it serves as a way to compare the relative performance of two configurations).

[0300] In Figure 43B, the same curves are plotted for an array with the same parameters except that the delay time through the delay loop has been reduced from 50 microseconds to 0.5 microsecond. The shorter delay time moves the detection range upward, making the detection range more suitable for a noisy environment. In contrast, the longer delay time is more suitable for a quieter environment.

[0301] To obtain the combined dynamic range of Figures 43A and 43B, an array would have to be constructed with both a short delay loop and a long delay loop. An array that includes two delay coils, designed such that the pulses returning from all the sensors and the delay coils are separable (in time or wavelength), can be easily constructed, as illustrated above in Figures 7, 19 and 21. In the illustrated configurations, each sensor returns two signals, each of which has a detection ranges corresponding to those of Figures 43A and 43B. In a quiet environment, the signal from the longer delay loop would be used. In the presence of a large acoustic signal that saturates the response from the longer delay loop, the output from the shorter

delay loop would be used. Delay coil switching such as this would allow the array to function in environments in which the magnitude of acoustic signal varies dramatically over time. However, the most useful implementation of multiple delay loops in a Sagnac-based array would combine the signals from each delay loop instead of switching between them. By combining the signals to produce a single output signal which has a true detection range given by the union of the detection ranges of the signals from each delay loop, the array could simultaneously detect down to the noise floor with the longer delay loop in one frequency regime, while handling an extremely large acoustic signal (which saturates the longer delay loop) in another frequency regime. To do this, an algorithm is used that receives as inputs a respective output signal from a given sensor from each delay loop and that returns a signal which has a detection range that comprises the union of the detection ranges of the output signal from the short delay loop and the output signal from the long delay loop.

[0302] If the signal from the shorter delay loop were the same as that from the longer delay loop but with a reduced scale factor, then such an algorithm would be straightforward. However, because the two signals have different frequency responses and sample the acoustic signal at different times, the two signals have little obvious correlation. To illustrate this, consider an acoustic signal which produces the hydrophone phase variation with time shown in Figure 44A. Figures 44B and 44C are plots of the induced phase difference due to the phase signal of Figure 44A for the signal which travels through the longer delay loop (Figure 44B) and the shorter delay loop (Figure 44C). The correlation is not obvious, and it is not clear how to combine these two signals to produce a single signal.

[0303] Figures 45A and 45B illustrate an acoustic sensor array 2200 which works with a linear extrapolation algorithm that combines the signals from two delay loops to reconstruct the phase signal with a dynamic range dramatically increased over that possible with a single delay loop. Figures 45A and 45B correspond to Figures 38A and 38B; however, in Figure 45A, the front end portion of the system includes a first signal source 2210 that outputs a first sequence of optical signal pulses at a first

wavelength  $\lambda_1$  and includes a second signal source 2212 that outputs a second sequence of optical signal pulses at a second wavelength  $\lambda_2$ . For example, the first wavelength  $\lambda_1$  is advantageously approximately 1,520 nanometers, and the second wavelength  $\lambda_2$  is advantageously approximately 1,550 nanometers. The outputs of the two signal sources, 2210, 2212 are combined via a wavelength division multiplexing (WDM) coupler 2214 so that a single signal stream comprising the two sequences of signal pulses is applied to the collimator 1630.

[0304] The system of Figures 45A and 45B further includes a first detection subsystem 2220 and a second detection subsystem 2222 to replace the single detection subsystem 1650 in Figure 38A. For example, the two detection subsystems 2220, 2222 are advantageously coupled to the output of the beamsplitter 1632 via a collimator 2224, an optical fiber 2226, and a WDM coupler 2230 that couples the optical signals at the first wavelength  $\lambda_1$  and the second wavelength  $\lambda_2$  to a first optical fiber 2232 and a second optical fiber 2234, respectively. The first optical fiber 2232 propagates the light at the first wavelength  $\lambda_1$  to the first detection subsystem 2220 via a collimator 2236. The second optical fiber 2234 propagates the light at the second wavelength  $\lambda_2$  to the second detection subsystem 2222 via a collimator 2238.

[0305] The system of Figures 45A and 45B further differs in that the system includes two delay loops 2240 and 2242 in the delay path from the collimator 1680 to the Faraday rotating mirror (FRM) 1346 in place of the single delay loop 1344 of Figure 38A. In particular, the first delay loop 2240 is a longer delay loop that provides a delay of approximately 100 microseconds, and the second delay loop 2242 is a shorter delay loop that provides a delay of approximately 100 nanoseconds. As illustrated, the two delay loops 2240, 2242 are in parallel and are coupled to the common delay fiber 1342 via a first WDM coupler 2244 and a second WDM coupler 2246. Thus, light from the third port 1676 of the polarization beam splitter 1670 passes through the collimator 1680 and enters the first WDM coupler 2244. The first WDM coupler 2244 directs light from the first source 2210 at the first wavelength  $\lambda_1$  to the first delay loop 2240 and directs light from the second source 2212 at the second wavelength  $\lambda_2$  to the second delay loop 2242. The two portions are

recombined in the second WDM coupler 2246, and the combined portions are incident on the Faraday rotating mirror 1346. The reflected signal portions are again split in the second WDM coupler 2246 such that the portion at the wavelength  $\lambda_1$  again passes through the first (longer) delay loop 2240 and the portion at the wavelength  $\lambda_2$  passes through the second (shorter) delay loop 2242. Thus, the light incident on the third port 1676 of the polarization beam splitter 1670 has a first pulse at the first wavelength  $\lambda_1$  that has been delayed by a longer delay than a second pulse at the second wavelength  $\lambda_2$ . The two WDM couplers 2244, 2246 have fairly broad passbands which direct light to the two separate delay coils 2240, 2242. Thus, for example, light from 1,525 nanometers to 1,535 nanometers, which includes the first wavelength  $\lambda_1$ , is advantageously directed to the longer delay loop 2240 while light from 1,545 nanometers to 1,555 nanometers, which includes the second wavelength  $\lambda_2$ , is advantageously directed to the shorter delay loop 2242.

[0306] From the foregoing description, it can be seen that the signals received by the first detection subsystem 2220 provide a first acoustic dynamic range determined by the delay through the first (longer) delay loop 2240, and the signals received by the second detection subsystem 2222 provide a second acoustic dynamic range determined by the delay through the second (shorter) delay loop 2242. It is assumed that all other components of the system of Figures 45A and 45B are broadband to act sufficiently the same across all wavelengths used.

[0307] The phase modulation,  $\phi(t)$ , at the hydrophone in a given sensor is directly proportional to the acoustic signal amplitude. In a Sagnac-based TDM array, each sensor is sampled with a repetition period,  $\tau$ , and the returned signal is a phase difference,  $\phi(t) - \phi(t - T_d)$ , where  $T_d$  is the coil delay. Thus, for a single-delay coil sensor, as previously described, the discrete sampling of a given sensor yields the samples  $S_i$  given by:

$$\begin{aligned}
& \vdots \\
S_{-1} &= \phi(-\tau) - \phi(-\tau - T_d) \mod 2\pi \\
S_0 &= \phi(0) - \phi(-T_d) \mod 2\pi \\
S_1 &= \phi(\tau) - \phi(\tau - T_d) \mod 2\pi \\
& \vdots \\
S_i &= \phi(i\tau) - \phi(i\tau - T_d) \mod 2\pi
\end{aligned} \tag{25}$$

from which the phase difference is recovered through

$$\phi(i\tau) - \phi(i\tau - T_d) = S_i + 2\pi n_i \tag{26}$$

where  $S_i$  has been measured by the array and  $n_i$  is the fringe count which is calculated through a fringe count algorithm,  $F$ , which takes as input the current and previous samples,

$$n_i = F(S_i, S_{i-1}, \dots) \tag{27}$$

[0308] The standard fringe count algorithm,  $F$ , for Mach-Zehnder and Sagnac arrays with a single delay coil is given by:

$$n_i = \begin{cases} n_{i-1}, & |S_i - S_{i-1}| \leq \pi \\ n_{i-1} + 1, & (S_i - S_{i-1}) < -\pi \\ n_{i-1} - 1, & (S_i - S_{i-1}) > \pi \end{cases} \tag{28}$$

and is based on minimizing the phase difference between samples. It greatly extends the dynamic range of the sensor beyond that of a sensor which does not use fringe counting. The embodiment of Figures 45A and 45B enables the use of an improved algorithm which uses information from the additional, shorter delay loop 2242 in the Sagnac-based TDM array to extend the dynamic range beyond the capabilities of the standard fringe count algorithm of Equation 28.

[0309] As discussed above, the Sagnac-based array in Figures 45A and 45B incorporates multiple delay coils 2240, 2242. The broadband WDM couplers 2244, 2246 direct fairly broad passbands to the separate delay loops 2240, 2242. Thus, in the disclosed embodiment, for example, light in the range from 1,525 nanometers to 1,535 nanometers is advantageously directed to the longer delay loop 2240 while light



in the range from 1,545 nanometers to 1,555 nanometers is advantageously directed to the shorter delay loop 2242.

[0310] With multiple delay loops on separate wavelengths, the received data set,  $S^{\lambda_1}$ , for a given sensor and the first wavelength  $\lambda_1$  through the first delay loop 2240 is given by:

$$\begin{aligned}
 S_{-1}^{\lambda_1} &= \phi(-\tau) - \phi(-\tau - T_d^{\lambda_1}) \bmod 2\pi \\
 S_0^{\lambda_1} &= \phi(0) - \phi(0 - T_d^{\lambda_1}) \bmod 2\pi \\
 S_1^{\lambda_1} &= \phi(\tau) - \phi(\tau - T_d^{\lambda_1}) \bmod 2\pi \\
 &\vdots \\
 S_i^{\lambda_1} &= \phi(i\tau) - \phi(i\tau - T_d^{\lambda_1}) \bmod 2\pi
 \end{aligned} \tag{29}$$

[0311] The data set,  $S^{\lambda_2}$ , of the same sensor and the second wavelength  $\lambda_1$  through the second delay loop 2242 is given by:

$$\begin{aligned}
 S_{-1}^{\lambda_2} &= \phi(-\tau + \delta) - \phi(-\tau + \delta - T_d^{\lambda_2}) \bmod 2\pi \\
 S_0^{\lambda_2} &= \phi(\delta) - \phi(\delta - T_d^{\lambda_2}) \bmod 2\pi \\
 S_1^{\lambda_2} &= \phi(\tau + \delta) - \phi(\tau + \delta - T_d^{\lambda_2}) \bmod 2\pi \\
 &\vdots \\
 S_i^{\lambda_2} &= \phi(i\tau + \delta) - \phi(i\tau + \delta - T_d^{\lambda_2}) \bmod 2\pi
 \end{aligned} \tag{30}$$

where  $\delta$  describes the relative phase between the input (and thus returned) signals from the wavelengths  $\lambda_1$  and  $\lambda_2$ . If  $\delta = 0$ , the input pulses at the two wavelengths are coincident in the input fiber. As the input pulse at  $\lambda_2$  is delayed relative to that at the  $\lambda_1$ ,  $\delta$  increases. The delay,  $\delta$ , can be advantageously set to an arbitrary value based on the needs of the algorithm.

[0312] For the algorithm to work, a constraint is imposed on the longer delay loop time,  $T_d^{\lambda_1}$ , such that:

$$T_d^{\lambda_1} = p\tau \tag{31}$$

where  $p$  is an integer such that the longer delay loop time is an integral multiple of  $\tau$ . The purpose of this constraint will be discussed below.

[0313] Based on the foregoing information, a new fringe counting algorithm,  $F'$ , is developed to use the information from multiple delay loops to increase the dynamic

range over the capability of the old, single delay coil algorithm  $F$  defined by Equation 28. The algorithm is developed by plotting the signal from a given sensor from the longer delay loop 2240,  $\beta(t) = \phi(t) - \phi(t - T_d^{\lambda 1})$  in Figure 46A. Figure 46A depicts the standard fringe counting algorithm,  $F$ . The array measures the samples  $S_1$  and  $S_2$ , and because  $S_1 - S_2 > \pi$ ,  $2\pi$  is added to the sample  $S_2$  to recover  $\beta(2\tau)$ , in accordance with the algorithm of Equation 28. The plot in Figure 46A indicates that the fringe count of  $\beta(2\tau)$  could be calculated with more accuracy if the slope of  $\beta(t)$  were known. If, for example, the slope,  $\beta'(t)$ , of  $\beta(t)$  is measured at a frequency  $1/\tau$ . If these measurements are phased to give  $\beta'(t)$  at  $t = \tau$ ,  $t = 2\tau$ , etc., the fringe count of  $\beta(2\tau)$  can then be predicted by using a linear extrapolation form  $\beta(\tau)$ , i.e.,:

$$\beta(2\tau) \approx \beta(\tau) + \frac{\tau}{2} [\beta'(2\tau)], \quad (32)$$

as shown in Figure 46B. The measurement  $S_2 = \beta(2\tau) \bmod 2\pi$  gives a more exact value for the sub- $2\pi$  part of  $\beta(2\tau)$ , but the linear extrapolation of Equation 32 is more accurate to determine the fringe count as shown below in Equation 35 for the new algorithm  $F'$ .

[0314] It is also reasonable to use the slope at the midpoint ( $t = 1.5\tau$ ) instead of at the endpoints ( $t = \tau, 2\tau$ ). In fact, doing this yields substantially similar results with slightly higher low-frequency dynamic range and slightly lower high frequency dynamic range. Since the algorithm has dramatically increased the low-frequency dynamic range almost to the point of not needing any more, we have chosen to use the endpoint algorithm to give a little more high-frequency dynamic range.

[0315] In order to complete the algorithm,  $\beta'$  is measured. This is accomplished through the use of the second, smaller delay loop 2242. The process of measuring  $\beta'$  starts with an expression for  $\beta'(i\tau)$ ,

$$\begin{aligned} \beta'(i\tau) &\approx \frac{\beta(i\tau) - \beta(i\tau - \Delta)}{\Delta} \\ &\approx \frac{\phi(i\tau) - \phi(i\tau - T_d^{\lambda 1}) - \phi(i\tau - \Delta) + \phi(i\tau - \Delta - T_d^{\lambda 1})}{\Delta} \\ &\approx \frac{[\phi(i\tau) - \phi(i\tau - \Delta)] - [\phi(i\tau - T_d^{\lambda 1}) - \phi(i\tau - \Delta - T_d^{\lambda 1})]}{\Delta} \end{aligned} \quad (33)$$

By identifying  $\Delta$  as being equal to  $T_d^{\lambda_2}$ , then the first and second bracketed terms in the final line of Equation 33 are recognized as measurements of the second delay coil with  $\delta=0$  in Equation 30.

[0316] Writing  $(\phi(i\tau) - (\phi(i\tau - T_d^{\lambda_2}))) = S_i^{\lambda_2} + 2\pi n_i^{\lambda_2}$  and  $(\phi(i\tau - T_d^{\lambda_1}) - (\phi(i\tau - T_d^{\lambda_1} - T_d^{\lambda_2}))) = S_{i-p}^{\lambda_2} + 2\pi S_{i-p}^{\lambda_2}$  (see Equation 34) gives:

$$\beta'(i\tau) \approx \frac{(S_u^{\lambda_2} + 2\pi n_i^{\lambda_2}) - (S_{i-p}^{\lambda_2} - 2\pi m_{i-p}^{\lambda_2})}{T_d^{\lambda_2}} \equiv \beta'_i \quad (34)$$

The standard algorithm of Equation 28 is used to calculate the fringe count,  $n^{\lambda_2}$ , on the shorter delay loop 2240.  $\beta'$  is then measured from the shorter delay loop 2240, and with this information, Equation 32 is used to measure the fringe count of each sample from the longer delay loop 2242.

[0317] In mathematical terms a parameter  $\gamma_{i-1}$  is defined as  $\gamma_{i-1} \equiv \frac{\tau}{2}(\beta_{i-1} + \beta_i)$ , and the new linear extrapolation algorithm,  $F'$ , is given by:

$$n_i^{\lambda_1} = \begin{cases} n_{i-1}^{\lambda_1} + \text{Int}([S_{i-1} + \gamma_{i-1}]/(2\pi)), & ([S_{i-1} + \gamma_{i-1}] \bmod 2\pi - S_i) \leq \pi \\ n_{i-1}^{\lambda_1} + \text{Int}([S_{i-1} + \gamma_{i-1}]/(2\pi)) - 1, & ([S_{i-1} + \gamma_{i-1}] \bmod 2\pi - S_i) < -\pi \\ n_{i-1}^{\lambda_1} + \text{Int}([S_{i-1} + \gamma_{i-1}]/(2\pi)) + 1, & ([S_{i-1} + \gamma_{i-1}] \bmod 2\pi - S_i) > \pi \end{cases} \quad (35)$$

where  $\text{Int}(x)$  returns the largest integer less than or equal to  $x$ .

[0318] The limitations of the standard fringe counting algorithm,  $F$ , of Equation 28 and the new two-delay loop linear extrapolation algorithm,  $F'$ , of Equation 35 are compared below. An accurate analysis of the dynamic range of an interferometric sensor array is quite involved and difficult to reduce to a single figure of merit. For simplicity, the following comparison compares the maximum tonal phase amplitude at the hydrophone as a function of frequency such that no fringe count errors occur. This analysis will illustrate the relative performance of the two algorithms as well and the two sensor types (Mach-Zehnder and Sagnac).

[0319] Beginning with the standard fringe counting algorithm,  $F$ , it can be shown that a fringe count error occurs if the magnitude of the difference between two samples exceeds  $\pi$ ,

$$|\beta(t) - \beta(t - \tau)| \geq \pi \quad (36)$$

where, as before,  $\beta(t) = \phi(t) - \phi(t - T_d)$  for a Sagnac sensor and  $\beta(t) = \phi(t)$  for a Mach-Zehnder sensor. Writing  $\phi(t) = A \sin(2\pi f t + \theta)$ , then for a Mach-Zehnder array, the standard fringe counting algorithm,  $F$ , accurately demodulates a tonal phase signal given by  $A \sin(2\pi f t + \theta)$  if:

$$A < \frac{\pi}{2 |\sin(\pi \tau)|} \quad (37)$$

and for a single delay coil Sagnac array if

$$A < \frac{\pi}{4 |\sin(\pi f T_d) \sin(\pi f \tau)|} \quad (38)$$

[0320] The analysis of the new linear extrapolation algorithm,  $F'$ , is more involved. Two conditions must be met for the algorithm to correctly calculate the fringe count:

1. No fringe count errors on the shorter delay loop 2240. The shorter delay loop uses the standard fringe counting algorithm,  $F$  to calculate its fringe counts, as if there were no longer delay loop in the system. Because of the short length of the delay loop 2240, the standard fringe counting algorithm,  $F$ , performs substantially better on it than it does on the longer delay loop.
2. Linear extrapolation accurately predicts the fringe count. The linear extrapolation algorithm,  $F'$ , assumes that the phase difference measured by the long delay loop 2242 varies linearly. For large enough curvature on the phase difference, this condition will not be met and the algorithm will fail.

[0321] The requirement for the first condition is given by Equation with  $T_d$  replaced by  $T_d^{\lambda^2}$  as follows:

$$A < \frac{\pi}{4 |\sin(\pi f T_d^{\lambda^2}) \sin(\pi f \tau)|} \quad (39)$$

[0322] For the second condition, a fringe count error occurs when the linearly extrapolated value of the next phase difference,  $\hat{\beta}(t+\tau)$ , and the actual next phase difference,  $\beta(t+\tau)$ , differ by more than  $\pi$ . To see when this occurs, the linearly extrapolated prediction is written as  $\hat{\beta}(t+\tau) = b(t) + \frac{\tau}{2}(\beta'(t) + \beta'(t+\tau))$ . Thus, the condition for no fringe count error is

$$\begin{aligned} \pi &> |\hat{\beta}(t+\tau) - \beta(t+\tau)| \\ &= |\beta(t) + \frac{\tau}{2}(\beta'(t) + \beta'(t+\tau)) - \beta(t+\tau)|. \end{aligned} \quad (40)$$

Writing  $\beta(t) = (A \sin(2\pi ft + \theta) - A \sin(2\pi f(t - T_d^{1/2}) + \theta))$  and simplifying gives:

$$A < \frac{\pi}{4 \sin(\pi f T_d^{1/2}) [\sin(\pi f \tau) - \pi f \tau \cos(\pi f \tau)]} \quad (41)$$

where it is assumed that  $f T_d^{1/2} \ll 1$ . This is always the case since  $T_d^{1/2}$  is chosen to be very small in order to extend the dynamic range upward.

[0323] For the linear extrapolation algorithm to function, Equation 39 and Equation 41 must be satisfied. For comparison, the maximum value of A before fringe count errors occur is plotted as a function of frequency in Figure 47 for  $T_d^{1/2} = 100$  microseconds,  $\tau = 50$  microseconds, and  $T_d^{1/2} = 100$  nanoseconds. Also shown are the results of a numeric simulation of the dynamic range for a Mach-Zehnder array (plotted with the points represented by  $\square$ 's), a Sagnac array with a single delay loop (plotted with the points represented by  $\diamond$ 's), and a Sagnac array with two delay loops employing the linear extrapolation algorithm presented above (plotted with the points represented by  $\Delta$ 's).

[0324] Note in Figure 47 that for the two-delay loop linear extrapolation method, the limit in the Equation 39 and the limit in the Equation 41 must both be satisfied. Thus, the simulation follows the minimum of the two curves. At lower frequencies, the simulation follows the curve of Equation 39, and at higher frequencies, the simulation follows the curve of Equation 41.

[0325] Figure 47 shows that the linear extrapolation algorithm behaves as predicted and dramatically increases the dynamic range (e.g., by 3 orders of magnitude from DC to 400 Hz, and by 2 orders of magnitude up to 1 kHz) over that possible with a Mach-Zehnder array or a single delay loop Sagnac array.

[0326] The foregoing describes an algorithm for using two delay loops 2240, 2242 and two wavelengths  $\lambda_1$ ,  $\lambda_2$  in a Sagnac-based array to increase the dynamic range of the sensor substantially above that possible with a single delay coil, which is already much greater than that possible in a Mach-Zehnder array. The improvement in maximum tonal amplitude that can be detected is quite substantial, calculated to be 2 orders of magnitude or more up to 1 kHz in one particular example. This algorithm is straightforward to implement and requires very little additional computation on the receiver side. Thus, there are very few barriers to its implementation if the dynamic range it affords is deemed necessary.

[0327] Note further that the foregoing embodiments have been described in connection with superfluorescent light sources. One skilled in the art will appreciate that other light sources (e.g., laser sources) may also be advantageously used.

[0328] Although the foregoing description of the array in accordance with the present invention has addressed underwater acoustic sensing, it should be understood that the present invention can be used to sense any measurand which can be made to produce non-reciprocal phase modulations in a fiber. If, for example, the hydrophones were replaced with an alternative sensing device which responds to a different measurand, the array would detect that measurand in the same manner as acoustic waves are detected. The array of the present invention can be advantageously used to sense vibrations, intrusions, impacts, chemicals, temperature, liquid levels and strain. The array of the present invention may also be used to combine a number of different sensors located at either the same place or located in different places (e.g., for the detection of various faults at various points along the hull of a ship or a building). Other exemplary applications include the detection and tracking of moving automobiles on highways or airplanes on airstrips for traffic monitoring and control.

[0329] Although described above in connection with particular embodiments of the present invention, it should be understood the descriptions of the embodiments are illustrative of the invention and are not intended to be limiting. Various modifications and applications may occur to those skilled in the art without departing from the true spirit and scope of the invention as defined in the appended claims.

**WHAT IS CLAIMED IS:**

1. A sensor system that senses perturbations over first and second dynamic ranges, the sensor system comprising:

- a source of input light pulses at a first wavelength;
- a source of input light pulses at a second wavelength;
- an array of sensors;
- a first optical delay path at the first wavelength;
- a second optical delay path at the second wavelength;
- a first detection system responsive to light at the first wavelength;
- a second detection system responsive to light at the second wavelength; and

an input/output system that receives the input light pulses at the first wavelength and the second wavelength, the input/output system directing a first portion of each light pulse at the first wavelength having a first polarization through the array of sensors in a first direction, then through the first optical delay path, and then to the first detection system, the input/output system directing a second portion of each light pulse at the first wavelength in a second polarization orthogonal to the first polarization through the first optical delay path, then through the array of sensors in a second direction, and then to the first detection system, the first detection system detecting variations in received light caused by perturbations varying over the first dynamic range, the input/output system directing a first portion of each light pulse at the second wavelength having a first polarization through the array of sensors in a first direction, then through the second optical delay path, and then to the second detection system, and the input/output system directing a second portion of each light pulse at the second wavelength in a second polarization orthogonal to the first polarization through the second optical delay path, then through the array of sensors in a second direction, and then to the second detection system, the second detection system detecting variations



in received light caused by perturbations varying over the second dynamic range.

2. An acoustic sensor system that senses acoustic signals over first and second dynamic ranges, the acoustic sensor system comprising:

- a source of input light pulses at a first wavelength;
- a source of input light pulses at a second wavelength;
- an array of acoustic sensors;
- a first optical delay path at the first wavelength;
- a second optical delay path at the second wavelength;
- a first detection system responsive to light at the first wavelength;
- a second detection system responsive to light at the second wavelength; and

an input/output system that receives the input light pulses at the first wavelength and the second wavelength, the input/output system directing a first portion of each light pulse at the first wavelength having a first polarization through the array of acoustic sensors in a first direction, then through the first optical delay path, and then to the first detection system, the input/output system directing a second portion of each light pulse at the first wavelength in a second polarization orthogonal to the first polarization through the first optical delay path, then through the array of acoustic sensors in a second direction, and then to the first detection system, the first detection system detecting variations in received light caused by acoustic signals varying over the first dynamic range, the input/output system directing a first portion of each light pulse at the second wavelength having a first polarization through the array of acoustic sensors in a first direction, then through the second optical delay path, and then to the second detection system, and the input/output system directing a second portion of each light pulse at the second wavelength in a second polarization orthogonal to the first polarization through the second optical delay path, then through the array of acoustic sensors in a second direction, and then to the second detection system, the

second detection system detecting variations in received light caused by acoustic signals varying over the second dynamic range.

3. A method of sensing perturbations, the method comprising:
  - inputting light pulses of a first wavelength into an array of sensors, the array of sensors including a first optical delay path at the first wavelength;
  - inputting light pulses of a second wavelength into the array of sensors, the array of sensors including a second optical delay path at the second wavelength, the second optical delay path having a different optical length than the first optical delay path;
  - directing a first portion of each light pulse at the first wavelength having a first polarization through the array of sensors in a first direction, then through the first optical delay path;
  - directing a second portion of each light pulse at the first wavelength in a second polarization orthogonal to the first polarization through the first optical delay path, then through the array of sensors in a second direction;
  - detecting variations in the first and second portions of each light pulse at the first wavelength caused by perturbations varying over a first dynamic range;
  - directing a first portion of each light pulse at the second wavelength having a first polarization through the array of sensors in a first direction, then through the second optical delay path;
  - directing a second portion of each light pulse at the second wavelength in a second polarization orthogonal to the first polarization through the second optical delay path, then through the array of sensors in a second direction; and
  - detecting variations in the first and second portions of each light pulse at the second wavelength caused by perturbations varying over a second dynamic range.

4. The method as defined in Claim 3, wherein the perturbations are acoustic signals.

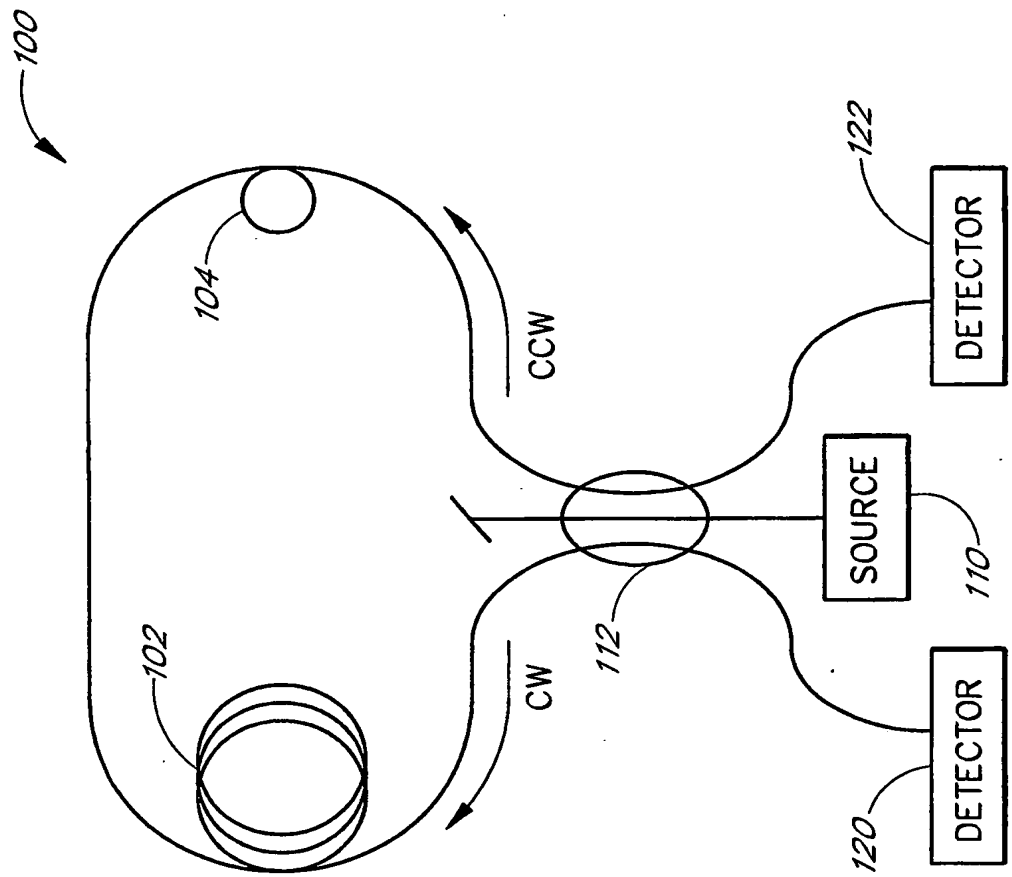


FIG. 1

2/60

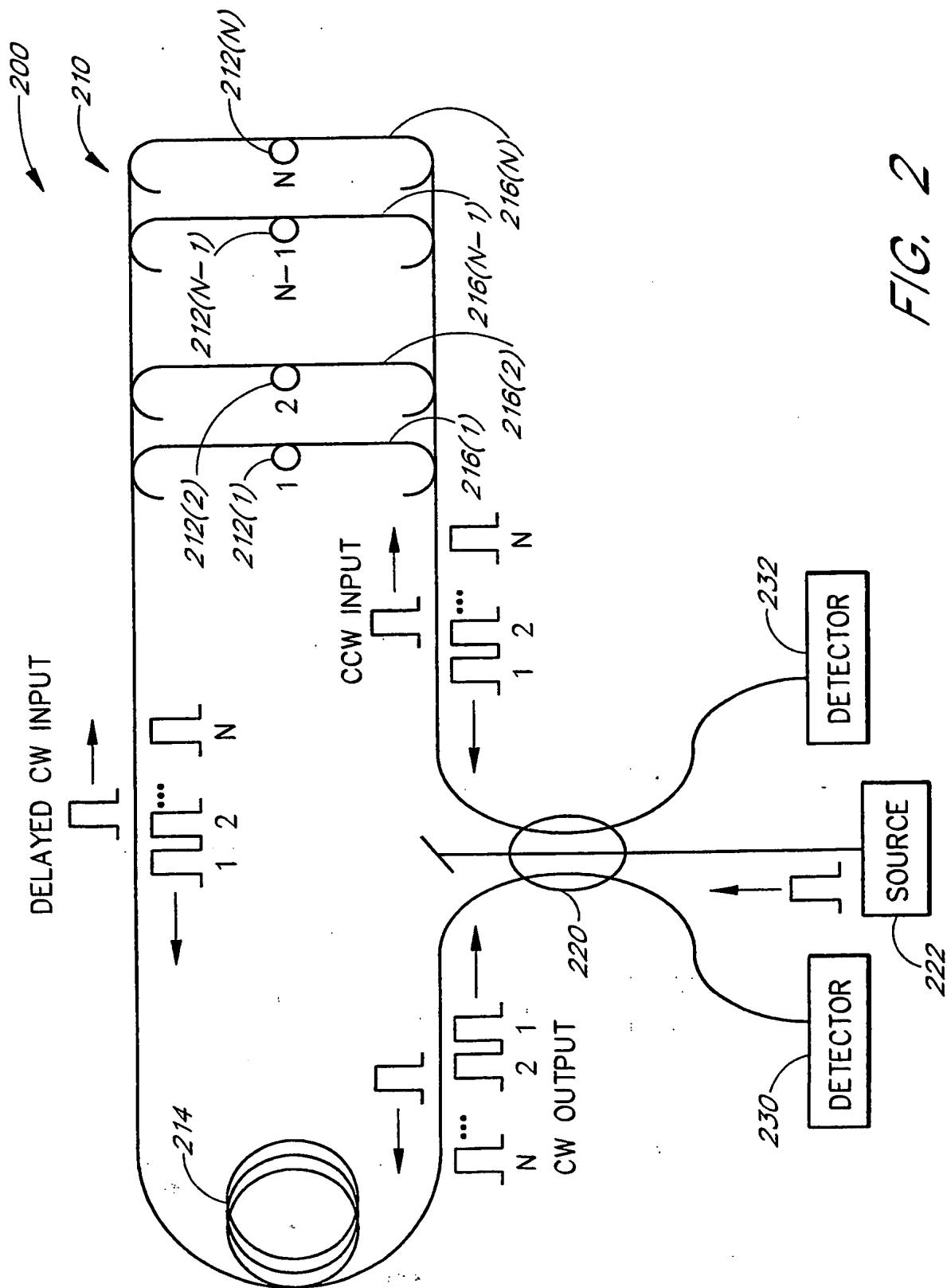


FIG. 2

3/60

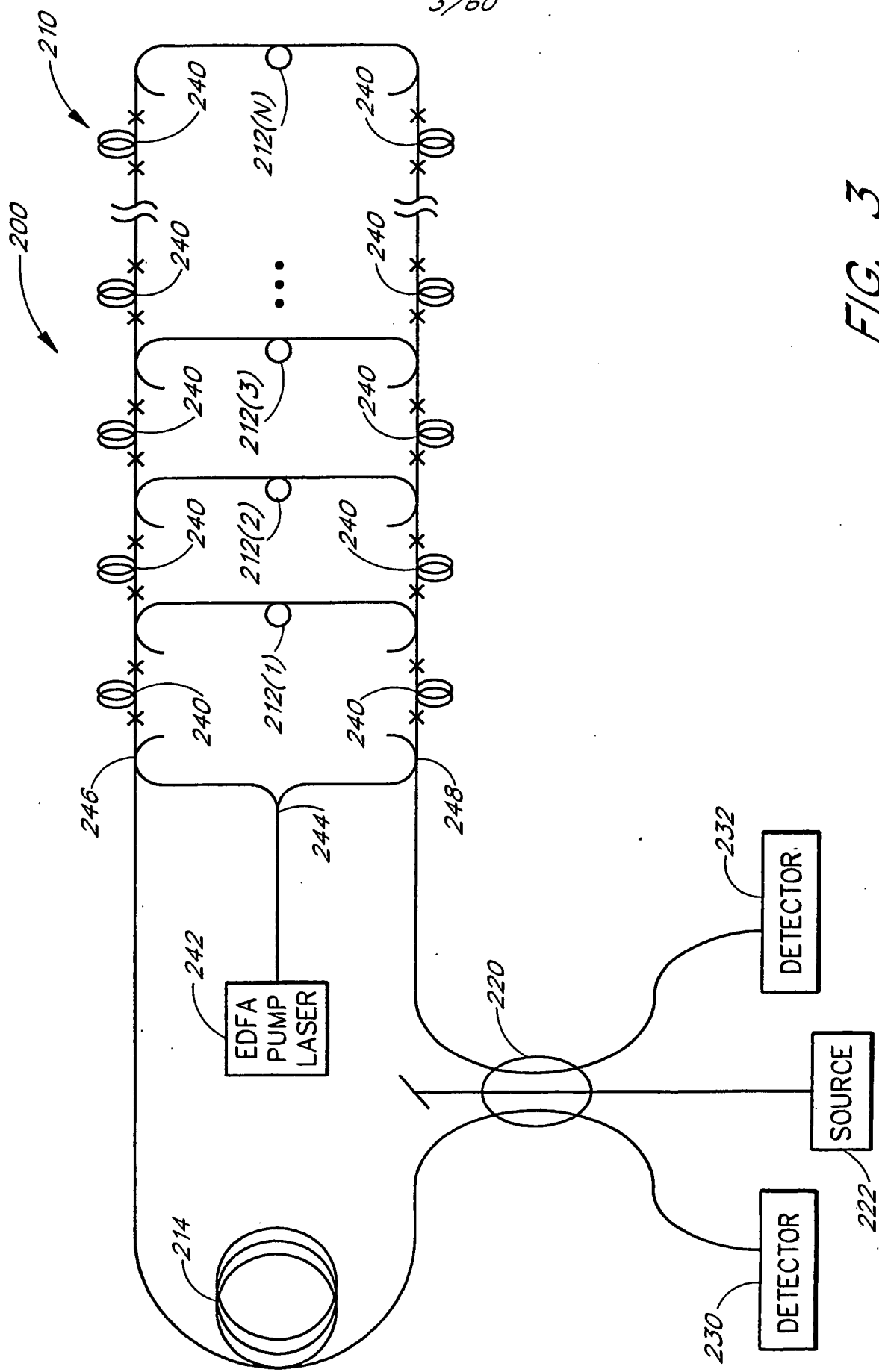


FIG. 3

4/60

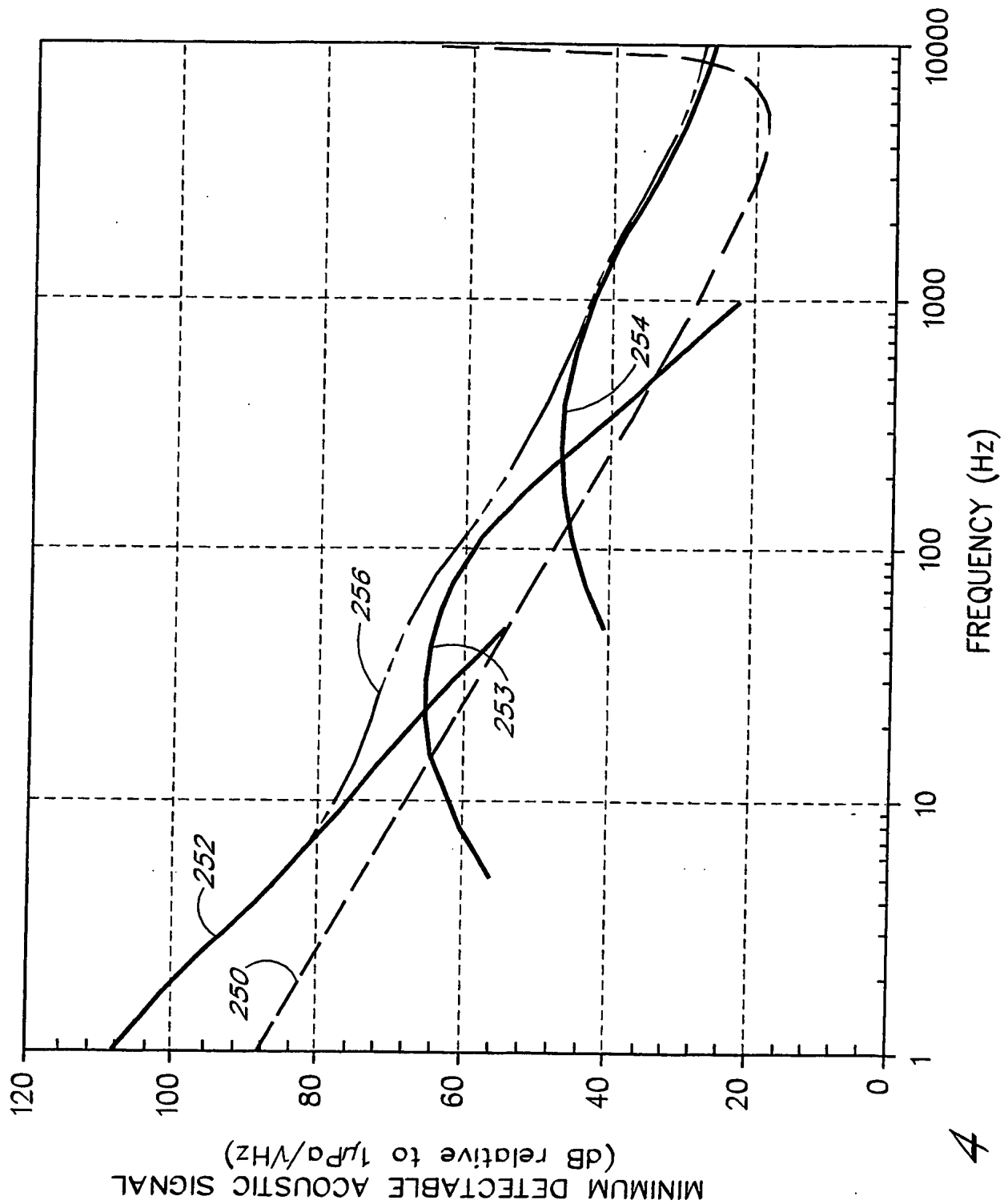


FIG. 4

5/60

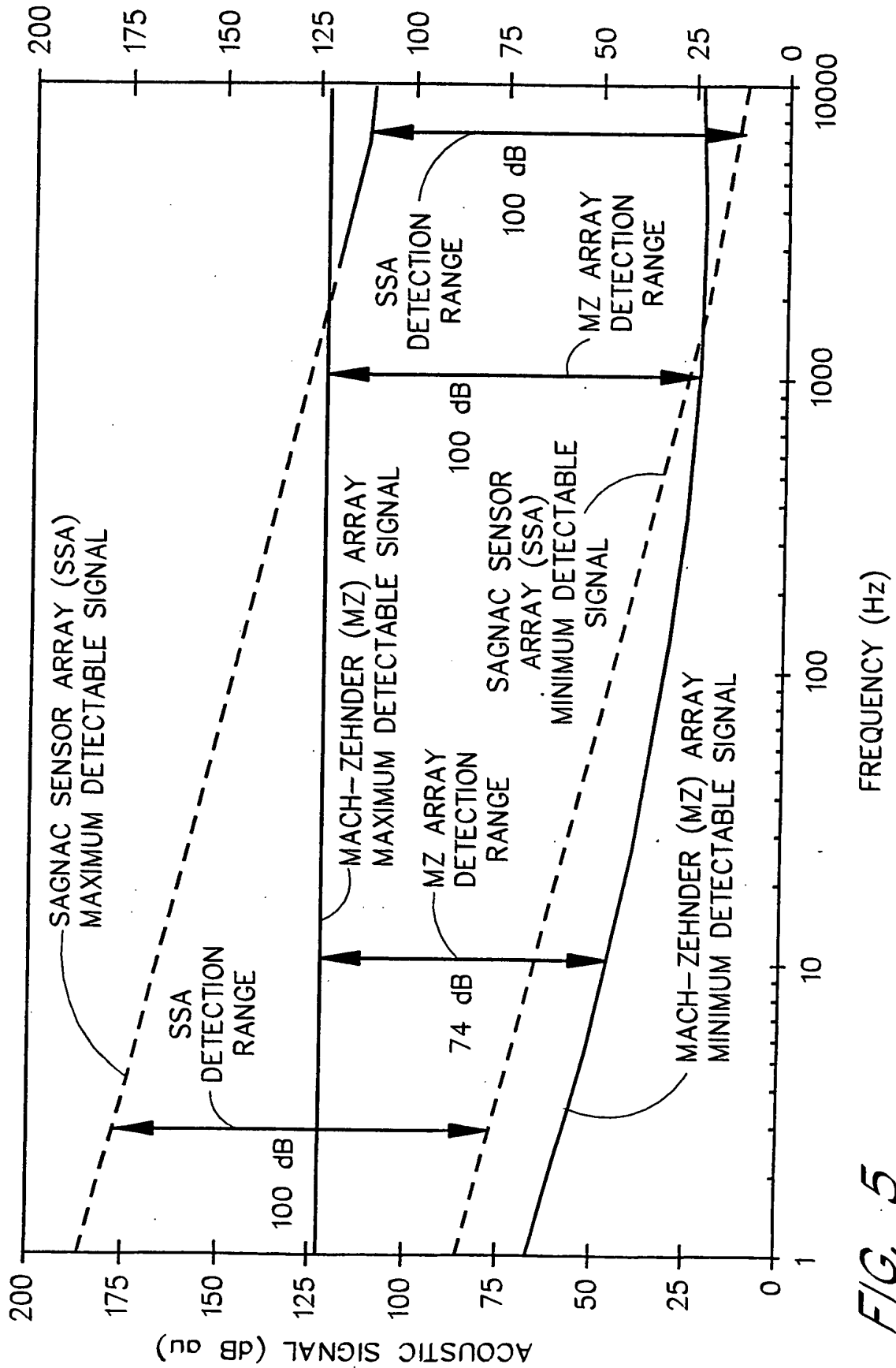


FIG. 5

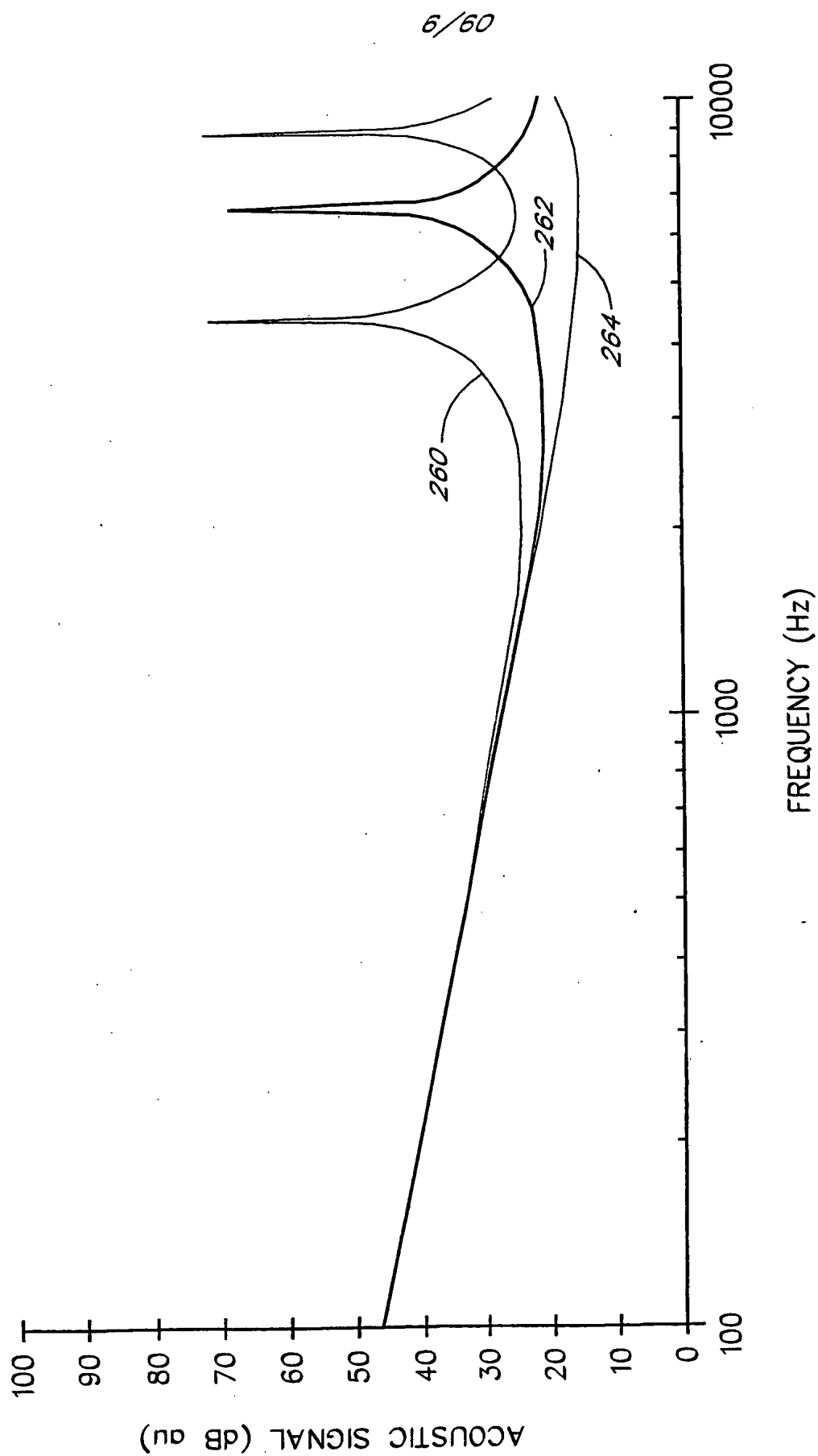


FIG. 6



7/60

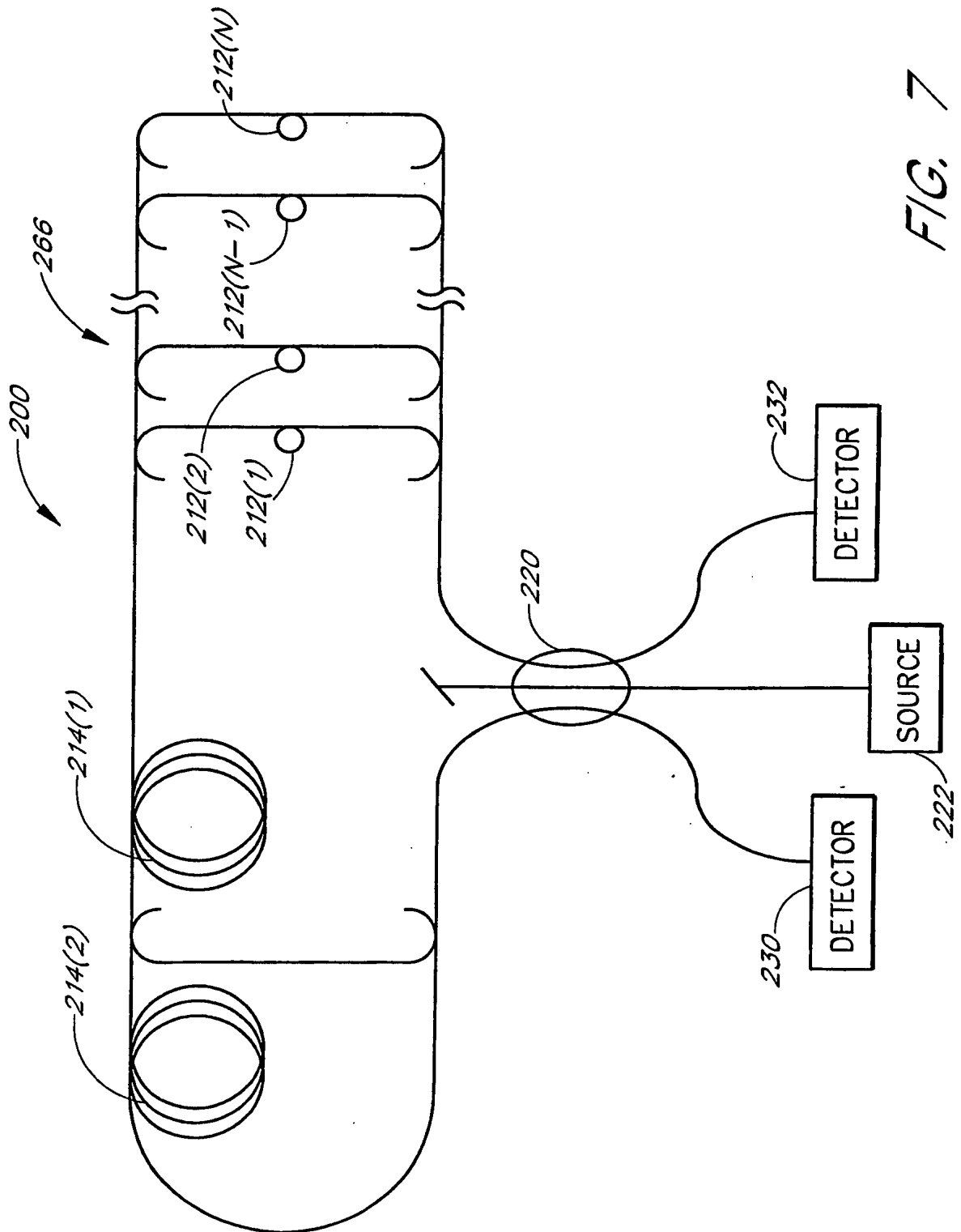


FIG. 7

8/60

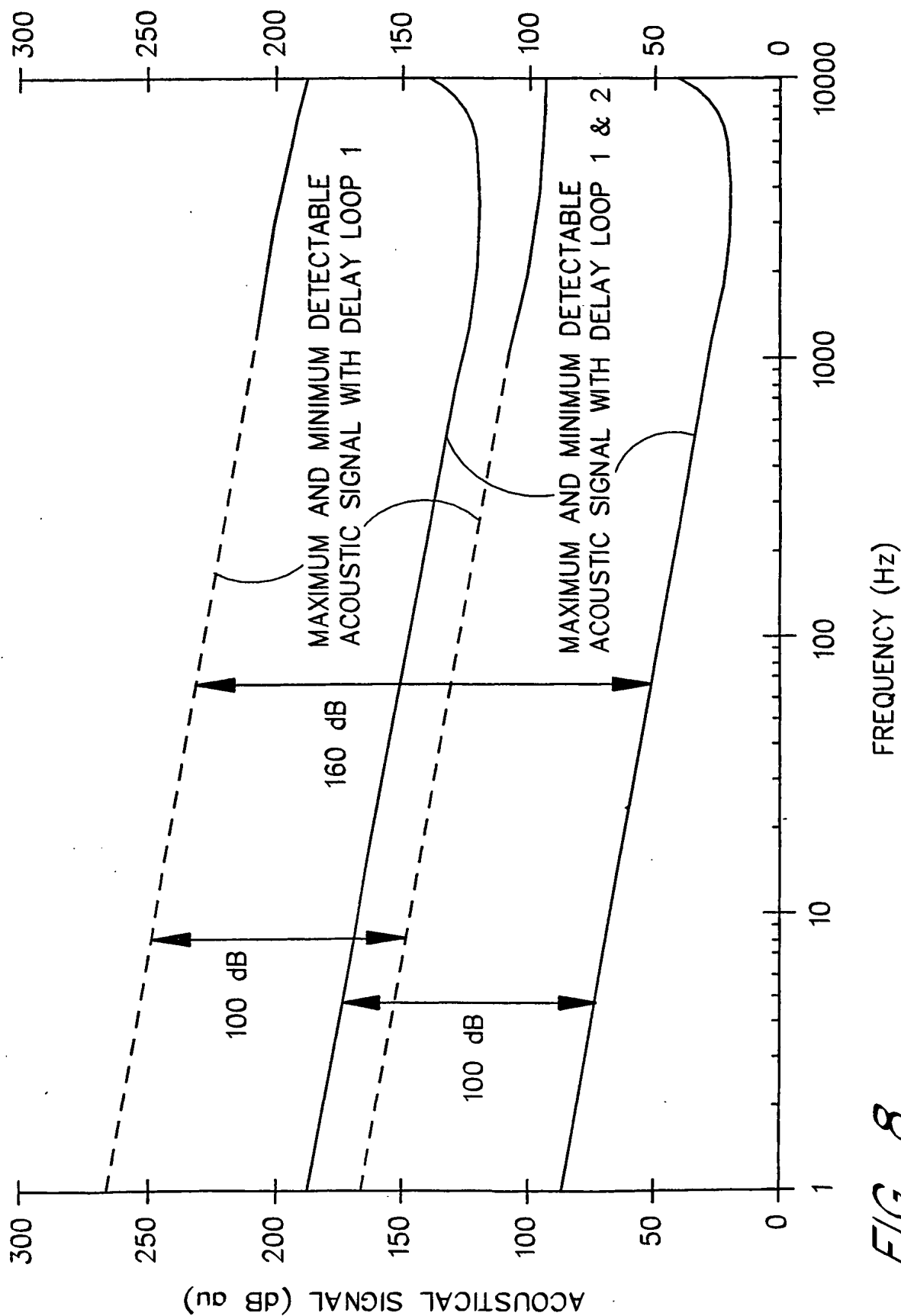
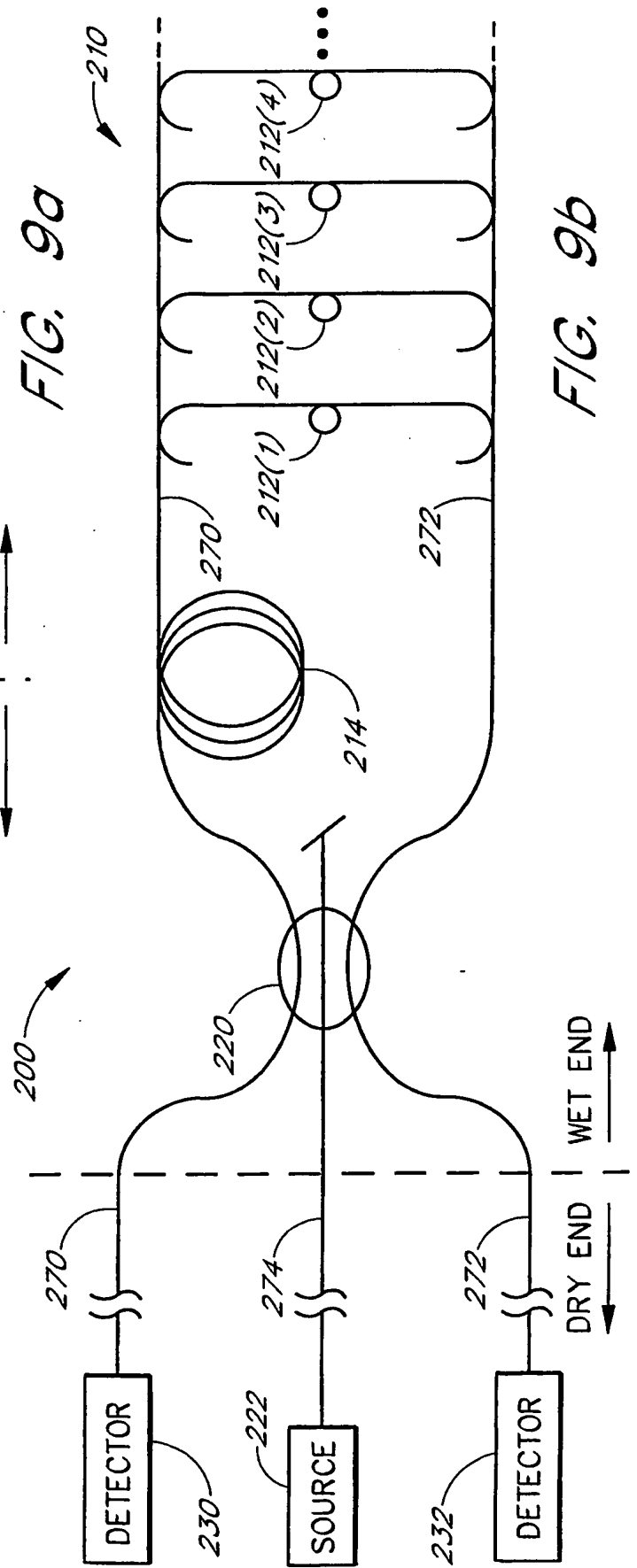
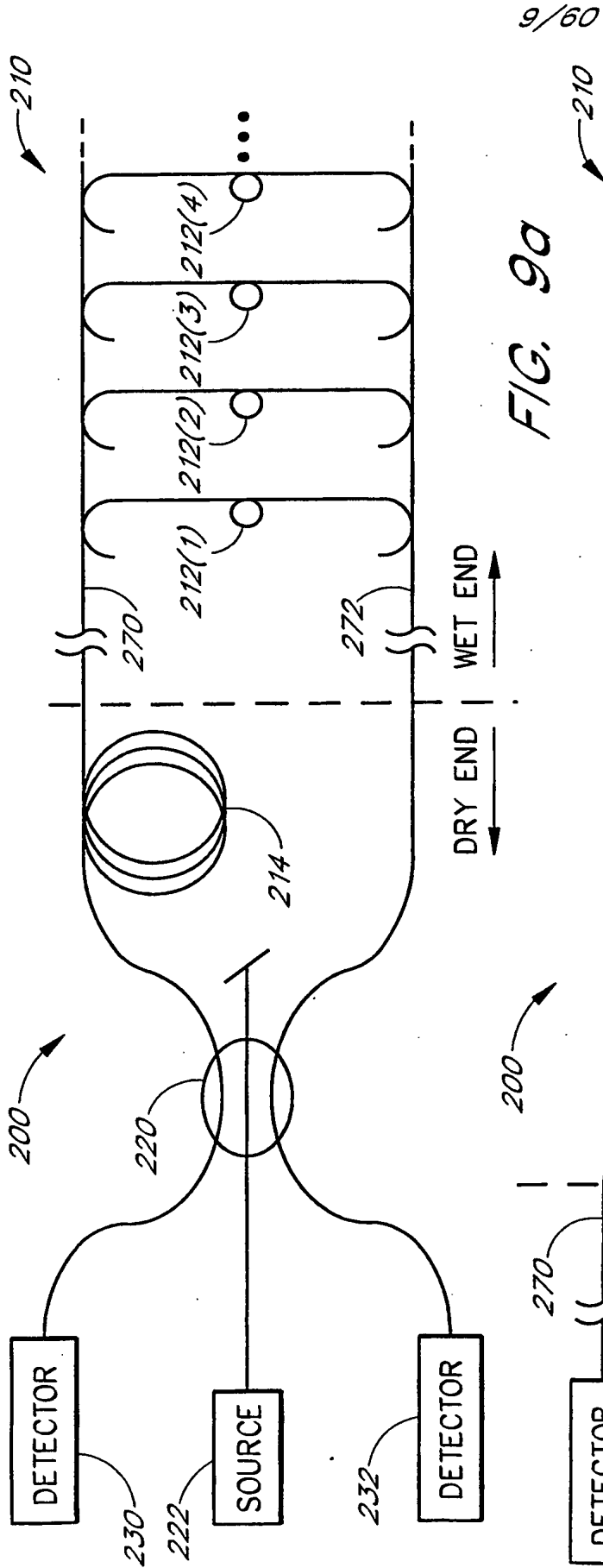


FIG. 8



10/60

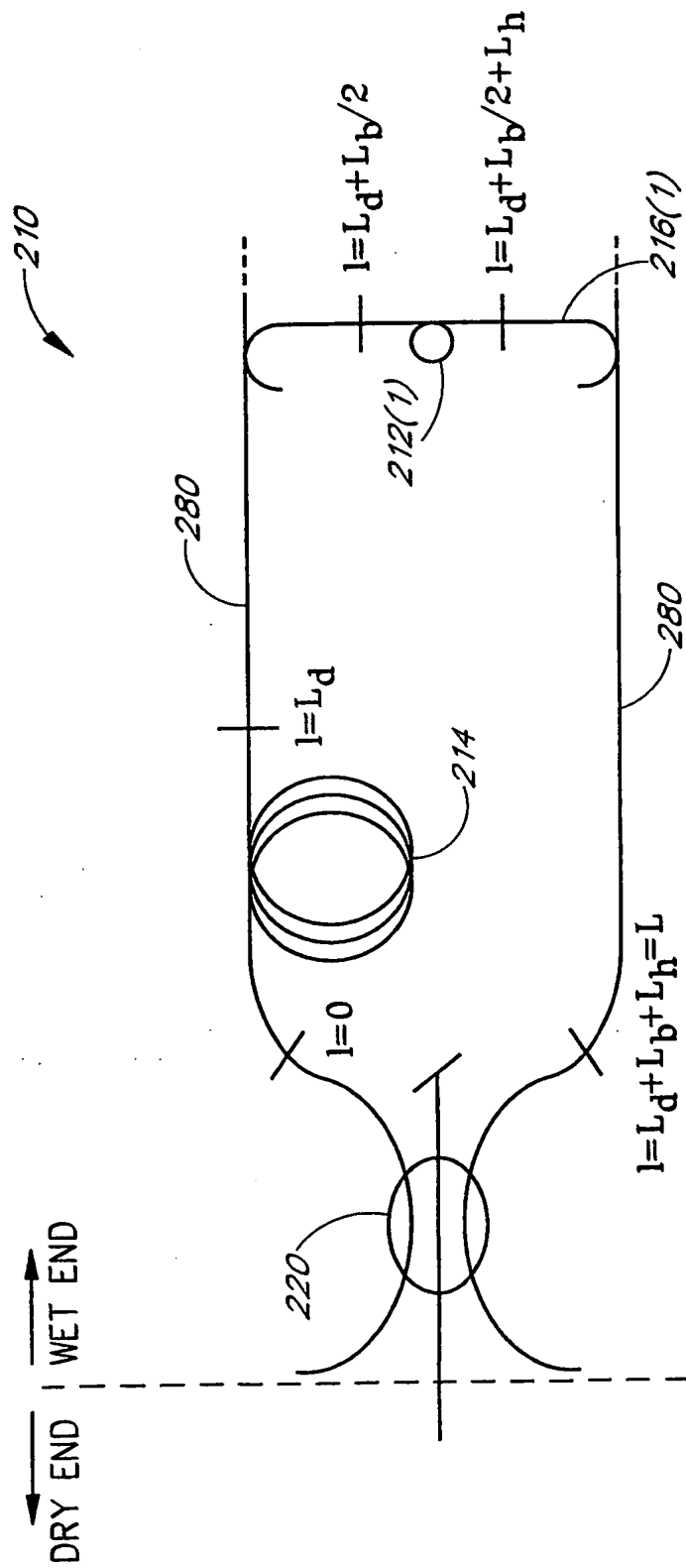


FIG. 10

11/60

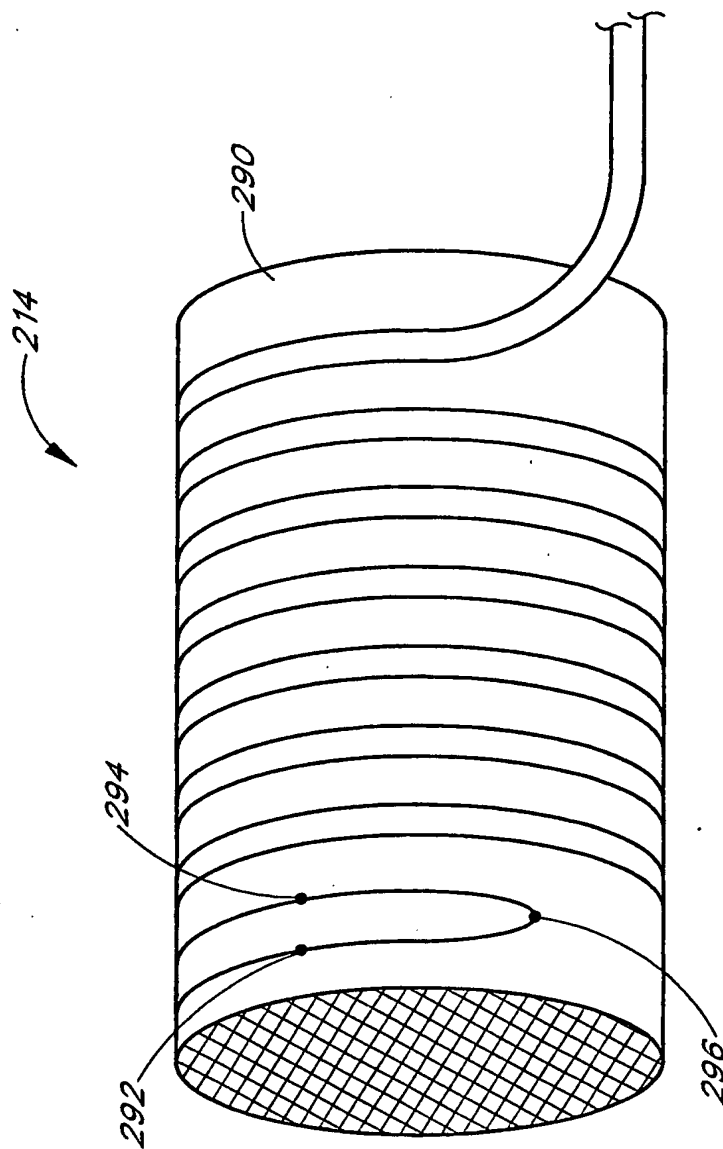


FIG. 11

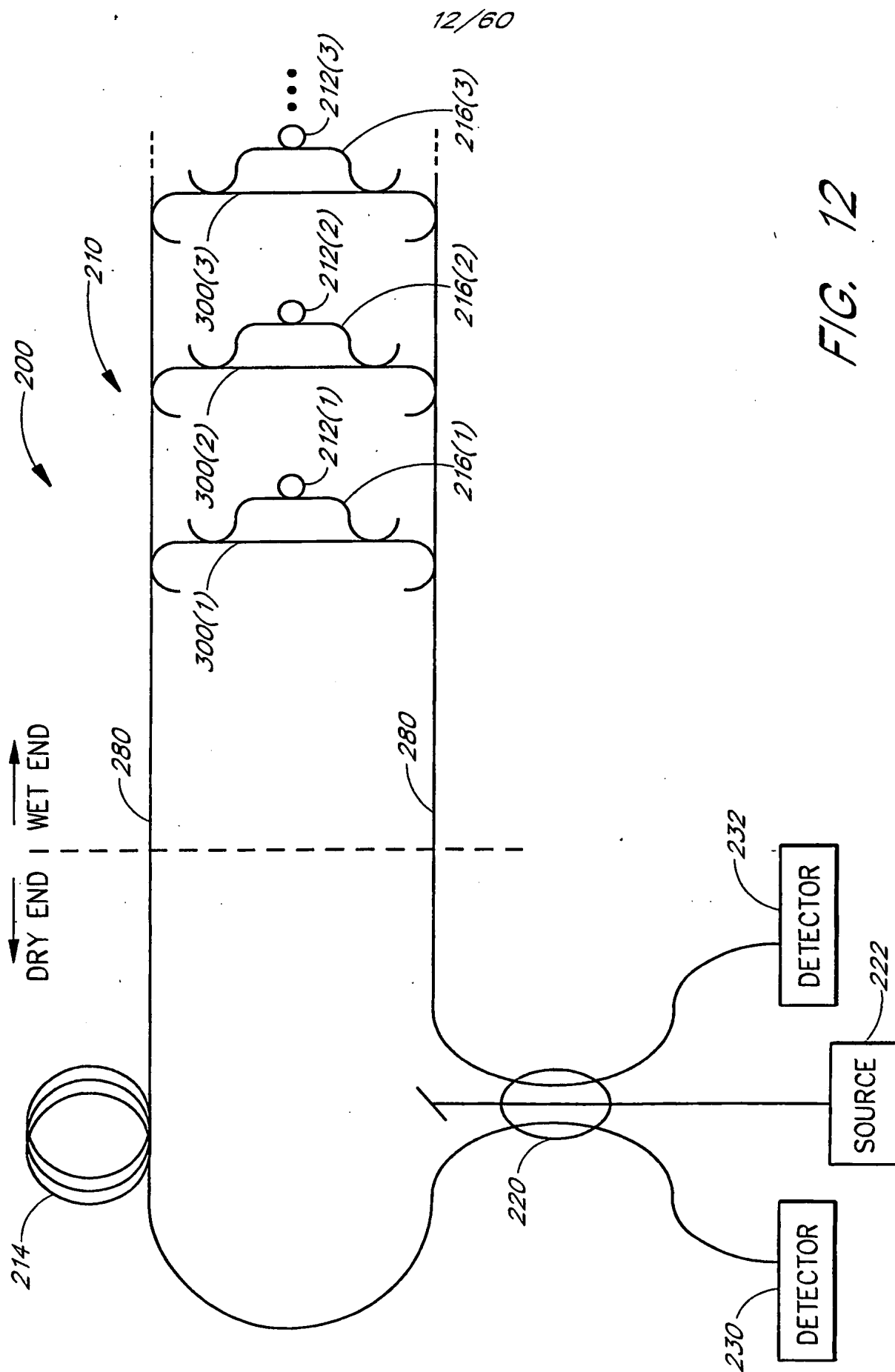


FIG. 12

13/60

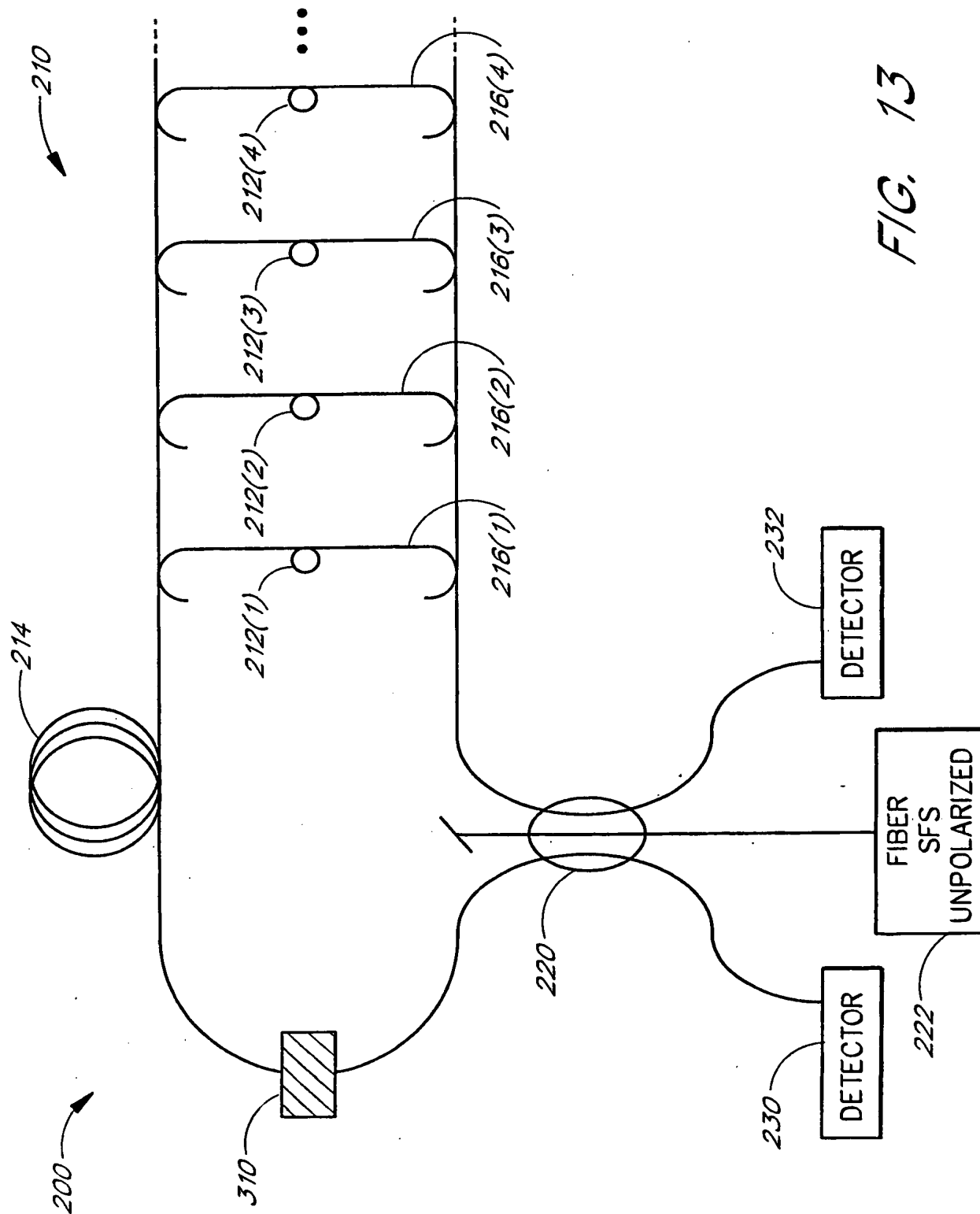


FIG. 13

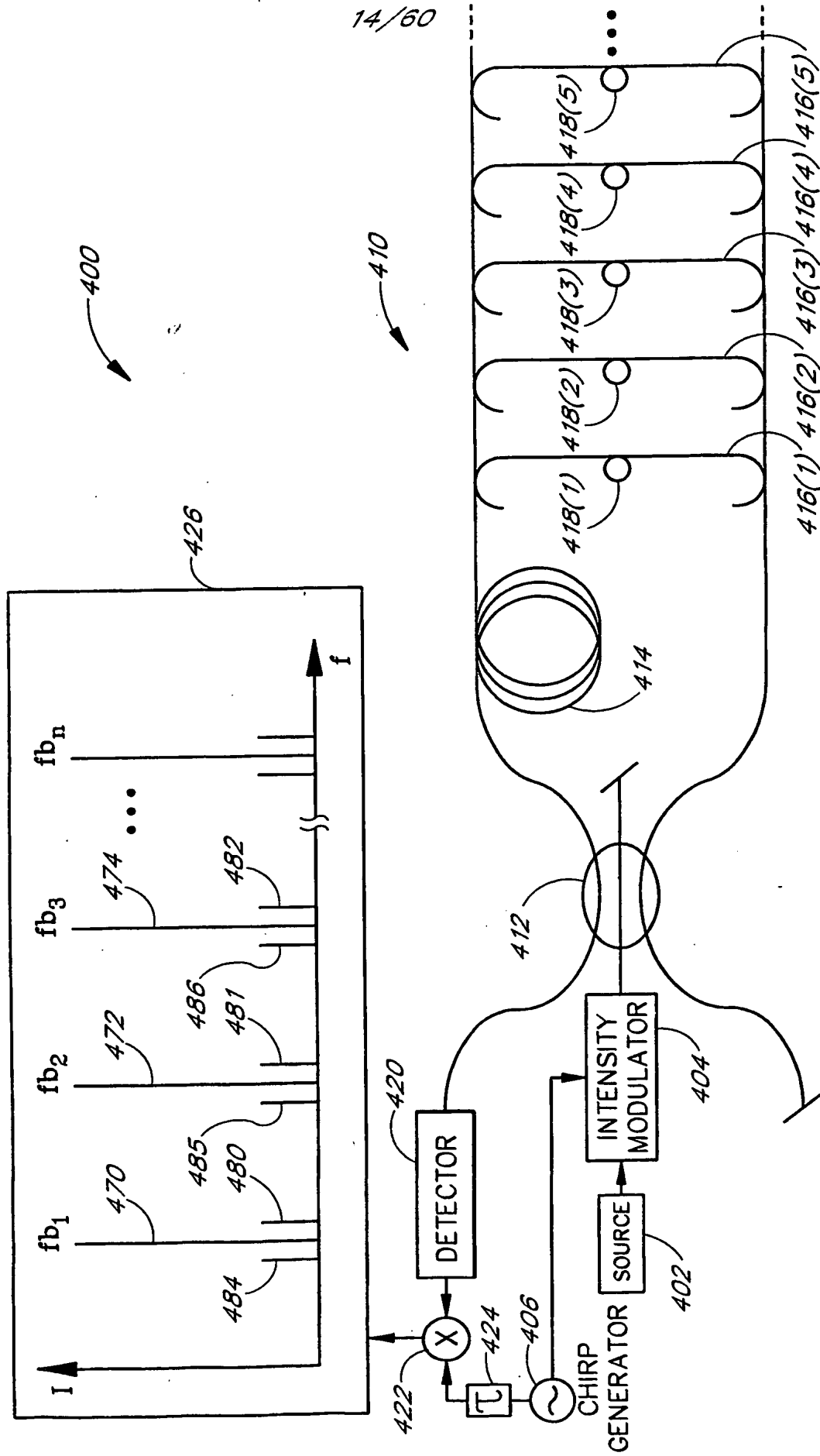


FIG. 14



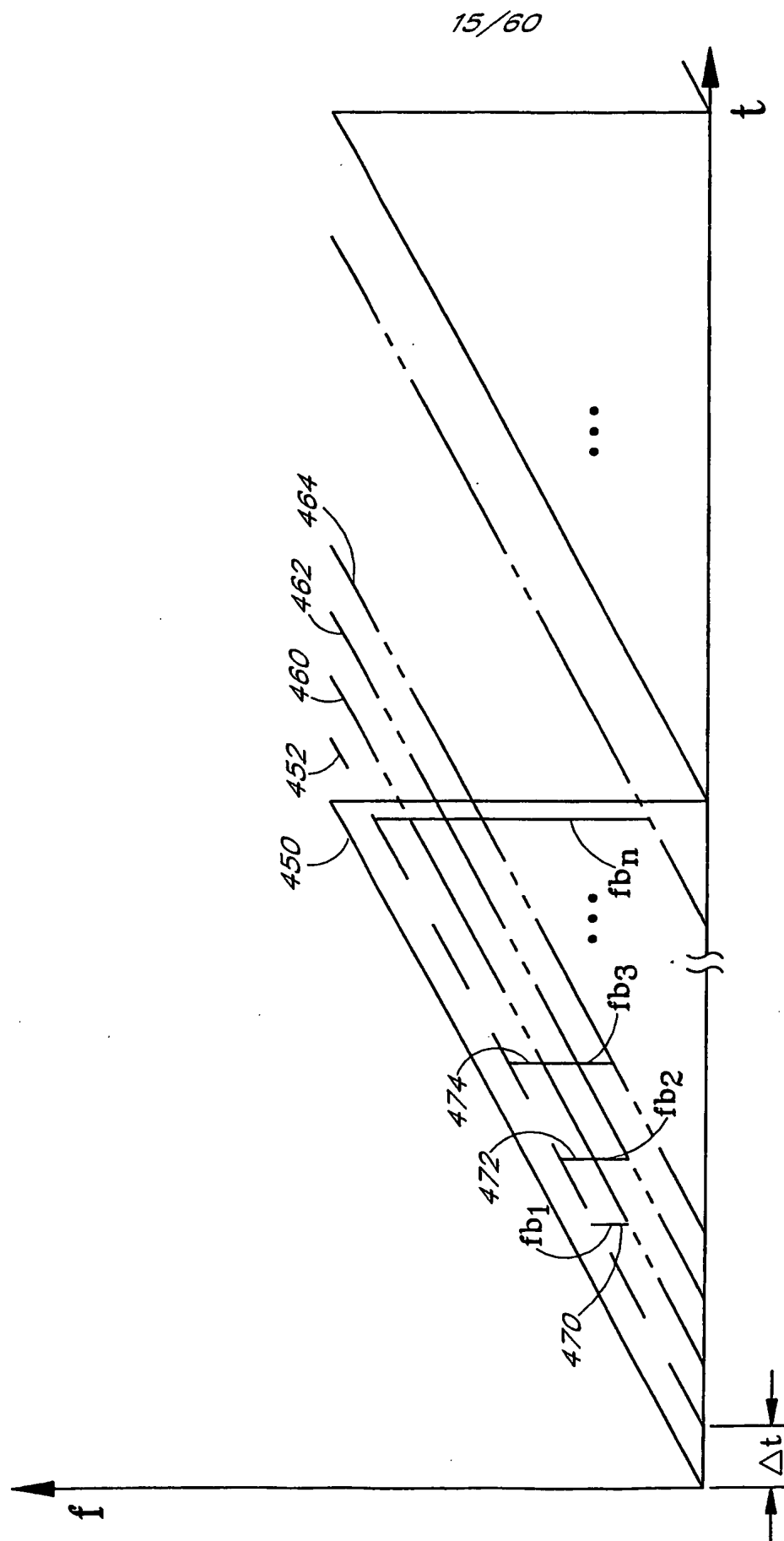


FIG. 15

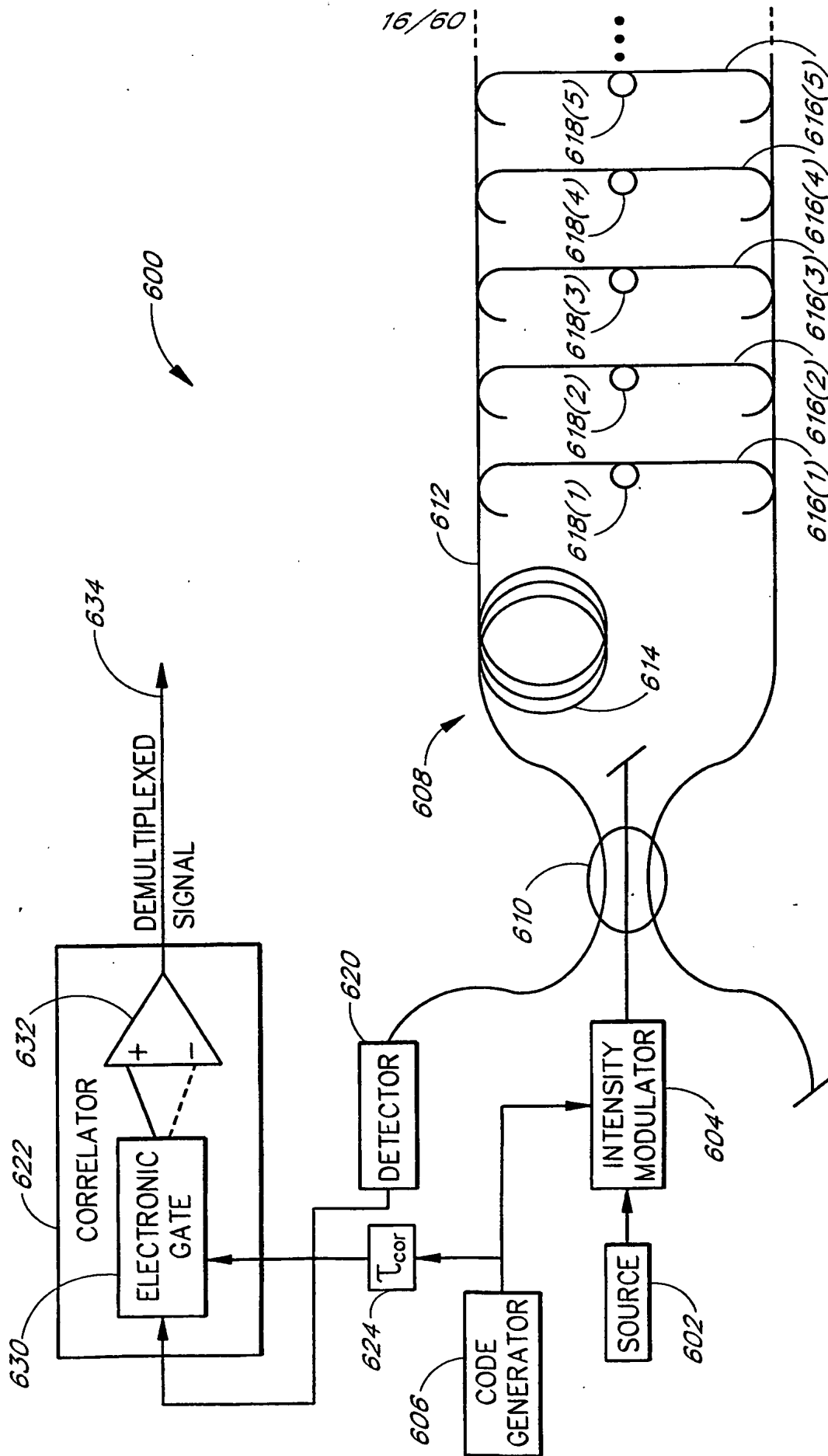


FIG. 16

17/60

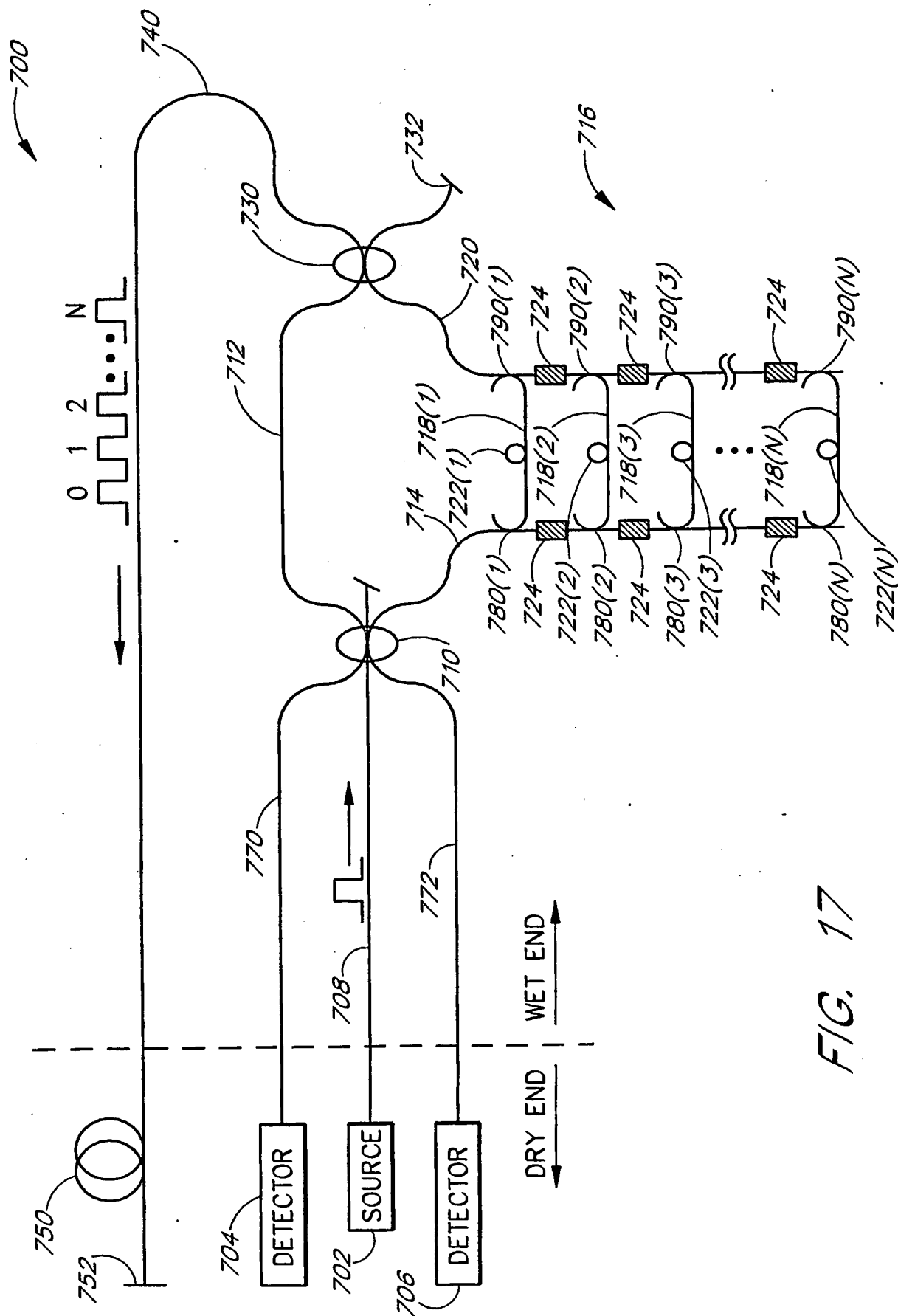


FIG. 17

18/60

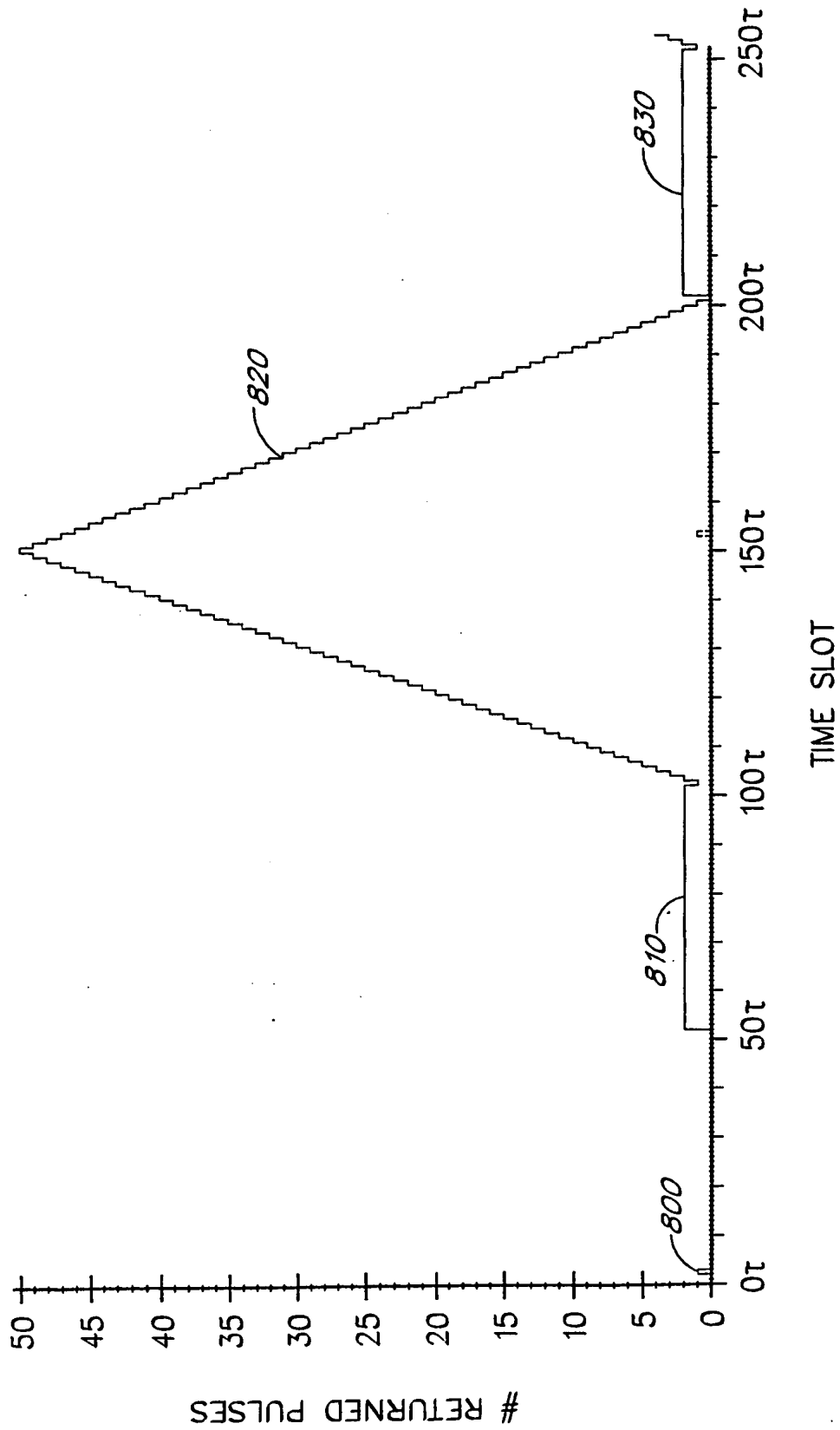


FIG. 18

19/60

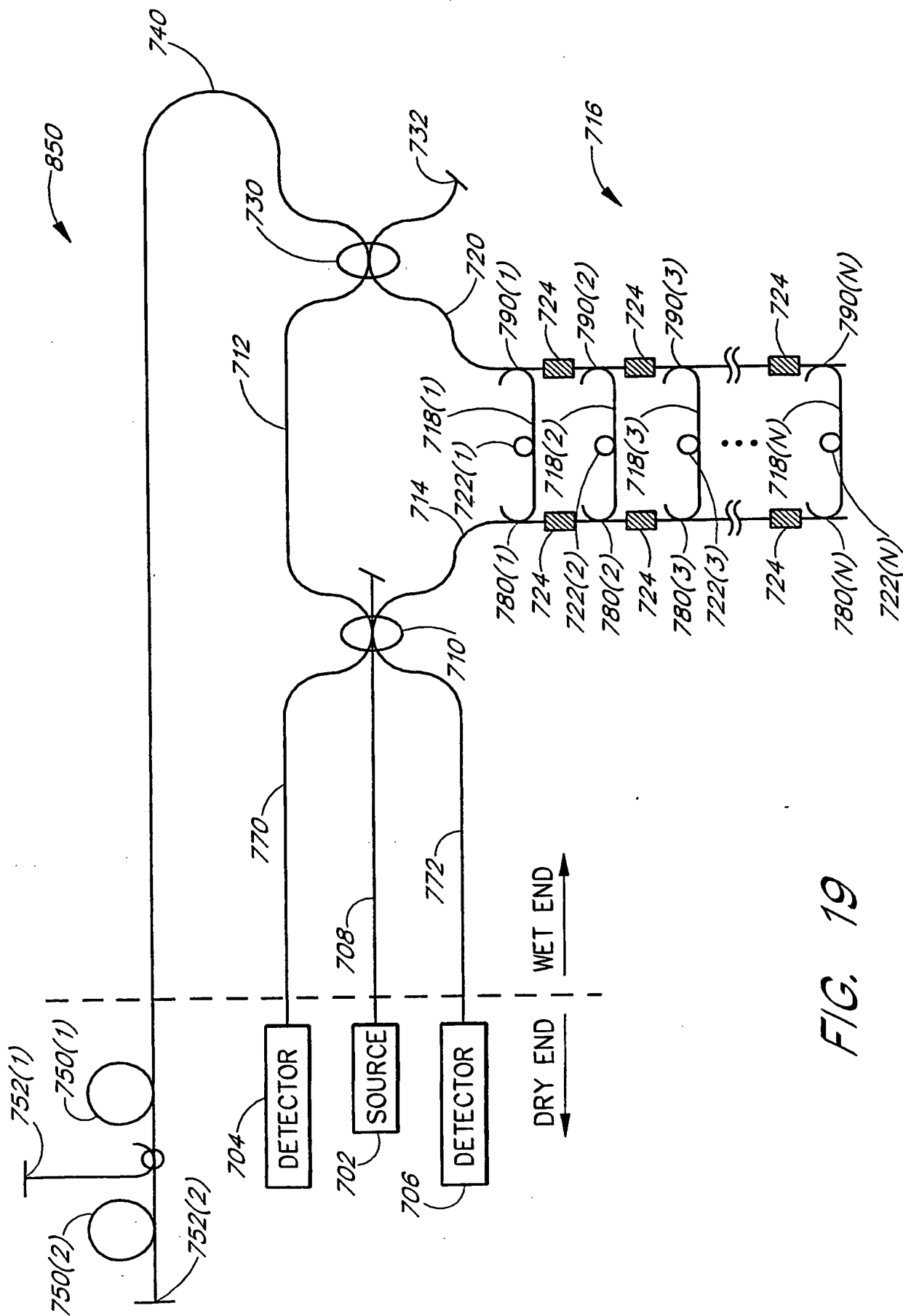


FIG. 19

20/60

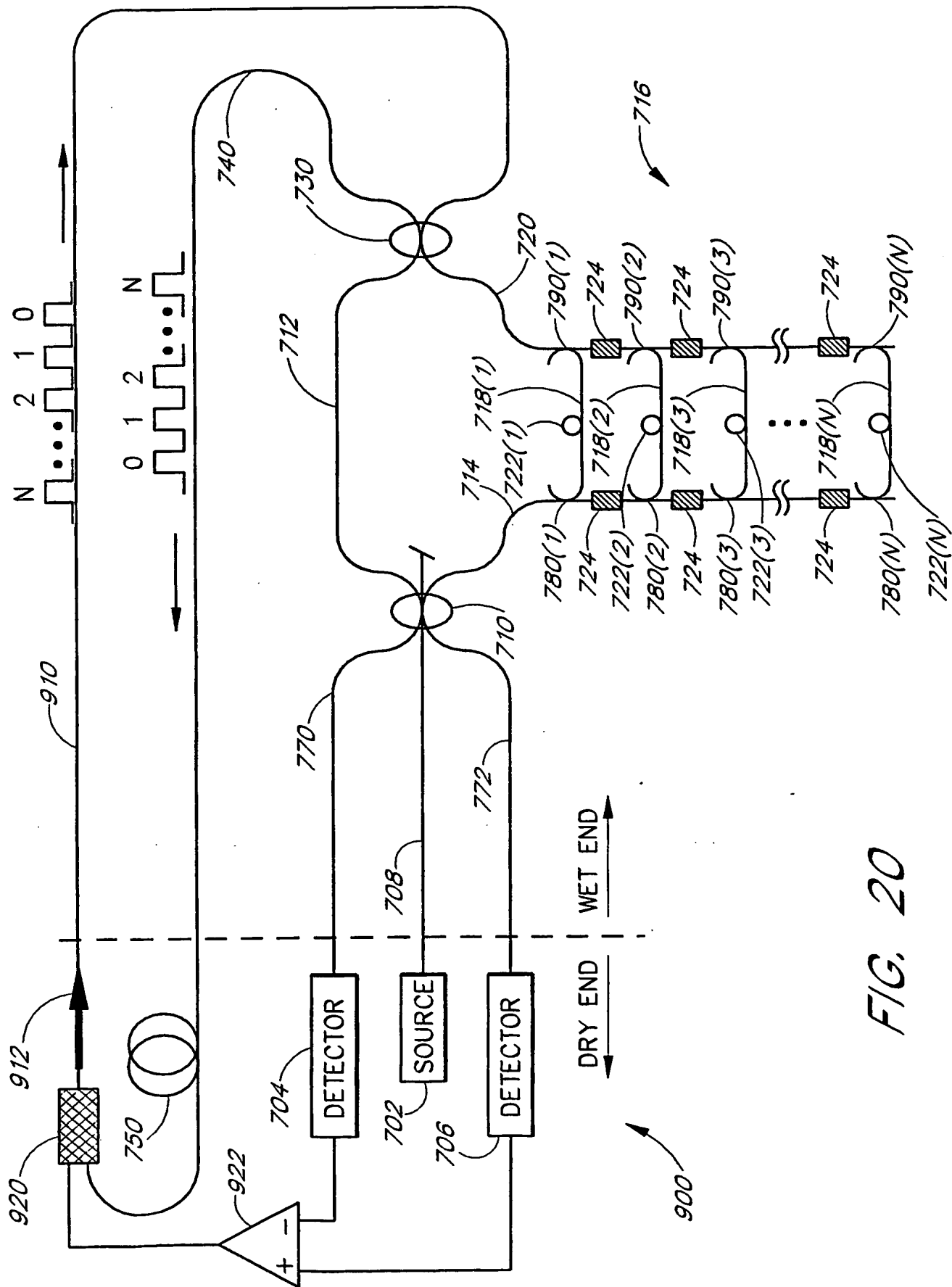


FIG. 20

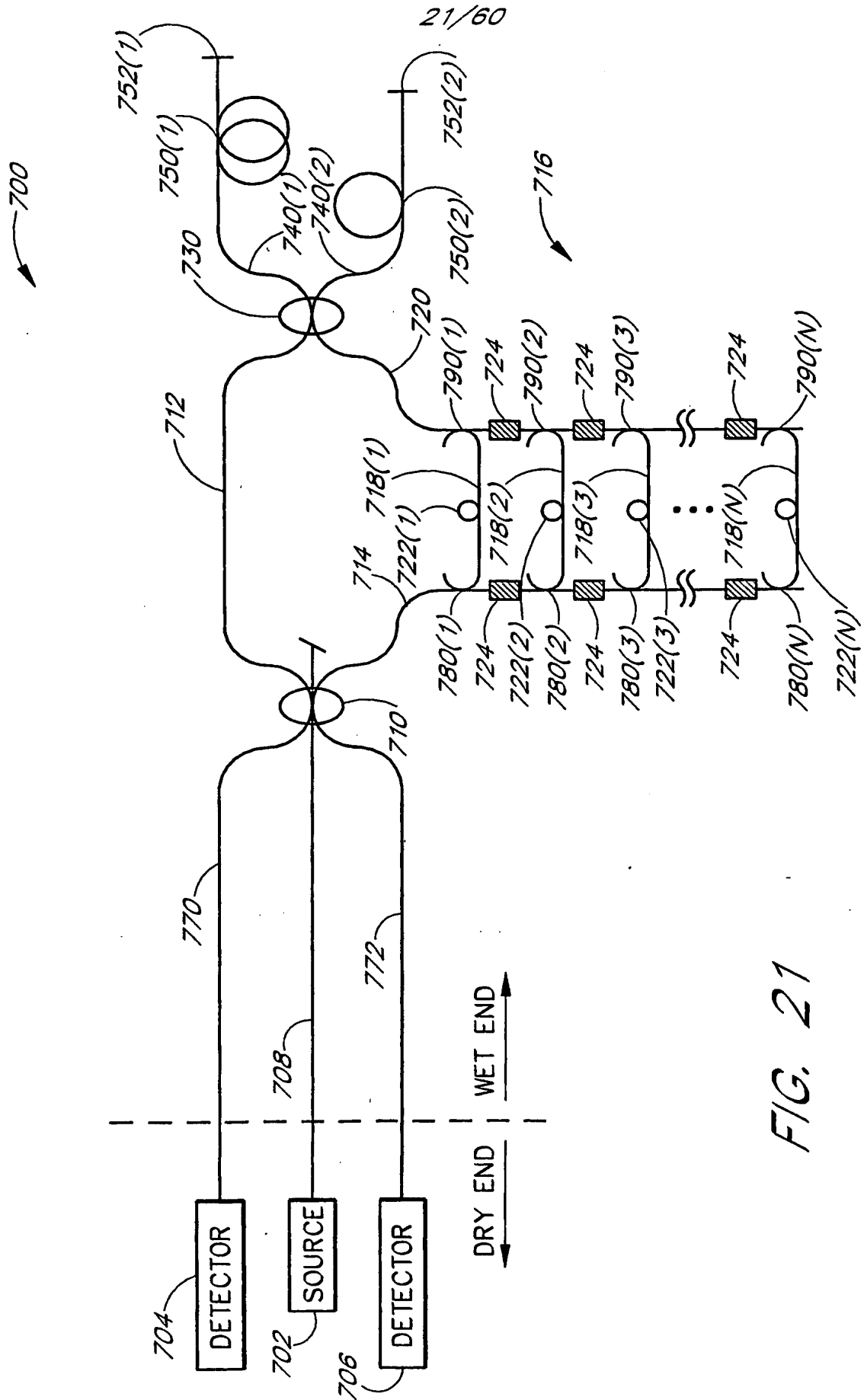


FIG. 21

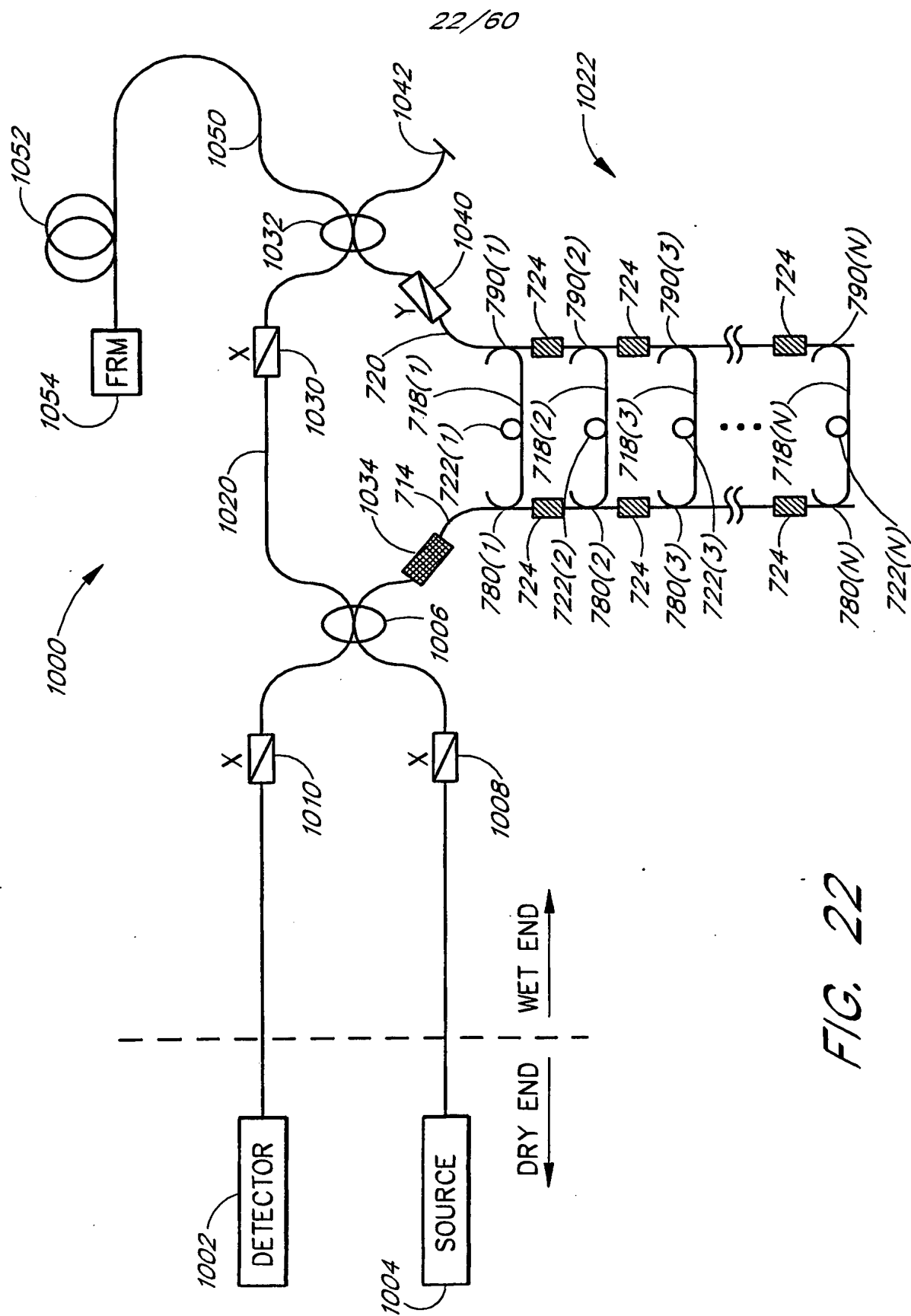


FIG. 22



23/60

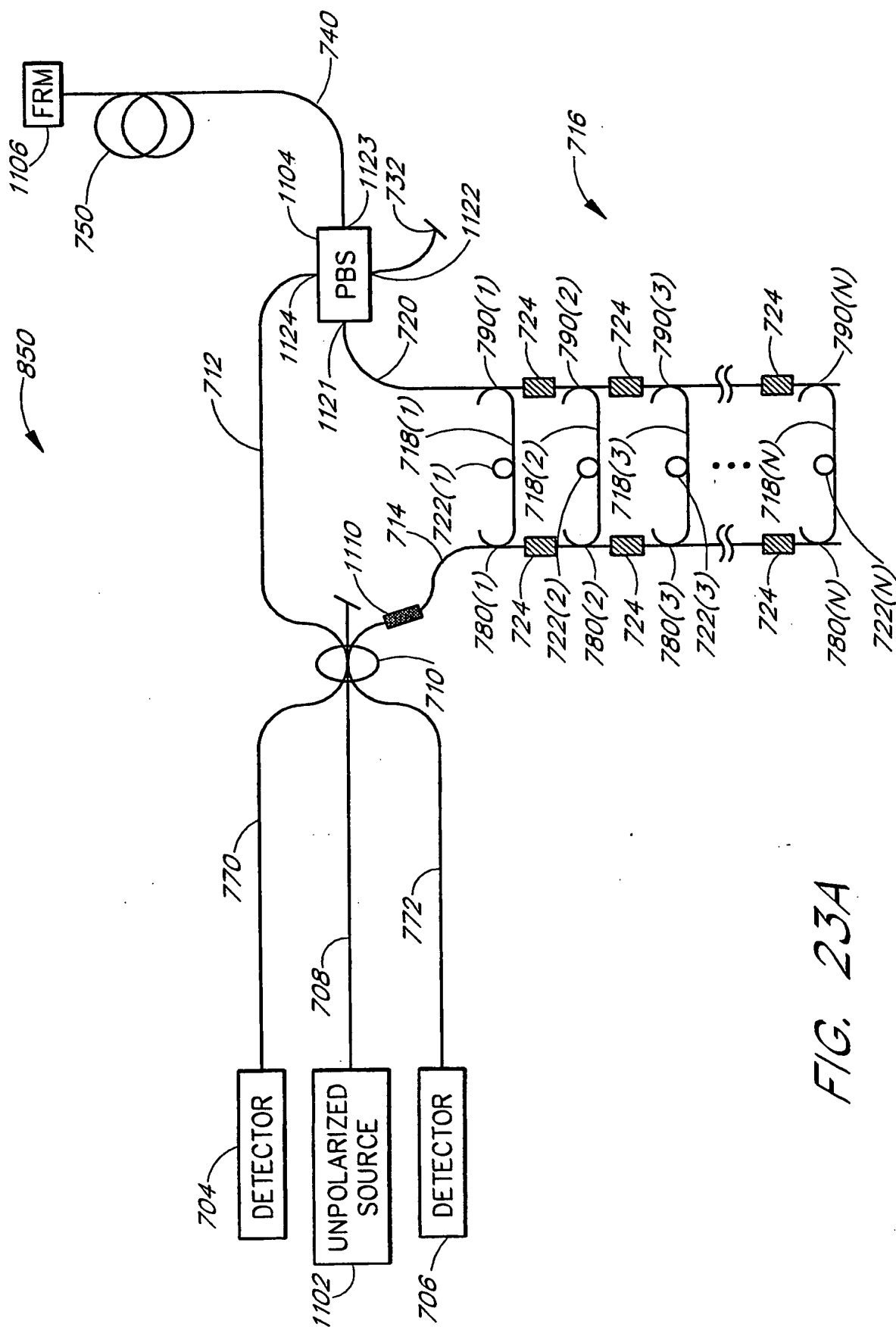
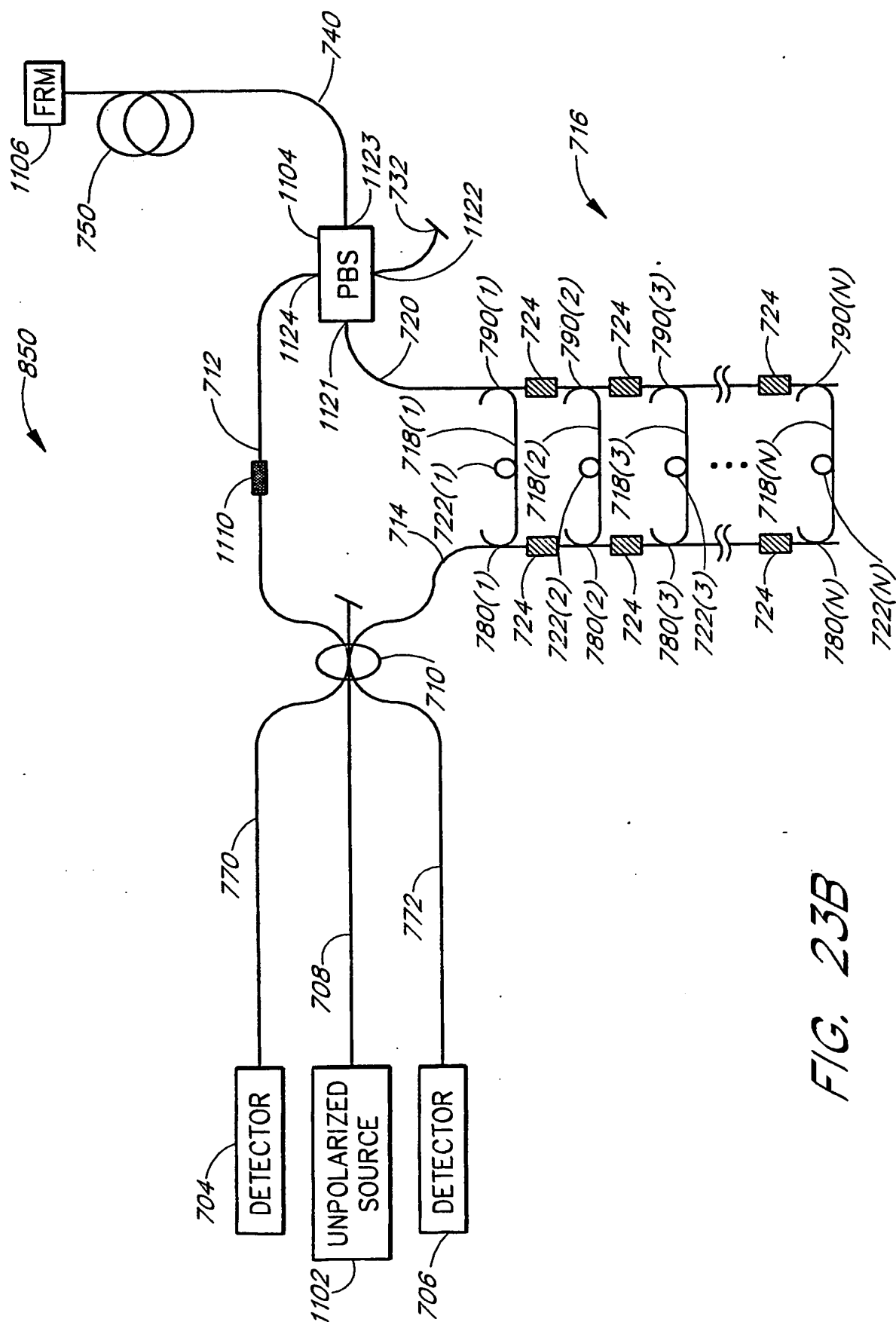
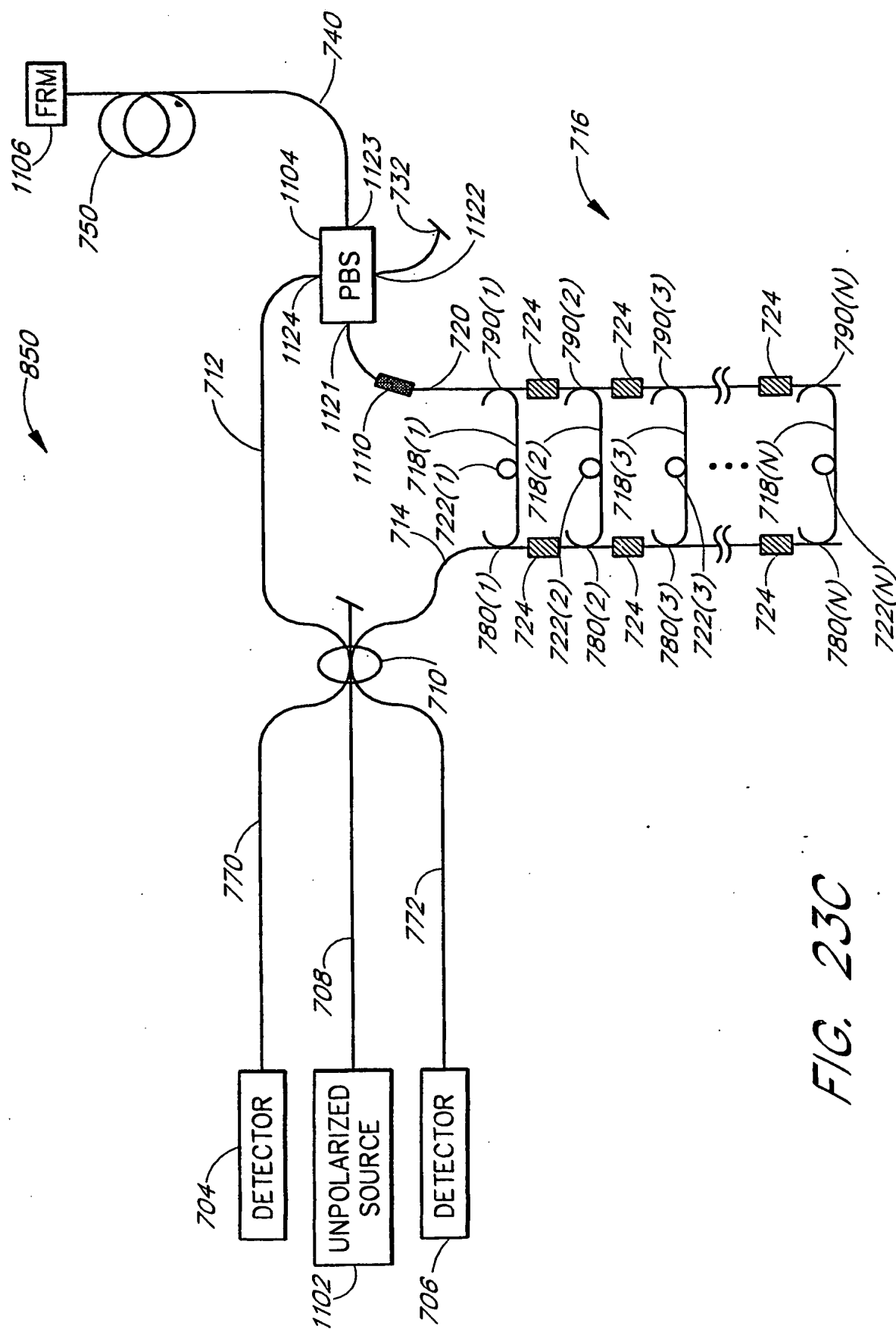


FIG. 23A

24/60



**FIG. 23B**



**FIG. 23C**

26/60

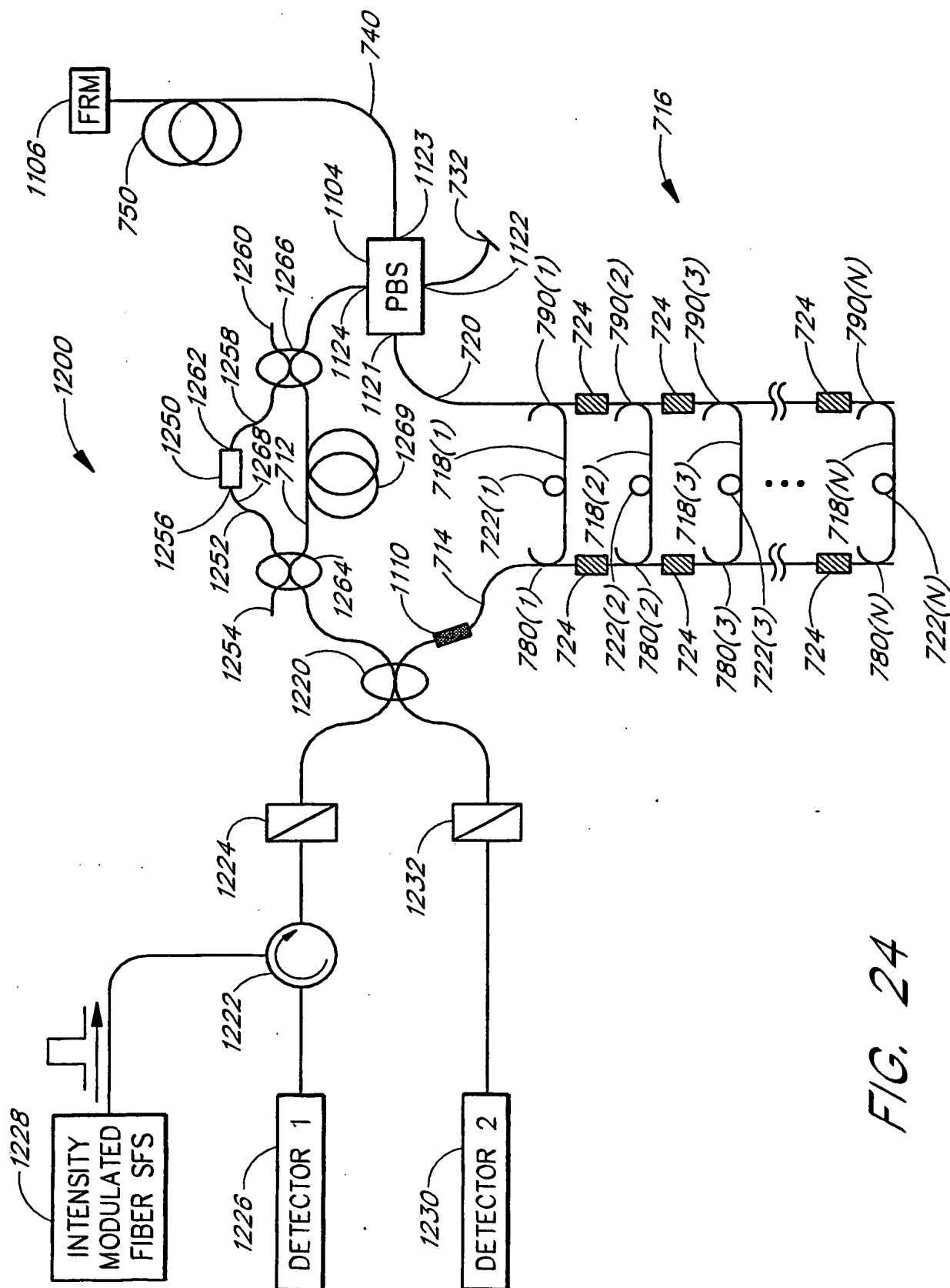


FIG. 24

27/60

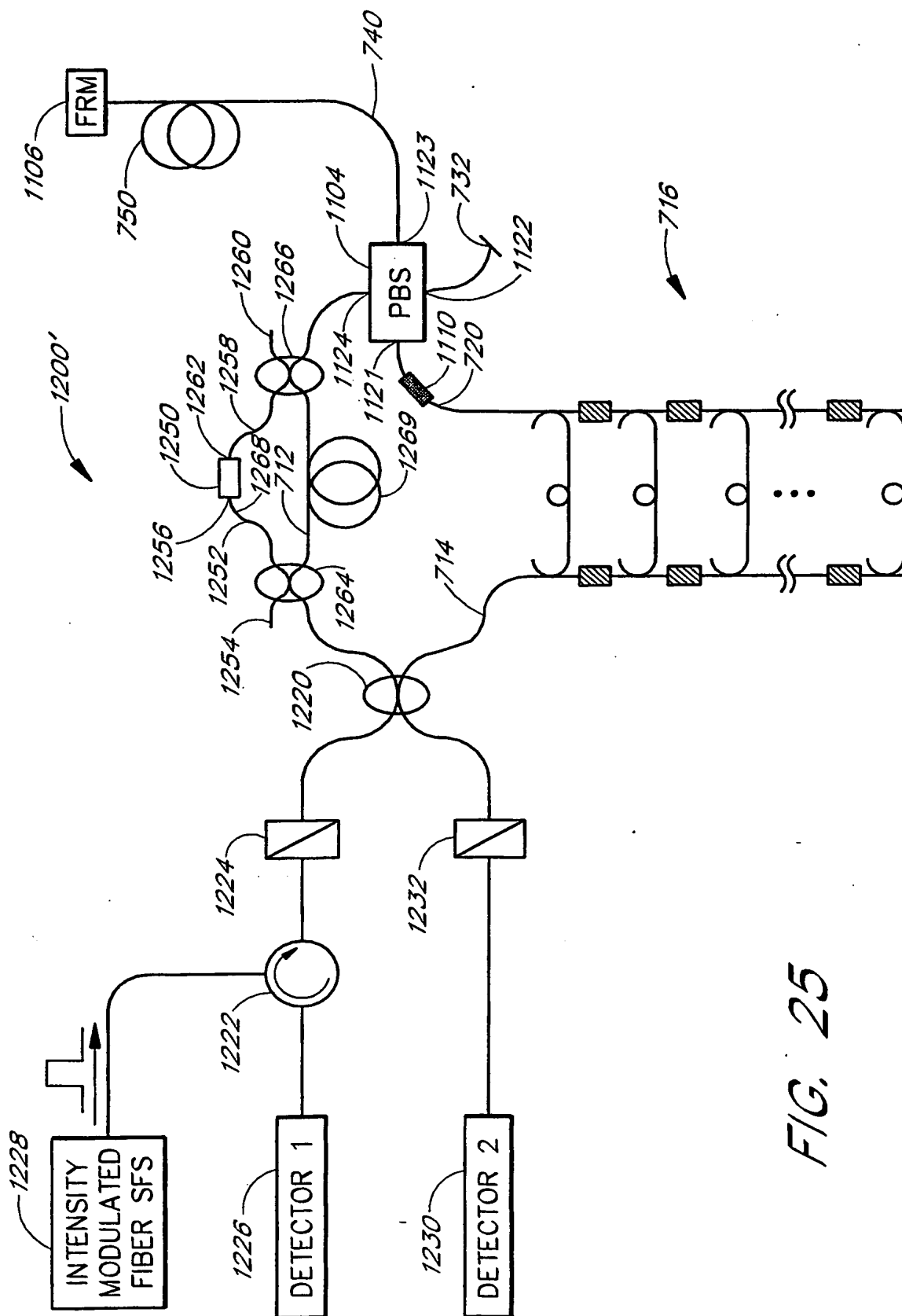
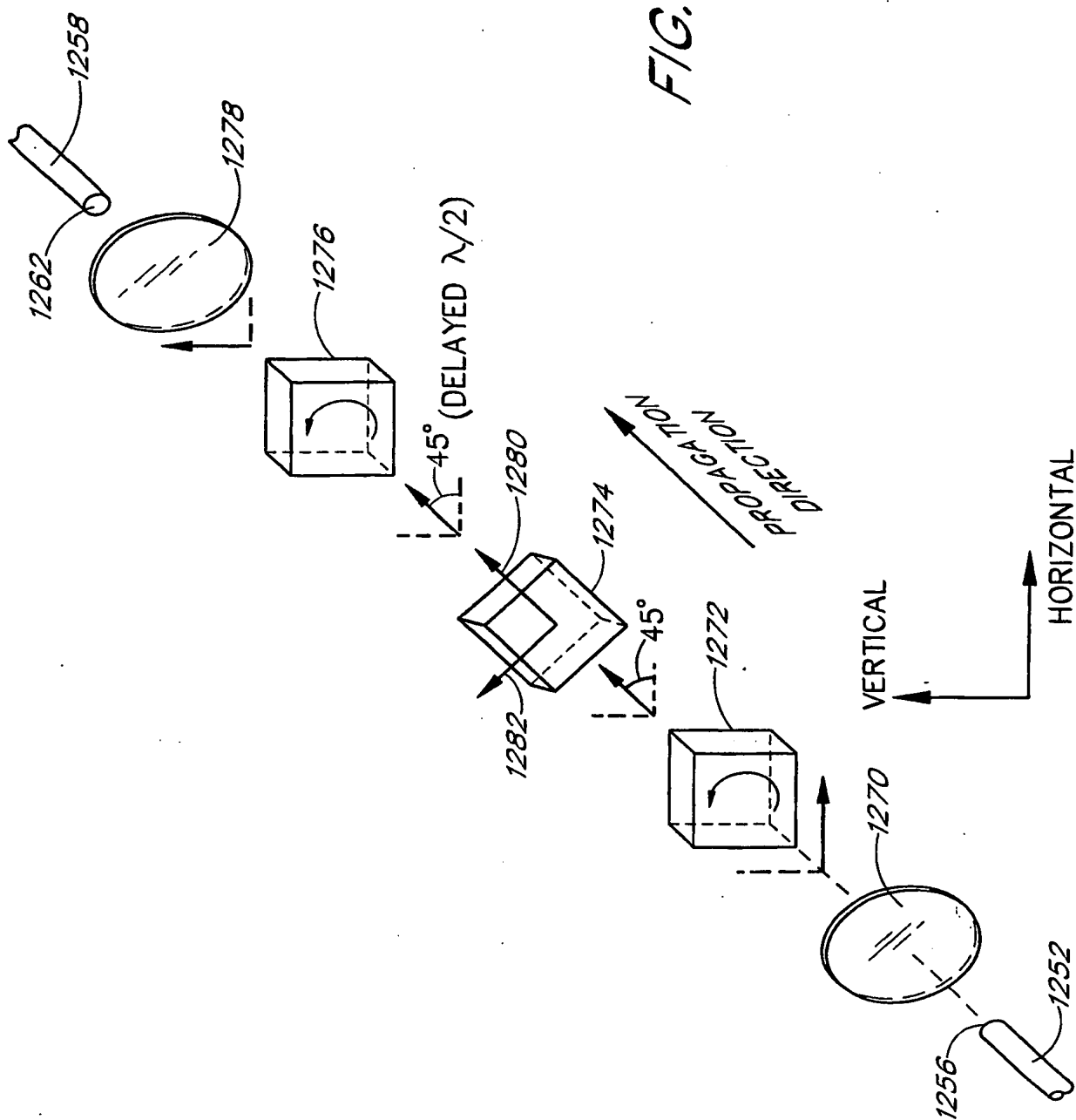


FIG. 25

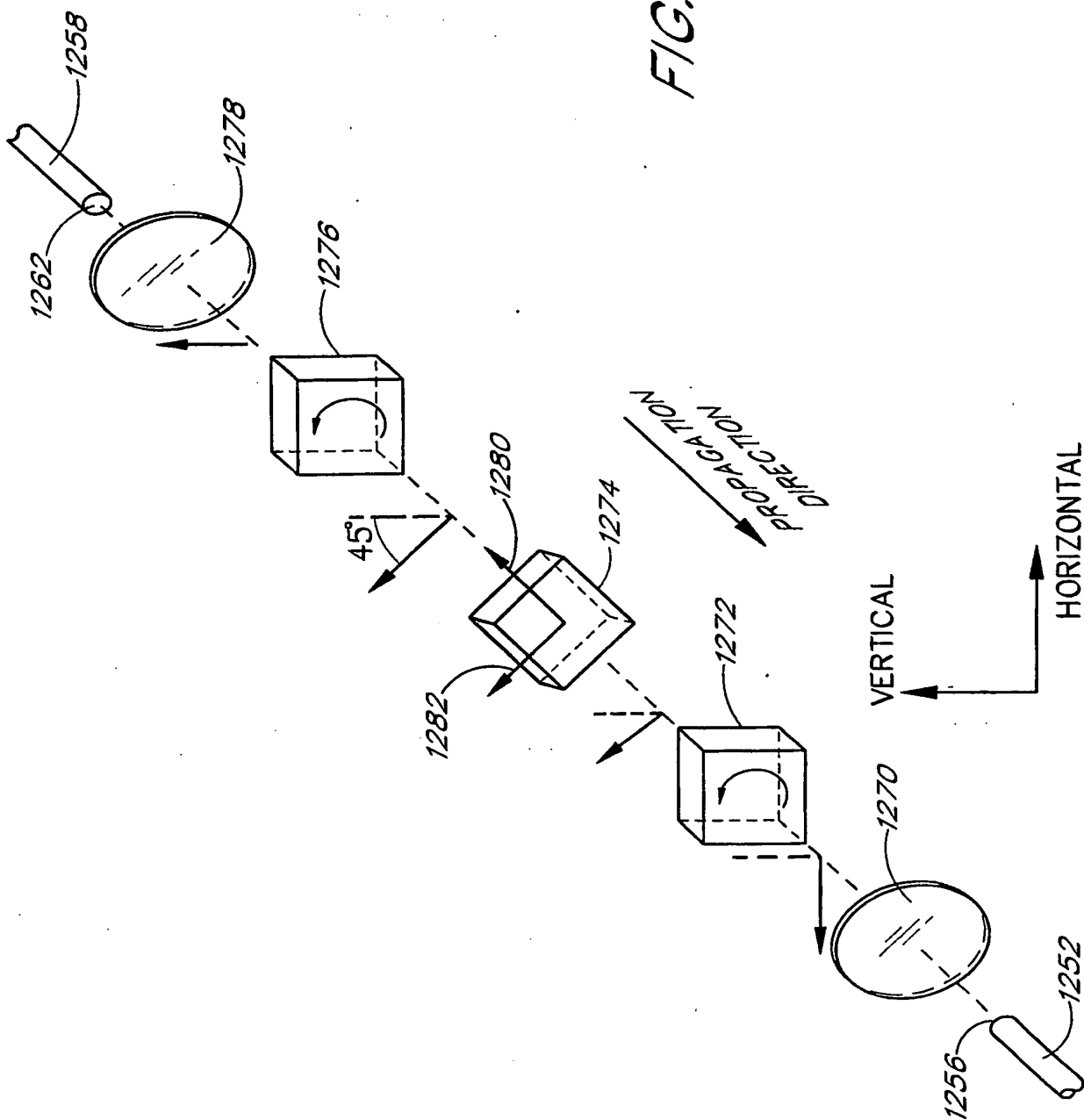
28/60

FIG. 26



29/60

FIG. 27



30/60

FIG. 28

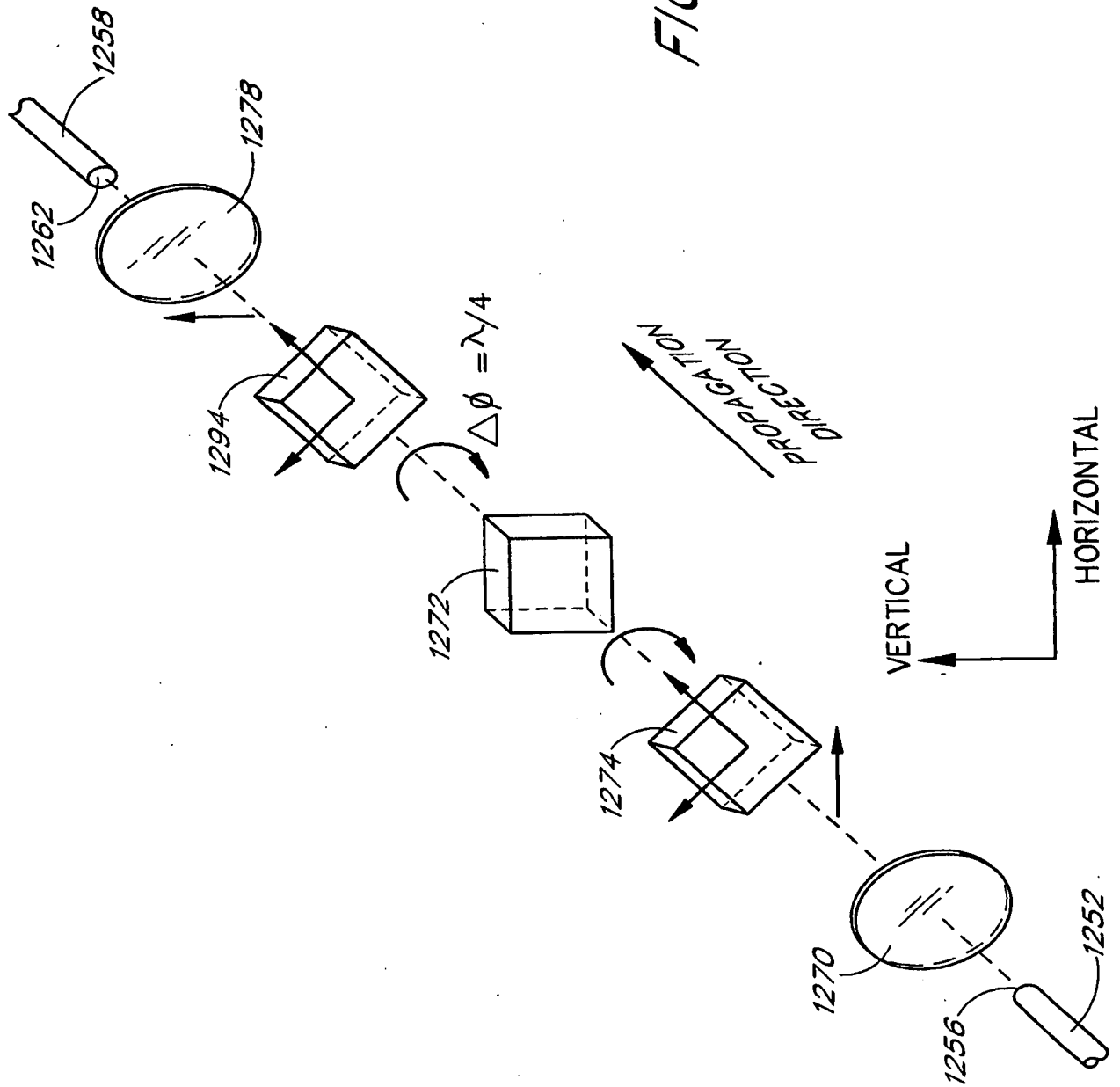
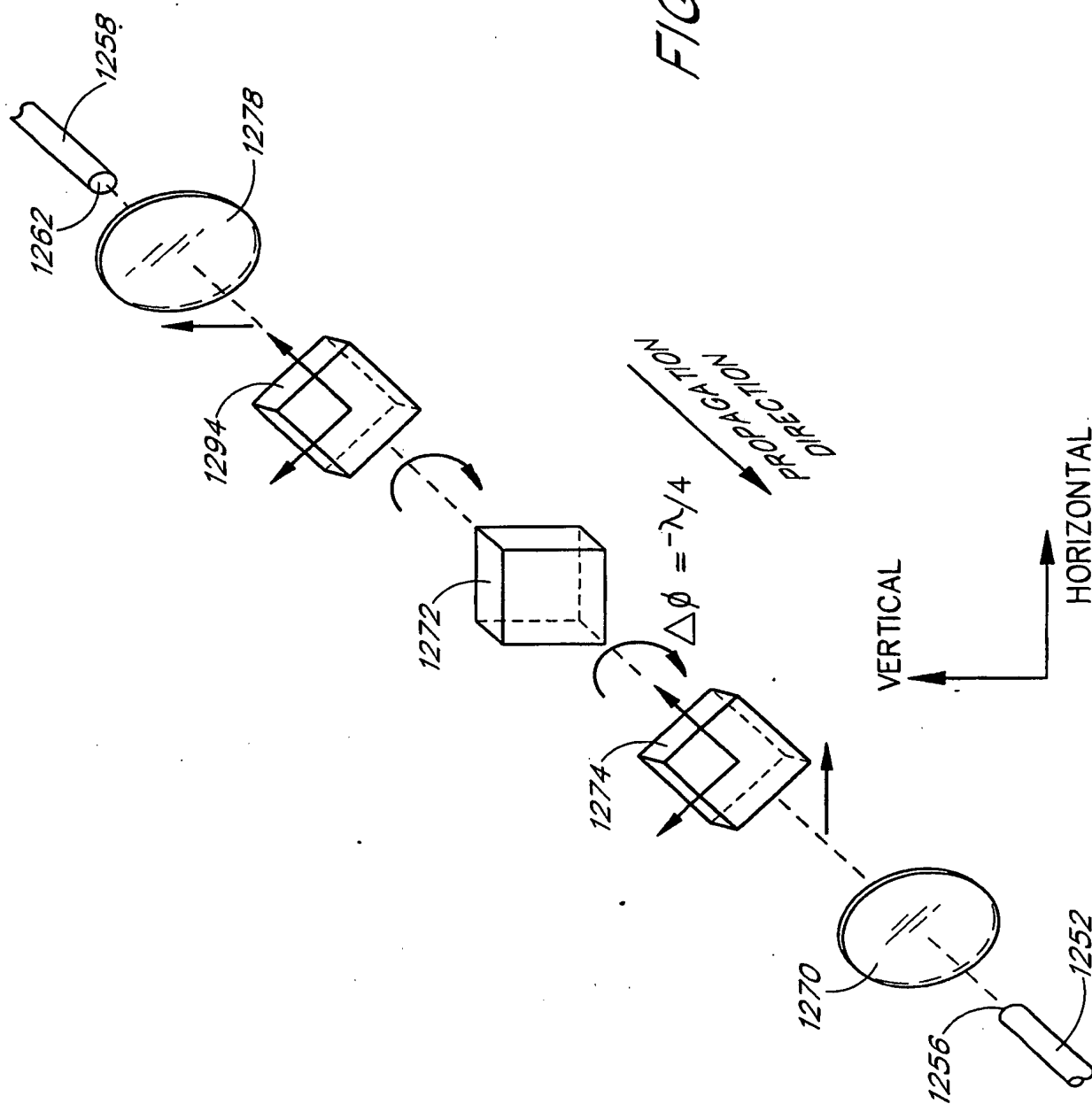
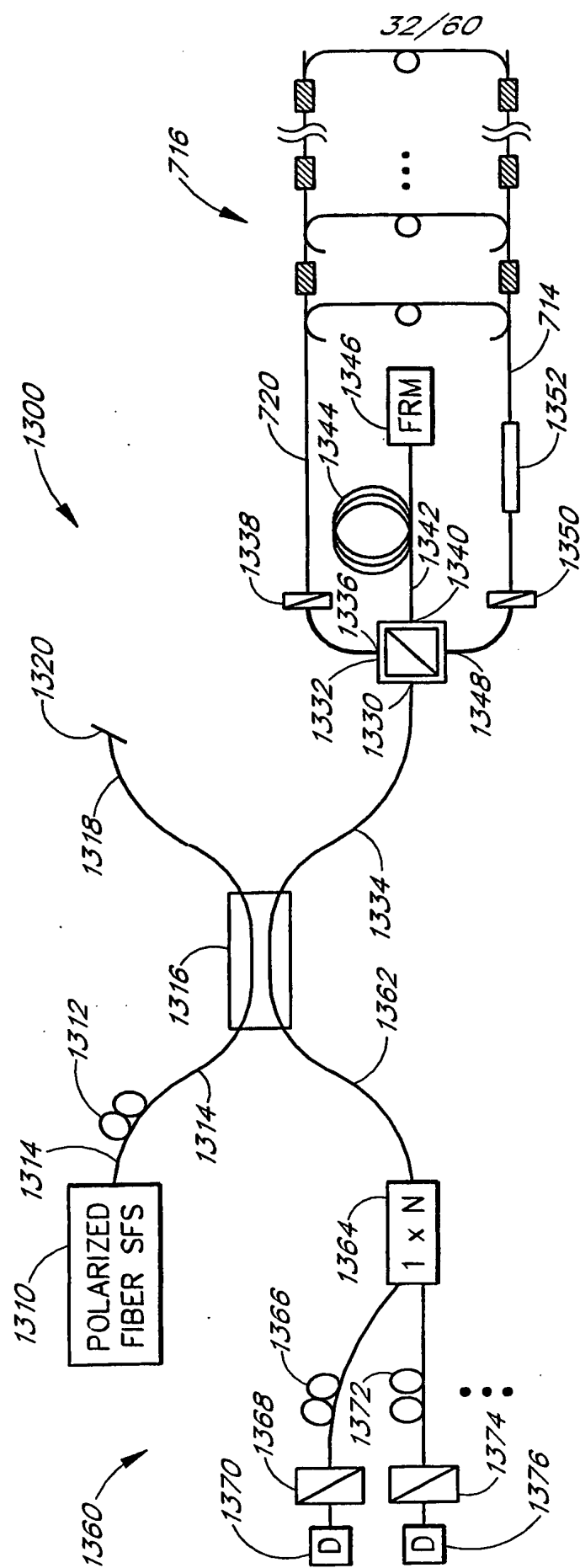




FIG. 29





**FIG. 30**

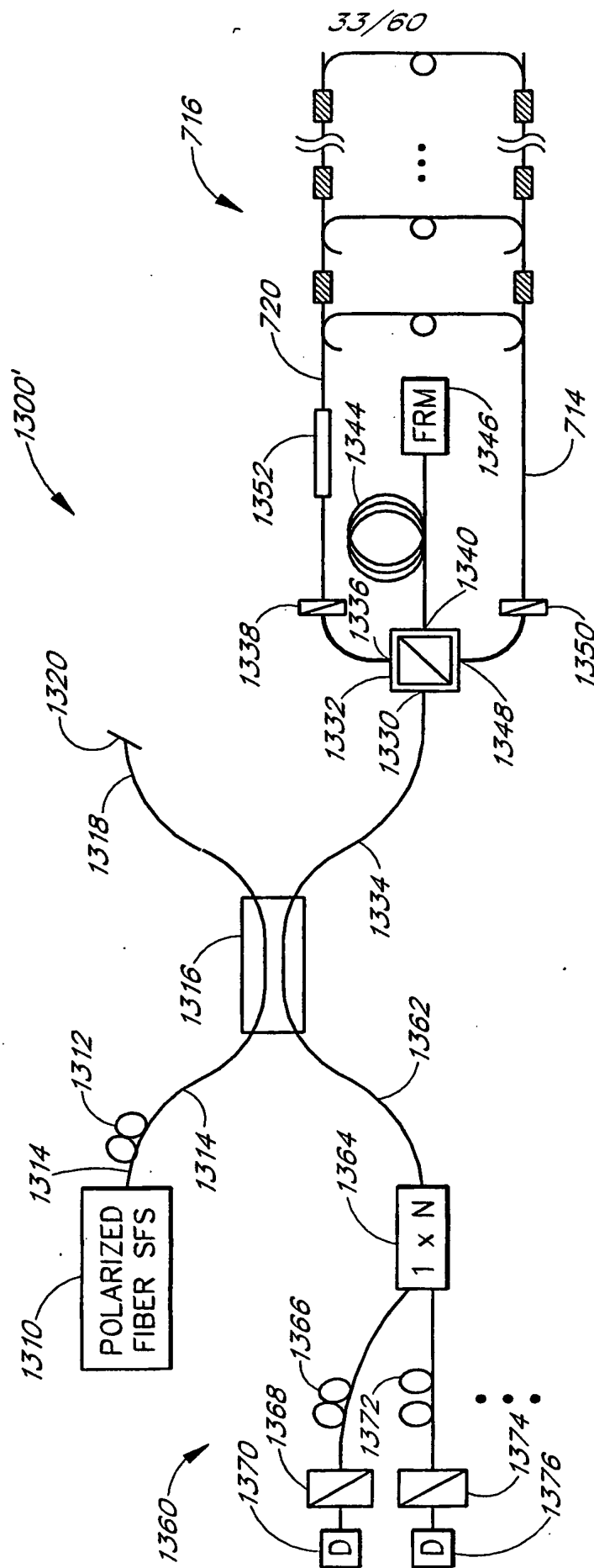


FIG. 31

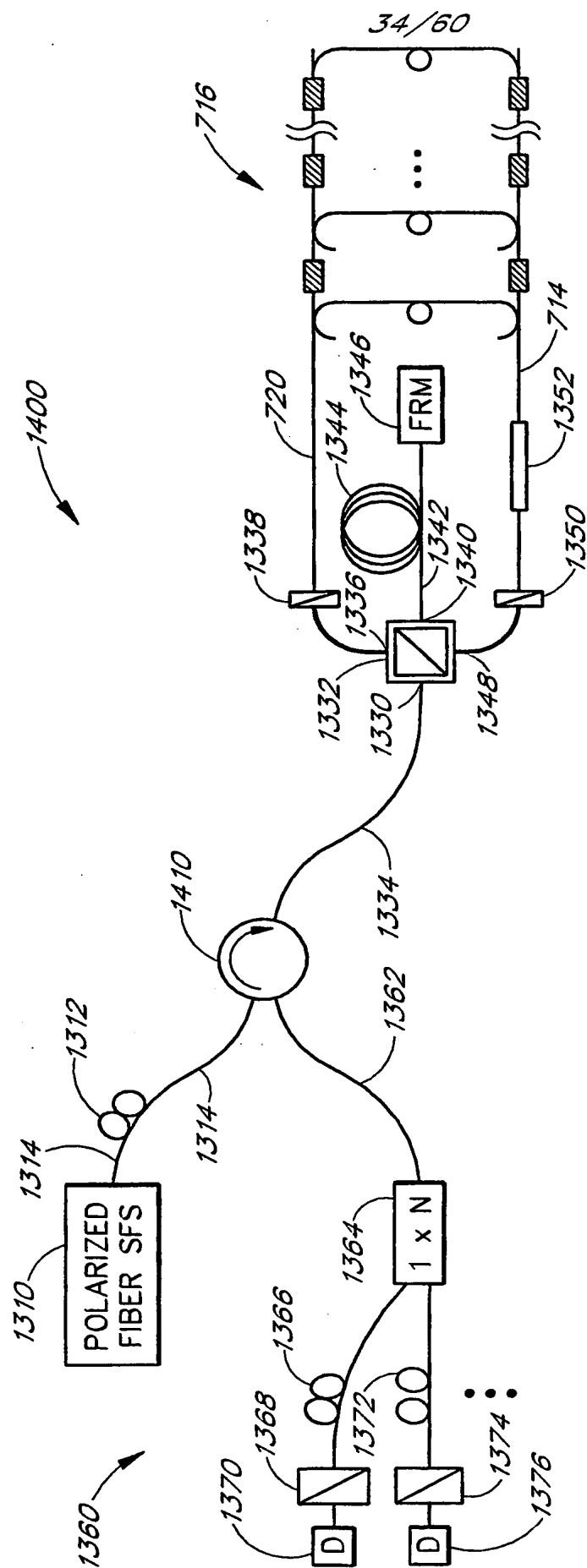


FIG. 32

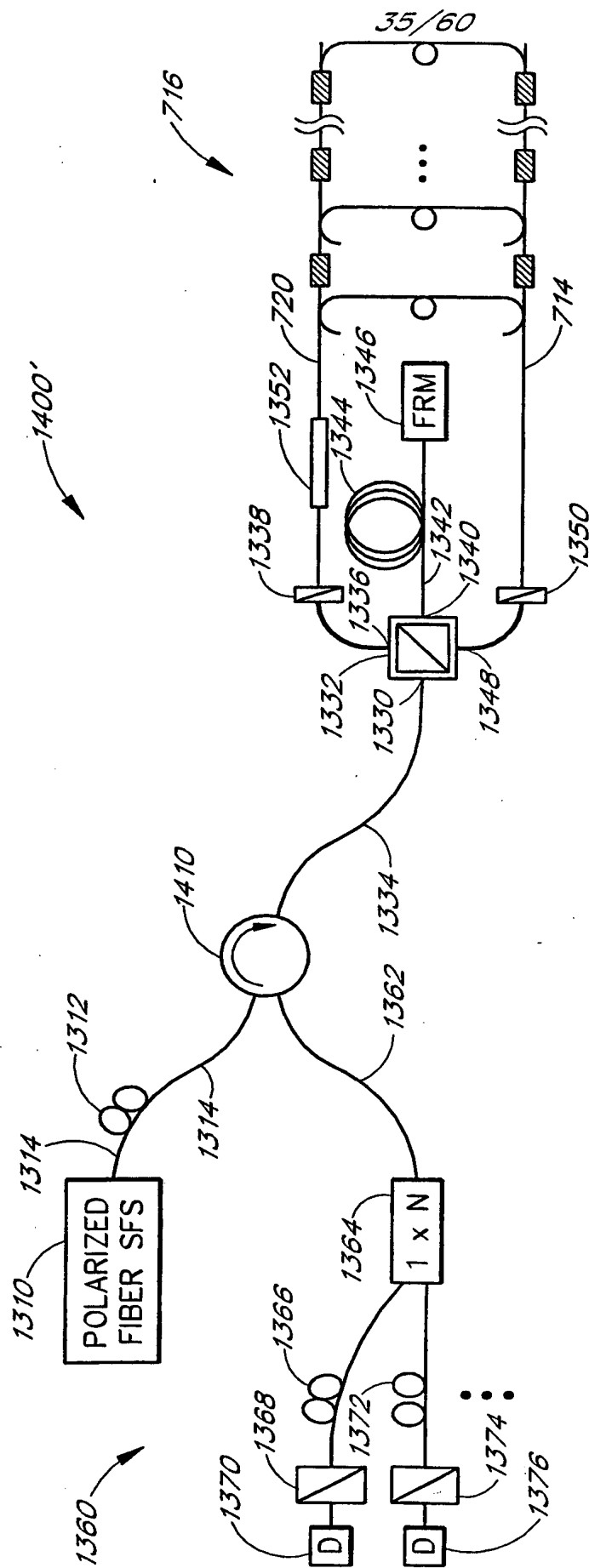
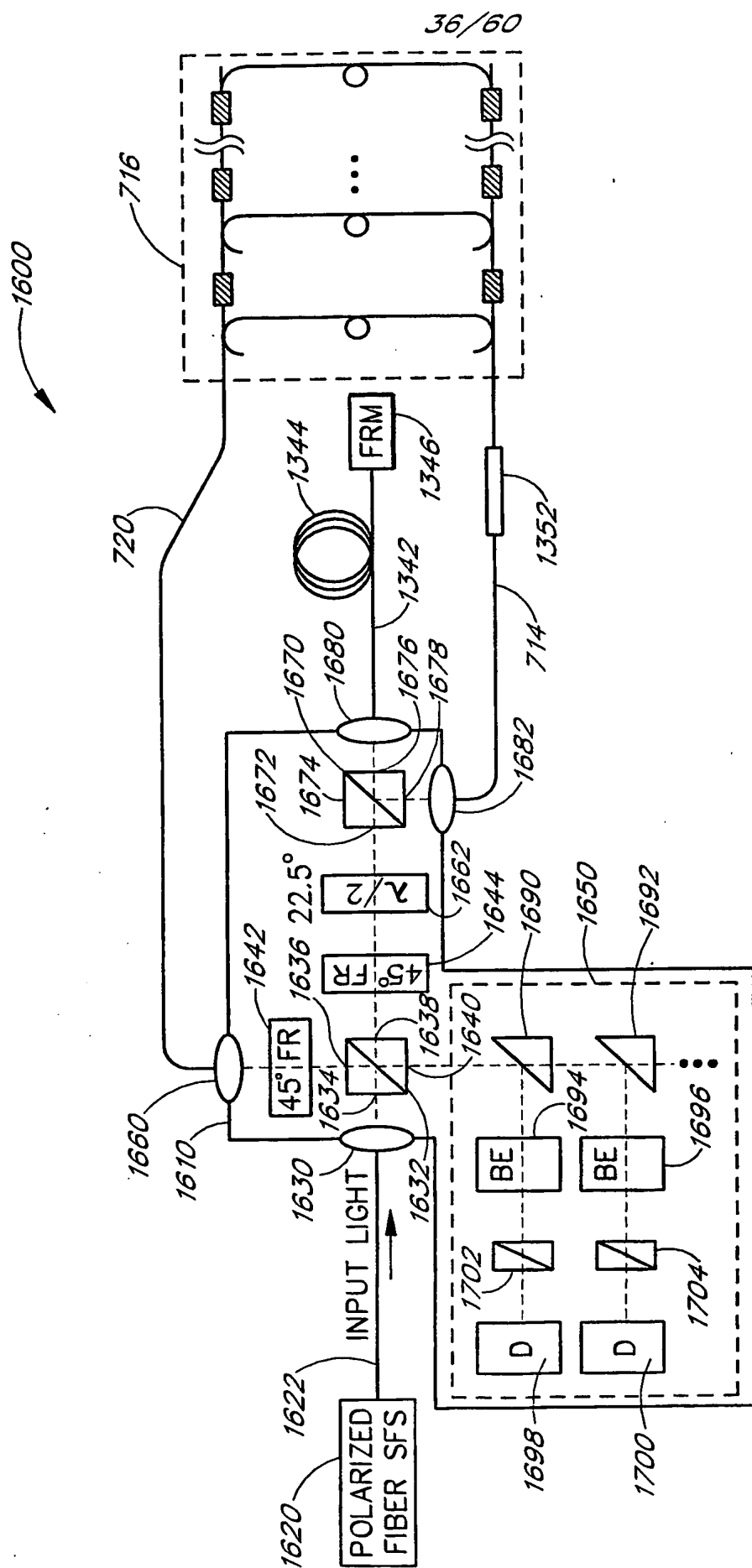
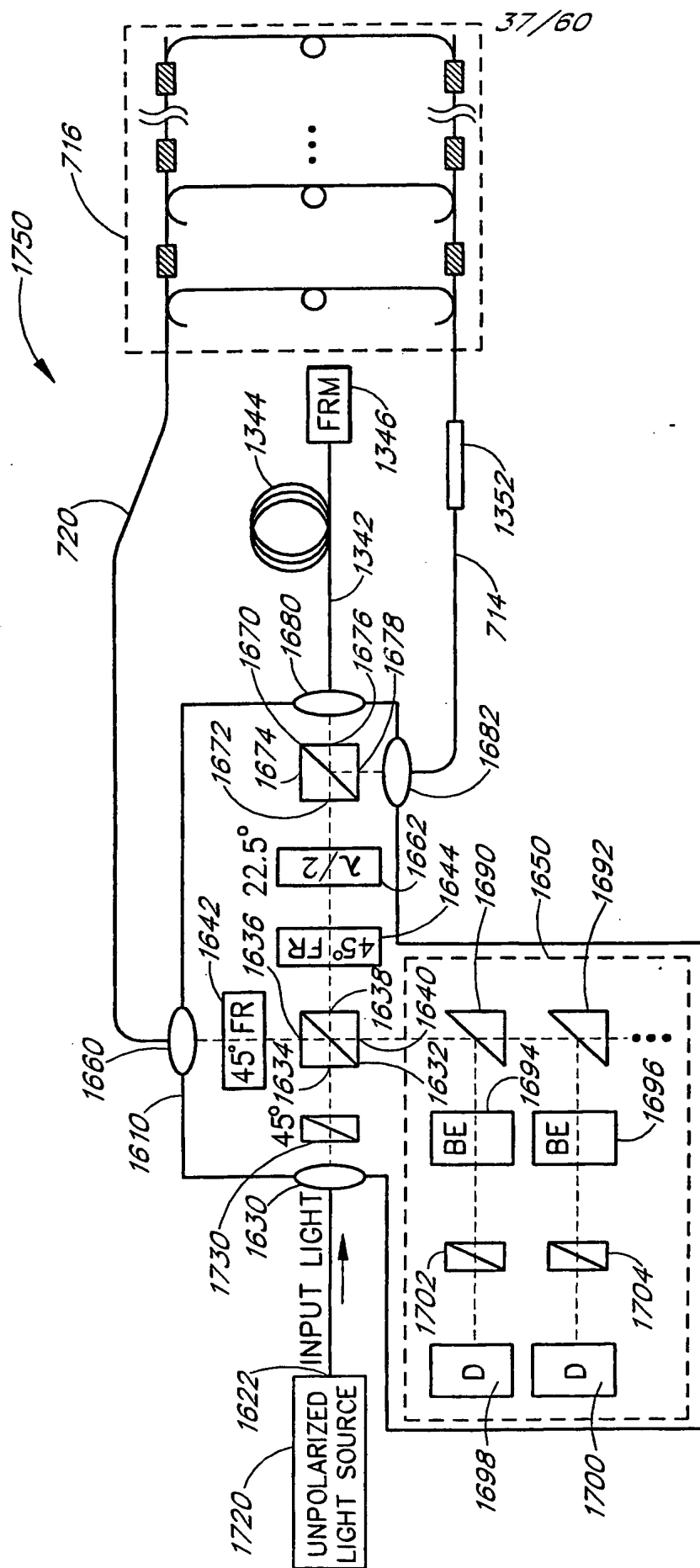


FIG. 33



**FIG. 34**



**FIG. 35**

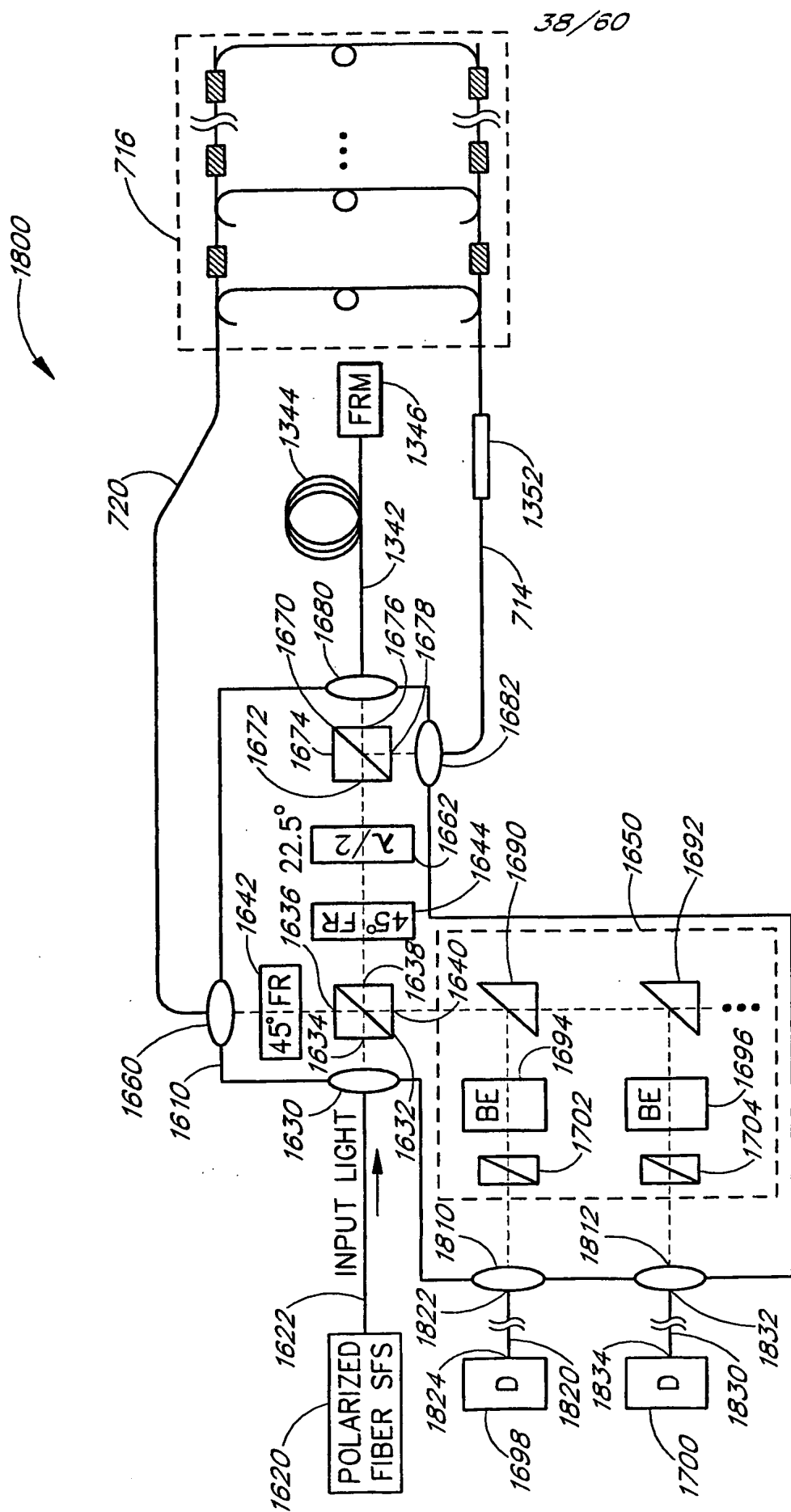


FIG. 36



39/60

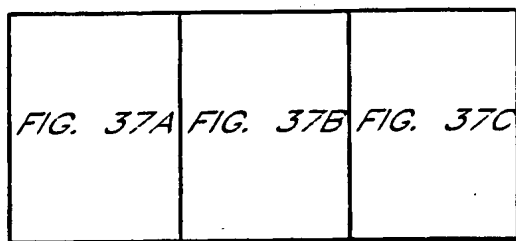


FIG. 37

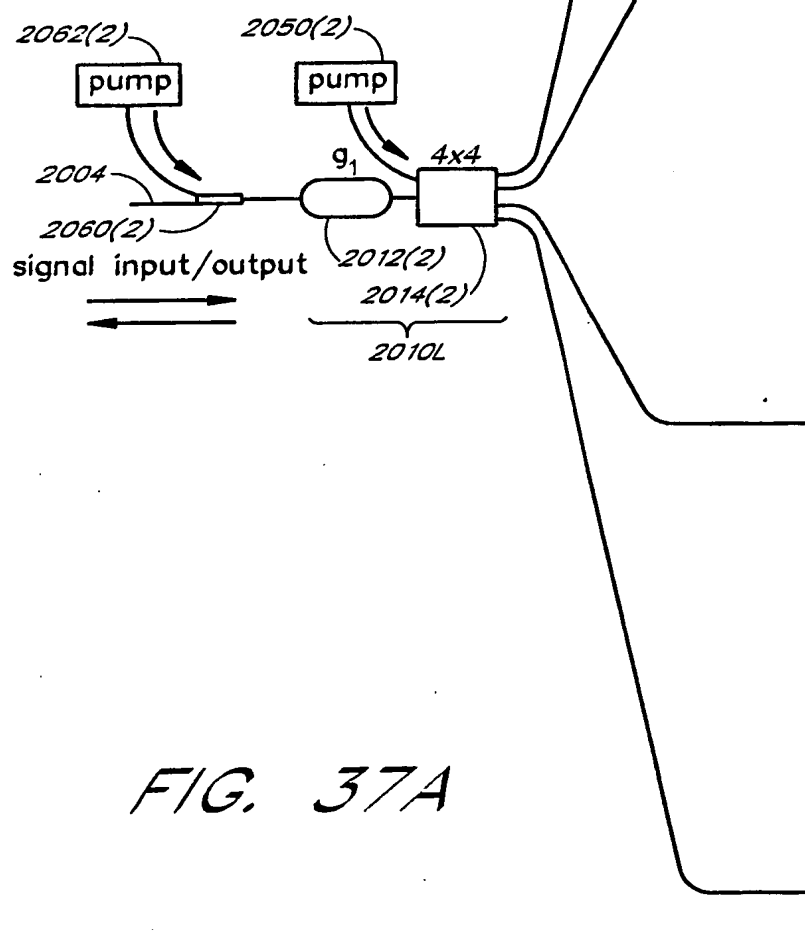
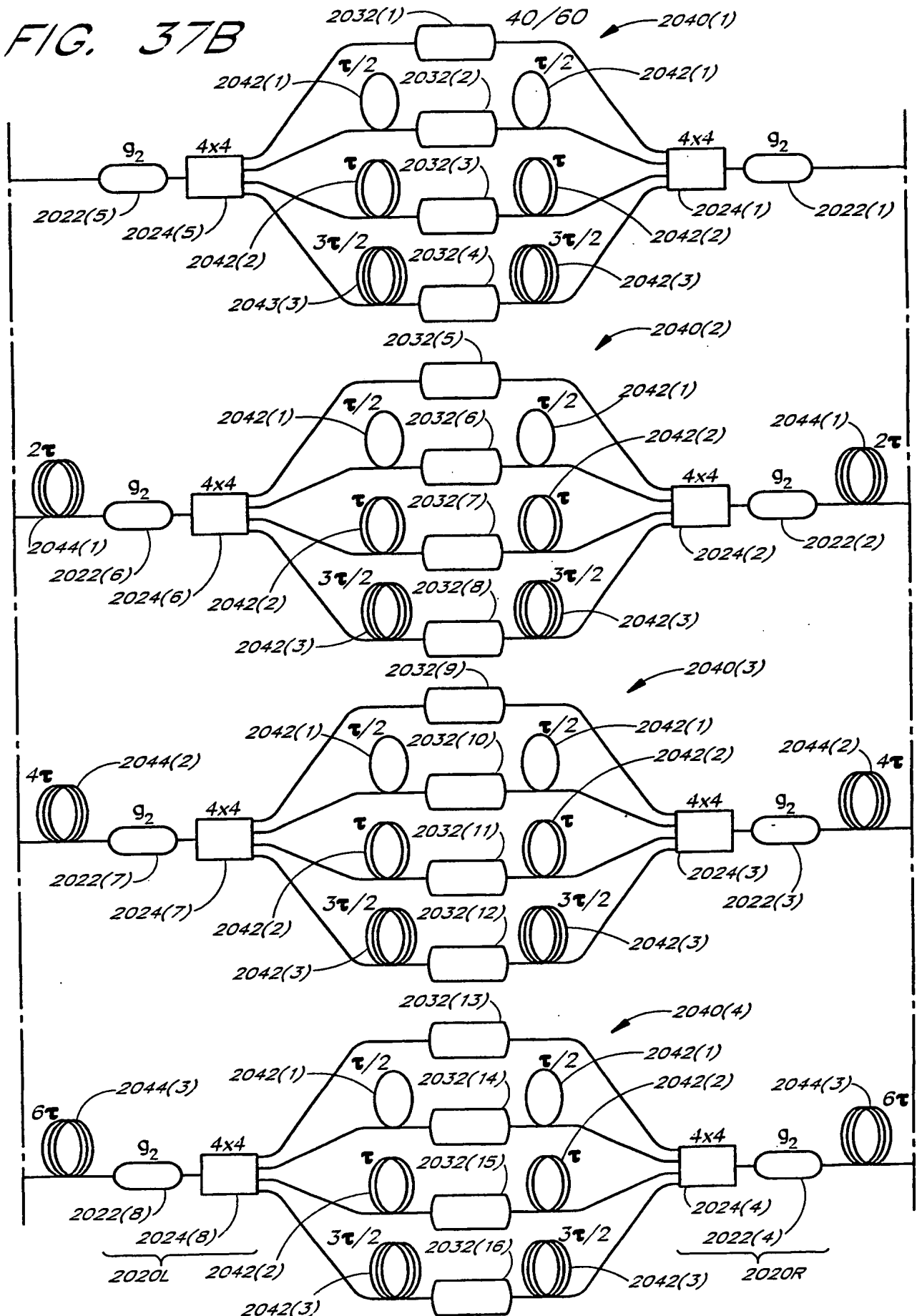


FIG. 37A

FIG. 37B



41/60

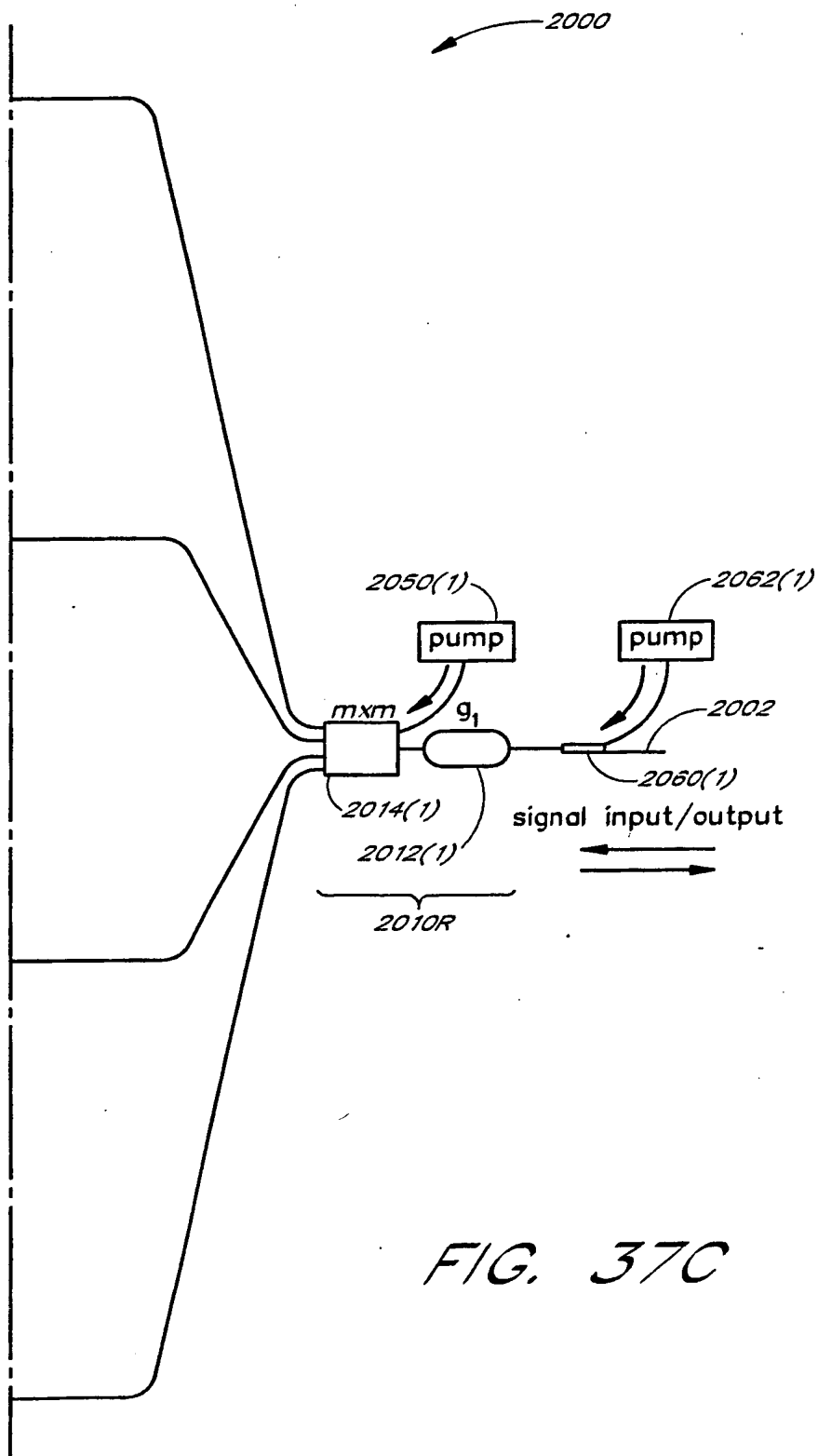


FIG. 37C

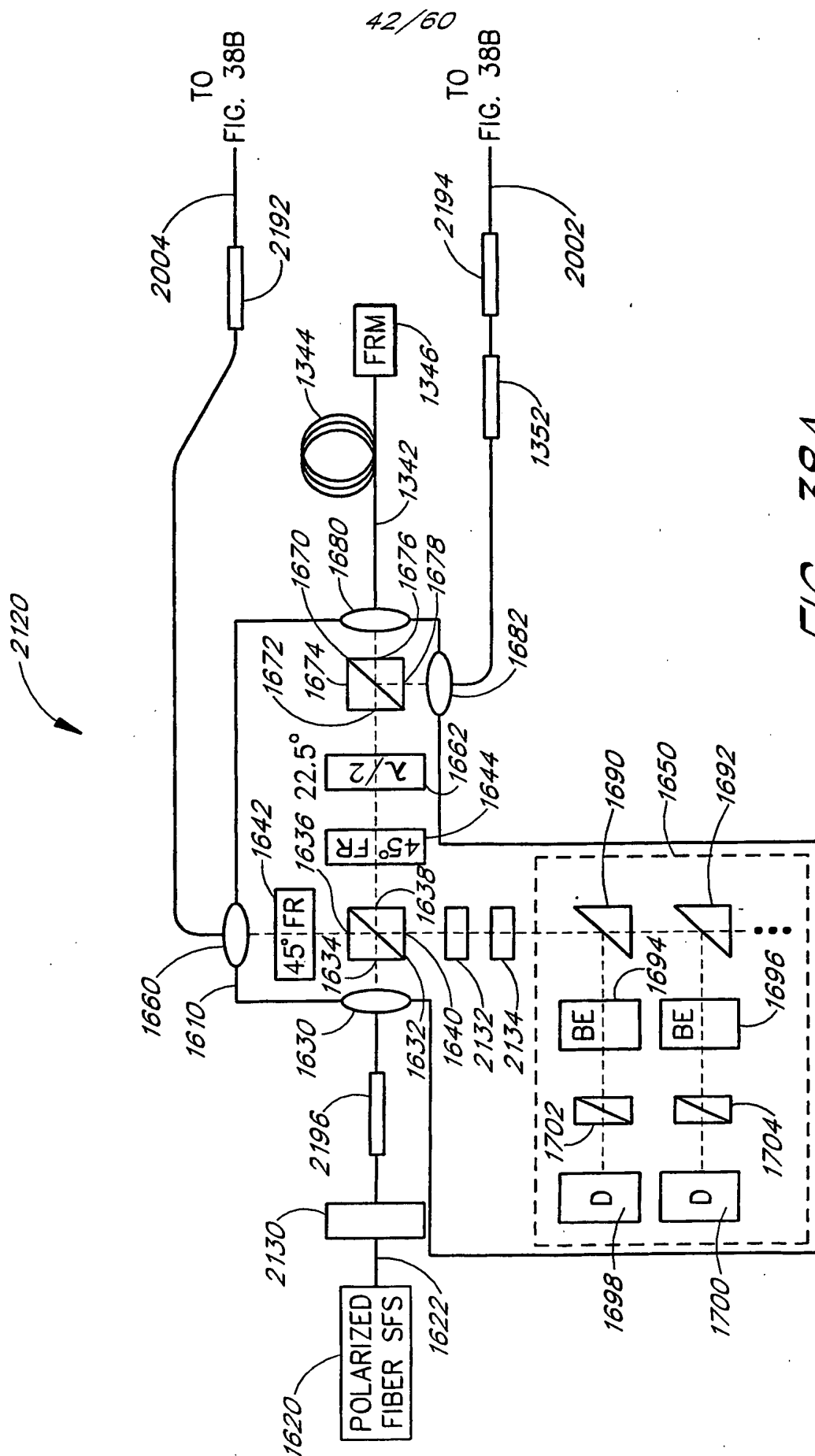


FIG. 38A

43/60

FIG. 38B<sub>1</sub>

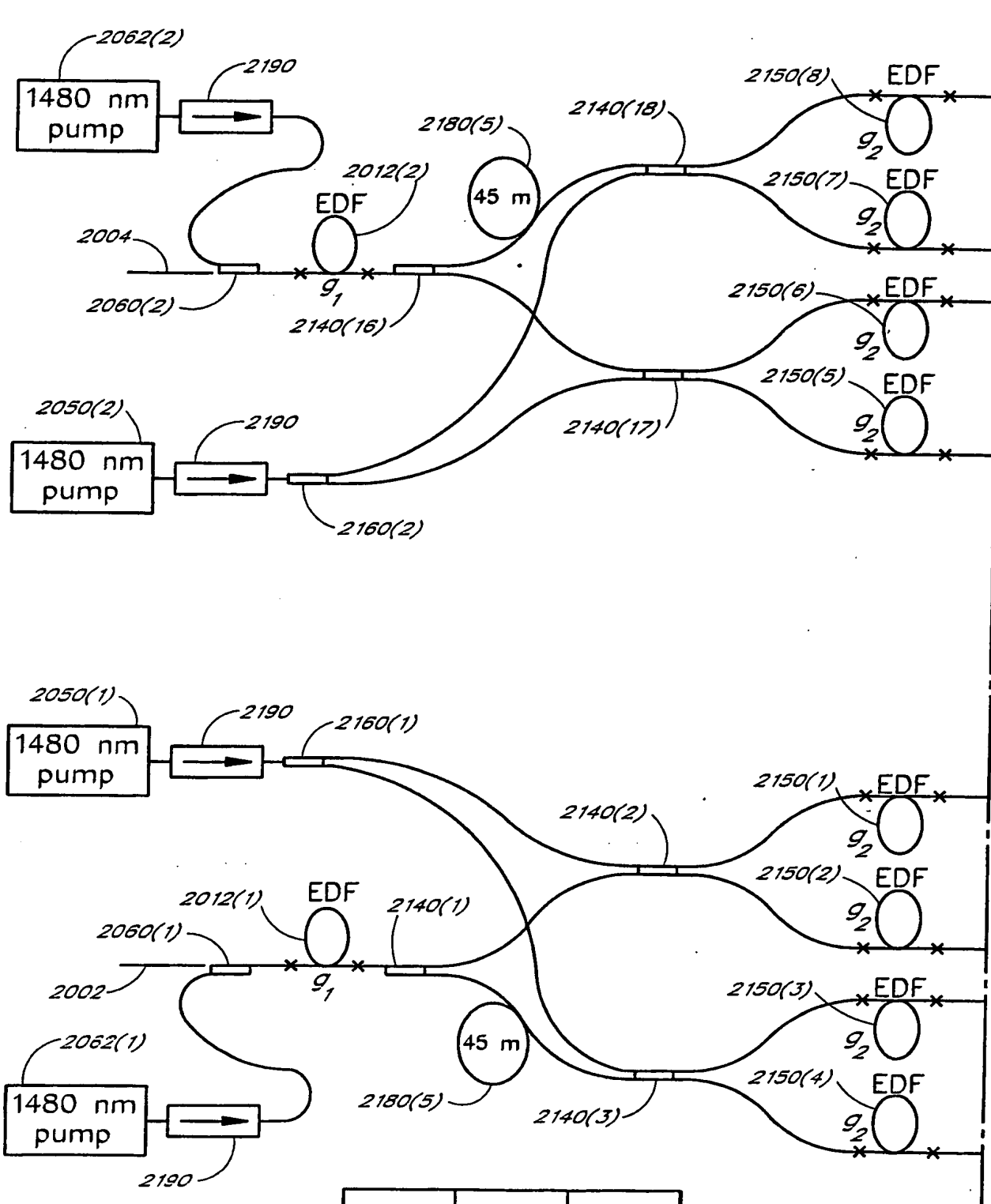


FIG. 38B

FIG. 38B <sub>1</sub>	FIG. 38B <sub>2</sub>	FIG. 38B <sub>3</sub>
-----------------------	-----------------------	-----------------------

44/60

2100

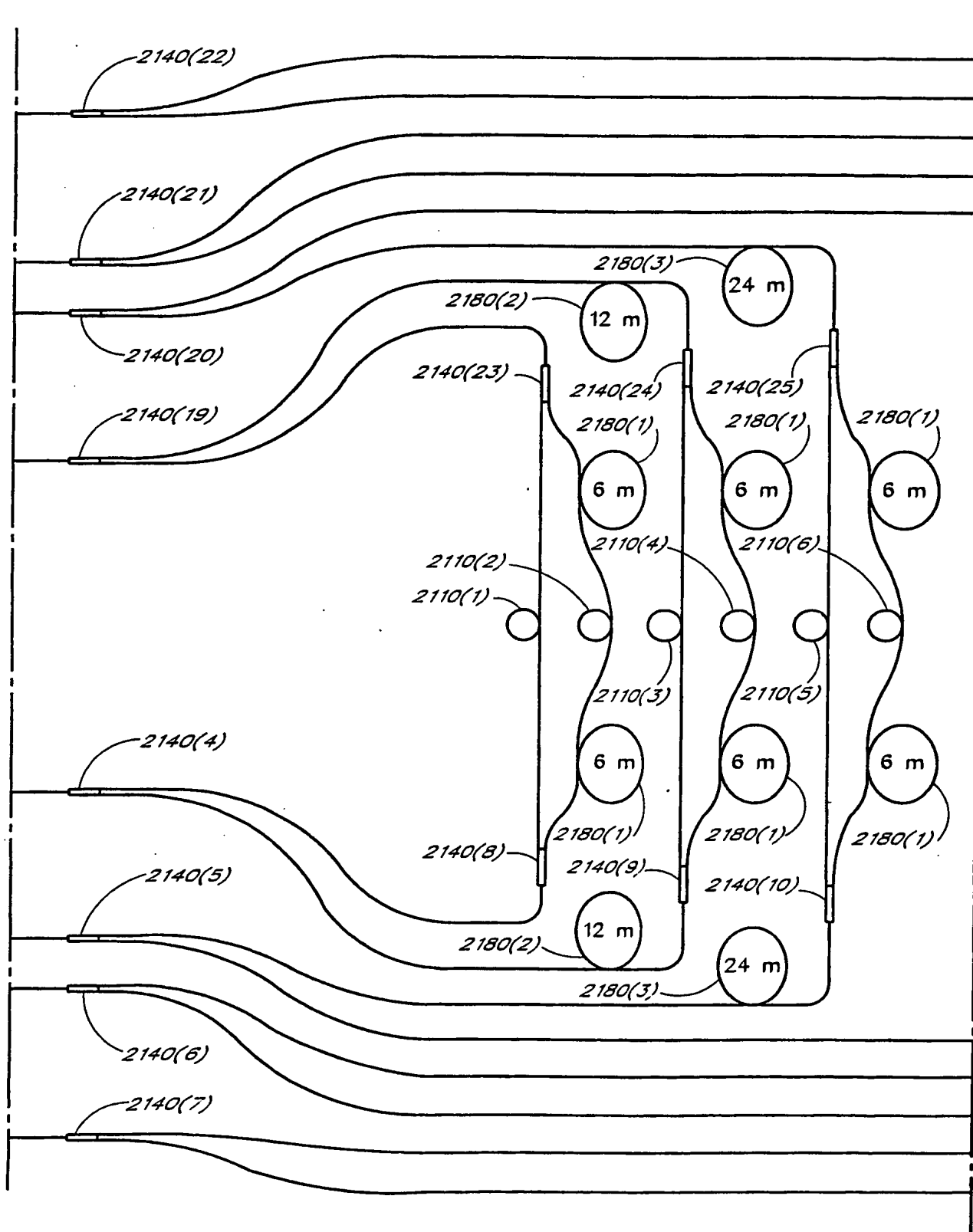
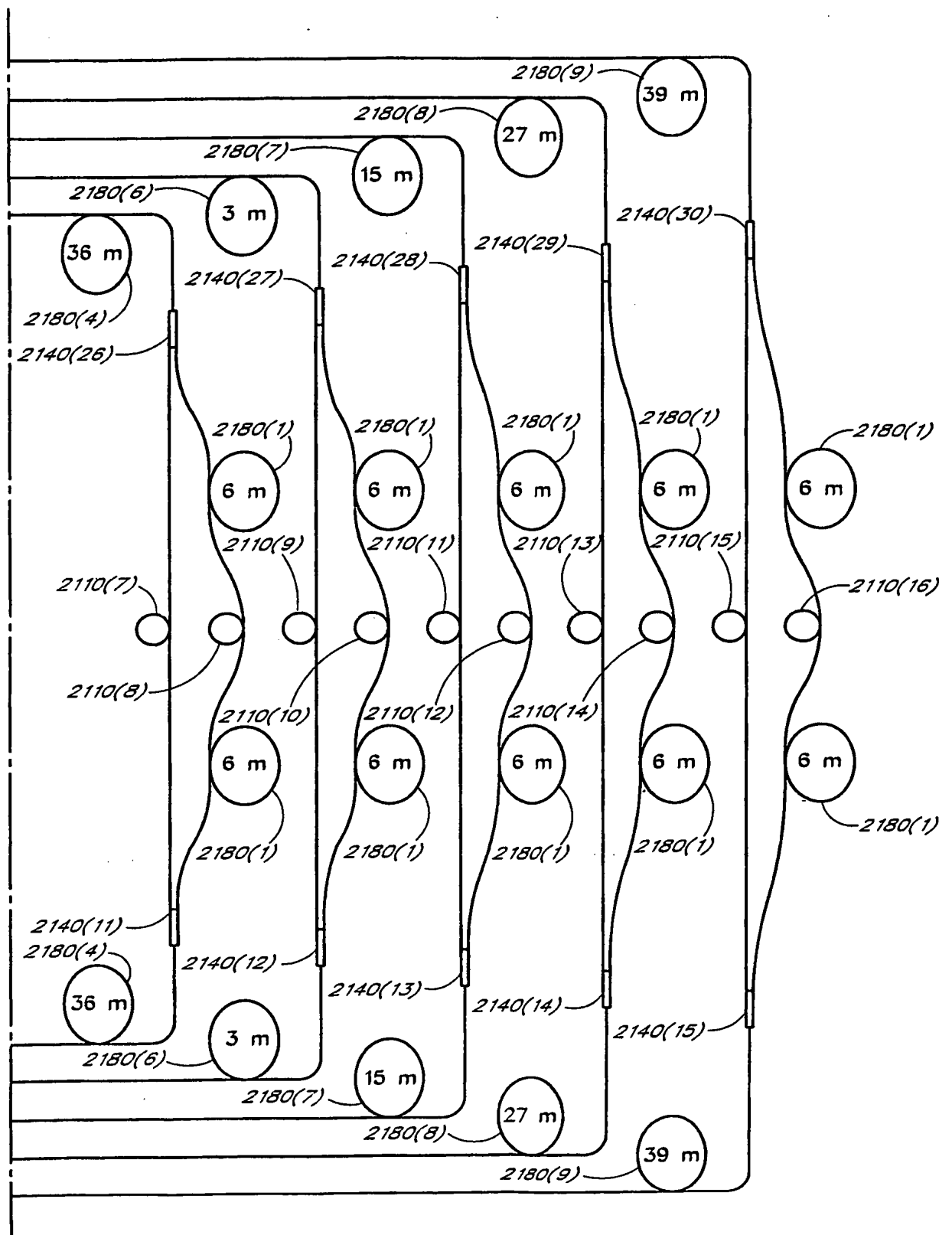


FIG. 38B<sub>2</sub>

45/60

FIG. 38B<sub>3</sub>

46/60

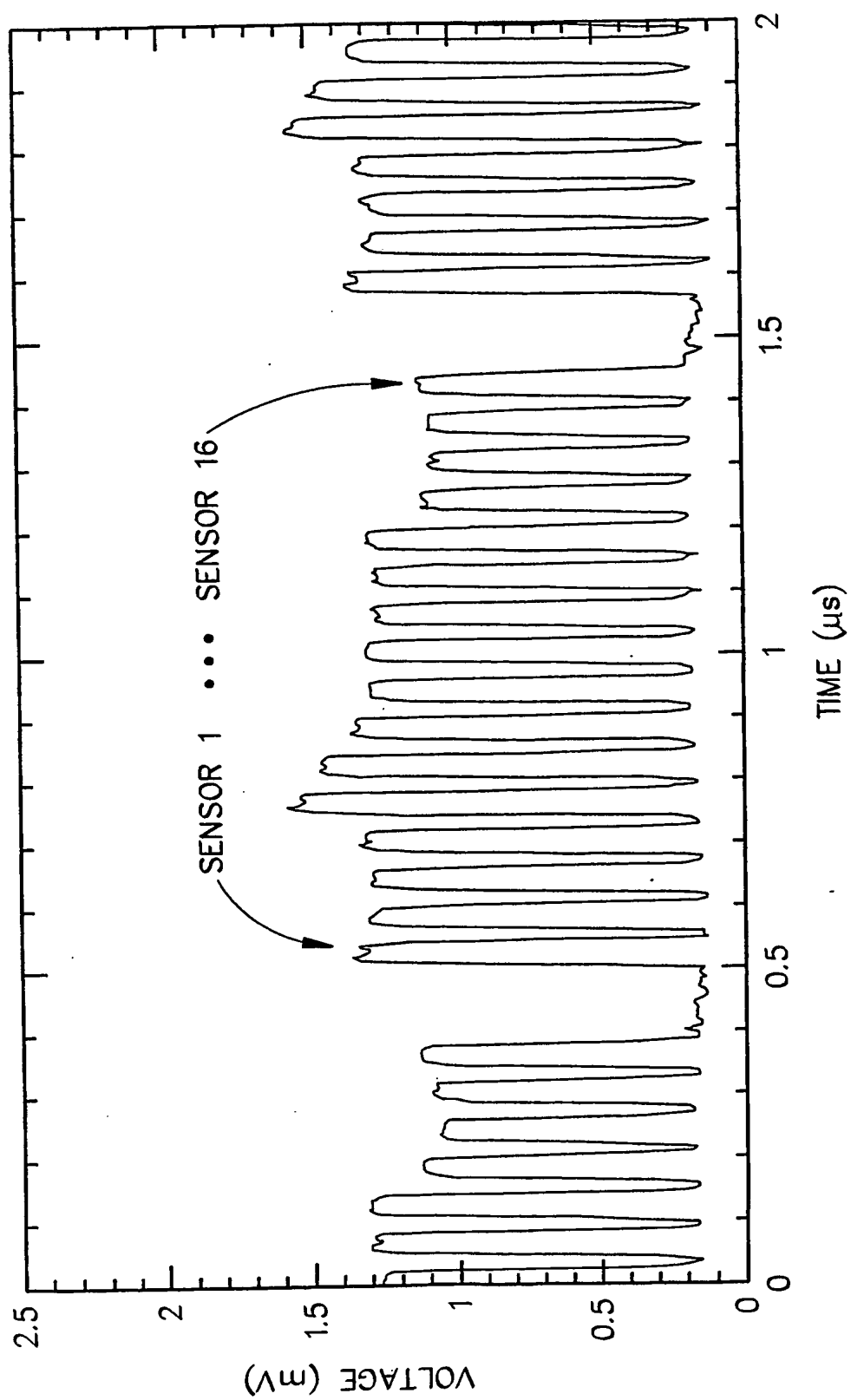


FIG. 39A



47/60

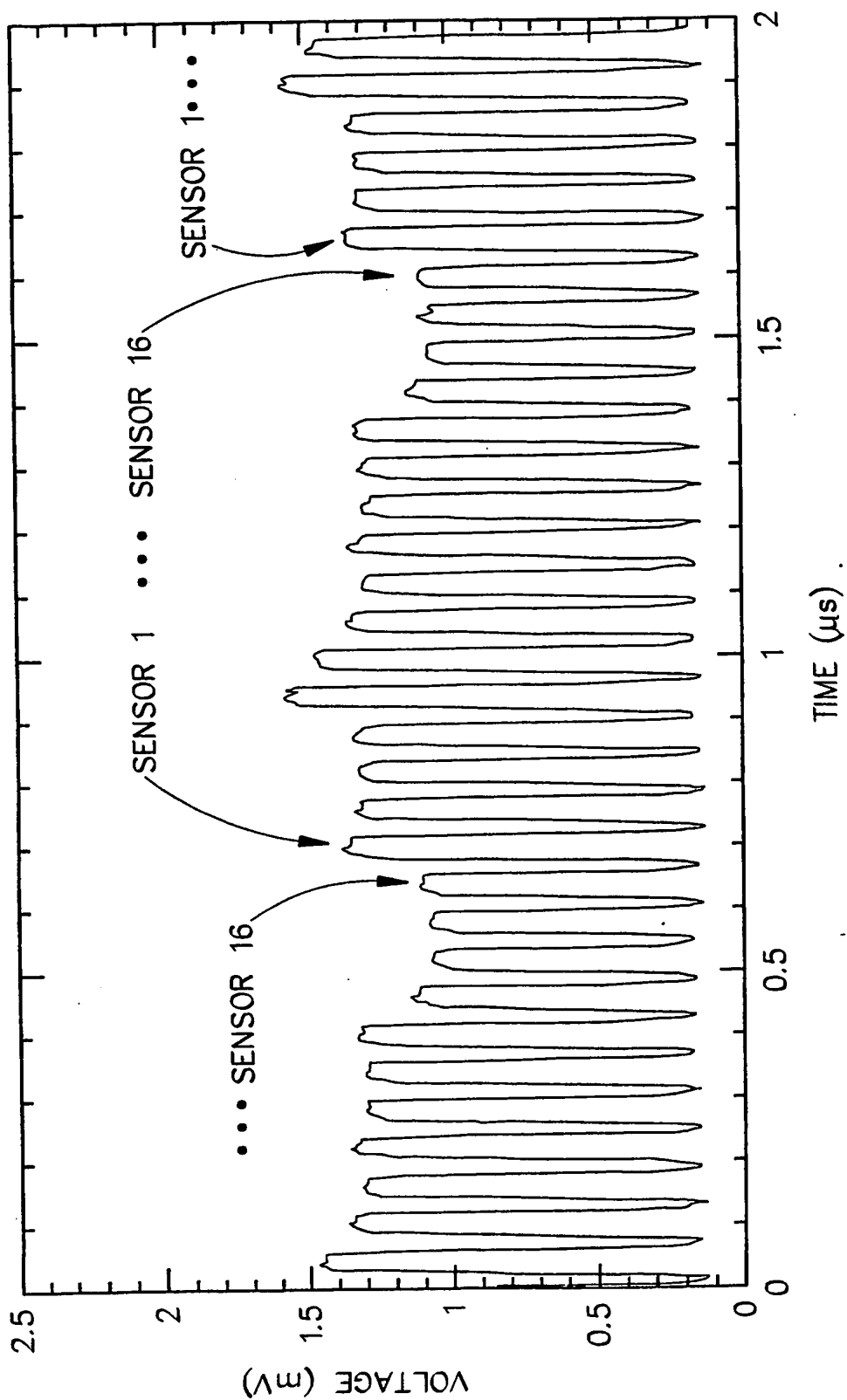


FIG. 39B

48/60

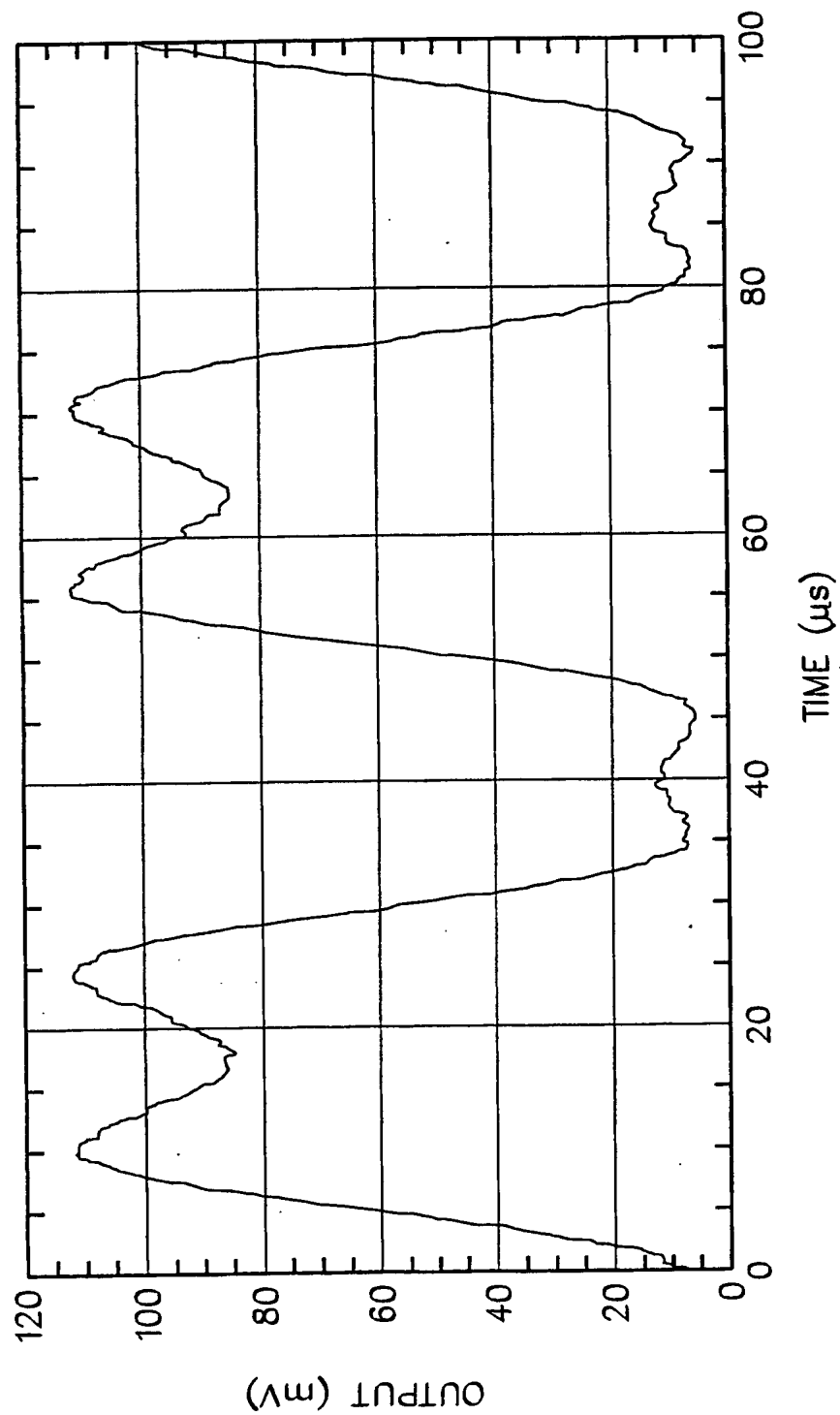


FIG. 40A

49/60

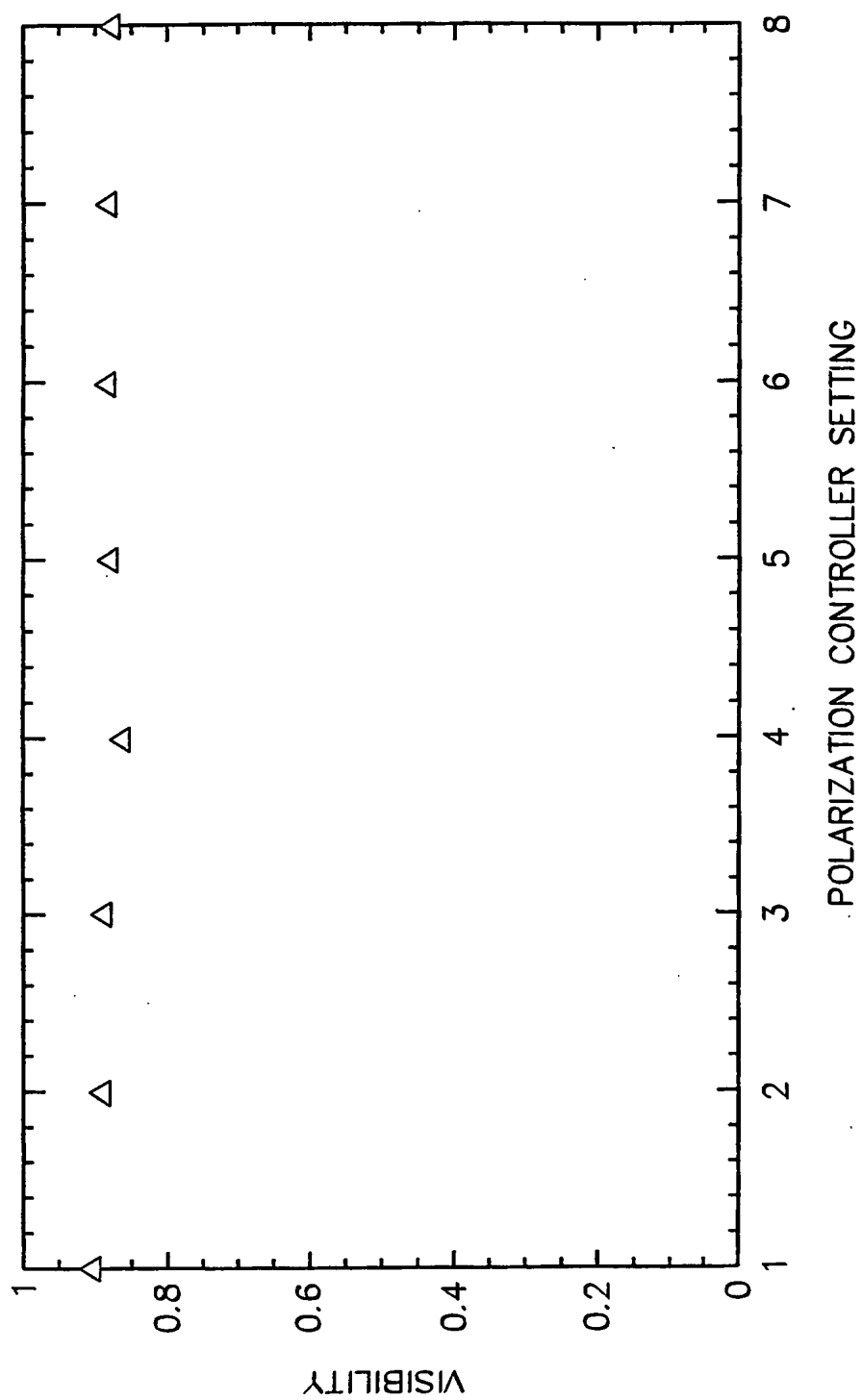


FIG. 40B

50/60

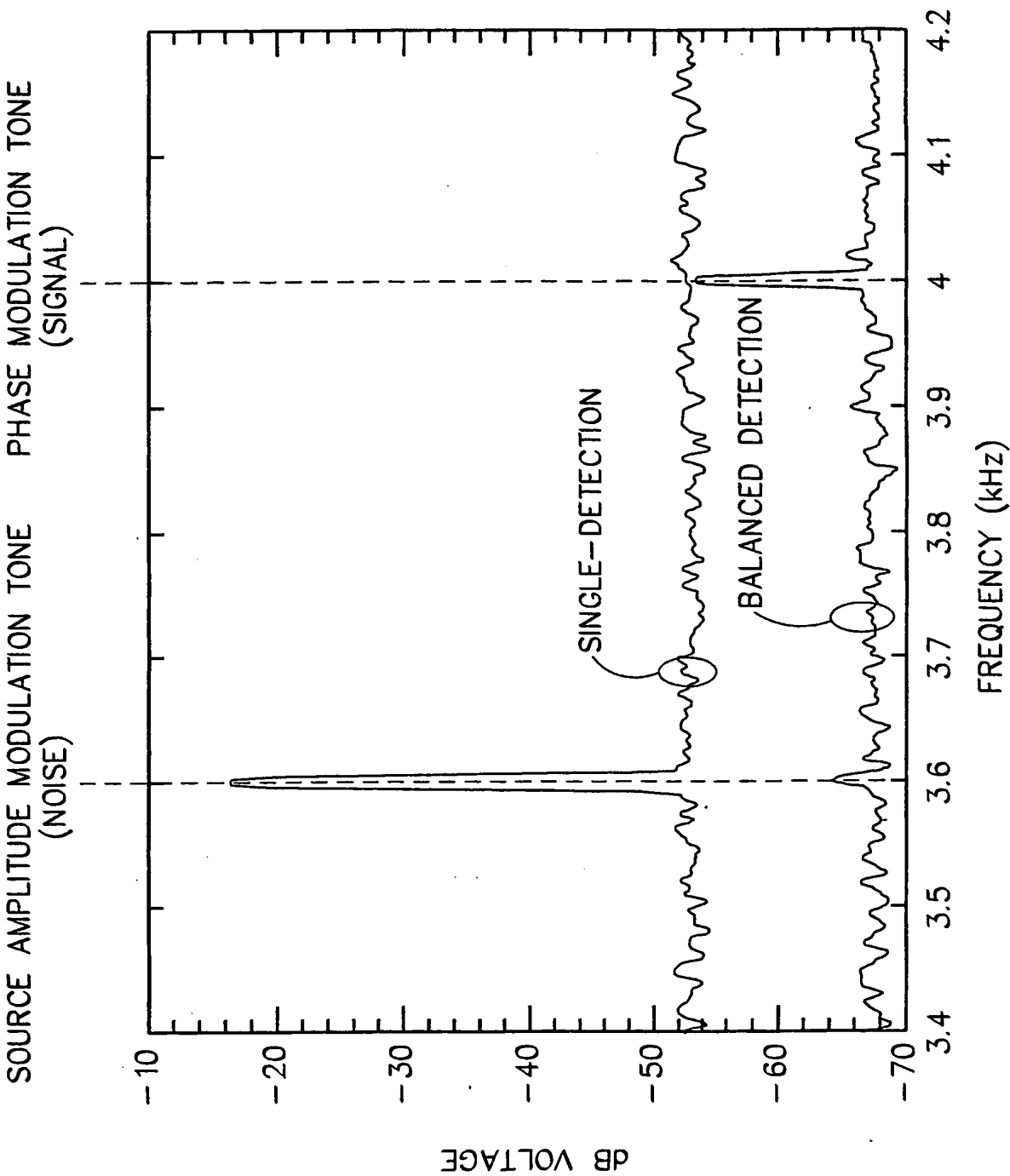
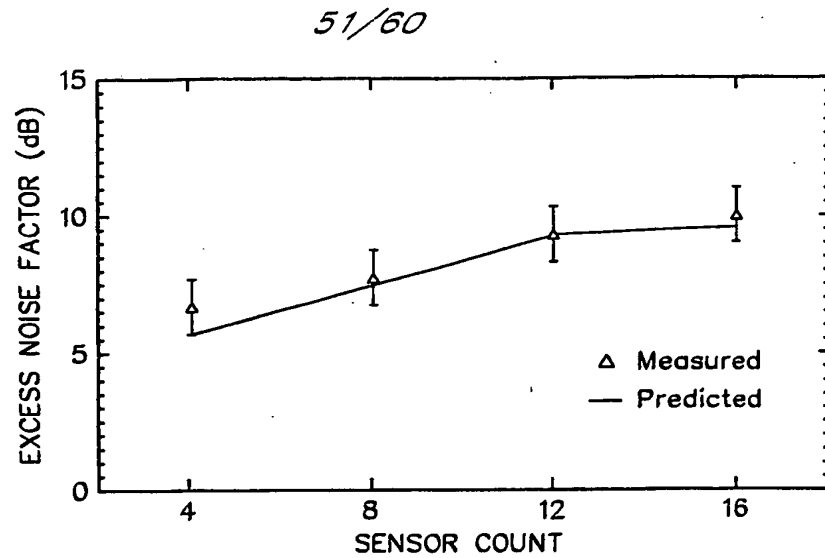
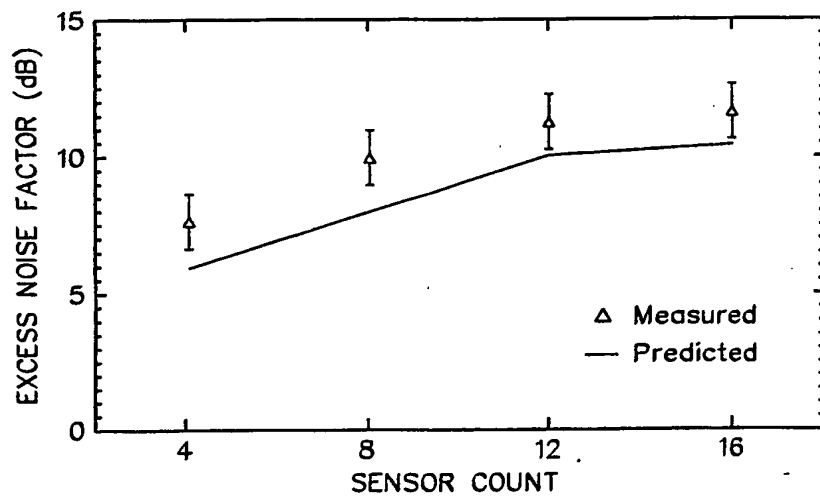
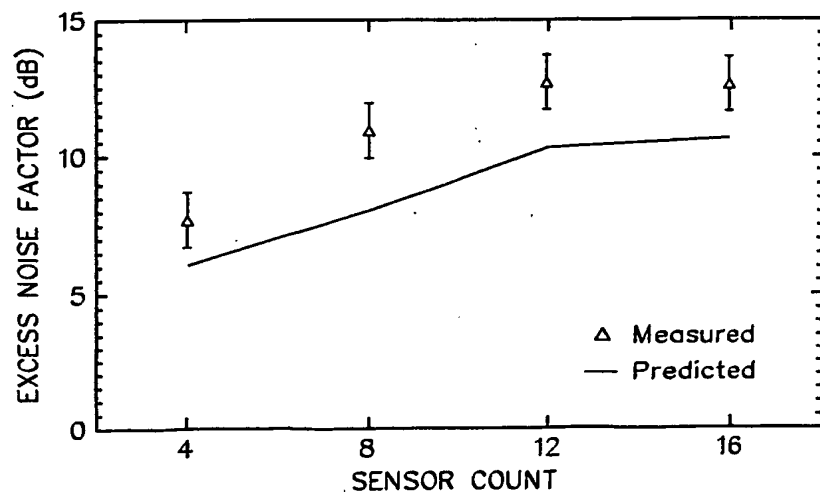


FIG. 41

*FIG. 42A**FIG. 42B**FIG. 42C*

52/60

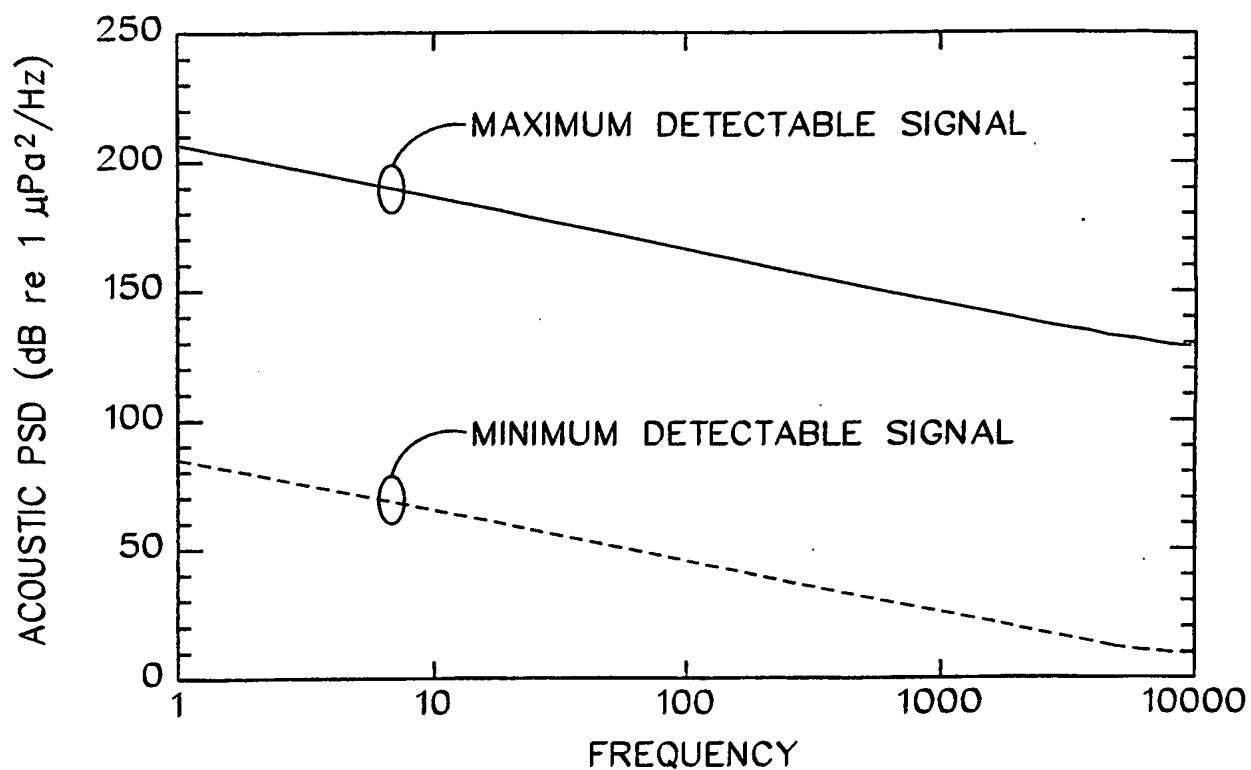


FIG. 43A

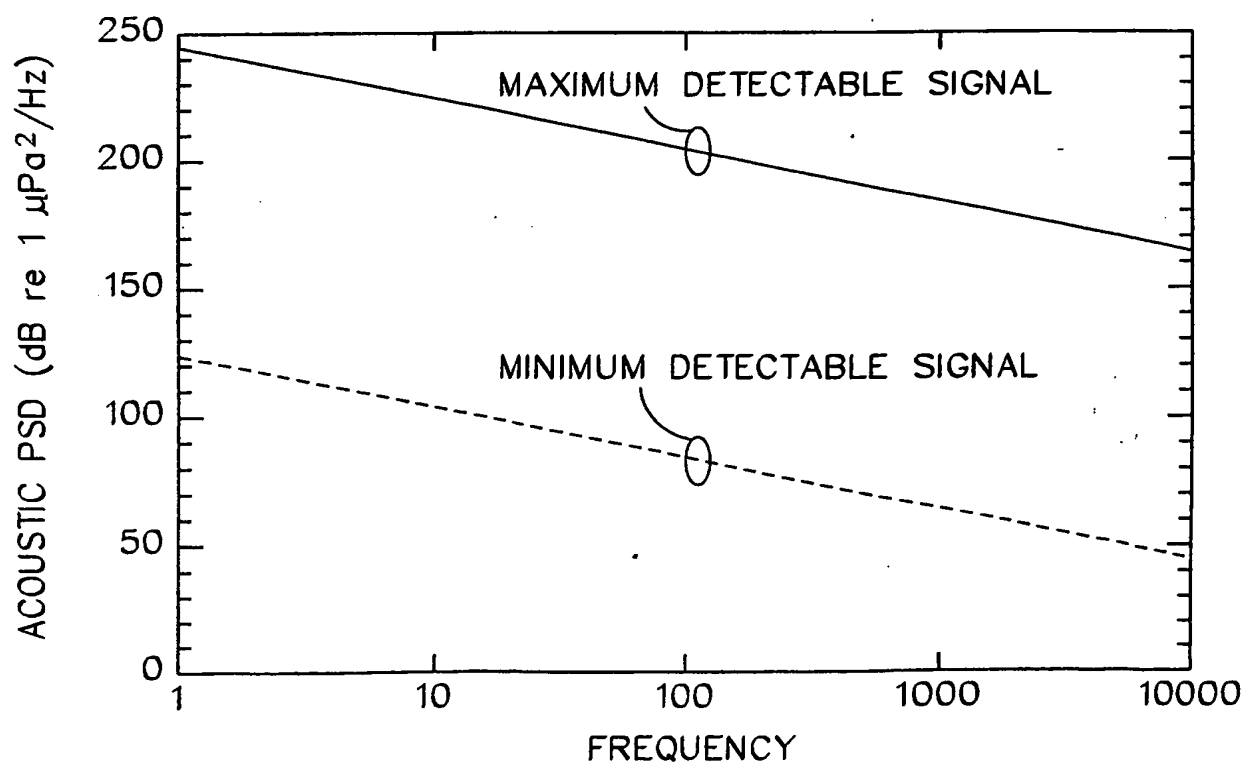
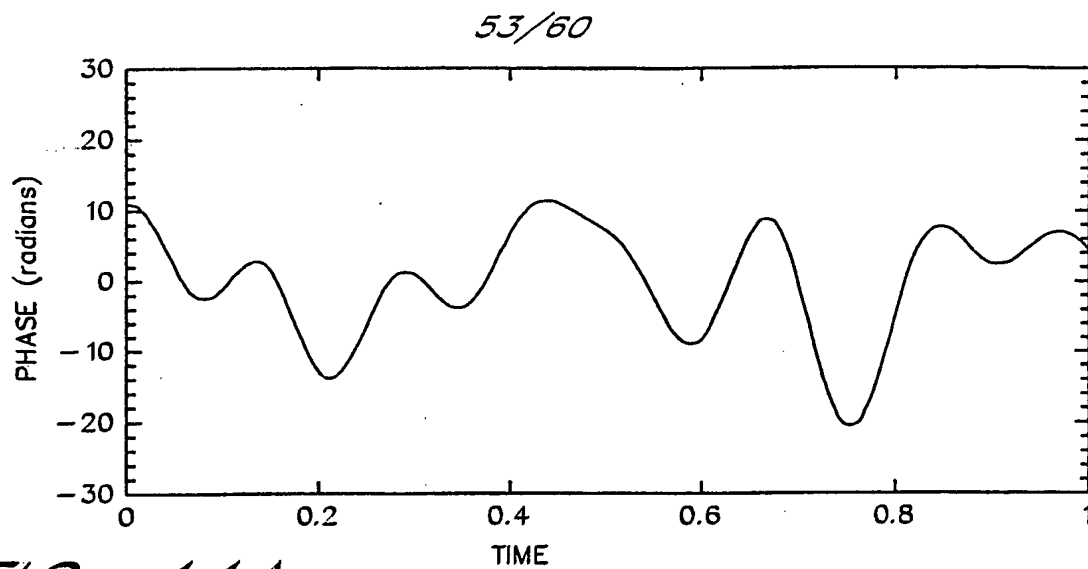
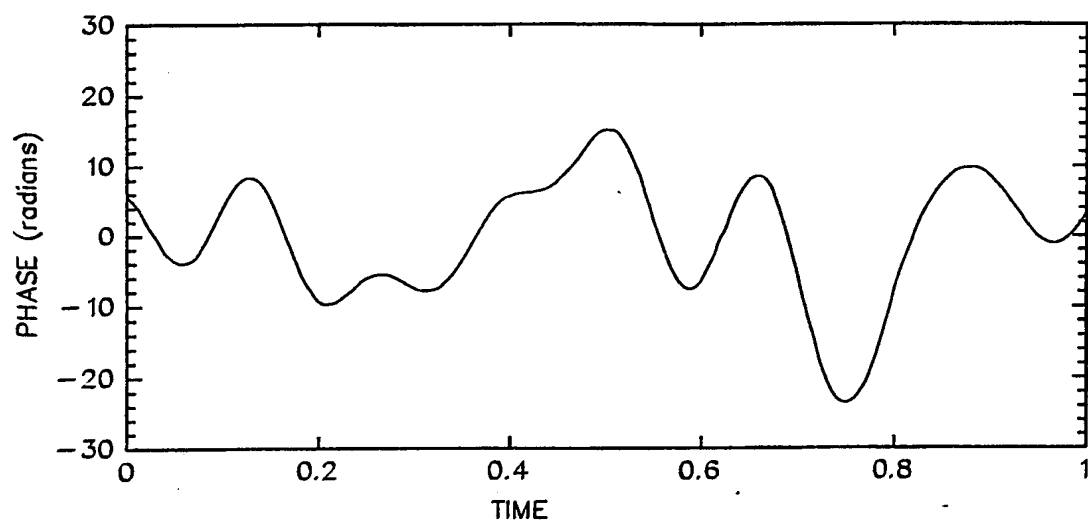
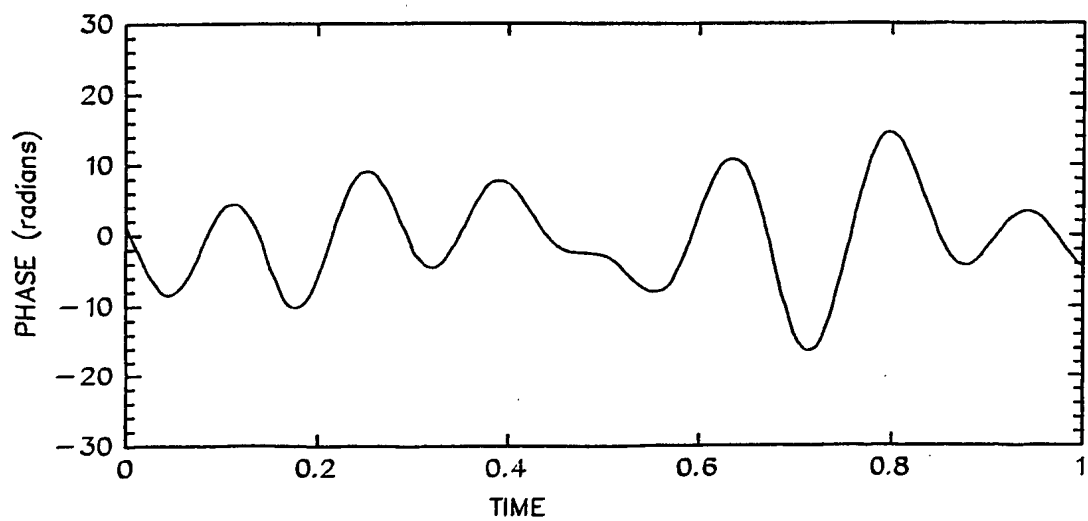


FIG. 43B

*FIG. 44A**FIG. 44B**FIG. 44C*

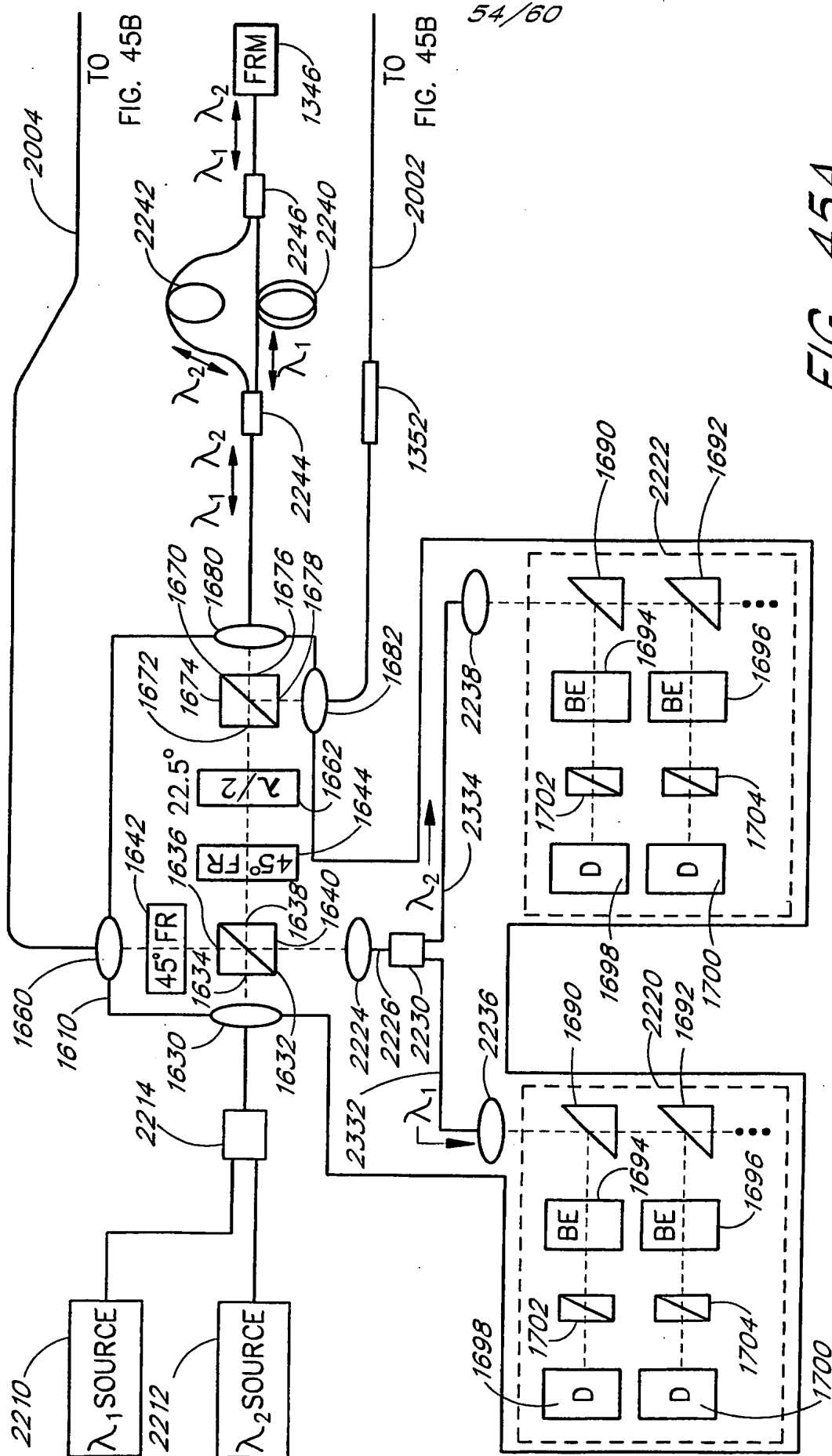


FIG. 45A



55/60

FIG. 45B<sub>1</sub>

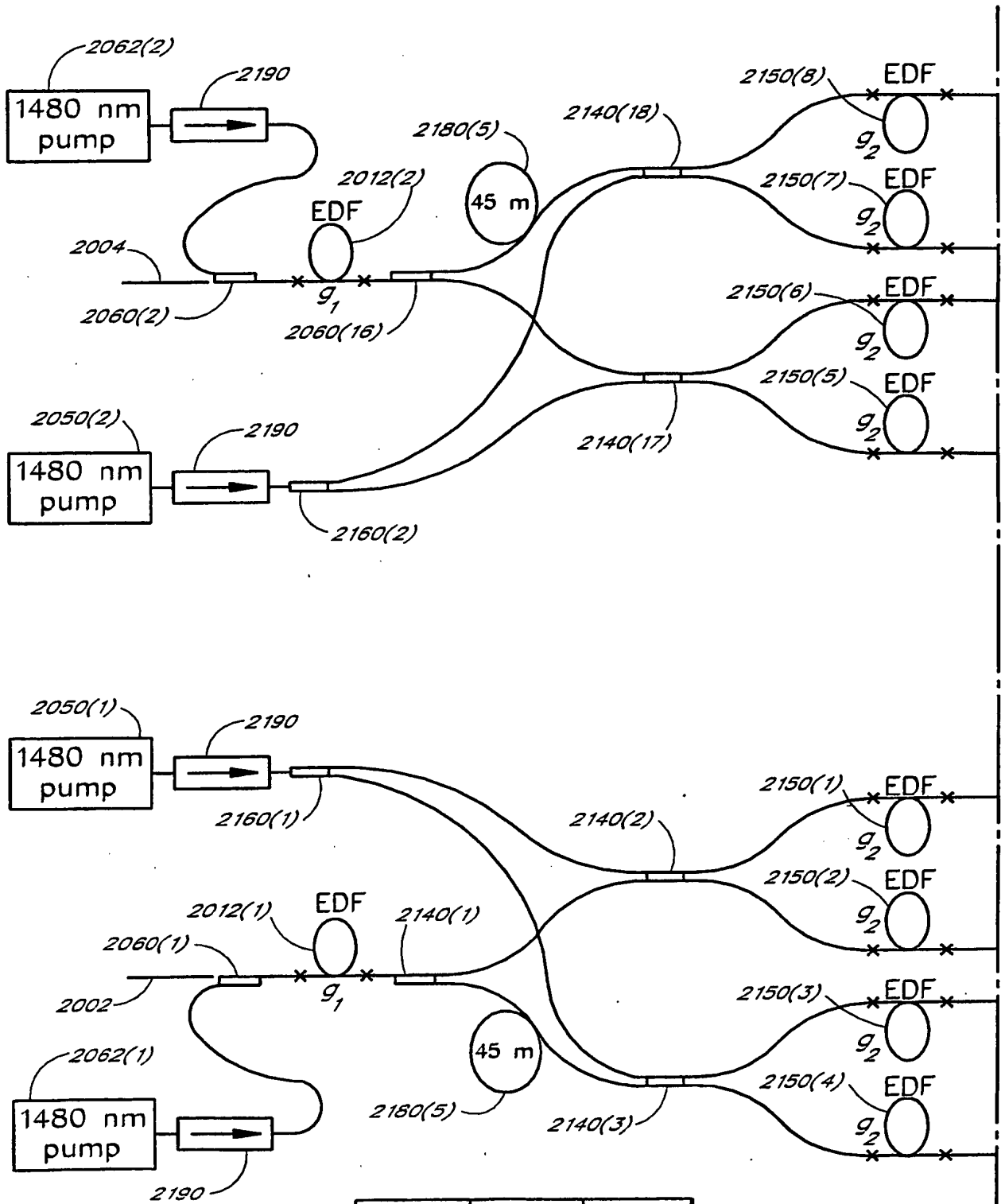
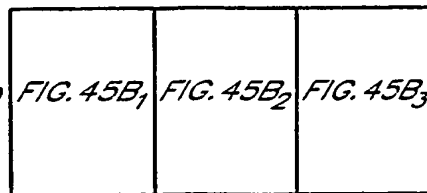


FIG. 45B<sub>1</sub> FIG. 45B<sub>2</sub> FIG. 45B<sub>3</sub>



56/60

← 2100

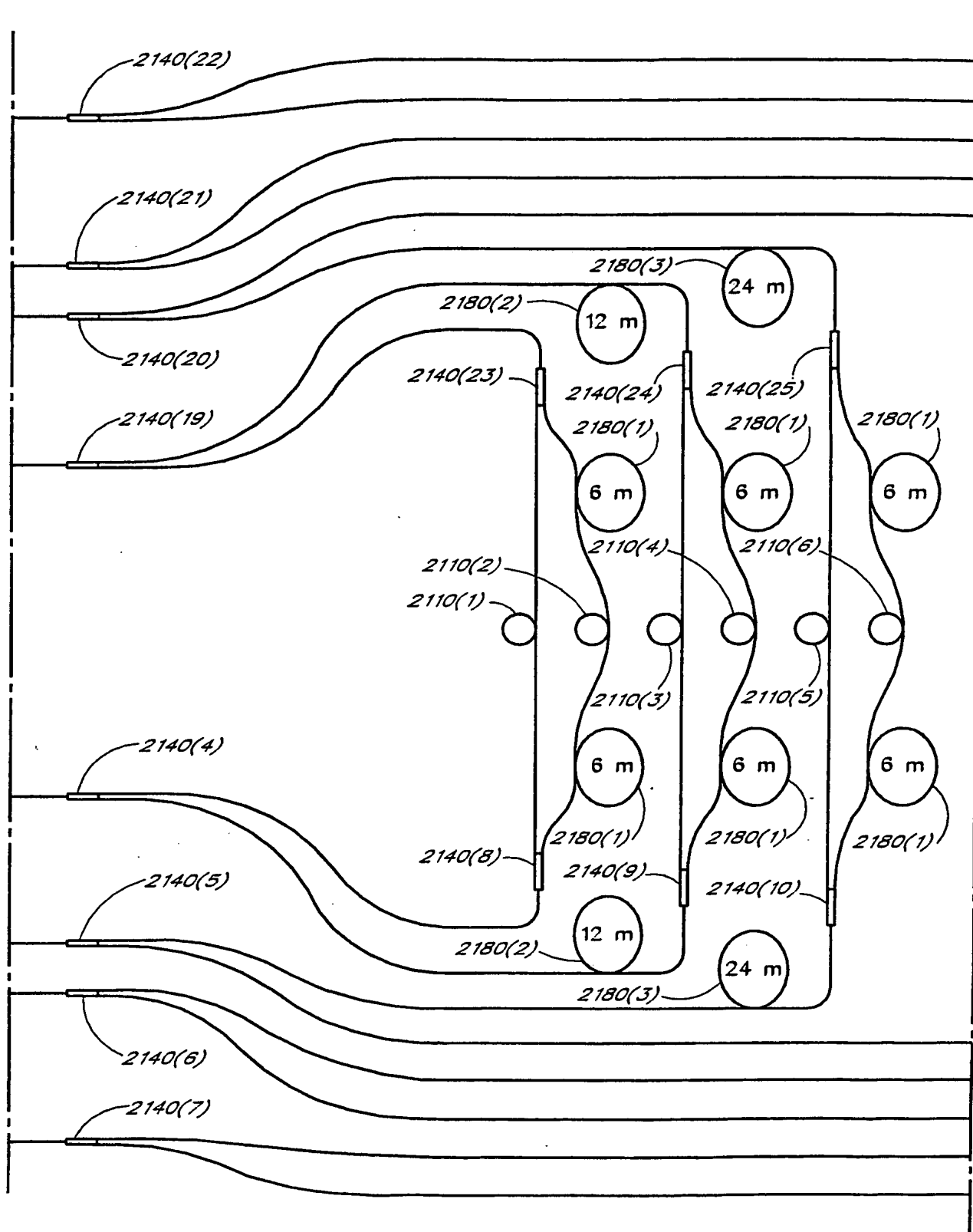
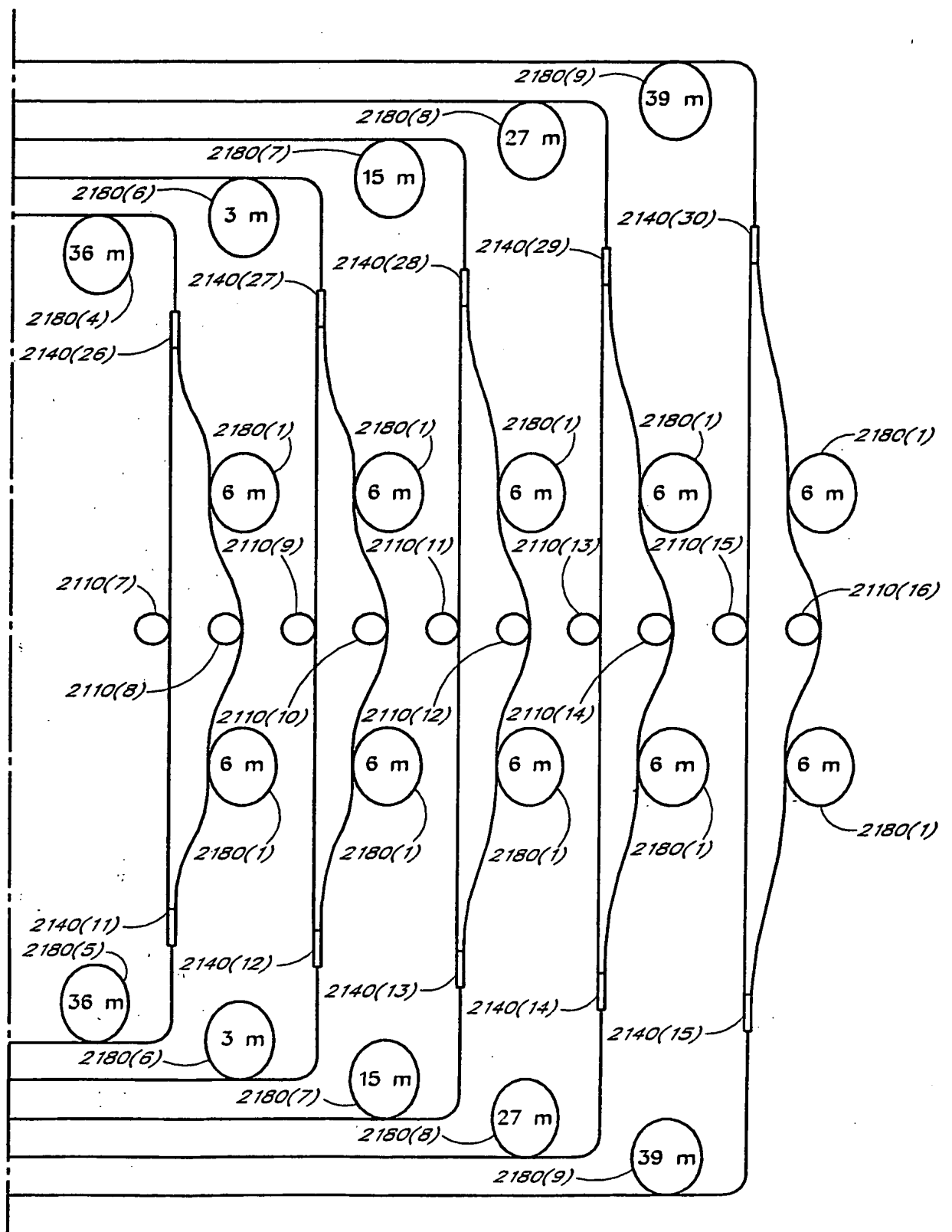


FIG. 45B<sub>2</sub>

57/60

FIG. 45B<sub>3</sub>

58/60

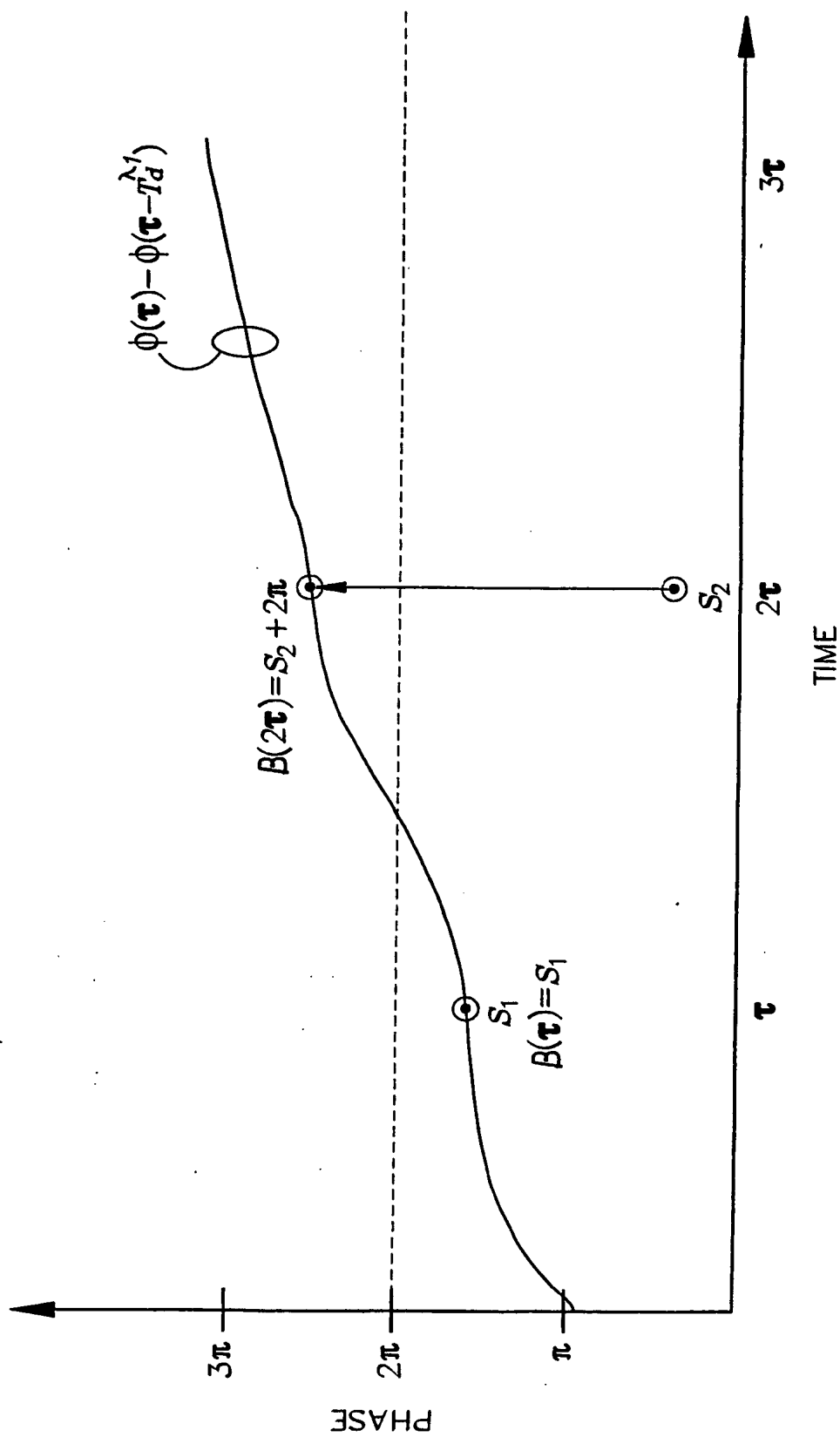


FIG. 46A

59/60

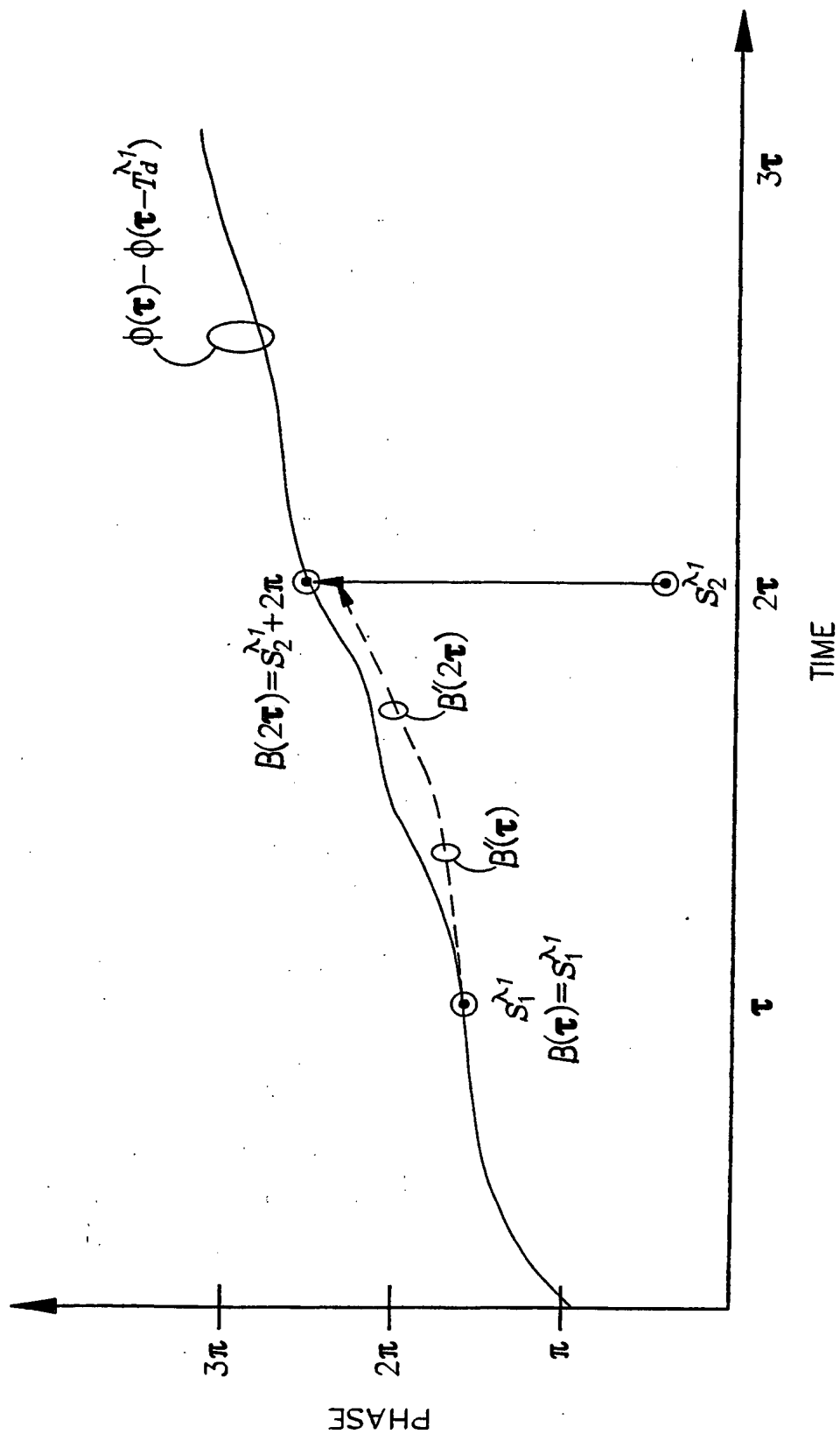


FIG. 46B

60/60

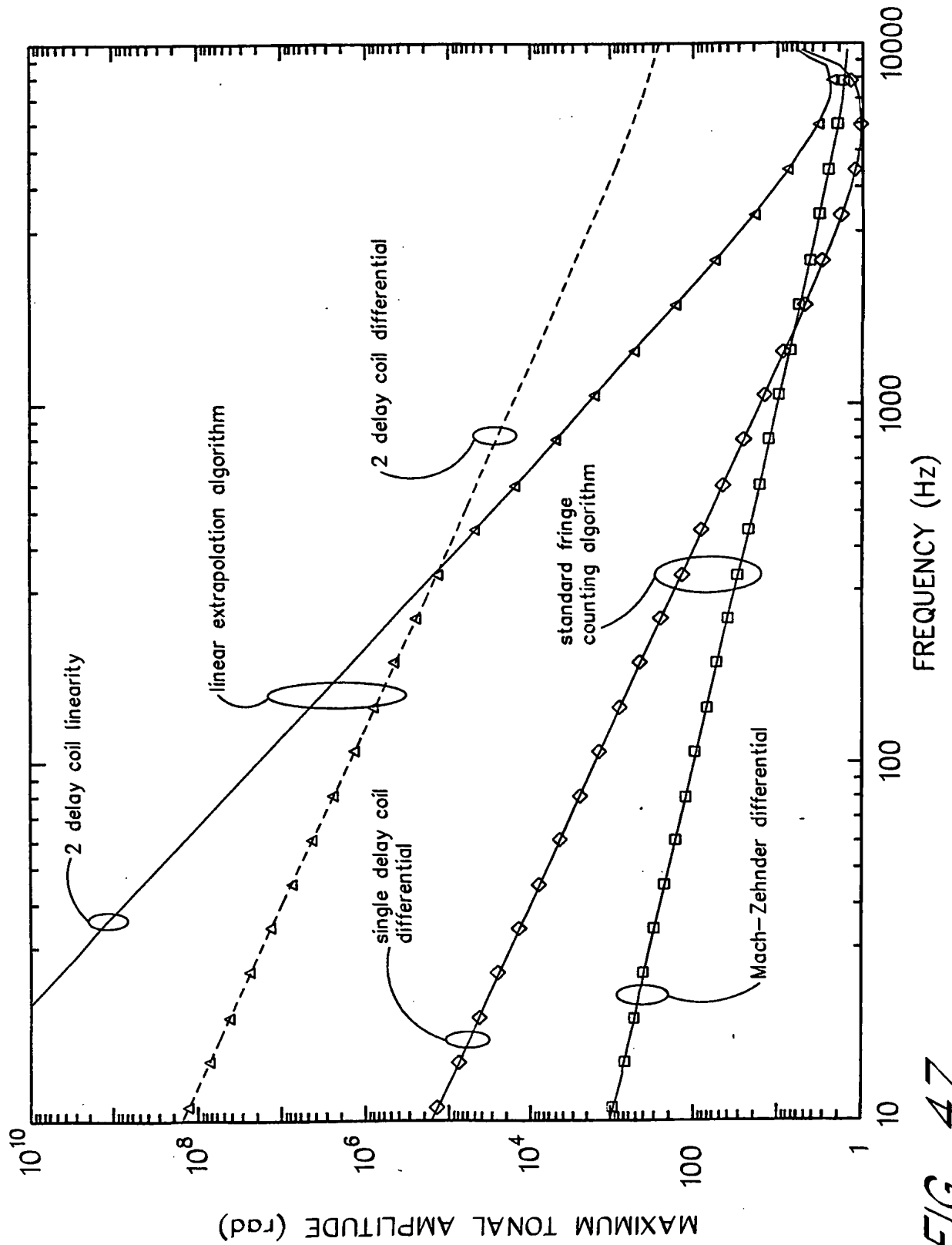


FIG. 47

(19) World Intellectual Property Organization  
International Bureau



(43) International Publication Date  
20 February 2003 (20.02.2003)

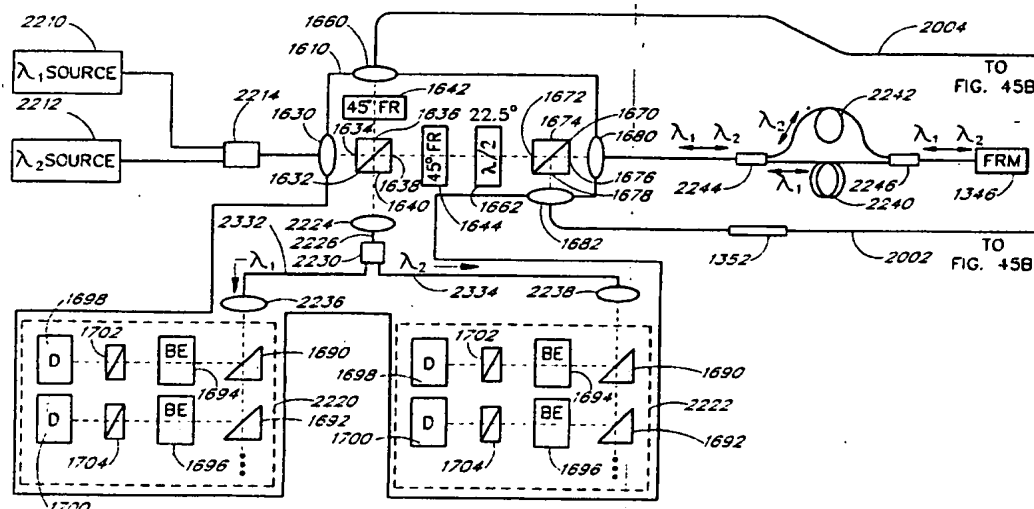
PCT

(10) International Publication Number  
**WO 03/014674 A3**

- (51) International Patent Classification<sup>7</sup>: **H04R 1/44**, G02B 6/00
- (21) International Application Number: PCT/US02/25246
- (22) International Filing Date: 7 August 2002 (07.08.2002)
- (25) Filing Language: English
- (26) Publication Language: English
- (30) Priority Data:  
60/311,757 10 August 2001 (10.08.2001) US  
60/311,874 13 August 2001 (13.08.2001) US  
60/355,657 7 February 2002 (07.02.2002) US
- (71) Applicant: **THE BOARD OF TRUSTEES OF THE LE-  
LAND STANFORD JUNIOR UNIVERSITY [US/US];**  
Stanford University, Stanford, CA 94305 (US).
- (72) Inventor: **VAKOC, Benjamin, J.;** 383 College Avenue,  
Palo Alto, CA 94306 (US).
- (74) Agent: **ALTMAN, Daniel, E.; KNOBBE, MARTENS,  
OLSON AND BEAR, LLP,** 620 Newport Center Drive,  
16th Floor, Newport Beach, CA 92660 (US).
- (81) Designated States (*national*): AE, AG, AL, AM, AT (util-  
ity model), AT, AU, AZ, BA, BB, BG, BR, BY, BZ, CA,  
CH, CN, CO, CR, CU, CZ (utility model), CZ, DE (util-  
ity model), DE, DK (utility model), DK, DM, DZ, EC, EE  
(utility model), EE, ES, FI (utility model), FI, GB, GD, GE,  
GH, GM, HR, HU, ID, IL, IN, IS, JP, KE, KG, KP, KR, KZ,  
LC, LK, LR, LS, LT, LU, LV, MA, MD, MG, MK, MN,  
MW, MX, MZ, NO, NZ, OM, PH, PL, PT, RO, RU, SD,  
SE, SG, SI, SK (utility model), SK, SL, TJ, TM, TN, TR,  
TT, TZ, UA, UG, UZ, VC, VN, YU, ZA, ZM, ZW.
- (84) Designated States (*regional*): ARIPO patent (GH, GM,  
KE, LS, MW, MZ, SD, SL, SZ, TZ, UG, ZM, ZW),  
Eurasian patent (AM, AZ, BY, KG, KZ, MD, RU, TJ, TM),  
European patent (AT, BE, BG, CH, CY, CZ, DE, DK, EE,  
ES, FI, FR, GB, GR, IE, IT, LU, MC, NL, PT, SE, SK,  
TR), OAPI patent (BF, BJ, CF, CG, CI, CM, GA, GN, GQ,  
GW, ML, MR, NE, SN, TD, TG).

[Continued on next page]

(54) Title: TWO DELAY COIL SAGNAC-BASED SENSOR ARRAY





**Published:**

--- with international search report

**(88) Date of publication of the international search report:**

28 August 2003

*For two-letter codes and other abbreviations, refer to the "Guidance Notes on Codes and Abbreviations" appearing at the beginning of each regular issue of the PCT Gazette.*



## INTERNATIONAL SEARCH REPORT

International application No.

PCT/US02/25246

**A. CLASSIFICATION OF SUBJECT MATTER**

IPC(7) : H04R 1/44; G02B 6/00

US CL : 367/149; 385/12, 13; 250/227.14, 227.15, 227.16

According to International Patent Classification (IPC) or to both national classification and IPC

**B. FIELDS SEARCHED**

Minimum documentation searched (classification system followed by classification symbols)

U.S. : 367/149; 385/12, 13; 250/227.14, 227.15, 227.16

Documentation searched other than minimum documentation to the extent that such documents are included in the fields searched

Electronic data base consulted during the international search (name of data base and, where practicable, search terms used)

**C. DOCUMENTS CONSIDERED TO BE RELEVANT**

Category *	Citation of document, with indication, where appropriate, of the relevant passages	Relevant to claim No.
A,P	US 6,278,657 B1 (VAKOC) 21 AUGUST 2001 (21.08.2001), ABSTRACT.	1-4

☐ Further documents are listed in the continuation of Box C.☐ See patent family annex.

## \* Special categories of cited documents:

"A" document defining the general state of the art which is not considered to be of particular relevance

"B" earlier application or patent published on or after the international filing date

"L" document which may throw doubts on priority claim(s) or which is cited to establish the publication date of another citation or other special reason (as specified)

"O" document referring to an oral disclosure, use, exhibition or other means

"P" document published prior to the international filing date but later than the priority date claimed

"T"

later document published after the international filing date or priority date and not in conflict with the application but cited to understand the principle or theory underlying the invention

"X"

document of particular relevance; the claimed invention cannot be considered novel or cannot be considered to involve an inventive step when the document is taken alone

"Y"

document of particular relevance; the claimed invention cannot be considered to involve an inventive step when the document is combined with one or more other such documents, such combination being obvious to a person skilled in the art

"&amp;"

document member of the same patent family

Date of the actual completion of the international search

28 October 2002 (28.10.2002)

Date of mailing of the international search report

30 MAY 2003

Name and mailing address of the ISA/US

Commissioner of Patents and Trademarks

Box PCT

Washington, D.C. 20231

Facsimile No. (703)305-3230

Authorized officer

Daniel Pihulic

Telephone No. 703-308-1113

Form PCT/ISA/210 (second sheet) (July 1998)